Dissertations   UAH Electronic Theses and Dissertations

2007

Three dimensional numerical modeling of a diagonal magnetohydrodynamic accelerator

Matthew William Turner

Follow this and additional works at: https://louis.uah.edu/uah-dissertations

THREE-DIMENSIONAL NUMERICAL MODELING OF A DIAGONAL MAGNETOHYDRODYNAMIC ACCELERATOR

by

MATTHEW WILLIAM TURNER

A DISSERTATION

Submitted in partial fulfillment of the requirements
for the degree of Doctor of Philosophy
in
The Department of Mechanical and Aerospace Engineering
to
The School of Graduate Studies
of
The University of Alabama in Huntsville

HUNTSVILLE, ALABAMA

2007

In presenting this dissertation in partial fulfillment of the requirements for a doctoral degree from The University of Alabama in Huntsville, I agree that the Library of this University shall make it freely available for inspection. I further agree that permission for extensive copying for scholarly purposes may be granted by my advisor or, in his/her absence, by the Chair of the Department or the Dean of the School of Graduate Studies. It is also understood that due recognition shall be given to me and to The University of Alabama in Huntsville in any scholarly use which may be made of any material in this dissertation.
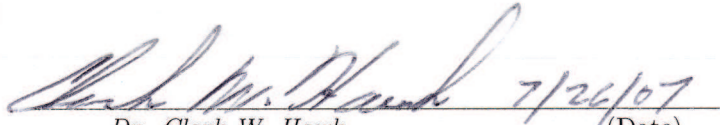
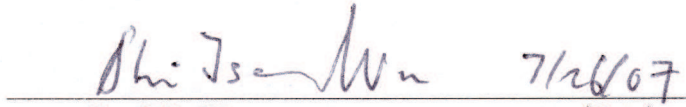_(Matthew William Turner)_

07/26/2007
(date)

DISSERTATION APPROVAL FORM

Submitted by Matthew William Turner in partial fulfillment of the requirements for the degree of Doctor of Philosophy in Mechanical Engineering and accepted on behalf of the Faculty of the School of Graduate Studies by the dissertation committee.

We, the undersigned members of the Graduate Faculty of The University of Alabama in Huntsville, certify that we have advised and/or supervised the candidate of the work described in this dissertation. We further certify that we have reviewed the dissertation manuscript and approve it in partial fulfillment of the requirements for the degree of Doctor of Philosophy in Mechanical Engineering.
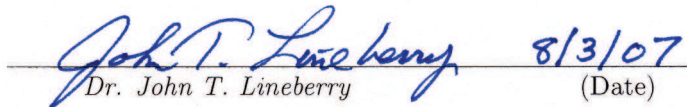
Dr. Clark W. Hawk   7/26/07   (Date)   Committee Chair

Dr. S.T. Wu   7/26/07   (Date)
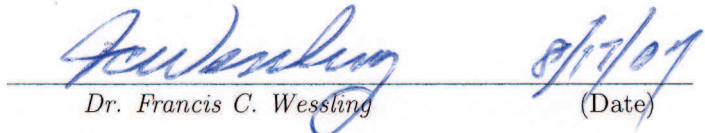
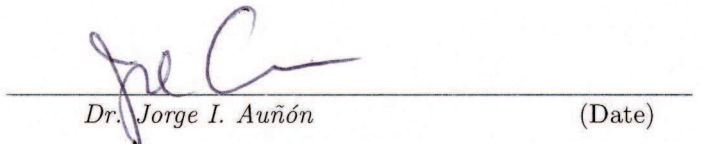Dr. Hugh W. Coleman   7/27/07   (Date)

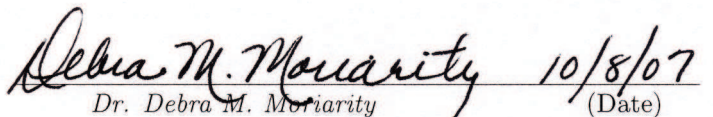Dr. John T. Lineberry   8/3/07   (Date)

Dr. Ron J. Litchford   8/4/07   (Date)

Dr. Francis C. Wessling   8/7/07   (Date)   Department Chair

Dr. Jorge I. Auñón   (Date)   College Dean

Dr. Debra M. Moriarity   10/8/07   (Date)   Graduate Dean

ABSTRACT

School of Graduate Studies
The University of Alabama in Huntsville

Degree   <u>Doctor of Philosophy</u>   College/Dept.   <u>Engineering/Mechanical and</u>

<u>Aerospace Engineering</u>

Name of Candidate   <u>Matthew William Turner</u>

Title   <u>Three-Dimensional Numerical Modeling of a</u>

<u>Diagonal Magnetohydrodynamic Accelerator</u>

The objective of this dissertation is to analyze the NASA Magnetohydrodynamic Augmented Propulsion Experiment (MAPX) using a three-dimensional numerical model—the results of which are intended to increase the understanding of the critical physical processes in the accelerator and provide pre-test configuration recommendations and performance predictions. Because of the three-dimensional (3-D) nature of magnetohydrodynamic (MHD) flows, a 3-D numerical model was required; however, no such numerical model existed for diagonal MHD accelerators.
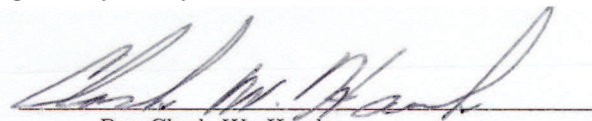
Therefore, a parabolic 3-D numerical model, capable of simulating diagonal MHD accelerator flows, was developed from an existing MHD generator model. This new model can simulate partially ionized flows through the incorporation of the NASA Chemical Equilibrium with Applications code for calculation of thermodynamic and species concentration properties and a numerical technique based on electron-neutral momentum transfer cross-sections to calculate electrical conductivity.

This new 3-D MHD accelerator model was then used to analyze the MAPX accelerator. The recommended configuration for the MAPX accelerator is as follows:

electrodes should have a 45 degree accelerator angle, the applied current should be 100 Ampheres, and the power takeoff should cover 5 electrodes at the entrance of the channel and two electrodes at the exit. Furthermore, the magnet pole flares located in the MAPX electromagnet should remain. Using this configuration, analysis shows an increase of 75% and a decrease of 25% in the cross-sectional averaged values of velocity and total pressure, respectively, from entrance to exit of the accelerator, with an electrical efficiency of approximately 45%. The low MAPX efficiency and total pressure losses result from the following sources of entropy. 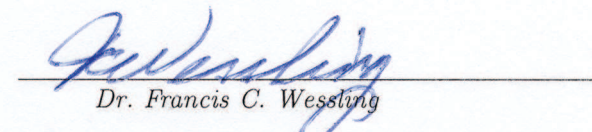The MAPX channel has a high surface-to-volume ratio, which promotes secondary flows and strong localized axial currents. Viscous effects cause the drop in total pressure while axial currents result in large concentrations of electrons near the anode and excessive Joule heating.

This research marks the first in-depth, 3-D numerical analysis of an experimental diagonal MHD accelerator. The results of this research have helped to define the experimental configuration of the MAPX accelerator and offer a better understanding of the critical physical processes—including flow and temperature development, MHD flow interactions, electrical current behavior, total pressure effects, and entropy sources—that occur within a diagonal magnetohydrodynamic accelerator.

Abstract Approval: Committee Chair _____
                                    Dr. Clark W. Hawk

                    Department Chair _____
                                    Dr. Francis C. Wessling

                    Graduate Dean _____
                                    Dr. Debra M. Moriarity

ACKNOWLEDGMENTS

Writing a dissertation is a very humbling process. For starters, it is difficult. When you begin, you think that you will have it finished in no time—then, nine months later, you realize that it is not that easy. However, even more humbling than the level of difficulty is that you realize, even though you are the one receiving the degree and accolades, that this is truly a group effort. Fortunately, I was blessed and lucky to have an incredible support structure—comprised of my committee, family, and friends.

Since I literally would not be here without them, I will start with my family. Unfortunately, my father's parents died when I was younger, so I did not know them very well. However, I do know that they were hard-working and put a lot of emphasis on education—I hope that this dissertation would make them proud. My Grandmother (on my mother's side) taught me to maintain a sunny disposition, and to try to see the bright side of everything—this is very important during the dissertation process. I owe my logical thinking skills to my Grandfather. He, too, was a mechanical engineer, and he taught me, by example, how to approach problems from a logical and reasoning point of view. My mother taught me how to write—and, in my humble opinion, she did quite well. Growing up with a grammarian was not always "fun," but being able to effectively express oneself is paramount to successful research. She also taught me how to strive in the face of adversity—which is useful when writing a dissertation, or doing something as simple as living your life. My father always said

to me, "You can accomplish whatever you put your mind to." After a while, I started to believe him; and, whether it is naive, I believe him still. Finally, even though I would never admit it to them, the (usually) friendly competitive rivalry that I have had with my siblings throughout the years has driven me to better myself in ways that I never would have alone. Each in his/her own way, my family has shaped me into the person I am today.

I was fortunate to have an amazing committee. Dr. Wu is a world-renowned expert in magnetohydrodynamics. The only thing that rivals his intellect is his graciousness—being able to go to him with questions has been a blessing. Dr. Coleman is the world's leader in uncertainty analysis—he literally wrote the book on the subject. Because of his expertise and affability, I was able to go to him with numerous questions throughout this dissertation process. Dr. Lineberry has an encyclopedic knowledge of MHD accelerators and generators—in most cases, he knows all about the MHD devices because he built them, and/or was in charge of the project. He has a "feel" for MHD devices that I can only dream of someday acquiring. Dr. Lineberry's help and advice has been invaluable throughout this project.

Dr. Litchford has helped me on a daily basis throughout my entire graduate career. I started working for Dr. Litchford during my Master's thesis project, where he taught me how to effectively operate an experiment. On this project, however— very different from an experiment—he showed me how to divide the numerical model into manageable sections, and to methodically solve the problems. He has endured my obsessive-compulsive tendencies, and my overly-long emails (I have been known to be a bit verbose). In short, Dr. Litchford taught me "how" one does "proper

research." Dr. Litchford has been the best research mentor I could hope for—as brilliant as he is understanding. Basically, he got me through all this.

In the Spring semester of 1997, my Thermodynamics I professor was Dr. Hawk. At the end of the course, Dr. Hawk asked if I wanted to work for him during that summer—well, it has been a long and hot summer, but I am so thankful that I took the offer. Dr. Hawk has been my academic advisor throughout my graduate career. I like to say that "I have learned so much from Dr. Hawk—and engineering, too." That is not to say that he lacks in engineering expertise—quite the contrary. What I mean, is that Dr. Hawk is more than an engineer or professor—he is an amazing manager and leader. Having a Ph.D. means that I, too, will (hopefully) someday lead others—and when that day comes, I know that I will be prepared, because I learned from the best.

I also owe a huge debt of gratitude to friends and colleagues who have helped me through this dissertation. I must first thank Dr. Robert Rhodes, of the University of Tennessee Space Institute, for his assistance and patience when UAH took control of this project from him. Dr. Rhodes did wonderful work, and it was a pleasure to continue it for him. Nobuomi Sakamoto, of the Nagaoka Institute of Technology in Japan, and I would frequently bounce MHD and programming ideas off each other, while we were both working on independent programs. Dr. Syri Koelfgen, a fellow graduate student, offered great advice during my dissertation and defense preparation. Dr. David Lineberry, also a fellow graduate student, offered excellent advice and counsel; furthermore, Dave is a whiz at uncertainty analysis and thermodynamics (which was also a huge help). Dr. Jason Cassibry probably suffered the most, as he

TABLE OF CONTENTS

LIST OF FIGURES

xix

LIST OF SYMBOLS

SYMBOL DEFINITION

Arabic

a The speed of sound.

$\mathbf{B}$ The magnetic field vector, given in units of Tesla in this dissertation.

c_p Specific heat at constant pressure.

c_v Specific heat at constant volume.

D_{ij} Multicomponent diffusion coefficient.

$\mathbf{E}$ The electric field vector.

$\mathbf{E}_d$ The equivalent electric field—the electrode voltage drop divided by the channel height.

eNe Total charge—the product of electrical charge and the total number of electrons.

$gasK$ The specific gas constant, which is the universal gas constant divided by the molecular weight for a specific gas.

h Enthalpy.

H Channel height.

I Electrical current—typically, total electrical current.

I/O   Input/Output.

$\mathbf{J}$ The current density vector.

J_{ld}	Load current density—load current per unit area.
J_x	Current density in the x-direction.
J_y	Current density in the y-direction.
J_z	Current density in the z-direction.
k	The Boltzmann constant, equal to 1.380 J/K.
K	Loading factor, or the chemical symbol for potassium.
m	Mass.
$\dot{m}$	Mass flow rate.
$Mach$	Mach number.
MW	Molecular weight.
n	Number density, in units of $\#/\text{kg}^3$.
N	Number, as in a total count of something.
Na	The chemical symbol for sodium.
NaK	The chemical symbol for sodium-potassium, the seed used in the MAPX channel.
P	Static pressure.
P_0	Total pressure.
P_{app}	Total applied electrical power density.
P_d	Dissipated power—often referred to as Joule dissipated power, or Joule heating.

P_p	Push power—the portion of the power that is utilized in moving the flow.
q	A charged particle.
q^{mn}	Coefficients to the simplified electron equilibrium Maxwellian distribution function.
q_w	Heat flux at the wall.
$\bar{Q}_{ij}^{(\ell,s)}$	The Maxwellian velocity-averaged collision cross-section between species i and j.
R	Universal gas constant.
t	Time.
T	Temperature.
$\mathbf{u}$	The velocity vector.
u	Velocity in the x-direction.
v	Velocity in the y-direction.
V_d	Electrode voltage drop.
w	Velocity in the z-direction.
W	Channel width.
$\hat{\mathbf{x}}$	The x unit vector. In this dissertation, indicating that a parameter/quantity is in the x-direction.
$\hat{\mathbf{y}}$	The y unit vector. In this dissertation, indicating that a parameter/quantity is in the y-direction.
$\hat{\mathbf{z}}$	The z unit vector. In this dissertation, indicating that a parameter/quantity is in the z-direction.

Greek

β Hall parameter—a dimensionless comparison of the gyral frequency to the collision frequency of a charged particle.

γ The ratio of specific heats.

Δ Dimensionless voltage drop.

η_a Accelerator efficiency.

θ Electric field angle, E_y/E_x. Also used to describe the accelerator or generator electrode angle, as measured from the positive y-axis.

θ_d Diagonalization angle.

θ_w Wall angle.

μ_e Electron mobility, which is the Hall parameter divided by the magnetic field intensity.

μ_ℓ Laminar viscosity.

ρ Mass density (mass divided by volume), typically in units of kg/m^3.

σ Electrical conductivity, typically given in units of S/m.

τ Shear stress.

$\phi(y, z)$ The two dimensional electric potential.

φ The electric field direction.

ψ The total electric potential.

$\Omega_{ij}^{(\ell,s)}$ Collision integral.

Subscripts

a	Refers to accelerator parameters.
app	Refers to an externally applied value/parameter.
e	Used for exit conditions. In some cases, used to indicate electrons.
i, j	Used to indicate that a parameter has two components—typically in the x- and y-directions, respectively.
in	Used for entrance condition.
p	Conditions at some point, p, off the wall.
t	Used to indicated turbulence parameters.
w	Conditions at the wall.
x	Used for quantities in the x-direction. In this dissertation, the x-direction is the axial direction in the channel.
y	Used for quantities in the y-direction.
z	Used for quantities in the z-direction. Sometimes used to indicate "zero" quantities/parameters (that is, those that equal to zero).
1	Used to indicate electrons.

Acronyms

AEDC	Arnold Engineering Development Center.
CEA	The Chemical Equilibrium with Applications code developed by Gordon and McBride at the NASA Glenn Research Center.
DCW	Diagonal conducting wall—relating to diagonal MHD generators and accelerators.

LOX	The oxidizer, liquid oxygen.
MAPX	The Magnetohydrodynamic Augmented Propulsion Experiment.
MGMHD	The Multi-Grid Magnetohydrodynamics numerical model developed by Bouillard, Krazinski, Vanka, and Berry at the Argonne National Laboratory in the 1980s.
MHD	Magnetohydrodynamics.
MSFC	The NASA Marshall Space Flight Center.
NASA	National Aeronautics and Space Administration.
NUT	Nagaoka University of Technology, in Nagaoka, Japan.
PTO	Power takeoff.
UAH	The University of Alabama in Huntsville.
UMF	Uncertainty magnification factor.
UMM	The UAH-MSFC-MGMHD numerical model, described within this dissertation.

Typography

SMALL CAPS	Small capitals are used to abbreviate the name of a numerical model or code. This is not the filename of the program, but the name with which the model is commonly known.
terminal font	Terminal font is used to indicate any name (filename, variable, subroutine, etc.) as it appears in a computer program. That is, terminal font is used for names that appear as they would on a computer screen.
Bold	Bold type is used to identify vectors—that is, quantities that have both magnitude and direction, and, in Cartesian coordinates, consist of x, y, and z components.

For Amy

*Research is what I'm doing
when I don't know what I'm doing.*

—Wernher von Braun

CHAPTER 1

INTRODUCTION

Space is big. You just won't believe how vastly, hugely, mind-bogglingly big it is. I mean, you may think it's a long way down the road to the drug store, but that's just peanuts to space.

—Douglas Adams

1.1 Motivation

The greatest obstacles to interplanetary transport and exploration are the immense time and space scales between celestial objects. Interplanetary distances, for instance, are measured on the scale of hundreds of millions of miles. At closest approach, Mars is two hundred times farther away than the Moon, and Pluto, at closest approach, is six billion miles from Earth. Consequently, human exploration of the solar system will require transportation of massive amounts of equipment and supplies over great distances [3] within relatively short periods of time—a task for which chemical rocket fuels are inadequate, and were actually never intended [4].

This is not to say that chemical-thermal fuels are incapable of interplanetary missions; on the contrary, several studies show that manned missions to Mars are theoretically possible using chemical propulsion, with certain disadvantages [3,5,6].

1

One such disadvantage is the limited energy density with the corresponding poor specific impulse (approximately 450 seconds) of chemical fuels [7,8]. This low specific impulse (I_{sp}) results in increased mission trip times [9], which, among other things, increases the risk of radiation exposure to the crew [10–12]. Clearly, improvements in specific impulse are crucial for successful interplanetary missions. An increase of 100 seconds in the specific impulse of the standard chemical-thermal system could translate into a savings of 50 to 100 days in total trip time for a Mars mission [13], a reduction in the fuel loading of the spacecraft [8], or a reduction in the operating fuel temperature [13].

Electromagnetic thrust augmentation represents one intriguing possibility for improving the fuel consumption of thermal propulsion systems and thereby increasing overall specific energy characteristics. NASA Marshall Space Flight Center is developing the Magnetohydrodynamic Augmented Propulsion Experiment (MAPX)—an experimental research facility for the investigation of the use of cross-field magnetohydrodynamic (MHD) accelerators as a possible thrust augmentation device for thermal propulsion systems [14]. The principle objective of this dissertation is to analyze the NASA MAPX accelerator using a three-dimensional numerical model. The results of this analysis are intended to aid in the understanding of some of the critical physical processes in the accelerator and to provide pre-test performance predictions.

Interest in MHD devices has traditionally focused on their use as electrical generators for commercial central power plants and mobile burst power systems. Magnetohydrodynamic accelerator research has historically focused on linear Faraday accelerators for use in hypersonic testing facilities. The NASA MAPX acceler-

ator constitutes the first experimental analysis of a diagonal MHD accelerator for use in propulsion applications; and consequently, this dissertation represents the first detailed, three-dimensional analysis of a diagonal MHD accelerator.

1.1.1 MHD Accelerator Applications

Generally speaking, chemical-thermal propulsion systems are capable of very high power but low specific energy. The former derives from exceptionally good chemical-to-thermal-to-kinetic energy conversion (greater than 98%) and easily scalable high mass flow rates (*i.e.*, high jet power), while the latter is a direct result of the limited energy content of available chemical fuels (approximately $10\,\mathrm{MJ/kg}$ for LOX/H$_2$) [15]. Furthermore, the thermal limits of existing materials would prevent full utilization of high-energy density fuels, assuming that such fuels were available. The performance of conventional thermal propulsion systems is fundamentally constrained by the specific energy limitations associated with the chemical fuels and the thermal limits of available materials [7]; therefore, it is only logical to consider electrical augmentation of thermal propulsion systems as a plausible means of increasing exhaust velocity and possibly improving specific energy attributes.

An MHD accelerator utilizes the Lorentz Force, a $\mathbf{J} \times \mathbf{B}$ body force, to increase gas velocity and, thus, total pressure and temperature. The essential argument favoring the utilization of a Lorentz Force acceleration mechanism is the ability to avoid the inherent physical limitation associated with pure thermal approaches. Basically, it is more effective to transfer electrical energy into directed kinetic energy instead of first degrading it into thermal energy. Cross-field acceleration is of special interest

in these cases because of its unique capacity for processing large amounts of power under conditions of high mass throughput, such as the mass flow rate of a thermal propulsion system.

The essential requirement for electromagnetic thrust augmentation is sufficient electrical conductivity in the exhaust jet from the thermal propulsion source. This can be accomplished by seeding the combustor flow of the chemical rocket with an alkali metal vapor, such as Cs, Rb, K, and associated compounds. The relatively low ionization potential alkali metals ensures that the energy consumed in the ionization process will only be a small fraction of the available thermal energy, and the relatively low working temperature of the plasma is comparable with current materials and regenerative cooling techniques [16]. Energetic rocket fuels seeded with alkali metals have produced supersonic plasmas with electrical conductivities on the order of 10^2 S/m [17, 18], which is sufficient for significant magnetohydrodynamic interaction [19].

Preliminary performance analyses indicate that the MAPX accelerator can deliver velocity increases of 150% above standard chemical-thermal systems [14], which shows the great promise of MHD diagonal accelerators. However, MHD accelerator research and small-scale MHD accelerator prototypes have focused on the design and production of hypersonic wind tunnels rather than propulsive devices. Testing with these prototype devices has clearly demonstrated flow acceleration [20], but diagnostic limitations have prevented complete delineation of the fundamental physical phenomena. Many uncertainties remain, including, but not limited to the relative importance of electromagnetic versus electrothermal effects, achievable accel-

erator efficiencies, achievable current densities, maximum sustainable axial electric field without inter-electrode arcing, effect of near-wall velocity overshoot phenomena, effect of micro-arcing in the cold electrode boundary layer, multi-terminal loading of diagonal wall configuration, and thermal loading and erosive effects with respect to long-term channel survivability [14]. It is therefore clear that research in magnetohydrodynamic accelerators as a propulsive device is severely lacking; the MAPX accelerator endeavors to answer some of these questions.

1.1.2 Historical Perspective

The origins of cross-field MHD accelerator development can be traced to the end of the 1950s, when it was realized that the Lorentz force could effectively accelerate plasmas to appropriate levels for propulsive devices. Subsequent research programs explored its feasibility in both equilibrium and nonequilibrium ionization conditions [21–27]. However, interest in MHD accelerators quickly waned as other electric propulsion technologies rose in importance and maturity.

Around the same time, because of the requirements of the military and the manned space program, a need arose for aerodynamic test facilities capable of simulating a broad range of hypersonic flight conditions—a task for which the traditional arc-heater based systems, with their lower stagnation pressures, were inadequate. Because of this, Ring [19], at the United States Air Force (USAF) Arnold Engineering Development Center (AEDC), and Wood [28], at the NASA Langley Research Center (LRC), independently recognized that MHD acceleration of an arc-heater exhaust was an effective non-thermal means of adding energy and momentum to a flow and

therefore achieving the required increase in stagnation pressure. Furthermore, Ring showed that seeded air could be accelerated to hyper-velocities at densities relevant to hypersonic flight [19].

The NASA Langley Research Center pioneered the development of MHD accelerators and sustained a productive research program for more than a decade. The initial research concentrated on small-scale, proof-of-principle experiments, consisting of a 1.0 cm square, 8.7 cm long segmented Faraday channel, which demonstrated a 50% increase in velocity and a 100% increase in stagnation pressure [29, 30]. The group's second accelerator was designed and constructed to serve as a pilot model for a practical scale device [31, 32]. The 2.54 cm square by 30 cm long channel yielded a 3-fold increase in velocity. The group's third and final accelerator was a 20 MW facility based on a 6.35 cm square by 50 cm long segmented Faraday channel, which was unfortunately limited to preliminary testing [33,34]. The NASA Langley program was very successful, as their analysis, engineering, and technology provide value to contemporary efforts.

The USAF conducted two parallel MHD accelerator programs at AEDC during the 1960s to fulfil its own hypersonic testing requirements: the LORHO (low density focus) and HIRHO (high density focus) programs [35]. The LORHO program was formulated as a long-term technology development plan, beginning with proof-of-concept experiments, advancing to pilot scale facility, and ending with a full-scale steady-flow facility. The HIRHO was formulated to address high-density hypersonic flight regimes of interest to the USAF, and like LORHO, it was envisioned as a three-

phase program from proof-of-concept, through pilot scale program, to full-scale test facility.

The LORHO proof-of-concept experiments, concentrating primarily on potassium seeded air, resulted in three different Faraday accelerator configurations using a 1.2 MW arc-heater and a 2 Tesla magnetic field, demonstrating 100% increases in velocity [36, 37]. The follow-on 20 MW pilot scale facility was designed as a matched MHD generator/accelerator system [38, 39]—the idea being that the MHD generator would provide the required power to the MHD accelerator. The rocket-driven MHD Hall generator was successfully fired with toluene, producing 18 MW of electrical power. A two-terminal Diagonal Conducting Wall (DCW) MHD accelerator was designed and built, but unfortunately never tested. Brogan, the principle architect of the design, recently published a summary and critique of this innovative system [39]. The design principles and experience derived for the LORHO DCW accelerator are of special interest and importance to the MAPX program, which is also based on a two-terminal diagonalized channel [14].

The HIRHO proof-of-concept experiments were implemented through MHD augmentation of the AEDC-VKF Tunnel J shock tube facility [40]. The diverging Faraday accelerator used potassium-seeded air as the driven gas, and demonstrated an 80% increase in velocity. More importantly, these experiments demonstrated an electric-to-kinetic conversion efficiency of at least 85%. Unfortunately, the HIRHO program was cancelled at this stage, as interest in hypersonic flight declined.

Reentry vehicle development during the 1970s maintained a modest interest in MHD augmented, high-enthalpy test facilities [41]. Fortunately, the 1970s con-

cern for energy resulted in major new programs in the application of MHD power generation for the utility industry; thus, research and development programs into MHD generator technology began [42–48]. In the accelerator environment, current densities and wall heat loads are more severe than the generator operating conditions, but the extensive generator technology base provides excellent resources for accelerator technology. Super-conducting magnet technology, high-temperature materials, high-current electrical power generation and control, advanced cooling technology, and computational fluid dynamics and heat-transfer codes are some of the critical technological areas that saw improvement during this period.

A renewal of hypersonic flight vehicle research in the mid-1980's, along with hypersonic air-breathing development, brought new interest to MHD-augmented simulation facilities [49, 50]. The AEDC efforts in the HIRHO and LORHO programs established a major portion of the technical base unique to MHD accelerator development [35, 51]. Litchford *et al.* [14] contains a more complete history of MHD accelerator research and Crawford *et al.* [20] contains an extensive list of historical references for further reading.

1.1.3 Current Research and Development Programs

Recently, MHD research and development has seen a rise in popularity. Much of the new research, including this dissertation, focuses on computer simulations and modeling of MHD flows—a task that until the late 1990s, could not be accomplished by anything smaller than a mainframe computer. There are also some interesting new MHD flight concepts, including MHD thrust augmentation and MHD energy-bypass.

This section outlines some of the current MHD research and development programs that are pertinent to this dissertation.

Even with the recent advances in computer technology, three-dimensional numerical simulation of MHD flows remains processor intensive; therefore, some research groups choose to focus on other aspects of MHD modeling. The Computational Plasma Dynamics Research Laboratory at Kettering University began with a one-dimensional Hall thruster modeling program [52–54] that evolved into a two-dimensional modeling program [55]. While it is generally accepted that one-dimensional and two-dimensional models cannot completely describe the magneto-hydrodynamic processes [20], Roy and Pandey offer an interesting description of the plasma-wall interaction [52] and, just as this dissertation discusses in Section 4.2.2, they use electron momentum-transfer cross-sections to determine electrical conductivity [55]. Wichita State University [56–59] and the Air Force Research Laboratory (AFRL) at the Wright-Patterson Air Force Base [60] have independent programs simulating supersonic magnetohydrodynamic flow over a flight vehicle. While this work is two-dimensional and not directly related to MHD channel flow, they do offer some interesting perspectives on the MHD boundary and shear layers.

Princeton University has a two-dimensional MHD accelerator modeling program, with plans for experimental verification [61, 62]. The goal of this project is to accelerate unseeded cold hypersonic flow using nonequilibrium electrical conductivity sustained by electron beams to enhance the performance of hypersonic wind tunnels. While this research focuses on Faraday accelerators ionized by electron beams,

their theoretical analysis of partially and weakly ionized plasmas, which is of special interest to this research, is extremely thorough [62].

Many current research programs are using different three-dimensional numerical modeling techniques to simulate magnetohydrodynamic flows. Kyoto University started with a three-dimensional parabolized Navier-Stokes and two-equation turbulence model [63], and most recently changed to a time-dependent fully three-dimensional Navier-Stokes without turbulence model [64]. In both cases, they simulate MHD generators and use a curve fit to calculate electrical conductivity, but these simulations allow for the comparison of parabolized and non-parabolized three-dimensional calculations. Perhaps the most sophisticated and comprehensive engineering MHD simulation capability as been established by Merkle using a full three-dimensional Navier-Stokes with two-equation turbulence numerical model [65–68] where, in order to remove physical difficulties with boundary conditions, the computational domain is extended to encompass the plasma channel, the conducting and dielectric walls, and the surrounding air. However, Merkle's model assumes that the electrical conductivity of the flow is either fixed or a function of the equilibrium ionization. Because of the extended computational domain, convergence times for this model are on the order of weeks.

The MHD research program at the Nagaoka University of Technology (NUT) is of special interest to this dissertation. Initially, their research efforts began with a one-dimensional numerical model for simulation of a linear Faraday accelerator with a non-equilibrium working fluid [69]. This code later evolved into a quasi-one-dimensional numerical model that could simulate Faraday, Hall, and diagonal acceler-

ators in chemical and thermal equilibrium [70]. Recently, the group has acquired and improved a parabolic three-dimensional numerical model, which they compared to their one-dimensional model [71]. Improvements to their parabolic three-dimensional code allowed them to simulate Faraday, Hall, and diagonal accelerators and generators, with a Hall Current Neutralized (HCN) option while in diagonal mode [72, 73], which is very similar to the numerical model discussed in this dissertation. The NUT simulation code, however, lacks a proper power takeoff (PTO) scheme and uses a transport property model limited to a temperature of 4000 K, which is inadequate for most near-wall simulations in the MAPX accelerator.

The NASA Ames Research Center (ARC) currently has theoretical and experimental research programs studying whether a magnetohydrodynamic energy-bypass scheme can improve the performance of a scramjet propulsion system [74–81]. Basically, an MHD generator upstream of the scramjet combustion chamber slows the flow so that the Mach number at the entrance of the combustion chamber is kept below a specified value, and an MHD accelerator downstream of the combustion chamber accelerates the flow, expending the electrical power produced by the generator [74]. The ARC research team began initial theoretical analysis of the MHD Energy-Bypass with a one-dimensional code [75], to which they later added real gas [76] and non-equilibrium effects [79]. Researchers at Iowa State University aided the ARC team with a parabolic three-dimensional model, using frozen flow and constant conductivity assumptions [77].

As part of their research program, the NASA Ames Research Center also has an experimental, shock-tube driven MHD channel, physically located in the Ames

electric arc shock tube (EAST) facility [78]. The powered section of the MHD channel is 21.59 cm long, has a constant width of 2.03 cm, and diverges in height from 1.37 cm at the first electrode to 1.95 cm at the last electrode. The primary mode of operation for the MHD channel will be a segmented Faraday accelerator, but the electrodes can be connected into Faraday, Hall, or diagonal configurations in both accelerator and generator modes. With a magnetic field of 0.92 Tesla, tests showed a velocity increase of 40%, and the researchers predict a velocity increase of 120% with a magnetic field of 3.0 Tesla. Researchers at Iowa State University simulated the ARC MHD accelerator with a parabolic three-dimensional numerical model, using constant or curve fit transport properties [80, 81].

Other research teams have recently performed theoretical studies of the magnetohydrodynamic scramjet energy-bypass. At the AFRL, researchers modeled the MHD scramjet energy-bypass system using a three-dimensional numerical model, with assumed conductivity profiles [82]. This analysis showed the potential of the MHD energy-bypass scheme, but the researchers concluded that more analysis and a better conductivity model is required. Researchers at the NASA Marshall Space Flight Center (MSFC) performed a thermodynamic cycle analysis of the MHD energy-bypass for hypersonic airbreathing engines [83]. They concluded that the energy-bypass scheme extends the operational Mach number envelope of conventional airbreathing engines, but that the system performance is extremely sensitive to nonisentropic losses in the MHD devices. Riggins, at the University of Missouri-Rolla, made similar observations in his analysis of the MHD energy-bypass for high speed airbreathing engines [84]. Moreover, Riggins stated that the MHD energy-bypass engine actually has lower

performance that traditional scramjet engines due to additional irreversibility and cooling requirements associated with the MHD components, and total pressure losses associated with the inverse cycle itself. Riggins' claims, however, are not without dissent [85, 86].

Clearly, magnetohydrodynamic research continues to progress, but much work remains. Most of the current research programs focus on numerical modeling of MHD flows. It should be noted, however, that even with recent developments in computing technology and MHD simulations, all of these numerical models are forced to make trade-offs, sacrifices, and assumptions—typically, in the modeling of transport properties in the flow (specifically, frozen flow and electrical conductivity assumptions). There have also been recent developments in experimental MHD research. This section outlined the MHD energy-bypass concept, while MHD thrust augmentation (the NASA MAPX accelerator) is discussed in Chapter 2.

1.2   Basic MHD Relations

Throughout this dissertation, electromagnetic acceleration and power generation is described using magnetohydrodynamics—where one assumes the ionized gas medium is a continuum fluid whose physical properties may be adequately characterized by a set of bulk parameters and whose dynamical behavior may be represented by an appropriate set of continuum conservation relations. Specific particle motions are used to aid in the description of the underlying physical phenomena, but all calculations and numerical modeling described herein assume the replacement of the discontinuous microscopic medium with a hypothetical continuum—with the notable

exceptions of electrical conductivity and Hall parameter, which are calculated using electron momentum-transfer cross-sections, as detailed in Section 4.2.2.

Magnetohydrodynamics essentially adds certain electromagnetic components to the standard equations of fluid dynamics. To the standard fluid transport properties of viscosity and thermal conductivity, MHD adds a bulk electrical conductivity. The Lorentz force, an electromagnetic body force, is added to the standard gasdynamic equation of motion. A term that allows for electric energy input is added to the energy equation, and ionization effects appropriately modify the equation of state and caloric relation. The magnetohydrodynamic equation set is closed using Maxwell's Equations and suitable constitutive relations, including Ohm's Law. Detailed development of this system of magnetohydrodynamic equations is well documented in texts devoted to this subject [15,87–89]. In the notation employed in this dissertation, these relations are expressed in the following manner.

Conservation of Mass:

$$\frac{\partial \rho}{\partial t} + \nabla \cdot (\mathbf{u}\rho A) = 0 \tag{1.1}$$

Equation of Motion:

$$\rho \left(\frac{\partial \mathbf{u}}{\partial t} + \mathbf{u} \cdot \nabla \mathbf{u} \right) = -\nabla p + (\mathbf{J} \times \mathbf{B}) + \mathbf{f}_{\mathrm{v}} \tag{1.2}$$

Energy Balance:

$$\rho \left(\frac{\partial}{\partial t} + u \cdot \nabla \right) \left(c_p T + \frac{u^2}{2} \right) = \frac{\partial p}{\partial t} + \mathbf{J} \cdot \mathbf{E} + \phi_t + \phi_v - \phi_r \tag{1.3}$$

Here t, p, ρ, c_p, and T are the time, pressure, density, specific heat, and absolute temperature of the gas, respectively; $\mathbf{u}$ is the flow velocity; $\mathbf{J}$, $\mathbf{E}$, and $\mathbf{B}$ are the current density, electric field, and magnetic field, respectively. Equation 1.3 assumes ideal gas. The symbols $\mathbf{f}_v$, ϕ_t, ϕ_v, and ϕ_r represent the net viscous body force density, the net thermal input by conduction processes, the net viscous dissipation, and the net radiant energy loss per unit volume, all of which, for the purposes of this simple derivation, are neglected.

The appearance of the Lorentz force, $\mathbf{J} \times \mathbf{B}$, as the electromagnetic body force in the equation of motion requires no explanation. However, the representation of the rate of total electric energy input, or power density, as $\mathbf{J} \cdot \mathbf{E}$, without any mention of $\mathbf{B}$, is not as obvious. In Equation 1.3, $\mathbf{J} \cdot \mathbf{E}$ actually represents both a dissipative, or Joule-heating, component and a useful work component; the latter of which is equal to the scalar product of the Lorentz force with the free stream velocity, and is known as the push power [90].

The conservation equations must be supported by an equation of state,

$$p = p(\rho, T), \tag{1.4}$$

or the Ideal Gas Law,

$$p = \rho RT. \tag{1.5}$$

A caloric expression relating the specific heat or specific enthalpy of the medium to its other thermodynamic properties,

$$c_p = c_p(\rho, T) \tag{1.6}$$

or

$$h = h(\rho, T), \tag{1.7}$$

is also required. While all of the transport coefficients—electrical conductivity, viscosity, thermal conductivity, and radiation—may be tensors, all except electrical conductivity,

$$\boldsymbol{\sigma} = \boldsymbol{\sigma}(\rho, T, E, B), \tag{1.8}$$

participate only in $\mathbf{f}_v$, ϕ_t, ϕ_v, and ϕ_r, and, therefore, they will be neglected in this exercise.

Only three of Maxwell's equations are strictly needed:

$$\nabla \times \mathbf{E} = -\frac{\partial \mathbf{B}}{\partial t}, \tag{1.9}$$

$$\nabla \times \mathbf{H} = \mathbf{J}, \tag{1.10}$$

and

$$\nabla \cdot \mathbf{B} = 0, \tag{1.11}$$

where the following electromagnet constitutive relations are almost always assignable to their vacuum values,

$$\mathbf{D} = \epsilon_0 \mathbf{E} \tag{1.12}$$

and

$$\mathbf{B} = \mu_0 \mathbf{H}, \tag{1.13}$$

where $\mathbf{D}$ is the electric displacement (assuming no polarization), and $\mathbf{H}$ is simply referred to as "$\mathbf{H}$" [91] (assuming no magnetization). Finally, closing the magnetohydrodynamic system of equations, is the generalized Ohm's Law, neglecting diffusion, electron inertia, and ion slip,

$$\mathbf{J} = \sigma \left(\mathbf{E} + \mathbf{u} \times \mathbf{B} \right) - \mu_e \left(\mathbf{J} \times \mathbf{B} \right), \tag{1.14}$$

where the electron mobility, μ_e, can be calculated by dividing the Hall parameter, β, by B, the magnetic field strength, giving $\mu_e = \beta/B$. The calculation of the electrical conductivity, σ, is discussed in detail in Section 4.2.2.

The Hall parameter can be thought of as a ratio of the particle's gyral, or cyclotron frequency, ω, to its collision frequency, ν_c, where

$$\omega = \frac{eB}{m_e}, \tag{1.15}$$

and where the collision frequency is usually expressed in terms of its inverse, the mean free time between collision,

$$\tau = \frac{1}{nQc_e}.$$ (1.16)

The electron Hall parameter can therefore be expressed as

$$\beta = \omega\tau = \frac{eB}{m_e nQc_e},$$ (1.17)

where, e, m_e, and c_e are the electron charge, electron mass, and electron mean random thermal velocity, respectively. The momentum-transfer cross-section is represented by Q, and n is the electron number density. From Equation 1.17, it is clear that, for a given plasma, increasing the magnetic field strength (which increases the particle's cyclotron frequency in relation to its collision frequency) would raise the Hall parameter.

It is important to note that the preceding equation set employs the magneto-hydrodynamic assumptions [15], which basically state that insignificant terms can be neglected. The displacement current term, $\partial\mathbf{D}/\partial t$, is neglected from Equation 1.10 because it is insignificant in comparison to the conduction current term [15, 16, 92]. Accordingly, current due to the transport of excess charge, $\rho_e\mathbf{v}$, is also insignificant in comparison to the conduction current, and can be neglected [15, 92]. Lastly, the electrostatic body force, $\rho_e\mathbf{E}$, on a laboratory or flight-vehicle scale, is several orders of magnitude less than the $\mathbf{J} \times \mathbf{B}$ portion of the Lorentz force [15], and can therefore be neglected from the equation of motion [16, 92], Equation 1.2. (On a planetary
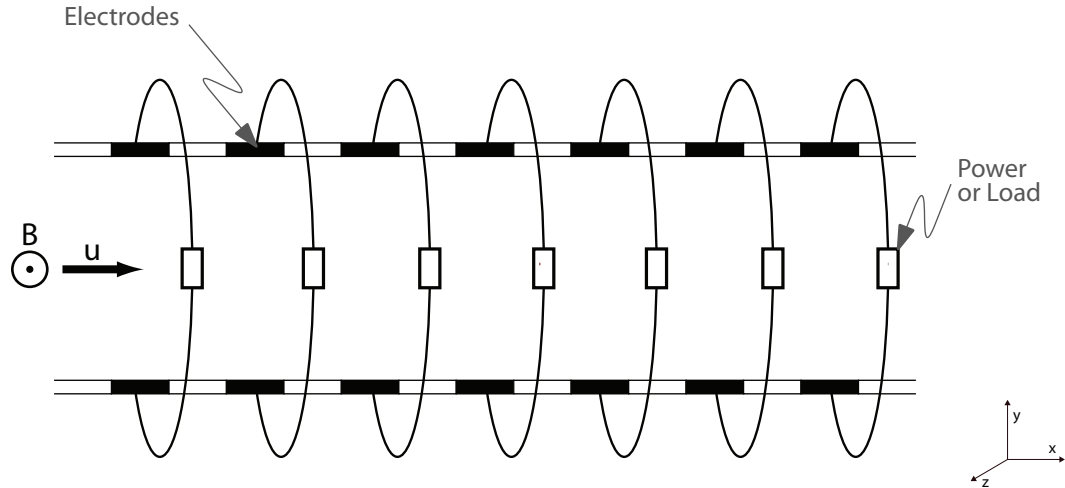
Figure 1.1: A simplified linear, segmented, cross-field MHD channel.

scale, however, the electrostatic body force can actually be larger than the Lorentz force, and can therefore not be neglected from the equation of motion.)

It is obvious from Equations 1.2, 1.3 and 1.14 that current density, $\mathbf{J}$, plays a key role in magnetohydrodynamic channel flow. Therefore, to determine MHD channel characteristics and configurations, it is necessary to solve the generalized Ohm's Law, Equation 1.14, for the individual, x-y-z, components of the current density. First, it will simplify the equations to define $\boldsymbol{\xi}$ as

$$\boldsymbol{\xi} = \mathbf{E} + \mathbf{u} \times \mathbf{B}, \tag{1.18}$$

which is the sum of the electric and motional EMFs. Therefore, Equation 1.14 can be rewritten as

$$\mathbf{J} = \sigma\boldsymbol{\xi} - \frac{\omega\tau}{B}\left(\mathbf{J} \times \mathbf{B}\right). \tag{1.19}$$

Consider a simple MHD channel, as shown in Figure 1.1, assuming a right-handed coordinate system where the magnetic field is only in the positive $\hat{\mathbf{z}}$ direction, $\mathbf{B} = B(z)$. The Lorentz force term can be expressed as

$$\mathbf{J} \times \mathbf{B} = \begin{vmatrix} \hat{\mathbf{i}} & \hat{\mathbf{j}} & \hat{\mathbf{k}} \\ J_x & J_y & J_z \\ 0 & 0 & B_z \end{vmatrix} = J_y B \hat{\mathbf{i}} - J_x B \hat{\mathbf{j}}, \tag{1.20}$$

which leaves the components of $\mathbf{J}$ being

$$J_x = \sigma \xi_x - \omega \tau J_y, \tag{1.21}$$

$$J_y = \sigma \xi_y + \omega \tau J_x, \tag{1.22}$$

and

$$J_z = \sigma \xi_z. \tag{1.23}$$

Isolating the individual currents gives

$$J_x = \frac{\sigma}{1 + \omega^2 \tau^2} \left(\xi_x - \omega \tau \xi_y \right), \tag{1.24}$$

$$J_y = \frac{\sigma}{1 + \omega^2 \tau^2} \left(\xi_y + \omega \tau \xi_x \right), \tag{1.25}$$

and J_z is given in Equation 1.23. The importance of the individual current densities and how they relate to the different MHD channel modes and configurations is discussed in the following sections.

1.2.1   MHD Modes

Depending on the direction of the Lorentz force, $\mathbf{J} \times \mathbf{B}$, vector, an MHD channel can be classified as a generator or an accelerator. Obviously, if the Lorentz force vector points in the direction opposite the primary flow, this would tend to decrease the flow velocity by extracting energy from the flow, and is therefore a generator. If the Lorentz force vector points in the same direction as the primary flow, it acts to add energy to the flow, and is therefore an accelerator. For simplicity, throughout this dissertation, unless otherwise noted, the magnetic field is assumed to be in the positive $\hat{\mathbf{z}}$ direction—*i.e.*, coming out of the page.

1.2.1.1   Generator

A individual charged particle, q, traveling with velocity $\mathbf{u}$ down an MHD channel experiences a force, the Lorentz force, given by

$$\mathbf{F} = q \left(\mathbf{E} + \mathbf{u} \times \mathbf{B} \right), \tag{1.26}$$

where $\mathbf{E}$ is the electric field in the laboratory frame of reference, and just as $\rho_e \mathbf{E}$ is neglected in Equation 1.2 in Section 1.2, $\mathbf{E}$ is neglected from Equation 1.26, leaving only the $\mathbf{u} \times \mathbf{B}$, or transverse deflection, term [93]. As shown in Figure 1.2, this transverse deflection causes electrons to drift upward and ions to drift downward [94], charging the two electrodes to two different potentials (assuming, as shown in Figure 1.2, $\mathbf{u} = u(x)$ and $\mathbf{B} = B(z)$).
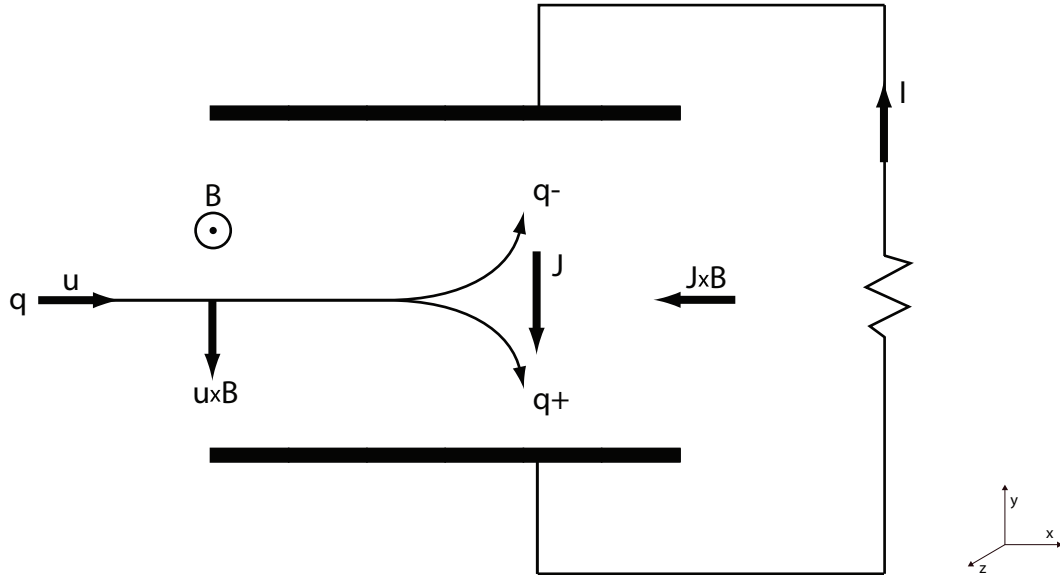
Figure 1.2: Charged particle, q, traveling through an MHD generator.

If the top and bottom electrodes are connected through an external load, as they are in Figure 1.2, then a net current density, $\mathbf{J}$, flows through the plasma in the $\mathbf{u} \times \mathbf{B}$, or negative $\hat{\mathbf{y}}$, direction. Electrical current can then be drawn from the electrodes without the inefficiency of a heat cycle [94]. Because energy is extracted from the flow, the resulting $\mathbf{J} \times \mathbf{B}$ Lorentz body force (from Equation 1.2) points in the opposite direction of the primary flowfield, $\mathbf{u} = u(x)$, and serves to slow the overall flow velocity.

1.2.1.2 Accelerator

The same principles used in MHD generators are applied in reverse for MHD accelerators [94]. An individual particle, q, traveling with velocity $\mathbf{u}$ down an MHD channel experiences the same $\mathbf{u} \times \mathbf{B}$ Lorentz force as described in Equation 1.26. However, instead of allowing the induced negative $\hat{\mathbf{y}}$ current to flow through an external
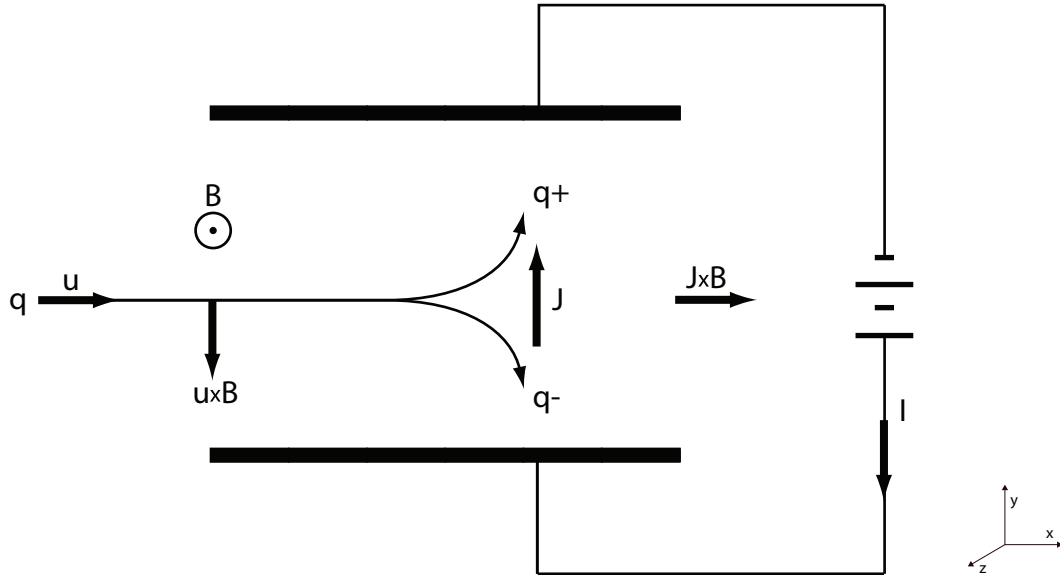
Figure 1.3: Charged particle, q, traveling through an MHD accelerator.

load, in MHD accelerator mode an external voltage is applied across the electrodes which drives a current $\mathbf{J}$ in the positive $\hat{\mathbf{y}}$ direction, as shown in Figure 1.3. The result of a positive $\hat{\mathbf{y}}$ current density is a Lorentz force, $\mathbf{J} \times \mathbf{B}$, that points in the direction of the primary flow (in Figure 1.3, in the positive $\hat{\mathbf{x}}$ direction). Both ions and electrons accelerate in the direction of the primary flow; which therefore, through collisions, accelerates the bulk of the continuum flow.

Obviously, since the natural state of the MHD channel, as depicted in Figures 1.2 and 1.3, is to induce a current $\mathbf{J}$ in the negative $\hat{\mathbf{y}}$ direction (resulting from the Lorentz force described in Equation 1.26), the applied voltage in Figure 1.3 must be strong enough to induce a current across the plasma in the positive $\hat{\mathbf{y}}$ direction that overpowers the negative $\hat{\mathbf{y}}$ current resulting from the $\mathbf{u} \times \mathbf{B}$ transverse deflection. As described in Chapter 5, it is not uncommon for an MHD accelerator to switch to generator mode at some point along the length of the channel, nor is it typically ad-
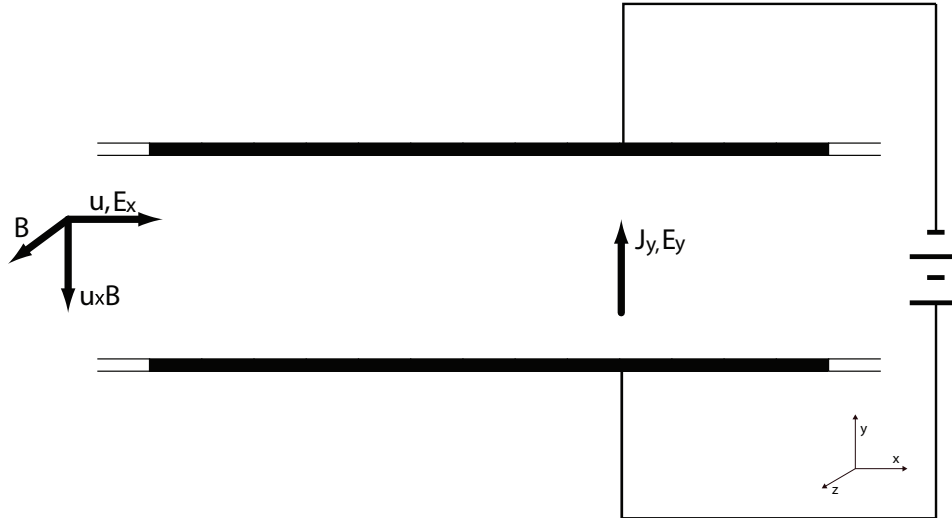
Figure 1.4: A simplified MHD accelerator with continuous electrodes.

vantageous. There can be several reasons for such an accelerator-to-generator change, some of which is described in Chapter 5.

Consider a simplified MHD accelerator as shown in Figure 1.4 with continuous electrodes that electrically connect the upstream and downstream portions of the channel, preventing an axial electric field (*i.e.*, $E_x = 0$). Because the $\mathbf{u} \times \mathbf{B}$ vector is only in the $\hat{\mathbf{y}}$ direction, Equation 1.18 becomes $\xi_x = 0$ and $\xi_y = E_y - uB$. Therefore, Equations 1.24 and 1.25 become

$$J_x = -\frac{\sigma\omega\tau}{1 + \omega^2\tau^2}\left(E_y - uB\right) \tag{1.27}$$

and

$$J_y = \frac{\sigma}{1 + \omega^2\tau^2}\left(E_y - uB\right), \tag{1.28}$$

respectively. The electrical power density, $\mathbf{J} \cdot \mathbf{E}$, becomes

$$P_{app} = \mathbf{J} \cdot \mathbf{E} = J_y E_y = \frac{\sigma}{1 + \omega^2 \tau^2} \left(E_y - uB \right). \tag{1.29}$$

The push power associated with the streamwise Lorentz force at any given cross-section is given by [90]

$$P_p = \mathbf{u} \cdot \left(\mathbf{J} \times \mathbf{B} \right)_x = u J_y B, \tag{1.30}$$

where the push power for this accelerator is given by

$$P_p = \frac{\sigma u B}{1 + \omega^2 \tau^2} \left(E_y - uB \right). \tag{1.31}$$

The electrical efficiency of an accelerator is simply the ratio of the push power to the applied power [90]

$$\eta_a = \frac{P_p}{P_{app}} = \frac{\mathbf{u} \cdot \left(\mathbf{J} \times \mathbf{B} \right)_x}{\mathbf{J} \cdot \mathbf{E}}, \tag{1.32}$$

where the efficiency for this accelerator is

$$\eta_a = \frac{u J_y B}{J_y E_y} = \frac{uB}{E_y}. \tag{1.33}$$

In this case, the "Hall effect" reduced J_y, the input power, P, and the push power, P_p, and caused the appearance of J_x, which flows downstream in the gas and returns in the electrode walls. As described at the beginning of this section, for accelerator operation (*i.e.*, for a positive J_y), the value of E_y must be greater than the product of uB, just as Equation 1.28 shows. Note that if the Hall parameter,
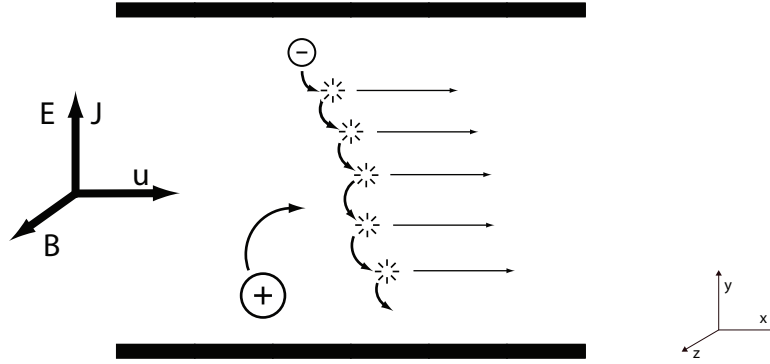
Figure 1.5: The transfer of the magnetic body force to the bulk flow by electron collisions.

$\omega\tau$ is greater than one, then $|J_x|$ would be greater than $|J_y|$. Furthermore, if the Hall parameter, $\omega\tau$, is greater than three, then the power density and push power are reduced by an order of magnitude. While the efficiency, η_a, is independent of the Hall parameter and current density, the useful power delivered to and used by the flow has been effectively reduced due to the Hall effect.

In order to properly understand the Hall effect, one must look at the process from the particle point of view, where the current-carrying particles, while attempting to follow the applied electric field, are turned into the stream direction by the magnetic field. Figure 1.5 illustrates the trajectory of an electron in crossed electric and magnetic fields, subject to collisions with other particles. In a normal MHD accelerator, the streamwise momentum acquired by electrons is transmitted to the bulk of the gas by collisions with heavy particles or by macroscopic polarization fields [16]. Since the magnetic field can do no work on the particle, it is assumed that net motion in the $\hat{\mathbf{z}}$ direction is zero. The electron motion in the x-y plane is influenced by the following factors:

1. Under the influence of the electric field alone, acceleration in the direction opposite to the electric field is balanced by collisions with other particles—the net effect of which is a steady $\hat{\mathbf{y}}$ directed diffusion velocity [94].

2. Under the influence of the magnetic field alone, the particle executes a circular motion in the x-y plane with a cyclotron frequency of $\omega \equiv |q|B/m$, where q is the charge of the particle and m is the particle mass [94].

3. The additional presence of an electric field, $\acute{\mathbf{E}} = \mathbf{E} + \mathbf{u} \times \mathbf{B}$, (which is the net effect of the transverse deflections from Equation 1.26 and the applied electric field, and is in a frame of reference moving with the mean fluid velocity, $\mathbf{u}$) causes a continual translation of the circular motion in the direction $\acute{\mathbf{E}} \times \mathbf{B}$, where particles of opposite charge translate in the same direction. This positive $\hat{\mathbf{x}}$ directed drift is what is meant by the "Hall effect" [93].

Figure 1.5 also shows the motion of ions in cross electric and magnetic fields. Notice that even though the ion begins at the opposite side of the channel and traces a circle in the opposite direction as the electron, the resulting drift for both ions and electrons is in the positive $\hat{\mathbf{x}}$ direction. Between collisions, both ions and electrons drift in the $\acute{\mathbf{E}} \times \mathbf{B}$ direction. However, it can be shown (with Equation 1.17) that ions, with their greater mass, have a much smaller Hall parameter than electrons, so that the $\acute{\mathbf{E}} \times \mathbf{B}$ drift velocity for ions can be considered negligible, leaving only the electron drift in the positive $\hat{\mathbf{x}}$ direction. Therefore a net current, the axial (also known as Hall) current, can flow in the negative $\hat{\mathbf{x}}$ direction [93], as shown in Equation 1.27. A

local axial current can also drive secondary flows in MHD channels, which is discussed in Chapter 5, and a detailed derivation can be found in Mitchner and Kruger [95].

1.2.2 Linear, Cross-Field, MHD Accelerator Configurations

For both modes (generator and accelerator) of linear, segmented, cross-field MHD channels, there are three primary configurations—Hall, Faraday, and diagonal. The configurations differ in how the external load/power is applied and the fundamental currents used to impact the flow. Each configuration has positive and negative aspects, depending on the desired implementation and outcome.

In this dissertation, a right-handed coordinate system is always used, and the primary flow is always in the positive $\hat{\mathbf{x}}$ direction, with the magnetic field in the positive $\hat{\mathbf{z}}$ direction, unless otherwise noted. Because this dissertation focuses on MHD accelerators, the following sections briefly outline and compare the first-order Hall, Faraday, and diagonal configurations of an MHD accelerator only, ignoring most secondary and induced effects—for a more complete description/derivation (including MHD generator configurations), please see sources dedicated to such material [15, 16, 87]. The three-dimensional modeling discussed in Chapters 3, 4 and 5 is much more sophisticated than that described in this section.

1.2.2.1 Hall

A linear, segmented, cross-field Hall accelerator is shown in Figure 1.6. Note that in this case, a single power supply is applied across the entire channel, in the axial, or $\hat{\mathbf{x}}$, direction. As discussed in previous examples, the $J_y B$ Lorentz force term
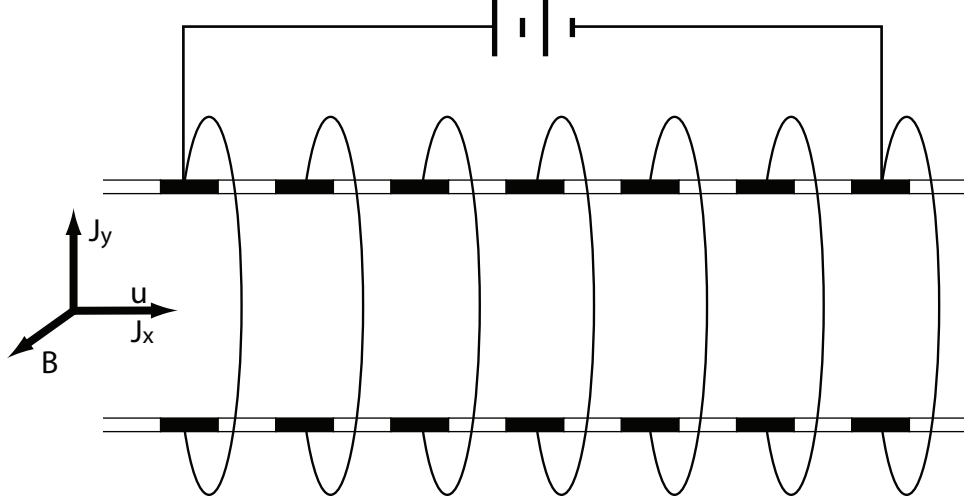
Figure 1.6: A linear, segmented, cross-field, Hall MHD accelerator.

accelerates the flow, which means that any axial, J_x, components of the total current density, $\mathbf{J}$, are not used in accelerating the flow.

Since the opposite electrodes are shorted, one can assume that $E_y = 0$, and Equation 1.18 becomes $\xi_x = E_x$ and $\xi_y = -uB$. Therefore, Equation 1.24 becomes

$$J_x = \frac{\sigma}{1 + \omega^2\tau^2}\left(E_x + \omega\tau uB\right),\tag{1.34}$$

and Equation 1.25 becomes

$$J_y = \frac{\sigma}{1 + \omega^2\tau^2}\left(\omega\tau E_x - uB\right).\tag{1.35}$$

The electrical power density for a segmented Hall accelerator becomes

$$P_{app} = \mathbf{J}\cdot\mathbf{E} = J_x E_x = \frac{\sigma E_x}{1 + \omega^2\tau^2}\left(E_x + \omega\tau uB\right),\tag{1.36}$$

and the push power is

$$P_p = \mathbf{u} \cdot (\mathbf{J} \times \mathbf{B})_x = u J_y B = \frac{u B \sigma}{1 + \omega^2 \tau^2} \left(\omega \tau E_x - u B \right). \qquad (1.37)$$

The efficiency of this segmented Hall accelerator is

$$\eta_a = \frac{P_p}{P_{app}} = \frac{\omega \tau u B E_x - u^2 B^2}{\omega \tau u B E_x + E_x^2}. \qquad (1.38)$$

It is sometimes advantageous to define the Hall loading factor [96]

$$K = \frac{E_x}{\omega \tau u B}, \qquad (1.39)$$

where, to accelerate the flow

$$K \geq \frac{1}{\omega^2 \tau^2}, \qquad (1.40)$$

and applied to Equation 1.38, the efficiency becomes

$$\eta_a = \frac{\omega^2 \tau^2 K - 1}{\omega^2 \tau^2 K (K + 1)}. \qquad (1.41)$$

As opposed to the simple MHD accelerator in Figure 1.4, the segmented Hall accelerator applies a J_x current and induces the accelerating J_y current. This results in an axial current which effectively serves to reduce the values of J_y, the electrical power density, and the push power (in comparison to the simple MHD accelerator in Figure 1.4). Furthermore, in this case, local efficiency is not independent of the

Hall parameter—Equations 1.38 and 1.41 show that to obtain a high local efficiency, the Hall parameter, $\omega\tau$, must also be high. Furthermore, Equations 1.17 and 1.38 show that relying solely on the intensity of the magnetic field B to increase the Hall parameter does not greatly improve the Hall accelerator efficiency. While increasing B does increase the value of the Lorentz force, Equation 1.17 shows that decreasing the number density and mean random thermal velocity are more efficient ways to increase the Hall parameter. For these reasons, the Hall configuration is generally more efficient for low-density flows [90], and it is typically advantageous to use a Hall accelerator when the Hall parameter is in excess of three [97, 98].

While the Hall accelerator suffers from reductions in electrical power density and push power and low efficiencies at lower Hall parameters, from a physical and design perspective, it can be a very attractive option. A Hall accelerator, as shown in Figure 1.6, requires only one power supply and has straight-electrode connections—a relatively simple design which translates to relatively low accelerator weight and cost. When designing an MHD accelerator for space travel, consideration is often given to simplicity, weight, and cost.

1.2.2.2 Faraday

A segmented Faraday accelerator is shown in Figure 1.7. Note that each pair of electrodes is independently powered, and the applied current is in the $\hat{\mathbf{y}}$ direction. In this configuration, there is no path for the axial current; therefore, $J_x = 0$, and Equation 1.24 becomes $\xi_x = \omega\tau\xi_y$. Equation 1.18 becomes $\xi_x = E_x$ and $\xi_y = E_y - uB$,
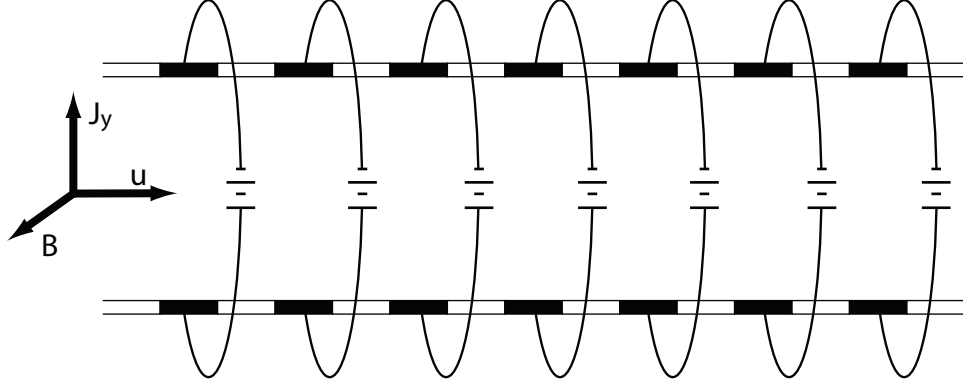
Figure 1.7: A linear, segmented, cross-field, Faraday MHD accelerator.

which combine to give $E_x = \omega\tau (E_y - uB)$, the axial electric field. From Equation 1.25, the J_y current for this accelerator is given by

$$J_y = \sigma (E_y - uB),\qquad(1.42)$$

and the electrical power density is

$$P_{app} = \sigma E_y (E_y - uB).\qquad(1.43)$$

The push power for the Faraday accelerator is given by

$$P_p = \sigma uB (E_y - uB),\qquad(1.44)$$

while the Faraday accelerator efficiency is

$$\eta_a = \frac{uB}{E_y}.\qquad(1.45)$$

The values for J_y current density, electrical power density, and push power are identical to those if one were to neglect the Hall parameter from the beginning—which is logical, because segmenting and independently conditioning each pair of electrodes completely neutralizes (in theory) the axial (J_x) current (which is actually the idea behind the segmented Faraday accelerator). Note that the efficiency in Equation 1.45 is the same as Equation 1.32, because the accelerator in Figure 1.4 is a Faraday with continuous electrodes.

The segmented Faraday accelerator's improvements in power and efficiency do not come without a cost, however. The design of a segmented Faraday accelerator—with individual power supplies—is quite complex, costly, and heavy. The performance and power advantages of the segmented Faraday accelerator have made it a popular choice, but because of its complexity and weight, its use has been limited to ground-based application, as detailed in Section 1.1.2. So, while the segmented Faraday accelerator's power and efficiency is much greater than that of a Hall accelerator, its complexity and weight have virtually precluded it from use in flight vehicles.

1.2.2.3   Diagonal

A linear, segmented, cross-field, diagonal MHD accelerator, as shown in Figure 1.8, is similar to a Hall accelerator, but with the electrode link having an angle, θ_w. Just as the Hall accelerator, there is a single power supply applied in the $\hat{\mathbf{x}}$ direction, while the accelerating current is, as always, in the positive $\hat{\mathbf{y}}$ direction. The general concept behind the diagonal accelerator is to use the simplicity of the Hall accelerator (*i.e.*, a single power supply) with the efficiency of a Faraday accelerator (*i.e.*, lowered
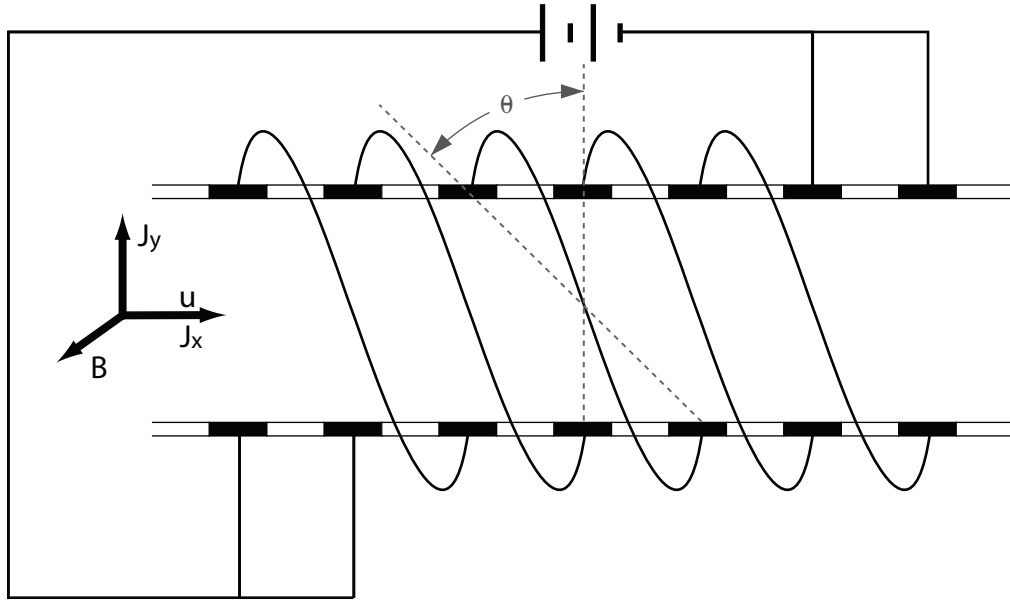
Figure 1.8: A linear, segmented, cross-field, two-terminal diagonally loaded MHD accelerator.

J_x current). This union of simplicity and efficiency is (hopefully) attained through the use of the diagonal connections between the electrodes.

There are numerous incarnations of the diagonal MHD channel—Figure 1.8 shows a two-terminal loading scheme; however, single-terminal devices follow the same principles. De Montardy suggested the series-connected scheme in which a segmented Faraday channel is externally diagonalized [99]. Dicks later extended this approach to a diagonal conducting-wall (DCW) configuration, as shown in Figure 1.9, in which slanted window-frame-like electrode elements are stacked with thin insulators to form a complete channel [100]. The DCW configuration is a conceptually simple design which has no performance penalties in comparison to the series connected device.

To understand the physics of a diagonal MHD accelerator, one must take a closer look at the angle of the diagonal link in relation to the field vectors in the
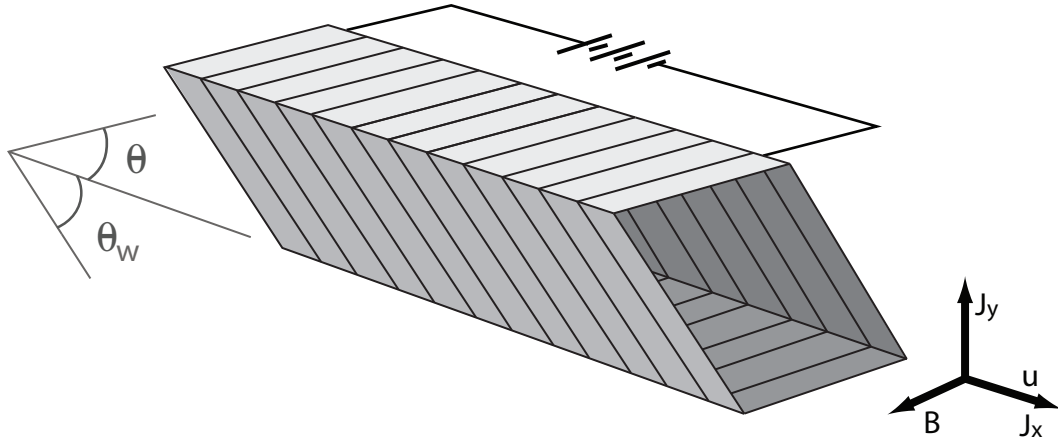
Figure 1.9: A linear, segmented, cross-field, diagonal conducting-wall MHD accelerator.

channel. Figure 1.10 shows that the electric field, **E**, points normal to the diagonal

link, where its relationship to the diagonal angle is

$$\frac{E_y}{E_x} = \tan \theta = \varphi, \tag{1.46}$$

where θ is the electric field angle, and φ is the electric field direction. It follows that

the diagonalization, or wall angle, is given by $\theta_w = \pi/2 - \theta$. The sign of φ depends on

the mode of operation. For an accelerator, $\mathbf{u} \times \mathbf{B}$ opposes J_y, the electric field angle

is $0 < \theta < \pi/2$, and the electric field direction is positive, $\varphi > 0$ [90]. For a generator,

$\mathbf{u} \times \mathbf{B}$ aligns with J_y, the electric field angle is $-\pi/2 < \theta < 0$, and the electric field

direction is negative, $\varphi < 0$ [90].
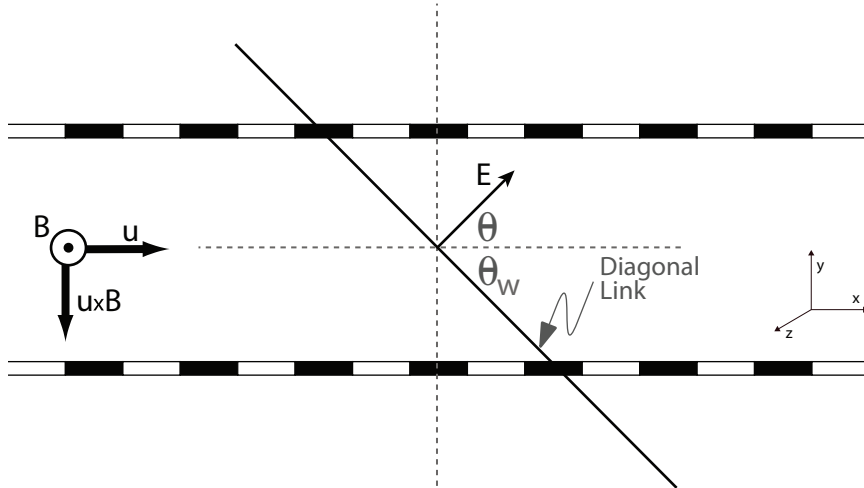
Figure 1.10: Orientation of field vectors in a diagonally connected cross-field MHD accelerator.

The total two-terminal current I for an MHD accelerator with diagonally linked electrode pairs, as shown in Figure 1.8, is given by

$$I = \int_{A_f} \mathbf{J} \cdot d\mathbf{A}_f = \mathbf{J} \cdot \mathbf{n} A_f, \tag{1.47}$$

where the integration is over the entire slanted area, A_f. In component form, the current is

$$I = \left(J_x + J_y \tan\theta\right) A = \left(J_x + \varphi J_y\right) A, \tag{1.48}$$

where A is the normal cross-sectional area of the channel, and relates to the slanted area with $A_f = A\sqrt{1 + \varphi^2}$.

Since there is no $\hat{\mathbf{x}}$ component to the $\mathbf{u} \times \mathbf{B}$ vector, Equation 1.18 becomes

$\xi_x = E_x$ and $\xi_y = E_y - uB$. Given this, Equation 1.24 becomes

$$J_x = \frac{\sigma}{1 + \omega^2\tau^2} \left[E_x \left(1 - \omega\tau\varphi\right) + \omega\tau uB \right], \tag{1.49}$$

while Equation 1.25 becomes

$$J_y = \frac{\sigma}{1 + \omega^2\tau^2} \left[E_x \left(\omega\tau + \varphi\right) - uB \right]. \tag{1.50}$$

The electrical power density at any cross-section in the channel is

$$P_{app} = \mathbf{J} \cdot \mathbf{E} = \frac{I}{A_f} \sqrt{E_x^2 + E_y^2}, \tag{1.51}$$

which, when combined with Equations 1.46, 1.48, 1.49 and 1.50, becomes

$$P_{app} = \frac{\sigma E_x}{1 + \omega^2\tau^2} \left[E_x \left(1 + \varphi^2\right) + uB \left(\omega\tau - \varphi\right) \right]. \tag{1.52}$$

The push power is $P_p = \mathbf{u} \cdot (\mathbf{J} \times \mathbf{B}) = uJ_xB$, which for this diagonal accelerator is

$$P_p = \frac{uB\sigma}{1 + \omega^2\tau^2} \left[E_x \left(\omega\tau - \varphi\right) - uB \right]. \tag{1.53}$$

As stated, the efficiency for an MHD accelerator is the ratio of the push power to the applied power, $\eta_a = P_p/P_{app}$, which in this case becomes

$$\eta_a = \frac{\omega\tau uBE_x + \varphi uBE_x - u^2B^2}{\omega\tau uBE_x - \varphi uBE_x + E_x\left(1 + \varphi\right)^2}. \tag{1.54}$$

For the diagonal MHD accelerator, the values for the J_y current density, power density, push power, and efficiency are lower than those for the segmented Faraday accelerator. However, in comparison to a Hall accelerator, the diagonal accelerator has a higher J_y current density, power density, push power, and efficiency, and a lower J_x current density. Compare Equations 1.35, 1.36, 1.37 and 1.38 for the Hall configuration to Equations 1.50, 1.52, 1.53 and 1.54, respectively, for the diagonal configuration, and notice that these characteristics are increased by the value of the electric field direction, φ; while J_x (Equation 1.34 for Hall and Equation 1.49 for diagonal) is lowered by the value of φ in the diagonal case. Also note that the relations for the linear segmented Hall accelerator are recovered in the extreme case where $\varphi = 0$.

The linear segmented diagonal accelerator offers improvements in power density, push power, and efficiency above that of the Hall accelerator without the added cost, complexity, and weight of the Faraday accelerator—as seen in Figure 1.8, the diagonal accelerator, like the Hall accelerator, requires only a single power supply and has a relatively simple connection scheme. The Faraday accelerator offers the best power and performance, but at the highest cost, complexity, and weight. The Hall accelerator offers a simple and light-weight system, but poor power and perfor-

mance at lower Hall parameters. The diagonal accelerator, however, offers adequate performance and power at a higher range of Hall parameters and at a low cost and weight—of the three segmented linear MHD accelerators outlined in this section, the diagonal accelerator offers the most promise for spacecraft with high-density exhaust.

1.3 Technical Objectives

The objective of this research is to analyze the NASA Magnetohydrodynamic Augmented Propulsion Experiment (MAPX) using a three-dimensional numerical model. The results of this analysis are intended to offer a better understanding of the critical physical processes and provide pre-test performance predictions. The NASA MAPX accelerator marks the first experimental study of a diagonal MHD accelerator, and this dissertation is the first detailed numerical analysis of a diagonal MHD accelerator.

As outlined in Chapter 2, the NASA MAPX channel seeks to improve the performance of existing thermal chemical propulsion systems by augmenting their exhaust with a linear, segmented, diagonal accelerator [14]. As shown in Sections 1.1.2 and 1.1.3, there have been no experimental studies of diagonal MHD accelerators, even though, as Section 1.2.2 shows, diagonal accelerators offer the best union of performance/power and cost/weight. The MAPX accelerator is the first of its kind and requires very thorough analysis.

Current MHD numerical modeling capabilities are severely lacking, as described in Section 1.1.3. Most numerical models offer only one or two dimensions, which is inadequate for proper MHD modeling [20]. All of the current numerical

models—one, two, and three-dimensional—use inadequate thermodynamic and/or electrical conductivity models. In most cases, electrical conductivity calculated via a curve-fit or simply assumed to be constant throughout the channel—these types of assumptions save time and computer cycles, but sacrifice accuracy. The three-dimensional numerical model used in this research is the first with the ability to simulate a segmented diagonal MHD accelerator using detailed, three-dimensional thermodynamic and electrical conductivity models, as described in Section 4.2.

CHAPTER 2

THE NASA MAGNETOHYDRODYNAMIC AUGMENTED

PROPULSION EXPERIMENT (MAPX)

> *The fundamental principle of science, the
> definition almost, is this: the sole test of
> the validity of any idea is experiment.*
>
> —Richard P. Feynman

2.1   MAPX Performance Analysis and Design

The NASA Marshall Space Flight Center (MSFC) Magnetohydrodynamic Aug-
mented Propulsion Experiment (MAPX) facility, illustrated in Figure 2.1, was de-
signed using the traditional flow-path configuration established by previous research,
as described in Section 1.1.2. First, the working fluid (air, nitrogen, etc.) is heated in
a $1.5\,\mathrm{MW_e}$ Aerotherm arc-heater to a stagnation temperature of $T_0 \approx 4000 - 4500\,\mathrm{K}$
at a stagnation pressure $P_0 \leq 10\,\mathrm{atm}$ [14]. The hot gas then travels through an isola-
tion flange and seed injector flange, where it is seeded with alkali metals (*e.g.*, NaK).
The seeded gas travels through a mixing chamber and is then expanded through a
primary nozzle to a Mach number $\mathrm{M} \approx 1.25 - 1.5$ [2]. The $2\,\mathrm{MW_e}$ MHD accelerator,
which is surrounded by a $2\,\mathrm{tesla}$ electromagnet, then directly increases the energy
and momentum of the flow, which is further accelerated through a secondary nozzle
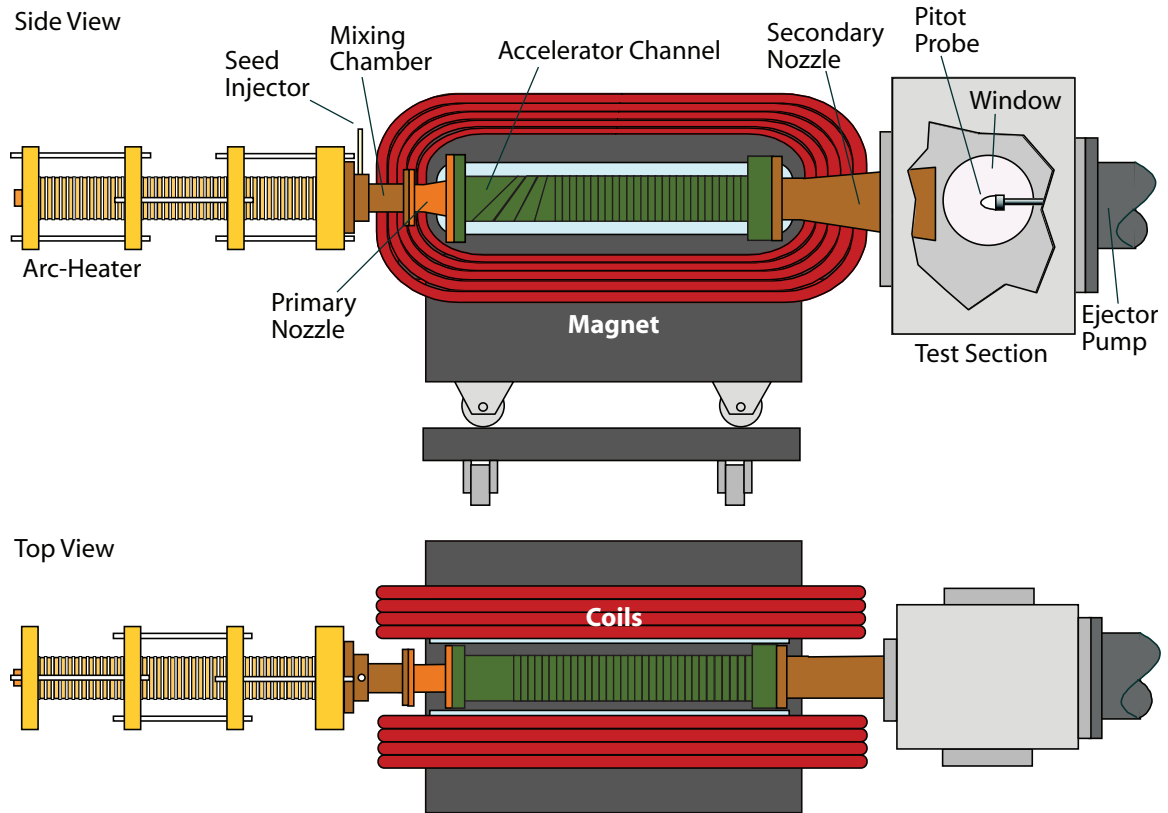
Figure 2.1: Schematic of the NASA MSFC MAPX facility. The major flow-path components are: (1) $1.5\,MW_e$ Aerotherm arc-heater, (2) seed injector and mixing chamber, (3) primary expansion nozzle, (4) $2\,MW_e$ MHD accelerator channel and 2 Tesla magnet, (5) secondary nozzle, (6) windowed test section, and (7) nitrogen driven ejector pump [1].

to obtain the desired jet velocity [14]. The secondary nozzle exhausts into a windowed test section equipped with a stinger mount and access for optical-based flow diagnostics. The test section is attached to a nitrogen driven ejector pump designed to maintain a back-pressure of less than 0.05 atm [14]. Details of some of the major flow-path components are discussed below.

2.1.1 Hot Gas Source and Entrance Flow-Path

The $1.5\,MW_e$ Aerotherm arc-heater, which was originally acquired by NASA MSFC to support materials testing and certification, is the thermal driver for the MAPX facility. The arc-heater's conventional design allows for an axial arc to be established between a fixed tungsten cathode button at the upstream end and a ring anode on the downstream end. A magnetic spin coil continuously rotates the ring anode and, therefore, the arc attachment point. The main body consists of segmented "packs"—water-cooled copper segments separated by boron nitride insulators—which the user can assembly as necessary [101]. The purpose of the thermal driver is to maximize the MHD interaction by delivering the highest possible mass throughput and maximizing the accelerator channel size [14].

This particular arc-heater model has seen considerable usage as Aerotherm's in-house research unit; therefore, it is possible to accurately predict the input conditions to the MHD accelerator [101]. Assuming fully powered operation and 20% heat loss in the mixing chamber and primary nozzle, preliminary analysis indicates suitable accelerator conditions could be obtained with $130\,g/s$ of air flowing through a $0.64\,inch$ ($1.6256\,cm$) diameter throat at the rated working pressure of $10\,atm$ [102]. The projected arc-heater conversion efficiency with a 3-pack configuration (27 inches, or $68.58\,cm$, long) exceeds 60% at the power levels of interest [103].

Figure 2.2 shows two photographs of the MAPX arc-heater. Part (a) shows a side-view of the arc-heater, where the three "packs" can easily be seen. The large-diameter red cables at the front and rear of the arc-heater supply the $1.5\,MW_e$ of
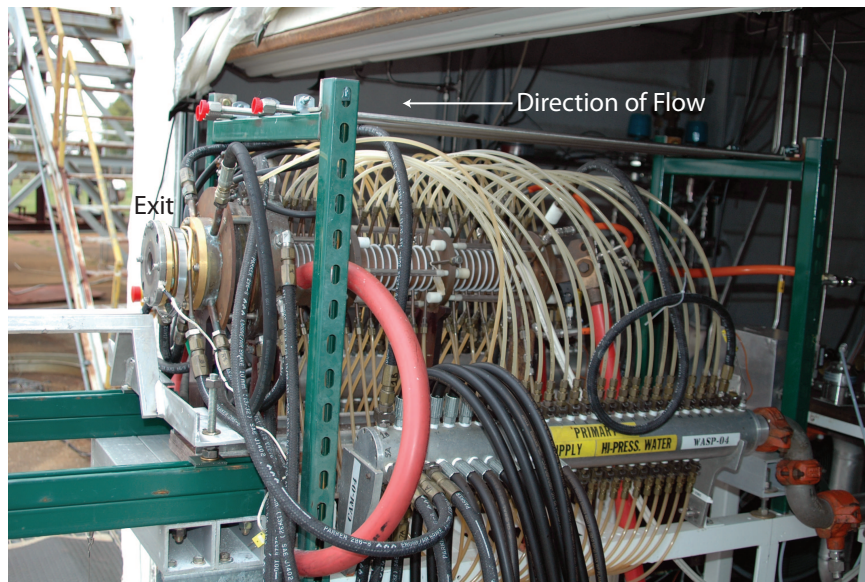
(a)
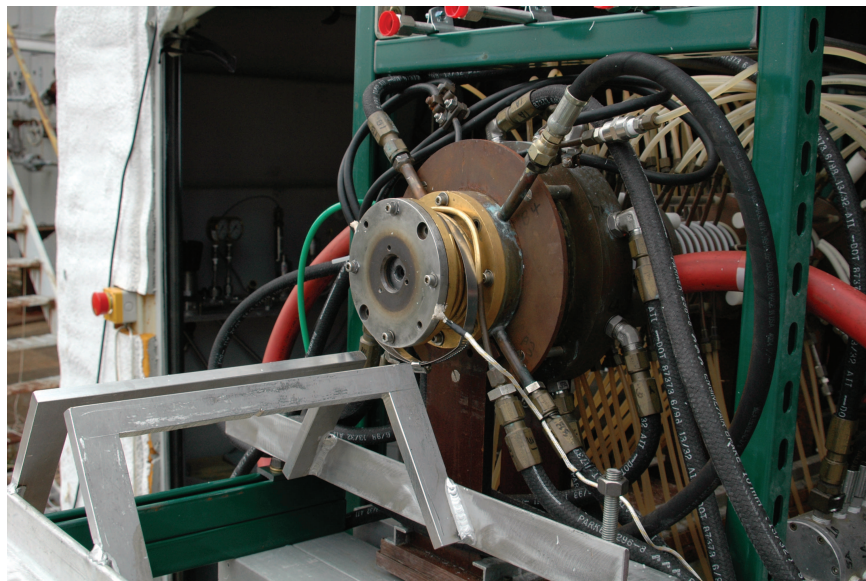
(b)

Figure 2.2: Photographs of the $1.5\,\mathrm{MW_e}$ Aerotherm arc-heater: (a) side-view of the arc-heater and (b) close-up of the exit of the arc-heater. In both photographs, the direction of flow is from right to left.

electrical power necessary to create the arc. The thinner orange tubing at the far right of the photo provides the working fluid for the arc-heater, and the white and black tubes provide cooling water to the arc-heater to prevent overheating. The silver flange on the left side of the photograph is actually the arc-heater mating flange (illustrated in Figure 2.3), within which is the graphite nozzle exit of the arc-heater—as shown in the close-up photograph in part (b) of Figure 2.2. After of the arc-heater exit, part (b) also shows the stand which will support the downstream components, discussed later in this section.

Ideally, the ionizing seed material and the primary working fluid would be both mixed and heated within the thermal source [102]. This is not possible in an arc-heater as it would reduce the plasma resistivity, repress Joule heating, and result in severe discharge instabilities. The best alternative, therefore, is to directly inject the seed material as a pure alkali metal vapor just downstream of the arc-heater, and allow sufficient distance for mixing upstream of the accelerator nozzle.

This particular approach was perfected by the NASA Langley group, which injected electrically-heated-vaporized cesium into the post-discharge region of the arc-heater [29–34]. This technique offers numerous engineering problems and requires considerable time and effort to perfect. While the cesium-based injection technique is the ultimate goal of the MAXP group, initial experimentation will implement a NaK aerosol injection scheme [14], originally developed by the Central Institute for Aerohydrodynamics (TsAGI) in Russia [104]. As a plasma seeding material, NaK has been shown to minimize plasma enthalpy contamination and degradation, reduce

Table 2.1: Primary nozzle performance using air as the working fluid seeded with 1% NaK, by weight.

Property	Mixing Chamber	Nozzle Throat	Accelerator Entrance
P (atm)	10.0	6.6	3.2
T (K)	4300	4000	2700
γ	1.198	1.186	1.213
u (m/s)	—	1210	1300
Mach No.	—	1.0	1.35
σ (S/m)	325	274	40

high frequency current fluctuations (when compared to other seed materials, such as K_2CO_3 or KOK), and achieve higher electrical conductivities [105].

The primary nozzle flow was analyzed using a modified version of the NASA SP-273 chemical equilibrium code [106,107] in which plasma electrical transport properties were computed according to the methods of Frost [18]. The results for air seeded with 1% NaK (by weight) are summarized in Table 2.1 [14], where γ and σ represent the ratio of specific heats and electrical conductivity, respectively. In this example, the primary nozzle expansion ratio is $A/A^* = 1.17$ [14]. The flow could not be expanded further without severely reducing the static temperature and electrical conductivity at the entrance to the MHD channel.

An exploded schematic of the entrance flow-path assembly is shown in Figure 2.3. This assembly accomplishes the following primary functions [14]: (1) electrical isolation of the arc-heater from the MHD accelerator and circular-to-square flow-path transition; (2) seed injection and mixing; and (3) flow acceleration via the nozzle. The isolation flange is designed for heat sink operation and is an expendable
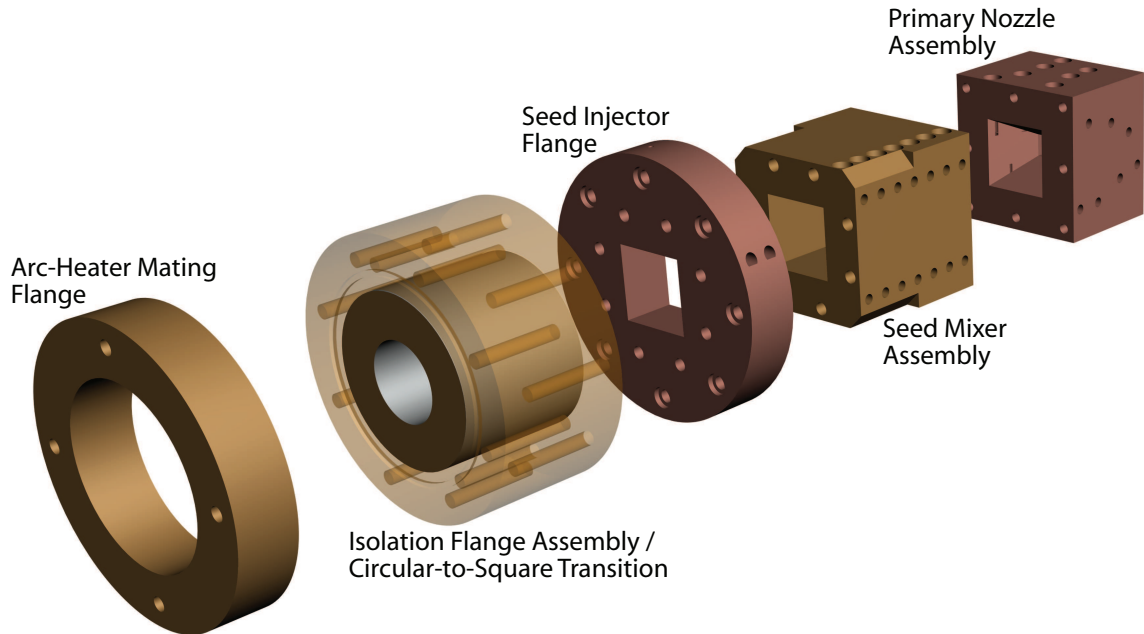
Figure 2.3: Exploded schematic of entrance flow-path assembly for MAPX. The major pieces include (1) the ceramic isolation flange, (2) the water-cooled seed injector flange and mixer assembly, and (3) the water-cooled primary nozzle assembly [2].

item, with the other components being water-cooled copper pieces intended for extended service [2]. An alumina insert is located inside the isolation flange (as shown in Figure 2.3) which provides the geometric transition of the flow passage from the circular geometry of the arc-heater exit to the rectangular geometry of the MHD accelerator [2]. This geometric transition is facilitated by the internal loft (flow area distribution) of the alumina insert, which gradually transforms from circular to square. It is also worth noting that, because the circular-to-square transition occurs along the length of the isolation flange assembly without a change in diameter (width), the cross-sectional area increases by a factor of $4/\pi$ [2].

2.1.2   MHD Accelerator Channel

2.1.2.1   Electrical Loading Configuration

The optimal MHD accelerator configuration is ultimately determined by the requirements of the application. As described in Section 1.2.2, the Hall configuration (Figure 1.6) is more effective for low-density flows, whereas the Faraday configuration (Figure 1.7), with segmentation to eliminate the axial current, is superior for high-density flows [19]. However, the Faraday configuration, with separate power conditioning for each pair of electrodes, is complex, costly, and massive—three attributes which make it unsuitable for flight applications.

Two diagonal configurations were presented in Section 1.2.2—the Diagonal Conducting Wall (DCW, see Figure 1.9) and the externally diagonalized (Figure 1.8). The DCW configuration not only simplifies the fabrication process and improves the strength of the accelerator, but it provides superior performance to the externally shorted (*i.e.*, series connected) device by allowing current to flow to the sidewalls [108]. The MAPX research team believes that the DCW configuration is the best candidate for flight implementation; however, for reasons of cost and flexibility (*e.g.*, the ability to adjust the effective wall angle), the MAPX accelerator is based on an externally diagonalized series connected configuration.

2.1.2.2   Engineering Design

MHD accelerator development presents interesting engineering design challenges. In an accelerator environment, current densities, stagnation enthalpies, and

wall heat loads are much more intense than the generator operating conditions [20]. Therefore, the accelerator environment is more energetically stressed due to increased thermal loading and erosive effects.

The "velocity overshoot" and boundary layer microarcs phenomena amplify these difficulties [14]. The increased stagnation temperature of the accelerator environment results in high recovery temperatures, especially in the boundary layer. Joule heating in the concentrated current region near the electrodes further elevates the near-wall temperature of the flow, which consequently, increases the electrical conductivity of the flow in the boundary layer. This highly-conductive, low-density region near the sidewalls is Lorentz accelerated to velocities higher than the core flow [109], and is commonly called the "velocity overshoot" region. Furthermore, the highly-conductive, high-temperature boundary layer regions are more susceptible to electrical breakdown at the electrode surface, leading to microarcs which erode the accelerator walls [110].

In the severe thermal environment of an MHD accelerator, designers typically rely on water-cooled copper alloy or silver electrodes and boron nitride or beryllia insulators [36,37]. However, because short run times ($\approx 1\,\text{sec}$) were acceptable, the MAPX accelerator was designed as an expendable heat sink device, with graphite electrodes, alumina insulators (between electrodes) and alumina insulating sidewalls [111], the cross-section of which is shown in Figure 2.4. The MAPX accelerator is designed to be simple and inexpensive to build, while durable enough to support several test runs before refurbishment is required. The electrode and sidewalls are encased in a G-11 phenolic fiberglass reinforced box structure, which seals the channel and provides
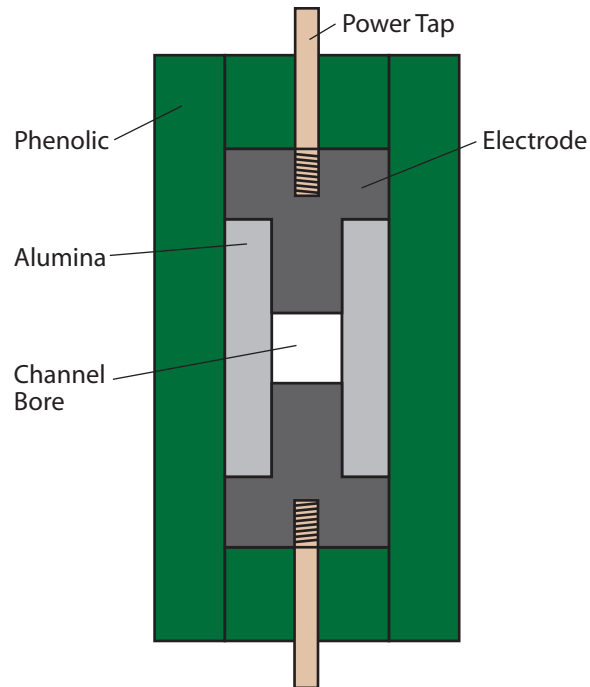
Figure 2.4: Cross-section of heat-sink accelerator channel illustrating construction detail [2].

structural support [14]. The G-11 material has an upper temperature limit of 450 K, which is the principal thermal constraint of this design [111].

The channel inner bore necessitates an insulating sidewall thickness of less than one inch (2.54 cm) [111]. Therefore, the sidewall construction is comprised of ¹/₂ inch (1.27 cm) alumina and ³/₈ inch (0.9525 cm) thick G-11 phenolic [14]. The alumina has a low thermal conductivity, and will immediately experience a rapid rise in surface temperature when exposed to the hot plasma; however, the back-facing temperature (which is in contact with the G-11 phenolic) will peak three to five minutes after the test run [111]. Therefore, the MAPX accelerator will have a cooling purge before and after each firing [14].

Table 2.2: Physical specifications of the MAPX accelerator.

Characteristic	Value
Inlet Height $\times$ Width (cm^2)	1.56×1.56
Channel Divergence (degrees)	1.2
Electrode Width (cm)	1.0
Insulator Width (cm)	0.5
Active Length (cm)	90.5
Powered Electrodes (N_p)	60
Total Length (cm)	99.5
Total Electrodes (N)	66
Exit Height $\times$ Width (cm^2)	3.64×3.64

The electrode walls will be exposed to basically the same thermal flux as the insulating sidewalls. While there are no geometric constraints on the height of the electrodes, the same temperature limitations apply at the interface between the electrode and the G-11 phenolic. Because the graphite has a much higher thermal conductivity than the alumina, it is required to be thicker. Furthermore, the expected erosion of the graphite in the oxygen carrying plasma will increase heat transfer [110]. The erosion will, obviously, be more pronounced at the entrance of the channel, but it is not expected to be significant enough to warrant surface coating of the graphite [14].

The electrodes and alumina insulators are keystone shaped pieces that are locked into position by the alumina sidewall blocks. Once installed in the outer G-11 structure, the refractory materials can be floating, meaning that no rigid attachment to the outer walls is required [14]. Axial motion is prevented by the entrance and exit flanges, while diagonal shorting of the electrodes is accomplished by running short
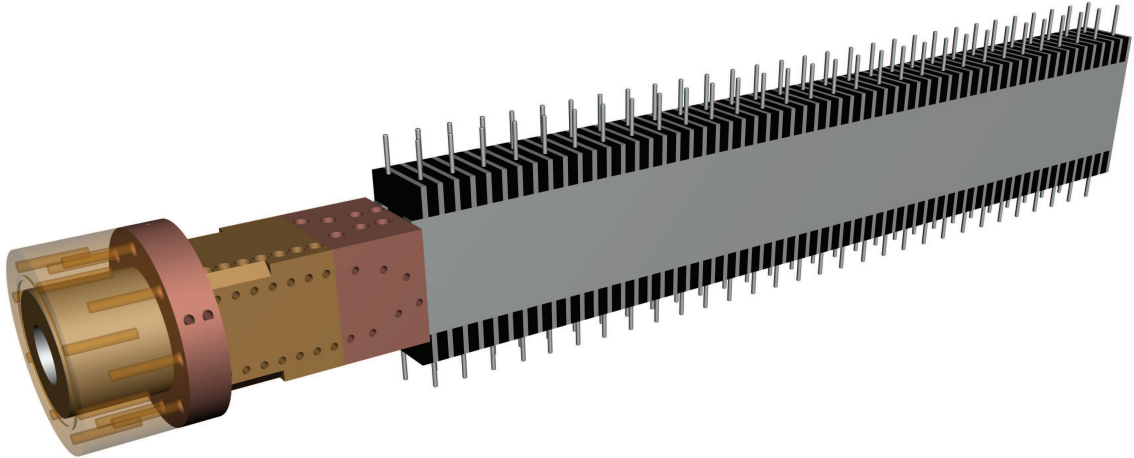
Figure 2.5: Schematic of fully assembled MAPX accelerator channel, shown without external G-11 phenolic support structure and magnet bore [2].

leads of wire between the external channel assembly and the magnet pole cap [14]. The MAPX accelerator physical specifications are detailed in Table 2.2.

The fully assembled accelerator (without the external G-11 phenolic enclosure) is shown schematically in Figure 2.5. The graphite electrodes are black in color, while the alumina insulators and sidewalls are gray. Note that the entrance flow-path assembly (detailed in Figure 2.3) is shown upstream of the accelerator. LyTec, LLC (of Tullahoma, Tennessee) designed and fabricated the MAPX accelerator, and it currently resides at the Marshall Space Flight Center awaiting testing.

Figure 2.6 shows photographs of the MAPX accelerator hardware. Most obvious in the photographs (parts (b) and (c)) is the brown external G-11 phenolic enclosure, used for protection and structural integrity. Part (a) shows that the power taps are basically threaded 1/4-20 rods with matching nuts, which secure the external electrode links made of low-gauge wire, as seen in parts (b) and (c). The entrance and
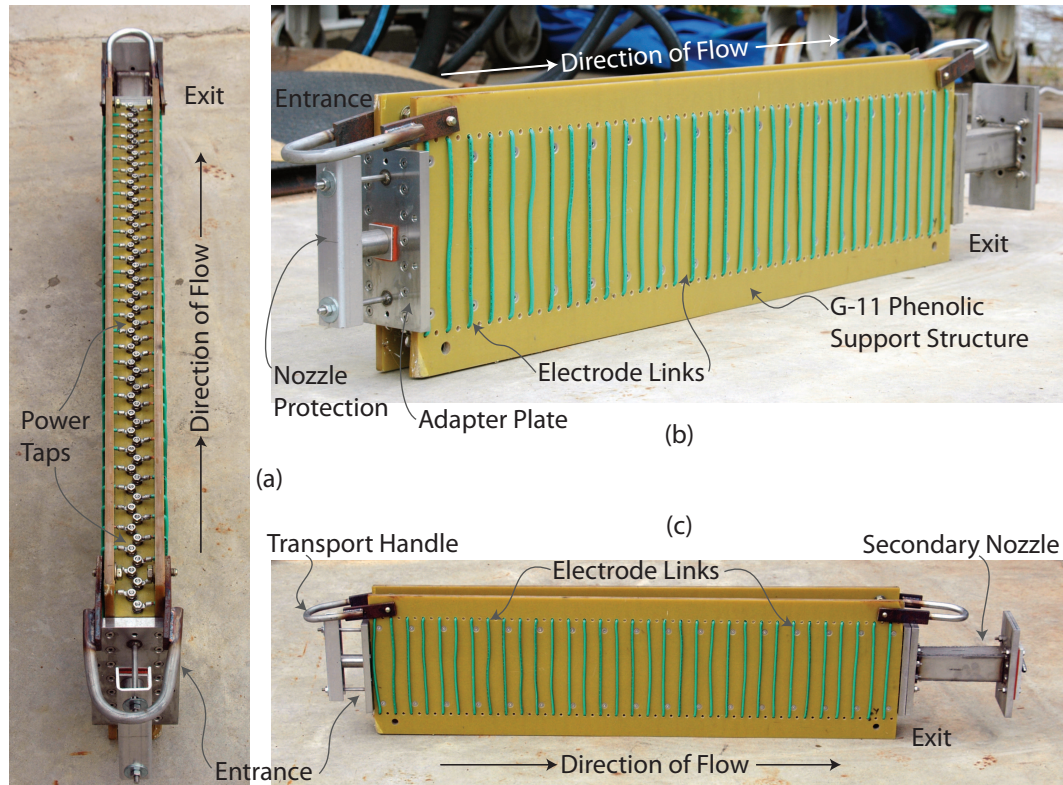
Figure 2.6: Photograph of the MAPX accelerator: (a) top view, showing the power taps and the channel divergence, (b) a perspective view, showing the electrode links and entrance adapter, and (c) a side view, showing the electrode links and the secondary nozzle at the exit.

exit of the channel are already fitted with adapter plates—and, as seen in part (c), the exit of the channel has already been fitted with the first half of the secondary expansion nozzle (the second half of the secondary nozzle is located inside the test section). Lastly, it is important to note that the electrodes have no diagonal angle—*i.e.*, the MAPX channel is in Hall configuration for all of the photos in Figure 2.6.

2.1.3   Secondary Nozzle and Test Section

Additional exhaust velocity can be achieved by expanding the residual pressure at the end of the MAPX accelerator, with the expansion being determined by the

backpressure of the evacuation system. In the MAPX facility, this is accomplished with a diverging duct.

The secondary nozzle for the MAPX facility is designed as an uncooled two-piece unit, with convenient separation for maintenance. The first stage section is 20 cm long with a 6 degree divergence. Two interchangeable 32.5 cm long secondary stage sections were designed, having divergence angles of 1.7 degrees and 2.5 degrees, respectively [14]. These nozzles consist of plasma sprayed carbon steel sheets, welded together to form an expanding duct. The secondary nozzles were sized to exhaust into a large test section, which is evacuated by a nitrogen ejector pump with a deadhead backpressure less than 0.05 atm. The secondary nozzles, test section, and ejector facility were all custom fabricated in NASA MSFC facilities.

Figure 2.7 show two photos of the (a) MAPX test section and (b) second half of the secondary nozzle (the first half of the secondary nozzle is attached to the end of the MAPX accelerator, and seen in Figure 2.6). Part (a) shows the large viewing windows and numerous access ports that the test section has to offer. Part (b) is a close-up photograph of the test section window, revealing inside the secondary nozzle already mounted. The test section as photographed obviously still requires much work before completion—custom fitted, high pressure, optical-grade glass will cover the windowed sections, while the numerous ports will allow for pluming and instrumentation.
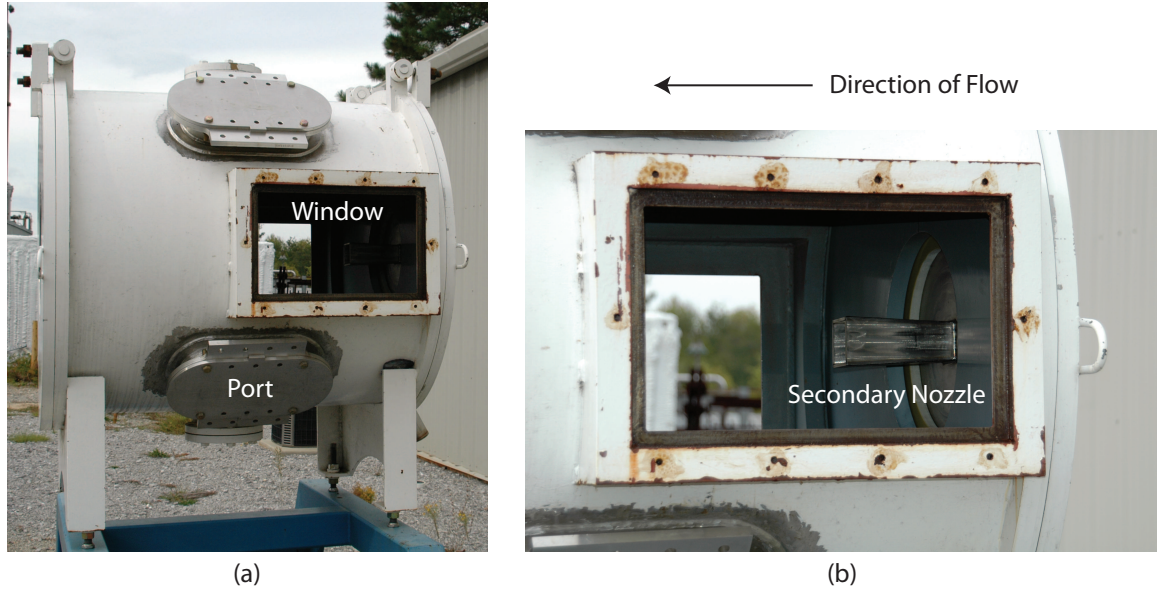
Figure 2.7: Photographs of the MAPX secondary nozzle and test section: (a) the entire test section vacuum chamber, with windows and ports, within which is the (b) plasma sprayed carbon steel secondary nozzle.

2.2 One-Dimensional Analysis

Preliminary performance analysis and design of the MAPX accelerator was performed using a one-dimensional engineering model with the adoption of major simplifying assumptions—including wall friction, wall heat flux, and near-electrode voltage drops which were calculated through physical sub-models for the boundary layer. This numerical model was originally developed within the Energy Conservation Division at the University of Tennessee Space Institute in support of the Department of Energy MHD Commercial Power Program [14, 112]. Under the direction of LyTec, LLC, of Tullahoma, Tennessee, the code evolved and expanded to cover a range of MHD generator and accelerator configurations [113]. This LyTec numerical model solves the governing internal duct flow equations for conservation of mass,

momentum, and energy, together with the equation of state using a fourth order Runge-Kutta integration technique. It uses a real-gas equation of state and assumes local thermodynamic equilibrium as predicted by the NASA SP-273 code [114] with modifications for computing the electrical transport properties according to the Frost mixing model [18].

2.2.1   Numerical Model

This particular version of the LyTec MHD accelerator Fortran code was specifically tailored for NASA MSFC for the design and performance evaluations of the MAPX accelerator using seeded air as a working fluid. The principle features of the numerical models are as follows [113]:

- Thermochemical equilibrium calculations for the definition of air thermodynamic properties (equation of state) are based on NASA SP-273 [114] and contained in a subroutine/module structure embedded within the code. Electrophysical properties and mass flow percentages of a seeded plasma—subject to seed specification (Cs, K, or Na), and based on Frost [18]—are also calculated within this same module.

- Governing internal duct flow equations for conservation of mass, momentum, and energy, together with the equation of state, are calculated using a fourth order Runge-Kutta integration scheme. Accelerator channel cross-section and mass flow rate are required inlet specifications.

- Wall losses—heat transfer to the channel walls and wall friction losses—are computed intrinsically within the code and require the user to define wall temperature and roughness height.

- The code can address variable user-defined MHD accelerator configurations:

  1. Segmented Faraday (requires Faraday load factor, Faraday current, or Faraday voltage).

  2. Diagonal connection (requires total current and wall angle).

  3. Hall configuration (requires total current input).

  4. Axial current neutralized (requires total current, while code computes sidewall angle).

- Near wall electrical losses are intrinsically computed through integration of the conductivity profile as defined from a flat plate, turbulent, velocity and thermal boundary layer correlation. Input of the initial boundary layer height and shear (viscosity as a function of temperature) are used to compute the boundary layer growth along the MHD accelerator. The velocity and temperature profiles are taken as $^1/n^{th}$ power law distributions, which relies on the user specification of the Rosa G factor to account plasma non-uniformities and effective voltage drop [87, 115].

- A user-defined near wall arcing temperature, together with the intrinsically calculated near wall temperatures, determines where arcing is assumed to occur in the channel.

The NASA SP-273 code can model up to 127 different chemical species [114]. The LyTec modifications to NASA SP-273 incorporate the Frost method for calculating electrical transport properties, which utilizes electron momentum-transfer cross-sections for electron-neutral interactions and a modified Spitzer equation for electron-ion interactions [18]. The LyTec MAPX MHD code has the NASA SP-273 module generate a table of thermodynamic species and plasma property data, which is then curve-fitted and read back into the MHD accelerator code [1]. The basic system of equations that the one-dimensional LyTec MHD accelerator code solves are as follows [112].

Conservation of Mass:

$$\rho u A = \dot{m} = \text{constant} \tag{2.1}$$

Equation of Motion:

$$\rho u \frac{du}{dx} + \frac{dP}{dx} = -J_y B - 4\frac{\tau_w}{D} \tag{2.2}$$

Energy Balance:

$$\rho u \frac{dh}{dx} + \rho u^2 \frac{du}{dx} = J_y E_y + 4\frac{q_w}{D} \tag{2.3}$$

In these equations, $\dot{m}$ and q_w are mass flow rate and wall heat flux, respectively. The wall shear stress, τ_w, is calculated by

$$\tau_w = \frac{\rho u^2 f}{2}, \tag{2.4}$$

where the friction factor, $f = f(Re_D, \varepsilon/D)$, is a function of Reynolds number (for duct flow), Re_D; surface roughness, ε; and hydraulic diameter, D. The equations of

state are

$$P = \rho RT, \tag{2.5}$$

$$h = h\left(P, T\right), \tag{2.6}$$

and

$$R = R\left(P, T\right), \tag{2.7}$$

where P, T, R, and h are pressure, temperature, gas constant, and enthalpy, respectively. Finally, the LyTec numerical model expresses the generalized Ohm's Law as [112]

$$\mathbf{J} = \sigma\left(\mathbf{E} + \mathbf{u} \times \mathbf{B}\right) + \sigma\mathbf{E}_d - \frac{\omega\tau}{B}\left(\mathbf{J} \times \mathbf{B}\right). \tag{2.8}$$

The equivalent electric field, $\mathbf{E}_d$, that accounts for the nearby electrode voltage drop, V_d, inside the boundary layer, is $\mathbf{E}_d = V_d/H$, where H is the MHD channel height [90]. Ohm's Law, with the Hall parameter assumed negligible, becomes

$$J^2 = \mathbf{J} \cdot \mathbf{J} = \sigma\left(\mathbf{J} \cdot \mathbf{E} + \mathbf{J} \cdot \left(\mathbf{u} \times \mathbf{B}\right) + \mathbf{J} \cdot \mathbf{E}_d\right), \tag{2.9}$$

or

$$\mathbf{J} \cdot \mathbf{E} = \frac{J^2}{\sigma} - J_y uB\left(1 - \Delta\right), \tag{2.10}$$

where the dimensionless effective voltage drop, Δ, can be expressed as $\Delta = E_d/uB$.

The specific methods used in the Runge-Kutta integration of this system of equations are provided in other sources [116]. The assumptions used to obtain this system of equations and carry out the numerical integrations are as follows [112]:

1. The gas is homogenous in species concentration and thermodynamic properties.

2. The flow is uniform to a plane perpendicular to the flow.

3. Induced magnetic fields are negligible.

4. Plasma-to-electrode voltage drops are proportional to generated voltage, (uBD).

5. The flow can be chemically frozen or in chemical equilibrium.

6. If any one of the four variables—u, P, T, or A—is *a' priori* specified as a function of x (distance along the channel), the axial distributions of the other three variables are found by numerical integration.

2.2.2   Results

Detailed design of any accelerator depends on the available magnet and power supply equipment. A water-cooled $2\,\mathrm{T}$ electromagnet, as seen in Figure 2.8, was acquired from the University of Tennessee Space Institute (UTSI) and refurbished to support the general MHD research at NASA MSFC. The lighter colored coils (marked "4" and "5" in part (b) of Figure 2.8) were recently added to the electromagnet to increase the overall magnetic field strength. The specifications for this electromagnet are detailed in Table 2.3. A new $3000\,\mathrm{A}$, $75\,\mathrm{V}$ DC power supply was acquired to power the electromagnet, and the entire system was integrated into the MAPX facility [14].

Based on existing power availability and preliminary sizing calculations, it was concluded that $2\,\mathrm{MW_e}$ of accelerator power would be sufficient to meet the research goals of the MAPX program and still fit within the facility power and program fiscal
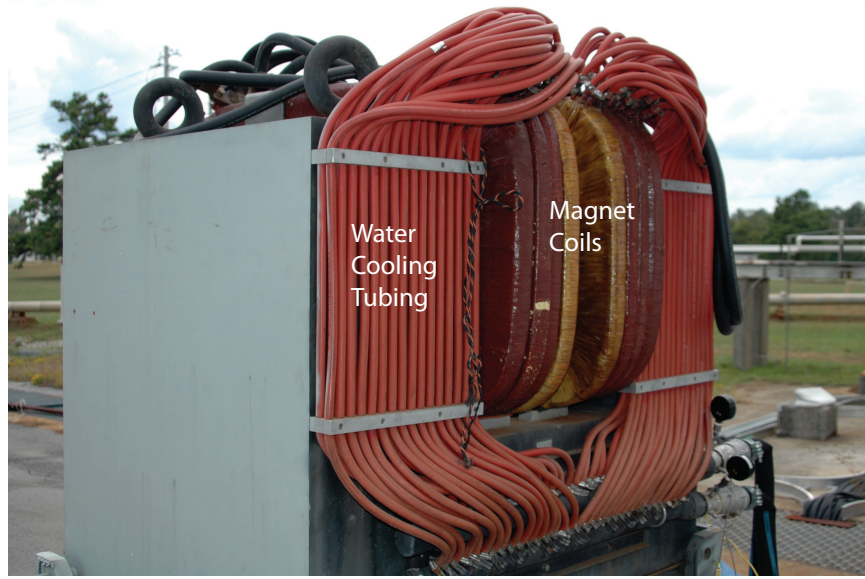
(a)

(b)

Figure 2.8: Photographs of the water-cooled 2 T electromagnet acquired from UTSI and refurbished for use at NASA MSFC: (a) the upstream end of the magnet, showing the large coils and the cooling tubes, and (b) the downstream end of the magnet, showing the large-diameter cables which provide power to the coils.

Table 2.3: Performance specifications for the MAPX electromagnet.

Characteristic	Value
Field Strength (tesla)	2.0
Air Gap (inches, cm)	4.0, 10.16
Pole Cap (inches, cm)	36.0, 91.44
Voltage (volts)	65.0
Maximum Current (A)	2400
Cooling Water (gpm at 70 psig, L/min at 482.6 kPa)	50.0, 189.3

budgets [14]. The MAPX team chose a variable voltage DC power supply capable of supplying up to 10 kV, with a nominal output of 6700 V at a current load of 300 A. This power supply and control unit have been integrated into the MAPX facility [14].

The detailed design process entailed several iterative calculations using the LyTec one-dimensional MHD accelerator code in an attempt to optimize the stagnation pressure rise by varying current load, channel divergence, and channel length. These calculations were performed assuming a Rosa G factor of $G \approx 2$ and a uniform 2 T applied magnetic field at full magnet power [14]. The height-to-width aspect ratio at the inlet was one, while the divergent **E** field and **B** field walls were to accommodate boundary layer growth and flow expansion. The final physical design of the MAPX accelerator is summarized in Table 2.2.

The predicted gasdynamic and electrical distributions, calculated using the LyTec one-dimensional MHD accelerator code, along the MAPX channel (in the $\hat{\mathbf{x}}$, or axial, direction) are shown in Figures 2.9 and 2.10, respectively, assuming the axial current neutralized condition (*i.e.*, $J_x = 0$) [14]. These calculations indicate
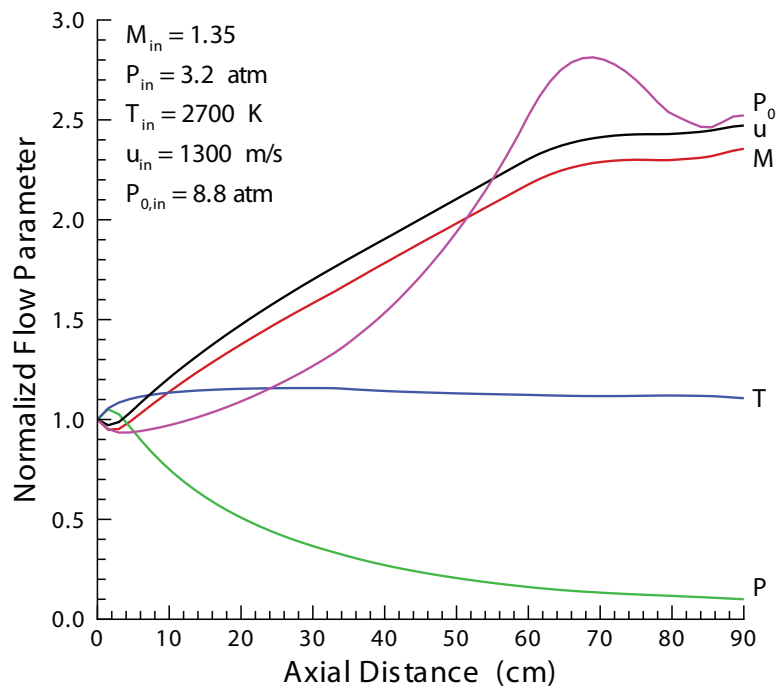
Figure 2.9: LyTec-MAPX 1-D predicted gasdynamic axial distributions.
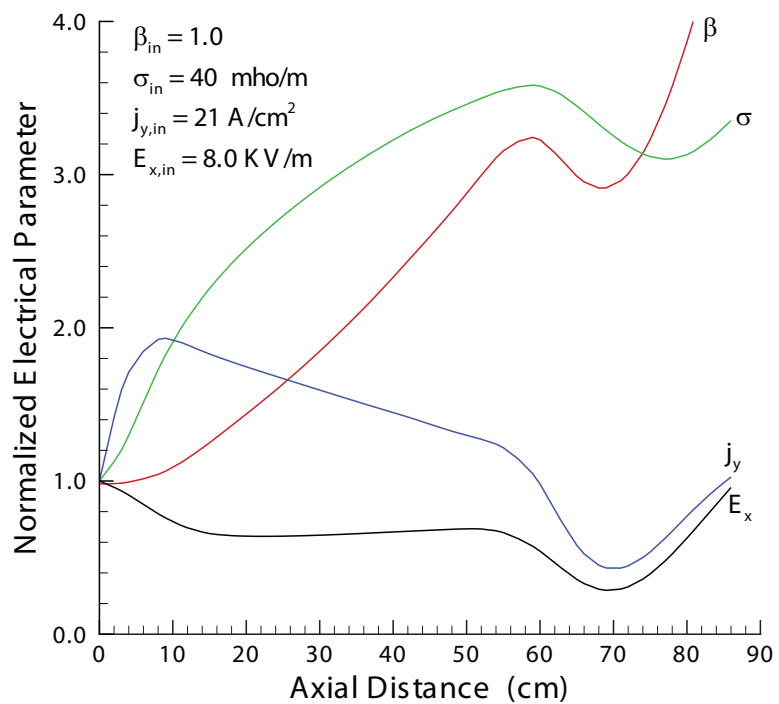
Figure 2.10: LyTec-MAPX 1-D predicted electrical axial distributions.

Table 2.4: Performance characteristics for MAPX accelerator, calculated using the LyTec one-dimensional MHD accelerator code with air as the working fluid.

Characteristic	Value
Seed (% NaK)	1.0
Applied Magnetic Field, B (tesla)	2.0
Flow Rate, $\dot{m}$ (g/s)	130.0
Inlet Stagnation Pressure, $P_{0,in}$ (atm)	8.8
Inlet Static Pressure, P_{in} (atm)	3.2
Inlet Temperature, T_{in} (K)	2700
Inlet Mach Number, M_{in}	1.35
Inlet Flow Velocity, u_{in} (m/s)	1300
Exit Stagnation Pressure, $P_{0,ex}$ (atm)	38.5
Exit Static Pressure, P_{ex} (atm)	0.28
Exit Temperature, T_{ex} (K)	3000
Exit Mach Number, M_{ex}	3.52
Exit Flow Velocity, u_{ex} (m/s)	3550
Applied Current, I_{app} (A)	300
Applied Voltage, V_{app} (V)	4400
Applied Electrical Power, P_{app} (MW)	1.3
Power Density (GW/m^3)	2.2
Accelerator Efficiency, η_a (%)	61
Dimensionless Effective Voltage Drop, Δ	0.28
Interaction Parameter, S_u	1.34
Enthalpy Addition Ratio	2.5
MHD Push Power, P_p (kW)	660
Total Joule (Power) Dissipation, P_d (kW)	330
Wall Heat Flux, q_w (W/cm^2)	890
$\varphi = E_y/E_x$ (effective value)	1.8

a total velocity increase of 150% with only a minor rise in static temperature. The static pressure at the end of the accelerator is about $0.3\,\mathrm{atm}$, which is sufficient for further expansion to the $0.05\,\mathrm{atm}$ backpressure limit of the test section. The current densities and axial electric fields were predicted to be slightly beyond the standard values accepted for continuous operation of MHD generators [14], but accelerators are far more energetically stressed, and the expected lifetime for many applications of interest can be measured in minutes rather than hours of operation. A summary of the LyTec one-dimensional MHD accelerator designs and performance predictions can be found in Table 2.4.

2.2.3   Limitations

The flow field of an MHD accelerator will exhibit features which require that, ultimately, a multidimensional evaluation be pursued [20]. There exists a myriad of experience and experimental data for conventional internal flows—which implies that established techniques for modeling turbulent flows using spatially integrated governing equations in one and two dimensions can be used with acceptable accuracy. Unfortunately, this is not the case for the MHD accelerator—specifically, when the MHD interaction is strong, plasma and electrical nonuniformities that develop cannot confidently be modeled with spatially integrated techniques. Although these techniques do have value in fundamental engineering studies (*e.g.*, to roughly size the accelerator, map its operational regimes, and view its operational and performance characteristics), detailed specifications for the system design and precision evaluations

of its performance can only be achieved through multidimensional analyses using basic plasma and electrical variables [112].

The LyTec one-dimensional numerical model is outlined in Section 2.2.1. This one-dimensional equation set is much simpler than the three-dimensional set presented in Section 1.2, with details of the one-dimensional assumptions and limitations provided in Section 2.2.1. Most importantly, a one-dimensional numerical model does not account for any nonuniformities in the cross-sectional flow field of the plasma. The cross-sectional plane of an MHD internal duct flow is far from uniform [117]. Some of the MHD channel nonuniformities have already been mentioned—velocity overshoots, high near-wall temperatures, and electrode arcs—while others will be mentioned in the following section.

Integration of the MHD flow field across the cross-section is unable to give researchers a full, detailed, three-dimensional view of an MHD accelerator/generator. As discussed in previous sections, in an MHD channel, the Hall effect leads to a component of the Lorentz force which drives secondary flow, normal to the direction of the primary flow [93]. This secondary flow can influence the heat transfer, current distributions, shear stress, and axial velocity of the primary flow—all of which cannot be expressed in a one-dimensional model [20]. Furthermore, because one-dimensional models integrate the flow across the cross-section, it is impossible to determine whether the bulk of the flow is acting in a manner consistent with the the average, or if the cross-sectional average has been disproportionately influenced by some local phenomenon. For example, it is possible to have a flow field characteristic with differing extreme values in the core-flow and near-wall regions—the

cross-sectional average of this flow field characteristic would yield a value that describes neither region. Simply put, the MHD flow field is multidimensional, therefore a multidimensional numerical model is necessary to properly describe it.

2.3 Three-Dimensional Analysis

The flow field within an MHD accelerator can be quite complex when compared to that of conventional aerodynamic internal flows. These complexities arise from the influence of electromagnetic phenomena. The degree of this influence is termed "MHD interaction" [20, 87]. A plasma flow which develops in the presence of strong MHD interaction exhibits spatial nonuniformities and temporal variations of gas dynamic properties and electrical parameters. These nonuniformities are three dimensional in character and their effects on system operation and performance must be understood and adequately modeled for both system design as well as interpretation of results.

Nonuniformities that develop within the MHD flow field are driven by gradients of thermodynamic and electrical transport properties [93]. These gradients are in part attributable to the same phenomena which exist in aerodynamic duct flows, *i.e.*, wall losses (viscous effects and heat transfer) [118]. However, in MHD these are very strongly coupled to spatial variations in the plasma impedance and the MHD electrical processes. For example, flow-field boundary layers, which describe the velocity and temperature distributions near the duct walls, give rise to exaggerated gradients in the plasma electrical conductivity, electrical fields, and current densities [110, 119, 120]. These electrical nonuniformities are in turn coupled to the plasma dynamics through the Lorentz force and Joulean heat dissipation [15]. Consequently, the MHD

interaction is distributed in intensity through the plasma over the cross-plane and along the length of the accelerator duct, and is therefore directly proportional to the scale of the MHD device. This distribution is a function not only of the gradients, but also of the accelerator configuration (*e.g.*, Faraday, Hall, diagonal) [20]. The nonuniformity of MHD interaction along with constraints imposed on the accelerator by its configuration (*i.e.*, electrical boundary conditions) lead to the development of unconventional profiles of electrical and plasma dynamic properties.

A three-dimensional numerical model is necessary to properly describe the physical phenomena within an MHD channel [112]. Therefore, the MAPX team decided that in order to properly characterize the flow inside the MAPX accelerator, they would require a three-dimensional MHD accelerator numerical model. The following sections detail the selection process—modeling requirements, existing models, and technical approach—used by the MAPX team to determine the most effective means to numerically model the MAPX accelerator.

2.3.1   Numerical Model Requirements

Based on the specifications of this project and the anticipated needs of future research, the MAPX team defined a set of requirements for their numerical model. The list of requirements is below, with a brief explanation following:

- Three-dimensional MHD accelerator code.

- Diagonal configuration.

- Varying diagonal angle with axial current neutralized mode.

- Power takeoff.

- Relatively fast convergence times.

- Thermodynamic model.

- Electrical transport property model.

Obviously, as the first requirement states, the numerical model must be three-dimensional and be capable of running in a diagonalized accelerator mode. Furthermore, the numerical model should give the user the ability define different angles for different regions of the accelerator—*i.e.*, the angle is not a constant throughout the accelerator. Along those same lines, the MAPX numerical model should be able to calculate and output to the user the required angles for the case where there is no J_x current, which is called the axial current neutralized mode.

"Power takeoff," which will be discussed in Section 4.3.5, is a term used to describe the division of the applied current across several of the entrance electrodes, essentially lowering the amount of applied current seen by the plasma as it enters the MHD channel, which is to prevent "MHD compression" [121]. MHD compression occurs when a plasma enters an MHD channel and immediately encounters a high applied current, which causes Joule heating of the plasma, which results in an increase in back pressure, which can cause flow reversal in the accelerator. Power takeoff is a "real world" application (*i.e.*, something that is implemented in MHD accelerator experiments) used to prevent MHD compression (and subsequent flow reversal), and is therefore necessary to accurately model the MAPX accelerator.

The MAPX accelerator was designed with the ability to be quickly and easily reconfigured (*e.g.*, changing the diagonal angle of the accelerator). In order to keep pace during tests and to avoid costly downtime, the MAPX numerical model must converge on the order of minutes—at most, about two hours. Obviously, this requirement alone would preclude certain processor-intensive numerical models, but for the purposes of this project, that is an acceptable trade. Furthermore, the numerical model would be required to run on a standard notebook computer (*i.e.*, the code would not require a mainframe or cluster to converge in two hours or less).

The numerical model should also calculate thermodynamic and electrical transport properties. The MAPX team would prefer that the thermodynamic properties be calculated by an established code, such as the NASA Chemical Equilibrium with Applications (CEA) code [106, 107], so that there will be no question of their validity. Furthermore, the electrical transport property model, specifically the calculation of electrical conductivity, will require a collision integral solution scheme, as the plasmas will be only partially ionized.

2.3.2   Existing Numerical Models

Unfortunately, there are not many available three-dimensional MHD numerical models. As discussed in Sections 1.1.2 and 1.1.3, most of the numerical modeling development focused on MHD generators or MHD accelerators used in hypersonic testing facilities (*i.e.*, Faraday accelerators). Based on this, the MAPX team realized that there would be no "perfect" numerical model—whichever model they chose would most likely require extensive modification to properly model the MAPX accelerator.

The most widely used MHD numerical model is MACH2 (Multiblock Arbitrary Coordinate Hydromagnetic), which is a $2^1/_2$-dimension magnetohydrodynamic simulation code. The code's capabilities include a numerically generated solution-adaptive grid which permits it to be used for Eulerian or Lagrangian flow problems, use of real equations of state and transport properties from the Los Alamos National Laboratory SESAME package, and a multi-grid implicit magnetic field diffusion solver which can be used to simulate problems with vacuum [122, 123]. The flexibility offered by MACH2 allows its use in a wide range of MHD applications—recently, it was used to numerically model a coaxial plasma accelerator for use in magnetized target fusion (MTF) [124].

Power and flexibility notwithstanding, MACH2 is not a good fit for the MAPX accelerator project. The MAPX accelerator will be partially ionized, requiring a collision-based electrical conductivity calculation—MACH2 typically uses the Spitzer equation to calculate electrical conductivity [123], which assumes full ionization of the plasma [88]. MACH2 does, however, have a neutral resistivity model for partially ionized hydrogen, where it assumes a constant electron cross-section [122]—however, this too is inadequate for modeling the MAPX accelerator. In MACH2 the Hall parameter is only used in calculations involving axisymmetric geometries [124]. While this would function properly for the current MAPX configuration, future configurations would be limited by this axisymmetric condition. Finally, and most importantly, MACH2 is only a $2^1/_2$-dimension numerical model. True, it does permit Eulerian or Lagrangian flow problems, but in both cases, it only allows characteristics to vary in two directions [124] (*e.g.*, all characteristics in the $\hat{\mathbf{z}}$ direction would be considered

constant). Therefore, this type of numerical model is inappropriate for modeling the MAPX accelerator.

As described in Section 1.1.3, the Merkle CFD Group at Purdue University has developed a time-dependent, fully three-dimensional numerical model capable of simulating MHD flows [65–68]. In order to remove physical difficulties with boundary conditions, the computational domain is extended to encompass the plasma channel, the conducting and dielectric walls, and the surrounding air [66]. However, Merkle's model assumes that the electrical conductivity of the flow is either fixed or a function of the equilibrium ionization [65]. Because of the extended computational domain, convergence times for this model are on the order of weeks. In its current form, the computation domain of this numerical model is too comprehensive for the MAPX accelerator (*i.e.*, simulations would require too much time), while the electrical transport model is inappropriate.

The Multigrid Magnetohydrodynamic (MGMHD) computer code developed at the Argonne National Laboratory in the 1980s is a parabolic three-dimensional numerical model capable of modeling MHD generator flows in Hall, Faraday, and diagonal configurations [125]. The term "parabolic" three-dimensional numerical model simply means that the code assumes that the flow is predominantly in the axial direction, with the appropriate approximations for this condition—the code (1) neglects diffusional fluxes in the axial direction and (2) considers the pressure gradient in the axial momentum equation to be uniform over the cross-section [125]. For MHD channel flows, the parabolic assumption does not introduce any significant errors [126], and

permits the solution to be marched forward plane by plane from the inlet to the exit, which greatly reduces convergence times [127].

The MGMHD code, however, does not contain its own thermodynamic or electrical transport numerical model. It offers several options for the equations of state and electrical properties, all of which are based on constant or curve-fitted assumptions. The MGMHD code does, however, offer the user the ability to input their own thermodynamic and electrical transport properties [125].

As is evident, none of the existing MHD numerical models were a perfect fit for the MAPX accelerator project. However, the MGMHD, while only an MHD generator code with no thermodynamic or electrical transport property models, offers fast convergence times and relatively simple user modifications, which make it the best candidate for the MAPX accelerator project. Obviously, the MGMHD code will require major modifications—an outline of the approach to these modifications is presented in the next section, with details of the MGMHD code in Chapter 3 and modifications in Chapter 4.

2.3.3   Technical Approach

The objective of this research is to analyze the NASA Magnetohydrodynamic Augmented Propulsion Experiment (MAPX) using a three-dimensional numerical model. At the start of the MAPX project, there were no suitable three-dimensional numerical models that met the requirements set forth in Section 2.3.1. Therefore, as explained in Section 2.3.2, an existing numerical model would be modified to meet the requirements of the MAPX project—with the Argonne National Laboratory MGMHD

code being the best candidate for modification. This section outlines the approach taken to transform the MGMHD generator code into the UAH-MSFC MHD code, capable of fulfilling all the requirements set forth by the MAPX research group.

Because the MGMHD code lacks a true thermodynamic and electrical transport property model, the new UAH-MSFC MHD code would be divided into two main sections—the MHD code and the thermo-electric codes. This division would accomplish three main goals—(1) allow for the use of most, if not all, of the current MGMHD generator code, (2) allow for updates to either the MHD or thermo-electric codes without impact on the other, and (3) assuming the same thermo-electrical input for various test runs (*i.e.*, tests where the only changes would be modifications to the MHD accelerator configuration, and hence MHD code), allow for faster run-times because previous thermo-electric data could be reused. Division of the UAH-MSFC MHD code also allows for easier error checking and debugging, which is essential in any numerical application.

It has been well documented that, in the absence of one, the most expedient approach to realizing a sound multidimensional numerical model for an MHD accelerator is through the adaptation of existing generator models [20]. The details of the modifications will be explained in Chapter 4, but a brief outline of the modifications to the existing MGMHD generator code is as follows:

- Accelerator mode was added.

- Varying diagonal angle (with a axial current, J_x, neutralized option) was added.

- A power takeoff scheme (variation of applied current) was added.

- Total (stagnation) pressure calculations were added.

- Thermodynamic and electrical property models were added.

The first four modifications listed above occur in the MHD portion of the UAH-MSFC code, while the last modification listed comprises the thermo-electric portion of the UAH-MSFC MHD code, and will be discussed in the following paragraph. Please note that all the modifications to the MGMHD code are additions, and that the original functionality of the MGMHD code remains.

As stated in Section 2.3.1, the MAPX code requires an established thermodynamic model, such as the NASA CEA code [106, 107]. The NASA CEA code, however, does not have its own electrical transport property model—therefore, it would be necessary to develop one. For proper integration with the MGMHD code, the thermoelectric codes would be required to pass the following six variables to the MHD code, at every point in the MHD grid, at every plane in the channel:

- Temperature.

- Molecular weight.

- Ratio of specific heats (gamma).

- Viscosity.

- Electrical conductivity.

- Total charge.

The first four variables would be provided by the NASA CEA code, while the last two would be calculated by the electrical property model. Both, the thermodynamic and electrical property, codes would be required to pass information back-and-forth to operate properly—the details of this procedure will be given in Section 4.2.2.4.

In short, the stated goal of this research is to numerically model the NASA MAPX accelerator. No suitable MHD accelerator models existed, therefore it would be required to develop one. An MHD generator code was chosen as a basis for the MHD accelerator code. This generator code had no thermodynamic or electrical transport property models; therefore, it would be required to develop them. The NASA CEA code was chosen for the basis of the thermodynamic model, but it lacked an electrical model—therefore, its development was necessary. Obviously, all the modified and new codes would have to communicate seamlessly in order to properly model the MAPX diagonal accelerator.

CHAPTER 3

BASELINE MODELING CAPABILITIES

*Consistently separating words by spaces be-
came a general custom about the tenth cen-
tury A.D., and lasted until about 1957,
when FORTRAN abandoned the practice.*

—Sun FORTRAN Reference Manual

3.1 Overview

As discussed in Section 2.3.3, the goal of this research is to analyze the NASA

MAPX accelerator using a three-dimensional numerical model—however, at the be-

ginning of this project, no appropriate numerical models existed. It was determined

that the most effective approach to realizing a sound multidimensional numerical

model for an MHD accelerator is through the adaptation of existing generator mod-

els, specifically, the MGMHD code. This chapter will detail the original state of the

MGMHD code—the gas dynamic model, electromagnetic model, state equations, so-

lution procedure, user options, and input instructions before any modifications were

made—and outline the modifications required to transform the MGMHD generator

code into a numerical model which can appropriately model the MAPX diagonal

accelerator.

The Multigrid Magnetohydrodynamic (MGMHD) computer code is an updated version of the single-grid Three-Dimensional Magnetohydrodynamic (TDMHD) code developed at the Argonne National Laboratory in 1982 for the analysis of magnetohydrodynamic generators and diffusers [125, 126, 128]. The MGMHD code retains the TDMHD formulation of three-dimensional partial differential equations for flow and electrical fields but incorporates an advanced multigrid solution algorithm to reduce computer convergence time [127, 129, 130]. The magnetohydrodynamic equation set comprises the mass continuity equation, three momentum equations, the energy equation, two turbulence models, and Maxwell's electrical equations. Turbulence is represented by a two-equation model in which partial differential equations are solved for the turbulence energy and its dissipation rate. Lastly, the MGMHD code provides two unique features:

- A full approximation storage (FAS), block implicit multigrid, finite-difference solution procedure for the cross-stream hydrodynamic equations.

- A FAS multigrid finite-difference solution procedure for cross-stream electrical potential equations.

3.2 Fluid Dynamic Model

The flow processes in an MHD generator can be represented by the three-dimensional Navier-Stokes equations [126, 128]. In an MHD channel, the flow is predominantly in the axial direction, which allows for certain simplifications considering the order of magnitude of various terms. The simplification made here is referred to

as the parabolic approximation [131, 132], which is akin to the boundary-layer approximation made in solving problems such as the flat-plate flow, and consists of the following assumptions:

1. Neglecting the diffusional fluxes in the axial directions

2. Considering the pressure gradient in the axial momentum equation to be uniform over the channel cross-section.

The parabolic approximation permits the solution to be marched forward plane-by-plane from the inlet to the exit of the channel. The pressure field, p, is split into two components: (1) $\tilde{p}$, the local cross-sectional pressure, and (2) $\bar{p}$, the cross-sectional average pressure, which, as Equation 3.1 shows, is only a function of the axial coordinate:

$$p\left(x, y, z\right) = \tilde{p}\left(x; y, z\right) + \bar{p}\left(x\right). \tag{3.1}$$

The parabolic approximation does not introduce any significant errors when the flow is predominantly in one direction, and it eliminates the need to iterate between the inlet and exit of the channel, thereby making the calculation converge more quickly [125].

3.2.1 Mean Flow Equations

The governing steady-state equation for a variable ϕ can be written as follows [125]:

$$\nabla \cdot \left(\rho \mathbf{u} \phi\right) + \mathbf{P}^{\phi} = \mathbf{S}^{\phi} + \nabla \cdot \left(\Gamma^{\phi} \nabla \phi\right), \tag{3.2}$$

where $\mathbf{P}^\phi$ is the pressure gradient term (when appropriate), $\mathbf{S}^\phi$ represents the source

terms, and Γ^ϕ is the diffusion coefficient. Application of Equation 3.2 in a Cartesian

coordinate system to the mass continuity equation, the momentum equations, and

the energy (enthalpy) equations yields the following set of equations [128].

Mass Continuity:

$$\frac{\partial}{\partial x}(\rho u) + \frac{\partial}{\partial y}(\rho u) + \frac{\partial}{\partial z}(\rho w) = 0 \tag{3.3}$$

x-Momentum (axial direction):

$$\frac{\partial}{\partial x}(\rho uu) + \frac{\partial}{\partial y}(\rho vu) + \frac{\partial}{\partial z}(\rho wu) = -\frac{\partial \bar{p}}{\partial x} + \frac{\partial \tau_{xy}}{\partial y} + \frac{\partial \tau_{xz}}{\partial z} + J_y B \tag{3.4}$$

y-Momentum:

$$\frac{\partial}{\partial x}(\rho uv) + \frac{\partial}{\partial y}(\rho vv) + \frac{\partial}{\partial z}(\rho wv) = -\frac{\partial \tilde{p}}{\partial y} + \frac{\partial \tau_{yy}}{\partial y} + \frac{\partial \tau_{yz}}{\partial z} - J_y B \tag{3.5}$$

z-Momentum:

$$\frac{\partial}{\partial x}(\rho uw) + \frac{\partial}{\partial y}(\rho vw) \frac{\partial}{\partial z}(\rho ww) = -\frac{\partial \tilde{p}}{\partial z} + \frac{\partial \tau_{zy}}{\partial y} + \frac{\partial \tau_{zz}}{\partial z} \tag{3.6}$$

Enthalpy (Energy):

$$\frac{\partial}{\partial x}(\rho uh) + \frac{\partial}{\partial y}(\rho vh) + \frac{\partial}{\partial z}(\rho wh) = -\frac{\partial q_y}{\partial y} - \frac{\partial q_z}{\partial z} + u\frac{\partial \bar{p}}{\partial x} + v\frac{\partial \tilde{p}}{\partial y} + w\frac{\partial \tilde{p}}{\partial z} + \frac{J^2}{\sigma} + D \tag{3.7}$$

The viscous dissipation rate, D, is calculated as follows:

$$D = (\mu_\ell + \mu_t) \left[2 \left(\left(\frac{\partial w}{\partial z} \right)^2 + \left(\frac{\partial v}{\partial y} \right)^2 \right) + \left(\frac{\partial w}{\partial y} + \frac{\partial v}{\partial z} \right)^2 + \left(\frac{\partial u}{\partial z} \right)^2 + \left(\frac{\partial u}{\partial y} \right)^2 \right].$$

(3.8)

In the above equations, u, v, and w are the x, y, and z components of the **u** velocity vector. Notice that the difference between the above equation set and Equations 1.1, 1.2 and 1.3 in Section 1.2 is the absence of time-dependence (derivatives with respect to time) in the MGMHD code. The MGMHD code assumes steady-state; therefore, any time-dependent fluctuations will not be captured with this numerical model. Furthermore, note that Equation 3.7 uses enthalpy where Equation 1.3 uses $c_p T$, the product of specific heat and temperature, in the energy equation. This is because the MGMHD code advances the energy equation using enthalpy, not temperature. Advancing the energy equation using temperature requires that one assume a constant specific heat (*i.e.*, taking c_p out of the derivative in Equation 1.3), which is not true in some temperature ranges. Advancing the energy equation using enthalpy (or internal energy) requires no such assumption.

3.2.2   Turbulence Model

The turbulent kinetic energy equation, k, performs better if coupled with a second modeling rate of change—either (1) dissipation, ϵ, or (2) turbulent length scale, L [133]. Because of the work by Jones and Launder [134], modeling the dissipation rate of change has become the preferred method. Flow velocities in an MHD channel are generally high, therefore turbulence effects must be calculated. The MGMHD code

uses the two-equation (k-ϵ) turbulence model, while shear stress and heat transfer fluxes are calculated from equations containing terms for the turbulent viscosity and the gradients of the flow variables [125]. For example, the total shear stress flux is the following:

$$\tau_{ij} = (\mu_t + \mu_\ell) \left(\frac{\partial u_i}{\partial x_j} + \frac{\partial u_j}{\partial x_i} \right), \tag{3.9}$$

and the heat transfer flux can be represent by the following:

$$q_i = - \left(\frac{\mu_t}{\sigma_h} + \frac{\mu_\ell}{\sigma_\ell} \right) \left(\frac{\partial h}{\partial x_i} \right). \tag{3.10}$$

The laminar viscosity, μ_ℓ will be discussed in Section 3.4, and the turbulent viscosity is calculated from the local values of the turbulent kinetic energy (k) and its dissipation rate (ϵ), using the formula [125]

$$\mu_t = C_\mu \left(\frac{\rho k^2}{\epsilon} \right). \tag{3.11}$$

The laminar Prandtl number, σ_ℓ, is the ratio of the kinematic viscosity to the thermal diffusivity, while σ_h and C_μ are dimensionless empirical constants whose recommended values are given in Table 3.1. The values of k and ϵ are obtained from the solution of the following transport equations [128].

Table 3.1: Recommended values of the constants in the $k - \epsilon$ model.

C_μ	C_1	C_2	σ_k	σ_ℓ	σ_h
0.09	1.47	1.92	1.0	1.3	0.9

Turbulent kinetic energy transport equation:

$$\frac{\partial}{\partial x}(\rho u k) + \frac{\partial}{\partial y}(\rho v k) + \frac{\partial}{\partial z}(\rho w k) = \frac{\partial}{\partial y}\left[\left(\frac{\mu_t}{\sigma_k} + \mu_\ell\right)\frac{\partial k}{\partial y}\right]$$
$$+ \frac{\partial}{\partial z}\left[\left(\frac{\mu_t}{\sigma_k} + \mu_\ell\right)\frac{\partial k}{\partial z}\right] + G - \rho\epsilon \quad (3.12)$$

Turbulent dissipation rate transport equation:

$$\frac{\partial}{\partial x}(\rho u \epsilon) + \frac{\partial}{\partial y}(\rho v \epsilon) + \frac{\partial}{\partial z}(\rho w \epsilon) = \frac{\partial}{\partial y}\left[\left(\frac{\mu_t}{\sigma_\epsilon} + \mu_\ell\right)\frac{\partial \epsilon}{\partial y}\right]$$
$$+ \frac{\partial}{\partial z}\left[\left(\frac{\mu_t}{\sigma_\epsilon} + \mu_\ell\right)\frac{\partial \epsilon}{\partial z}\right] + \frac{C_1 G \epsilon}{k} - C_2 \rho \frac{\epsilon^2}{k} \quad (3.13)$$

Here, C_1 and C_2 are dimensionless empirical constants (with recommended values given in Table 3.1), σ_ϵ and σ_k are effective "Prandtl numbers" which relate eddy diffusion of k and ϵ to the momentum eddy viscosity [133] (also with recommended values in Table 3.1), and G represents the production of kinetic energy of turbulence as a result of the interaction of the shear stresses and the velocity gradients. After neglecting the axial gradients, the expression for G is [128]

$$G = \mu_t \left[2\left[\left(\frac{\partial v}{\partial y}\right)^2 + \left(\frac{\partial w}{\partial z}\right)^2\right] + \left(\frac{\partial u}{\partial y}\right)^2 + \left(\frac{\partial u}{\partial z}\right)^2 + \left(\frac{\partial v}{\partial z} + \frac{\partial w}{\partial y}\right)^2 \right]. \quad (3.14)$$

On the right-hand-side of Equations 3.12 and 3.13, the first two terms represent diffusive transport, while the latter two terms represent the rate of production and the rate of dissipation of the respective quantities. For full justification and interpretation of these terms, please seek sources dedicated to such material [135]. Because there is no quantifiable evidence for the damping or generation of turbulence by MHD interaction, no specific terms are included for these phenomena [125]; however, MHD influences on k and ϵ are indirectly implied in these equations through the influence of Lorentz forces on the u, v, and w velocities.

3.2.3 Near-Wall Model

In turbulent flows, the gradients of flow variables adjacent to solid walls are very steep, and a very fine finite-difference mesh is required to properly resolve these gradients. Not only is such an approach expensive, but the present turbulent model, which is designed for high Reynolds numbers, is invalid in the near-wall regions [128]. Therefore, to correctly predict near-wall momentum and energy flux, the MGMHD code employs a procedure known as the "wall-function approach" [135], which implicity considers the steep gradients near the walls and avoids the need of a fine grid.

The first step of the wall-function approach is to place all the finite-difference grid nodes (except those representing the wall values) in the fully turbulent regions of the flow. Hence, the nodes adjacent to the walls must be located far enough from the wall for the local turbulent Reynolds number, $R_T = (y\rho\sqrt{k}/\mu_\ell)_P$, to be much greater than unity [125]. Based on the assumption that a logarithmic velocity profile prevails in the region between the wall and the adjacent node P, the axial velocity and the

wall shear stress are related by

$$\frac{u_P}{(\tau/\rho)^{1/2}_{wall}} = \frac{1}{\kappa} \ln\left(\frac{E_r y_P (\tau\rho)^{1/2}_{wall}}{\mu_\ell}\right),\tag{3.15}$$

where $\kappa = 0.4$ and $E_r = E_0 = 8.12$ for smooth walls, and where the subscript P denotes values at a grid node P. The axial velocity at point P, u_P, is assumed to be parallel to the wall shear-stress, and y_P is the distance from P to the wall.

The shear stress in the fluid layer between point P and the wall is then related to the kinetic energy of turbulence by considering that (in the uniform-shear-stress layer) the generation and dissipation of k are nearly in balance. This leads to the following relation [128]:

$$\tau_P = \tau_{wall} = \rho C_\mu^{1/2} k_p,\tag{3.16}$$

where the value of C_μ is constant and given in Table 3.1. By using Equations 3.15 and 3.16, the shear stress can be expressed by the relation

$$\tau_P = \frac{\rho\kappa C_\mu^{1/4} k_P^{1/2} w_P}{\ln\left(\frac{E_r y_P C_\mu^{1/4} \rho k_P^{1/2}}{\mu_\ell}\right)}.\tag{3.17}$$

The rate of dissipation of kinetic energy, ϵ_P, is fixed by the requirement that the length scale vary linearly with distance from the wall. The expression for ϵ_P is therefore [125]

$$\epsilon_P = \frac{C_\mu^{3/4} k_P^{3/2}}{\kappa y_P}.\tag{3.18}$$

The kinetic energy of turbulence, k_P, is calculated from Equation 3.12, but first the diffusion of energy term is set equal to zero and the generation term in the kinetic energy-energy equation is modified to account for the value of wall shear stress calculated from Equation 3.17 [118,133]. The dissipation term is also modified according to Equation 3.18 and is assigned an average (*i.e.*, "bar") value of the control volume for the near-wall node, giving [125]

$$\rho\bar{\epsilon} = \rho \int_0^{y_e} \epsilon dy = \rho C_\mu^{3/4} k_P^{3/2} \int_0^{y_e} \frac{1}{\kappa y}\, dy, \qquad (3.19)$$

where y_e is the distance between the edge of the control volume and the wall.

The wall functions for the transport of temperature (or enthalpy) are derived in a manner similar to that used in Equation 3.17. The near-wall variation of enthalpy is also assumed to be logarithmic, giving the equation [125]

$$\frac{\rho\kappa C_\mu^{1/4} k_P^{1/2} (h_P - h_{wall})}{q_{wall}} = \sigma_h ln \left(\frac{E_r y_P C_\mu^{1/4} \rho k_P^{1/2}}{\mu_\ell} \right) + \kappa P_r, \qquad (3.20)$$

where h_P and h_{wall} are the values of enthalpy at point P and the wall, respectively, and q_{wall} represents the heat flux from the wall. The term P_r (absent in Equation 3.17) is the additional resistance to the transfer of heat caused by the existence of the laminar sublayer and is the following function for smooth walls [132]:

$$P_r = P_0 = 9.24 \left(\frac{\sigma_\ell}{\sigma_h} - 1 \right) \left(\frac{\sigma_\ell}{\sigma_h} \right)^{-1/4}. \qquad (3.21)$$

The values of P_r and E_r are modified to account for rough surfaces. The roughness Reynolds number, R_r, is defined as $R_r = (\rho y_r u)/\mu_P$. E_0 and P_0 represent the values for the zero wall roughness case. The approach followed in the MGMHD code is that recommended by Jayatillaka [136], where the constants, E_r and P_r, are related to the equivalent sand-grain roughness height, y_r (which is a user-defined input), through the following formulae [125]:

For $0 \leq R_r \leq 3.7$,

$$E_r = E_0 = 8.12, \tag{3.22}$$

and

$$P_r = P_0, \tag{3.23}$$

which was given in Equation 3.21.

For $3.7 \leq R_r \leq 100.0$,

$$E_r = \left[\alpha \left(\frac{R_r}{30} \right)^2 + \frac{(1-\alpha)}{E_0^2} \right]^{-1/2}, \tag{3.24}$$

$$P_r = 3.15\sigma_h^{0.695} \left(\frac{1}{E_r} - 0.1231 \right)^{0.359} + 0.2846\frac{P_0}{E_0^{0.6}}, \tag{3.25}$$

$$\alpha = 1 + 2\chi_c^3 - 3\chi_c^2, \tag{3.26}$$

and

$$\chi_c = 0.02248 \frac{(100 - R_r)}{R_r^{0.584}}. \tag{3.27}$$

For $R_r > 100.1$,

$$E_r = \frac{30.0}{R_r}, \tag{3.28}$$

and P_r is calculated using Equation 3.25. Note that increasing the roughness decreases the value of E_r and increases the value of P_r.

3.3   Electrical Model

As previously stated, the MGMHD code is an MHD generator numerical model. The internal environment of an MHD accelerator is typically more severe than that of an MHD generator [20]; but both, generator and accelerator, experience the same (or similar) complex flows and electrical phenomena, such as velocity overshoots in the sidewall boundary layers, flow asymmetries, current constrictions, and intense secondary flows in the channel cross-section [15, 20, 87, 93]. These phenomena are highly coupled and three-dimensional in nature. Finite segmentation effects on the global performance of MHD generators have been shown to become negligible for medium- or large-base-load generators that have a pitch-to-height ratio on the order of 1-5% [125, 137–139]. For smaller generators, finite segmentation effects become more important and should be considered—infinite segmentation analysis of small generators usually over predicts their global performance [138, 139].

The slow calculation of the electrical potential solution is one difficulty in performing a complete three-dimensional flow and electrical finite segmentation analysis

of MHD generators. In this section, a cross-sectional infinite segmentation electrical model, developed by Ahluwalia [137], is presented. An infinte segmentation model, basically, neglects axial variations of the flow and electrical variables in comparison with their cross-plane variations [125, 128, 137]. This allows the solution procedure to "march" from the entrance of the channel to the exit. This model was successfully applied to the three-dimensional analysis of Faraday, diagonal insulating, and diagonal conducting sidewall MHD generators [125, 128, 129, 137, 140]. This electrical model is coupled to the fluid dynamic model presented in Section 3.2. A much more detailed derivation of this electrical model can be found in Appendix C.

3.3.1   Formulation and Analysis

In the MGMHD code, the electrical governing equations consist of Maxwell's steady-state equations and Ohm's Law. The electrical field, $\mathbf{E}$, and the current density, $\mathbf{J}$, are obtained by solving the following equations:

$$\nabla \times \mathbf{E} = 0, \tag{3.29}$$

$$\nabla \cdot \mathbf{J} = 0, \tag{3.30}$$

and

$$\mathbf{J} = \sigma \left(\mathbf{E} + \mathbf{u} \times \mathbf{B} \right) - \frac{\beta}{B} \mathbf{J} \times \mathbf{B}. \tag{3.31}$$

As typical for MHD channel flows, these equations are valid for low magnetic Reynolds number flows, where the induced magnetic fields can be neglected [125, 128, 137]. Note

that the three components of **E** are not really "independent." From Equation 3.29, the following relations can be derived:

$$\frac{\partial E_x}{\partial y} = \frac{\partial E_y}{\partial x}, \qquad \frac{\partial E_z}{\partial y} = \frac{\partial E_y}{\partial z}, \qquad \frac{\partial E_x}{\partial z} = \frac{\partial E_z}{\partial x} \tag{3.32}$$

Therefore, the form of Equations 3.29 and 3.30 makes it is possible to define an electric potential, ψ, such that [91, 141]

$$\mathbf{E} = -\nabla\psi, \tag{3.33}$$

which, because of the steady-state assumption ($\frac{\partial}{\partial t} = 0$), effectively reduces a vector problem to that of a scalar. Also note that the MGMHD code assumes that the magnetic field, **B**, is sectionally uniform and oriented in the positive $\hat{\mathbf{z}}$ direction, as seen in Figures 3.1 and 3.2.

The infinite segmentation model is constructed from Equations 3.29 and 3.30 by neglecting axial variations of the flow and electrical variables in comparison with their cross-plane variations. Consequently, the axial electric field, E_x, is assumed to be constant in a cross-sectional plane [137]. As detailed in Appendix C, by defining a set of oblique coordinates in the general case of a diagonal connection, the electric potential can be represented by [128, 129, 137, 138, 140]

$$\psi = -\left(x - y\cot\theta_d\right)E_x + \phi(y, z), \tag{3.34}$$

where θ_d is the diagonalization angle (measured in a counter-clockwise direction from the positive x-axis), and $\phi(y, z)$ is a two-dimensional potential. Please see Sec-
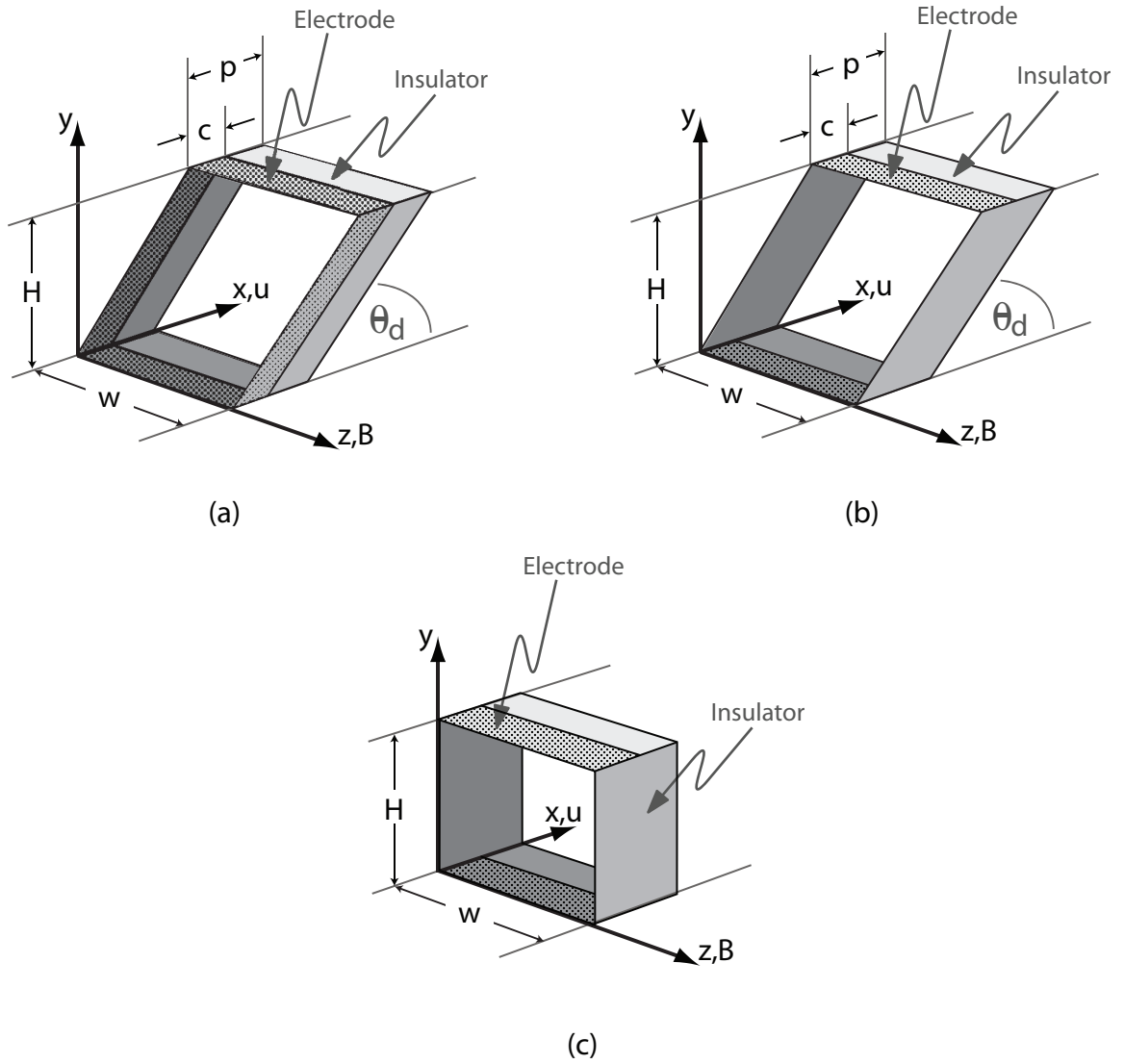
Figure 3.1: Schematic representation of generator configurations in Cartesian coordinates: (a) Diagonal conducting sidewall, (b) Diagonal insulating sidewall, and (c) Faraday.
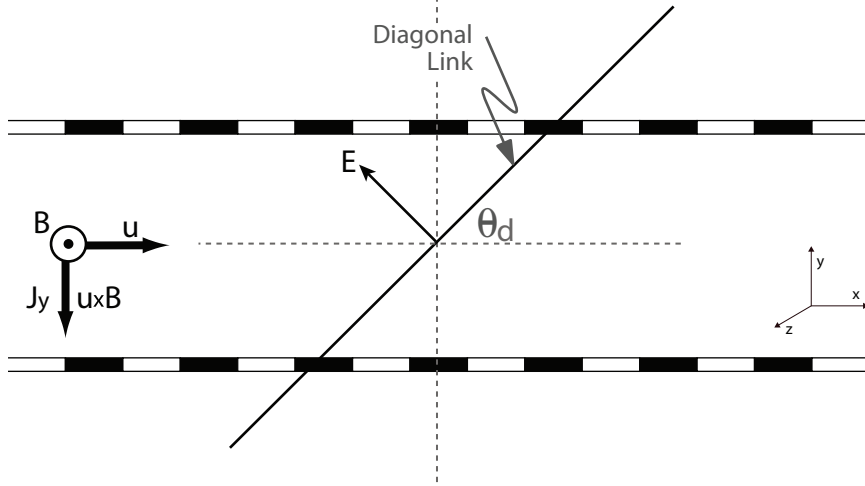
Figure 3.2: Orientation of field vectors in a diagonally connected cross-field MHD generator.

tion 3.3.2 for a more detailed explanation of the diagonalization angle. The first term on the right-hand-side of Equation 3.34 represents the contribution of the axial ($\hat{\mathbf{x}}$) electric field. Substituting Equation 3.34 into Equations 3.29, 3.30 and 3.31, results in the following equation for the two dimensional function $\phi(y,z)$,

$$\frac{\partial}{\partial y}\left(\sigma_n \frac{\partial \phi}{\partial y}\right) + \frac{\partial}{\partial z}\left(\sigma \frac{\partial \phi}{\partial z}\right) = E_x \frac{\partial}{\partial y}\left[(\beta - \cot\theta_d)\,\sigma_n\right] - \frac{\partial}{\partial y}\left[\sigma_n B\left(u - \beta v\right)\right], \quad (3.35)$$

where $\sigma_n = \sigma/\left(1 + \beta^2\right)$. Since E_x is not known *a' priori*, and because Equation 3.35 is linear in ϕ, a decomposition of the potential is permitted as follows [125]:

$$\phi(y,z) = E_x \phi_1 + \phi_2. \quad (3.36)$$

The two functions, ϕ_1 and ϕ_2, are governed by the following equations [128]:

$$L(\phi_1) = \frac{\partial}{\partial y} \left[(\beta - \cot \theta_d) \, \sigma_n \right] \tag{3.37}$$

and

$$L(\phi_2) = -\frac{\partial}{\partial y} \left[\sigma_n B \left(u - \beta v \right) \right], \tag{3.38}$$

where the operator, L, is [128, 137]

$$L = \frac{\partial}{\partial y} \left(\sigma_n \frac{\partial}{\partial y} \right) + \frac{\partial}{\partial z} \left(\sigma \frac{\partial}{\partial z} \right). \tag{3.39}$$

Note that the function ϕ_1 in Equation 3.37 is driven by the temperature nonuniformities, while ϕ_2 in Equation 3.38 is driven by temperature and velocity nonuniformities. Both functions are independent of E_x, which is reduced to a parameter of the problem to be determined later from the specification of the external electrical connection and loading. From Ohm's Law, the current density components—J_x, J_y, and J_z—can be expressed as

$$J_x = E_x \sigma_n \left(1 + \beta \cot \theta_d + \beta \frac{\partial \phi_1}{\partial y} \right) + \sigma_n \left[(\beta u + v) B + \beta \frac{\partial \phi_2}{\partial y} \right], \tag{3.40}$$

$$J_y = E_x \sigma_n \left(\beta - \cot \theta_d - \frac{\partial \phi_1}{\partial y} \right) - \sigma_n \left[(u - \beta v) B + \frac{\partial \phi_2}{\partial y} \right], \tag{3.41}$$

and

$$J_z = -E_x \sigma \frac{\partial \phi_1}{\partial z} - \sigma \frac{\partial \phi_2}{\partial z}. \tag{3.42}$$

To find the cross-sectional averages, $\langle J_x \rangle$ and $\langle J_y \rangle$, the cross-sectional spatial average, $\langle f \rangle$, must first be defined as

$$\langle f \rangle = \frac{1}{A} \int f(y,z)\, dA, \tag{3.43}$$

where A is the cross-sectional area normal to the channel, which yields [128, 137]

$$\langle J_x \rangle = E_x \left[\langle (1 + \beta \cot \theta_d)\, \sigma_n \rangle + \langle \sigma_n \beta \frac{\partial \phi_1}{\partial y} \rangle \right] + \langle \sigma_n \beta \frac{\partial \phi_2}{\partial y} \rangle + B \langle \sigma_n \left(\beta u + v \right) \rangle, \tag{3.44}$$

and

$$\langle J_y \rangle = E_x \left[\langle (\beta - \cot \theta_d)\, \sigma_n \rangle - \langle \sigma_n \frac{\partial \phi_1}{\partial y} \rangle \right] - \langle \sigma_n \frac{\partial \phi_2}{\partial y} \rangle - B \langle \sigma_n \left(u - \beta v \right) \rangle. \tag{3.45}$$

3.3.1.1 Boundary Conditions

In the original MGMHD generator code, boundary conditions for the functions ϕ_1 and ϕ_2 are defined by the channel configuration (as shown in Figures 3.1 and 3.2). Four types of connections are available [125]:

Case A: A Faraday connection for which the boundary potentials, $\Delta \phi$, are determined by the load factor K (where $K = [\Delta \phi]/[\langle u \rangle BH]$, with H being the channel height).

Case B: A Faraday connection for which the boundary potentials are defined in terms of an external resistance.

Case C: An insulating sidewall diagonal connection.

Case D: A conducting sidewall diagonal connection (also known as a "diagonal conducting wall," or DCW)

In the MGMHD code, these four types of connections are chosen by setting the parameter IOPT (= 1, 2, 3, or 4, respectively) as an input value [125]. Illustrations of these connections can be seen in Figure 3.1, noting that both Faraday cases are physically connected in the same manner. The following sections will detail each of the four configuration options.

Case A: Faraday connection with boundary condition defined in terms of load factor. For this type of connection, the parameter IOPT is set equal to 1, and the boundary conditions (for $z = 0$ and $z = W$, where W is the full width of the channel) are the following [128]:

$$J_x = 0, \tag{3.46}$$

for insulating sidewalls, where the definition of the load factor, K, is

$$K = -\frac{\phi_H - \phi_0}{\langle u \rangle BH}. \tag{3.47}$$

The potential ϕ_0 is arbitrary and can be set to zero. Because $\phi = E_x\phi_1 + \phi_2$ and $J_z = -\sigma(\partial\phi/\partial z)$, Equations 3.46 and 3.47 can be translated to the following set

of boundary conditions for ϕ_1 and ϕ_2 [128]:

$$\frac{\partial \phi_1}{\partial z} = 0, \qquad\qquad \frac{\partial \phi_2}{\partial z} = 0, \qquad\qquad \text{at } z = 0. \qquad (3.48)$$

$$\frac{\partial \phi_1}{\partial z} = 0, \qquad\qquad \frac{\partial \phi_2}{\partial z} = 0, \qquad\qquad \text{at } z = W. \qquad (3.49)$$

$$\phi_1 = 0, \qquad\qquad \phi_2 = 0, \qquad\qquad \text{at } y = 0. \qquad (3.50)$$

$$\phi_1 = 0, \qquad\qquad \phi_2 = -KuBH, \qquad\qquad \text{at } y = H. \qquad (3.51)$$

The load factor, K, can vary along the channel length and is input by the user [125]. From the above boundary conditions, it is clear that for a short-circuit case (where $\phi_1 = \phi_2$), $K = 0$, and for an open-circuit case (where $\phi_2 = uBH$), $K = 1$— therefore, standard K values for an MHD generator are $0 < K < 1$. E_x is determined by the characteristic of the electrical connection. The Faraday channel (where $\theta_d = 90$ degrees) is characterized by a zero cross-sectional average axial current—$i.e.$, $\langle J_x \rangle = 0$. Therefore, Equation 3.40 becomes [128]

$$E_x = \frac{\langle \sigma_n \beta \phi_{2y} \rangle + B \langle \sigma_n (\beta u + v) \rangle}{\langle \sigma_n \rangle + \langle \sigma_n + \beta \phi_{1y} \rangle}. \qquad (3.52)$$

Case B: Faraday connection with boundary conditions defined in terms of external loading resistance. For this type of connection, the parameter IOPT is set equal to two, and the Faraday potential $(\phi_H - \phi_0)$ and the average current density, $\langle J_y \rangle$, are related through the external resistance (R_{ld}), electrode pitch (p) in

meters (see Figure 3.1), and channel width in meters (W) [125]:

$$\langle J_y \rangle pW R_{ld} = \phi_H - \phi_0. \tag{3.53}$$

From Ohm's law, $J_x + \beta J_y = \sigma(E_x + vB)$, which for a Faraday connection leads to

$$\langle \beta J_y \rangle = \langle \sigma \rangle E_x + \langle \sigma v \rangle B. \tag{3.54}$$

For the boundary conditions to be decoupled, assume that in Equation 3.54,

$$\langle \beta J_y \rangle = \langle \beta \rangle \langle J_y \rangle. \tag{3.55}$$

Combining Equations 3.53, 3.54 and 3.55, and assigning a value of zero to ϕ_0, yields the following boundary conditions:

$$\phi_1 = \phi_2 = 0 \qquad\qquad \text{at } y = 0. \tag{3.56}$$

$$\phi_1 = \frac{\langle \sigma \rangle}{\langle \beta \rangle} pW R_{ld} \qquad\qquad \text{at } y = H. \tag{3.57}$$

$$\phi_1 = \frac{\langle \sigma v \rangle}{\langle \beta \rangle} BpW R_{ld} \qquad\qquad \text{at } y = H. \tag{3.58}$$

The inaccuracy introduced by the approximation made in Equation 3.55 is typically less than 1% of the total power density [137]. The external resistance and electrode pitch are allowed to vary in the axial direction, with the variations specified by the

user as input to the MGMHD code [125]. The axial electric field, E_x, is calculated using Equation 3.52.

Case C: Diagonal insulating sidewall connection. For this type of connection, the parameter IOPT is set equal to three. The boundary conditions for ϕ_1 and ϕ_2 in a diagonal connection may be written similar to the Faraday connection. For a diagonal channel with insulating sidewalls, the boundary conditions are as follows [128]:

$$\frac{\partial \phi_1}{\partial z} = \frac{\partial \phi_2}{\partial z} = 0 \qquad\qquad \text{at } x = 0 \text{ and } z = W. \qquad (3.59)$$

$$\phi_1 = \phi_2 = 0 \qquad\qquad \text{at } y = 0 \text{ and } y = H. \qquad (3.60)$$

For diagonal connections, the axial electric field, E_x, is calculated from the load current per unit area, J_{ld}, where

$$J_{ld} = \langle J_x \rangle - \langle J_y \rangle \cot \theta_d. \qquad (3.61)$$

The axial electric field is then determined by substituting Equations 3.40 and 3.41 into Equation 3.61, which yields [128]

$$E_x = \frac{J_{ld} - \langle \sigma_n \left(\beta + \cot \theta_d \right) \left(\phi_{2_y} + uB \right) \rangle - B \langle \sigma_n \left(1 - \beta \cot \theta_d \right) v \rangle}{\left(1 + \cot^2 \theta_d \right) \langle \sigma_n \left(\beta + \cot \theta_d \right) \phi_{1_y} \rangle}. \qquad (3.62)$$

Case D: Diagonal conducting sidewall connection. For the diagonal conducting wall (DCW) connection, the parameter IOPT is set equal to four, and the boundary conditions are as follows [128]:

$$\phi_1 = \phi_2 = 0 \qquad\qquad \text{at } z = 0 \text{ and } z = W. \qquad (3.63)$$

$$\phi_1 = \phi_2 = 0 \qquad\qquad \text{at } y = 0 \text{ and } y = H. \qquad (3.64)$$

Just as with the insulating sidewall case, the axial electric field, E_x, is given by Equation 3.62. Furthermore, in the infinite segmentation model, the following equations (which were derived from Equation 3.62) can be used to calculate the open-circuit electric field voltage, $E_{x_{oc}}$, and the short-circuit current density, $J_{ld_{sc}}$, for the diagonal connection:

$$J_{ld_{sc}} = \langle \sigma_n \left(\beta + \cot \theta_d\right) \left(\phi_{2_y} + uB\right)\rangle + B\langle \sigma_n \left(1 - \beta \cot \theta_d\right) v\rangle. \qquad (3.65)$$

$$E_{x_{oc}} = -\frac{\langle \sigma_n \left(\beta + \cot \theta_d\right) \left(\phi_{2_y} + uB\right)\rangle + B\langle \sigma_n \left(1 - \beta \cot \theta_d\right) v\rangle}{\left(1 + \cot^2 \theta_d\right) \langle \sigma_n\rangle + \langle \sigma_n \left(\beta + \cot \theta_d\right) \phi_{1_y}\rangle}. \qquad (3.66)$$

Note that Equation 3.66 reduces to Equation 3.52 when $\theta_d = 90$ degrees (when in Faraday configuration). Finally, for both diagonal configurations—insulating sidewall and conducting sidewall—the local line load is linear, therefore E_x is related to J_{ld} by

$$E_x = \left(\frac{1 - J_{ld}}{J_{ld_{sc}}}\right) E_{x_{oc}}. \qquad (3.67)$$

3.3.1.2 Anode and Cathode Voltage Drops

Because of the electrical and flow nonuniformities inherent in magnetohydro-dynamics, a nonuniform electrical potential distribution develops across the channel [119, 142]. The global performance of an MHD generator can be severely impacted by the electrical voltage nonuniformities that arise near the cold electrodes. The MGMHD code defines the anode and cathode voltage drops with the following equations, respectively [125]:

$$V_{d_a} = \frac{1}{W} \int_0^W \int_{H/2}^H [E_y(H/2, z) - E_y(y, z)] \, dydz \qquad (3.68)$$

and

$$V_{d_c} = \frac{1}{W} \int_0^W \int_0^{H/2} [E_y(H/2, z) - E_y(y, z)] \, dydz, \qquad (3.69)$$

where W and H are the the width and height of the channel, respectively. The total voltage drop, as defined [90] in Section 2.2.1, is calculated in the MGMHD code as follows:

$$V_d = V_{d_a} + V_{d_c}. \qquad (3.70)$$

3.3.2 Definition of the Diagonal Angle

There are many ways to describe the diagonal link between electrodes in diagonal generators and accelerators. As mentioned in Section 1.2.2.3, authors have traditionally defined an electric field angle, $\tan\theta = E_y/E_x$ (also, see Equation 1.46), and a wall angle, $\theta_w = \pi/2 - \theta$, to describe the degree of diagonalization of an MHD
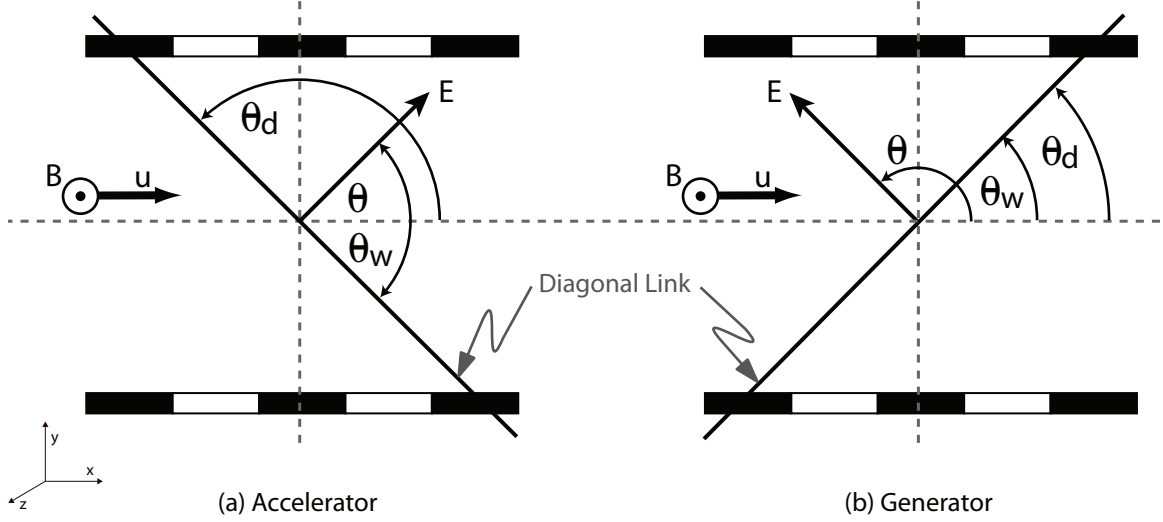
Figure 3.3: Definition of the different diagonal angles—θ, θ_w, and θ_d—for (a) an MHD accelerator and (b) an MHD generator.

generator or accelerator [39,42–44,71,73,87,90,108,121,143]. As shown in Figure 1.10, the electric field angle is measured from the positive x-axis in a counter-clockwise direction, while the wall angle (which is only a function of θ), is measured from the positive x-axis in a clockwise direction. It should be noted that the electric field angle is not only a function of the diagonal link between electrodes, but also dependent on the direction of the magnetic field and the MHD mode (*i.e.*, generator or accelerator).

Some authors (most notably, the MGMHD developers) defined a diagonalization angle, θ_d, which measures the physical angle to the diagonal link between electrodes [72, 125, 128, 137–140, 144]. As seen in Figure 3.2, the diagonalization angle is measured from the positive x-axis, always in a counter-clockwise direction. In this case, the angle θ_d is not a function of the electric field, but instead a function of the diagonal link and (just as with θ) the direction of the magnetic field, **B**.
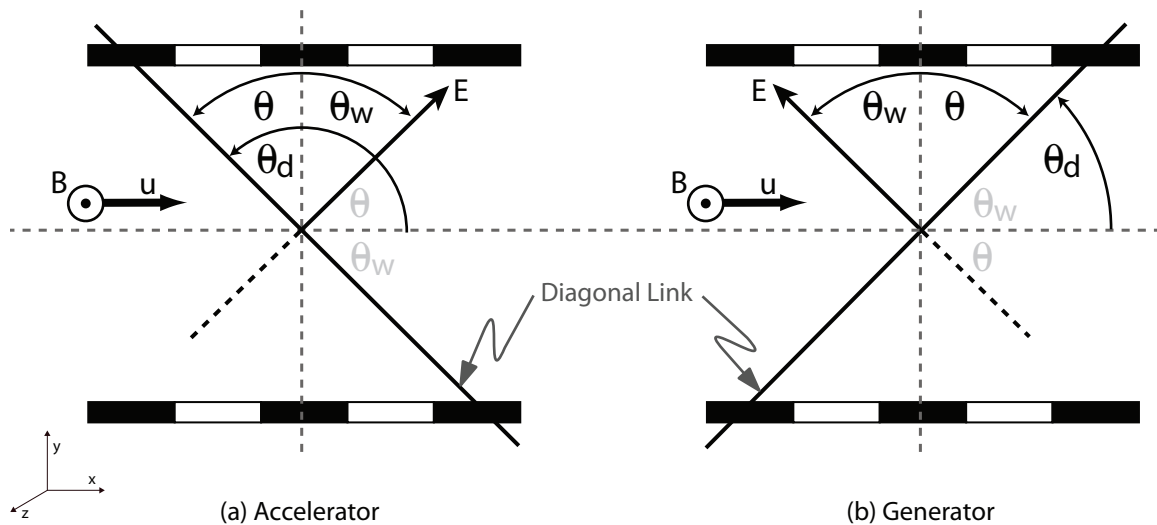
Figure 3.4: Alternative uses for the different diagonal angles— θ, θ_w, and θ_d—for (a) an MHD accelerator and (b) and MHD generator.

Figure 3.3 shows the relationship each angle—the electric field angle, θ; the wall angle, θ_w; and the diagonalization angle, θ_d—has to the diagonal link between electrodes, the magnetic field, the velocity vector, and each other. Note that in the accelerator case (in Figure 3.3), both θ and θ_w are acute, and "positive" (per their original definitions). In the generator case, θ is obtuse, which results in a "negative" value for θ_w (since $\theta_w = \pi/2 - \theta$ must be true). Opposed to θ, θ_d is obtuse for an accelerator and acute for a generator. (Please note that a 90 degree diagonalization angle, which translates to a 0 degree electric field angle, would result in a Hall mode of operation, as shown in Figure 1.6.)

It is important to realize, however, that because of the orthogonal relationship between the diagonalization angle and the electric field angle, each angle can be used to describe more than its definition. For instance, as Figure 3.4 shows, θ also describes the relationship of the diagonal link to the y-axis, with a positive rotation

for an accelerator and a negative rotation for a generator—in both cases, θ is an acute angle. Also shown in Figure 3.4, one can view θ as being positive for an accelerator, and negative for a generator (with its angle being measured from the positive x-axis). Accordingly, θ_w also changes directions of rotation. These usages are logical when one considers the definition of θ—from Equation 1.46, $\tan\theta = E_y/E_x$, where the range of tangent is typically considered to be from $-\pi/2$ to 0 and from 0 to $\pi/2$. Hence, as seen in Section 1.2.2.3, for a generator, the standard range for θ is $-\pi/2 < \theta < 0$; however, for an accelerator, it is $0 < \theta < \pi/2$ [90].

As seen in Figure 3.4, the diagonalization angle, θ_d, does not change from positive to negative, as θ does. As first seen in Equation 3.34, and later in Equations 3.40 and 3.41, the MGMHD code uses the cotangent of θ_d. Cotangent is defined from 0 to π; therefore, the diagonalization angle is defined in acute and obtuse angles. One must only remember that, for the diagonalization angle, an acute angle is a generator case and an obtuse angle is an accelerator case (with, of course, a 90 degree angle being a Hall case).

Of the three angles explained in this section, the electric field angle, θ is the most useful (and, hence, the most widely used). The electric field angle describes not only the the electric field direction in relation to the x-axis, but it also describes the diagonal link in relation to the y-axis. In practice, most researchers refer to θ by its positive acute value, relying on the fact that it is already known whether they are operating as a generator or accelerator. Visually, this reference is logical, if one considers that θ describes the offset angle from a pure Hall generator or accelerator. Even though the MGMHD code uses the diagonalization angle, θ_d, in its calculations,

this dissertation will use the more common electric field angle, θ, to when describing the diagonal link between electrodes. All angles will be given as positive acute values, with references to whether the angle describes a generator or accelerator case.

3.4 State Equations

In order to close the system of fluid dynamic and electrical equations, the relationship between the fluid properties and the chosen solution transport variables (u, v, w, $\bar{p}$, and h) must be established. In the MGMHD code, electrical and thermodynamic properties are calculated from two independent thermodynamic variables—($\bar{p}$,h) or ($\bar{p}$,T)—depending on which of the four following options are chosen by the user [125]:

1. Constant fluid properties.

2. Variable fluid properties with constant electrical properties.

3. Variable fluid properties with conductivity and hall parameters calculated from correlations.

4. Variable fluid properties calculated from curve-fit, fourth-order interpolation polynomials in $\bar{p}$ and h.

Each of the above options is determined by the user in the MGMHD code using the input parameter known as `IPROP` (where `IPROP` = 1, 2, 3, or 4, respectively). Each of these property-value choices is discrete (*i.e.*, element of one choice cannot be mixed with elements of another), and only one `IPROP` value can be chosen for each simulation

of the MGMHD code. The following sections will detail each of the above fluid state equation choices.

3.4.1 Constant Fluid Properties

When the value of `IPROP` is set equal to 1, the user has specified that the MGMHD code will use a constant fluid property model. In this scenario, the plasma density, specific heat, and laminar viscosity are constant and specified by the user. The temperature is calculated from the enthalpy, with the following equation [125]:

$$T = \frac{h}{c_p} \qquad (3.71)$$

3.4.2 Variable Fluid with Constant Electrical Properties

The user can specify that the MGMHD code operate with variable fluid properties and constant electrical properties by setting the value of `IPROP` equal to 2. The plasma density is calculated from the ideal gas law equation, $\rho = M\bar{p}/RT$, where M is the molecular weight as specified by the user [125]. The gas specific heat capacity is a second-order polynomial function of temperature, calculated from the following equation:

$$c_p = \text{ACP} + T\,(\text{BCP}) + T^2\,(\text{CCP})\,, \qquad (3.72)$$

where the constants ACP, BCP, and CCP are specified by the user [125]. The temperature is calculated from the enthalpy as in Equation 3.71. The laminar viscosity, μ_ℓ, is also a second-order polynomial function of temperature, calculated from the

following equaion:

$$\mu_\ell = \text{AMU} + T\,(\text{BMU}) + T^2\,(\text{CMU}), \tag{3.73}$$

where AMU, BMU, and CMU are constants specified by the user [125]. The ratio of specific heats, γ, is calculated from c_p and the universal gas constant, R, and is used to obtain the speed of sound, $a = \sqrt{\gamma RT}$ [125].

3.4.3 Variable Fluid and Electrical Properties

This option is defined by setting the value of `IPROP` equal to 3. The fluid properties are calculated as described above, for the case where `IPROP` equals 2. The electrical conductivity and Hall parameter are calculated using equations developed by Hara and Umoto [139], which are as follows:

$$\sigma = 3.21 \times 10^4\,(\bar{p})^{-0.51}\,T^{1.055}\exp\left(\frac{-2.5 \times 10^4}{T}\right) \tag{3.74}$$

and

$$\beta = 40.0\,(\bar{p})^{-0.99}\,T^{0.97}B. \tag{3.75}$$

In this option, a simplified arcing model is used to account for the conduction of constricted currents [125]. A user-defined arcing temperature, T_{arc}, is a cut-off criterion for the electrical conductivity and Hall parameter in the regions near the cold electrodes. If the calculated temperature falls below T_{arc} in these near-wall regions, the conductivity and Hall parameter are set to the values computed using T_{arc}. This simulates the incipient arcing phenomenon that takes place at T_{arc} for a given bound-

ary layer voltage drop. This technique also prevents numerical instabilities originating from the Joule energy dissipation term (J^2/σ) in the energy equation by restricting this term to a finite value when σ tends toward zero in the near-wall regions [125].

3.4.4 Variable Fluid and Electrical Properties using Fourth-Order Interpolation Polynomials

In order to enable the MGMHD code to allow the fluid and electrical properties to vary using fourth-order polynomials in $\bar{p}$ and h, the user must define `IPROP` equal to 4. In this option, the arcing model discussed for the `IPROP` = 3 case is used, and thermodynamic relations are expressed in terms of pressure and enthalpy. The expressions are written in terms of fourth-order polynomials of the form [125]

$$\Phi = \sum_{k=0}^{4} \sum_{l=0}^{4} \text{Tab}_\Phi \left(\bar{p}\right)^k h^l, \tag{3.76}$$

where Φ represents each of the five required parameters: temperature, T; molecular weight, MW; the ratio of specific heats, γ; electrical conductivity, σ; and electron number density, n_e [125]. The interpolation coefficients, Tab_Φ and the pressure-temperature domains are supplied by the user via an input file, while k and l are counting parameters that represent the order of the polynomial. The specific heat capacity is no longer calculated by Equation 3.72, but instead from Equation 3.76 [125]. The laminar viscosity, however, is still calculated using Equation 3.73, but the Hall

parameter is calculated using the following equation [125]:

$$\beta = \frac{\sigma B}{n_e e}. \tag{3.77}$$

3.5 Solution Procedure

Just as its predecessor, the TDMHD code [128], the MGMHD program uses a classical semi-implicit method for pressure-linked equations (SIMPLE) parabolic marching technique, described in Section 3.2, in the axial direction [132]. The cross-stream plane continuity and elliptic momentum equations are solved simultaneously by the full approximation storage (FAS) block implicit multigrid method (BLIMM) [130, 145–148]. Figure 3.5 offers an illustrated representation of the SIMPLE and BLIMM solution procedures. The cross-stream elliptical potential equations are then solved using a FAS multigrid procedure [149, 150].

An important difference between the SIMPLE and BLIMM algorithms is that BLIMM uses a coupled solution of momentum and continuity equations [145]. The pressure field is updated as part of the process of satisfying the mass continuity equation. The pressure-field appears in the momentum equation as a driving pressure-gradient term, but there is no explicit pressure equation like the one in the SIMPLE algorithm called "the p' correction equation" [128, 146]. That equation was obtained by substituting the momentum equation equations into the continuity equation and was independently solved, just as the momentum equations were [147]. One disadvantage of such a decoupled approach is that solution of the pressure equation lags
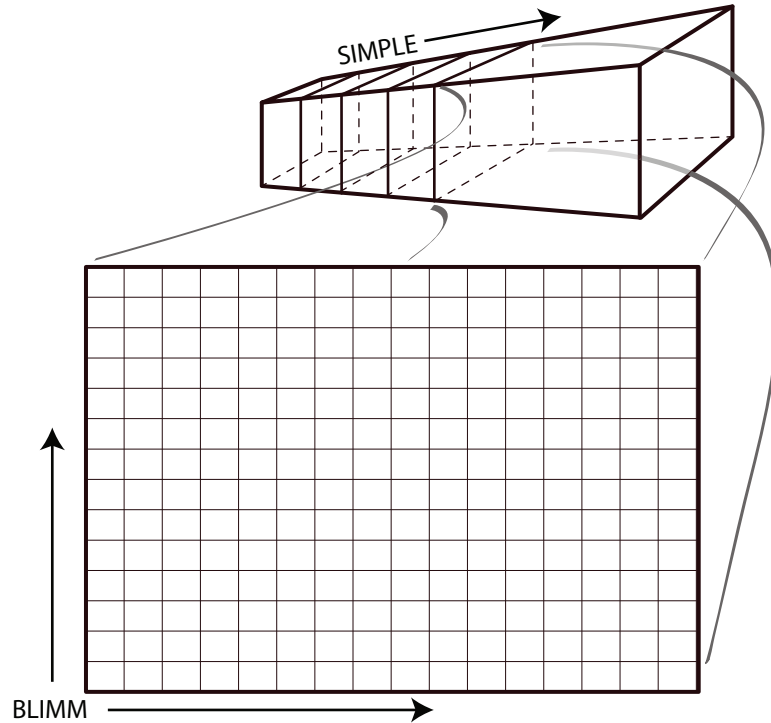
Figure 3.5: Illustration of the SIMPLE and BLIMM solution procedures.

behind the solution of the momentum equations, which slows the global convergence rate of the algorithm, which is one reason why the BLIMM algorithm couples the momentum and continuity equations [148].

The most salient feature of the MGMHD solution procedure is the use of the multigrid technique, the details of which can be found in other sources [125, 149, 150]. The SIMPLE and related algorithms use a single-grid strategy in which computations are performed on one grid that is chosen by the user at the beginning of the calculations [128, 129]. To obtain a grid-independent solution, a very fine grid is necessary, which would extend the convergence times of single-grid solution procedures. For elliptic equations, faster convergence can be obtained by employing multiple grids and continuously cycling the solution on coarse and fine grids [130, 145–150]. In the

MGMHD code, such a multigrid technique is used to accelerate the convergence rate of the cross-stream momentum and electrical equations.

The MGMHD procedure offers a three-dimensional parabolic solution while only requiring a two-dimensional computer storage. This is accomplished even though the flow is three-dimensional and the more general set of equations is elliptic. Consequently, axial and cross-stream momentum equations are decoupled, as are longitudinal and cross-stream pressure gradients [145].

For reasons of simplicity, the hydrodynamic and electrical solutions are decoupled [125]. The solutions of the k and ϵ equations should be decoupled from the momentum and continuity equations to avoid numerical instabilities [130]. The energy equation is also solved independency, since the temperature influences are only propagated through the viscosity and density, which are kept constant in the iterative solution of the momentum and continuity equations [128]. Because of the decoupling, the following sequence of calculations is adopted to each axial location until the exit of the channel is reached. At the inlet, variables are initialized with the values specified by the user. The MGMHD calculation sequence is as follows [125]:

1. New fluid properties are evaluated from the enthalpy calculated at the previous axial station and the pressure estimated at the present location.

2. The electrical potential equations are solved by means of an FAS multigrid procedure, and the electrical currents and fields are calculated.

3. The axial momentum equation is solved using the pressure gradient evaluated at the previous axial station. Adjustments of the axial velocity and pressure gradient are performed to satisfy the integral mass-conservation equation.

4. Cross-sectional plane velocity and pressure fields are solved by means of an FAS BLIMM algorithm.

5. The equations for kinetic energy of turbulence, dissipation rate, and enthalpy are solved.

6. The cross-sectionally-averaged axial pressure, $\bar{p}$, is updated using the previous axial station pressure and the new axial pressure gradient.

3.6 Required Modifications and Improvements

As stated in Section 2.3.2, the MGMHD code is not a perfect fit for the three-dimensional modeling of the MAPX accelerator—however, it does fulfil some of the basic requirements and its structure allows for the necessary modifications. As detailed in this chapter, the MGMHD code is a parabolic three-dimensional MHD generator numerical model. As outlined, the parabolic configuration enables three-dimensional modeling without the penalty of slow convergence times or the requirement of massive computing resources. The MGMHD code does offer a diagonal configuration; however, the diagonal angle must remain constant throughout the length of the MHD channel. Lastly, the thermodynamic and electrical conductivity models of the MGMHD code are, at best, generic curve-fits based on a few user-defined

constants—however, the code does allow the user to supply their own thermodynamic and electrical transport data via an input file.

In order to properly model the MAPX accelerator, the MGMHD code requires certain specific modifications, which are as follows:

- The MGMHD code must be modified to simulate Faraday, Hall, and diagonal configurations in both generator and accelerator modes.

- In order to simulate real world conditions, the MGMHD code must be modified to allow the diagonal angle to vary at different axial positions in the MHD channel.

- Thermodynamic and electrical transport property subroutines, which would supply the MGMHD code with the required variables described in Section 3.3.1.1, must be added.

Though not required for the modeling of the MAPX diagonal accelerator, there are several features that would enhance and improve the capabilities of the MGMHD code. These improvements are as follows:

- The addition of a power-takeoff scheme at the entrance and exit of the simulated MHD channel would help prevent MHD compression and allow for more realistic models.

- Accelerator efficiency calculations would allow the user to more quickly determine the optimum accelerator configurations.

- A three-dimensional calculation of total pressure would aid in the design of MHD accelerators.

- An axial current neutralized option (an extension of the varying diagonal angle) would allow researches to more quickly determine the optimum angle for eliminating the axial J_x current.

While the MGMHD numerical model functions properly for its designed purpose, many modifications and improvements are required (or recommended) for the proper modeling of the MAPX diagonal accelerator. Chapter 4 details the modifications and improvements to the MGMHD code, supplying the theoretical grounds and the computational analysis for such changes. Numerical simulations (using the modified MGMHD code), theoretical and physical interpretations of these simulations, and performance predictions/analyses are included in Chapter 5.

CHAPTER 4

EXTENDED MODELING CAPABILITIES

> *Science is what we understand well enough*
> *to explain to a computer. Art is everything*
> *else we do.*
>
> —Donald Knuth

4.1   Overview

As shown in Chapter 3, the original form of the MGMHD code is inadequate for the proper modeling of the NASA MSFC MAPX diagonal accelerator, and thus requires modifications and additional features. The resulting numerical model will be referred to as the UAH-MSFC-MGMHD (UMM) code, and as shown in Figure 4.1, can be separated into two main parts:

1. The MHD modeling code, which consists of a modified version of the MGMHD code, that is able to simulate generators and accelerators in Faraday, Hall, and diagonal configurations.

2. The thermoelectric codes, which consist of the thermodynamic model (powered by the NASA CEA code) and the electrical transport property model.
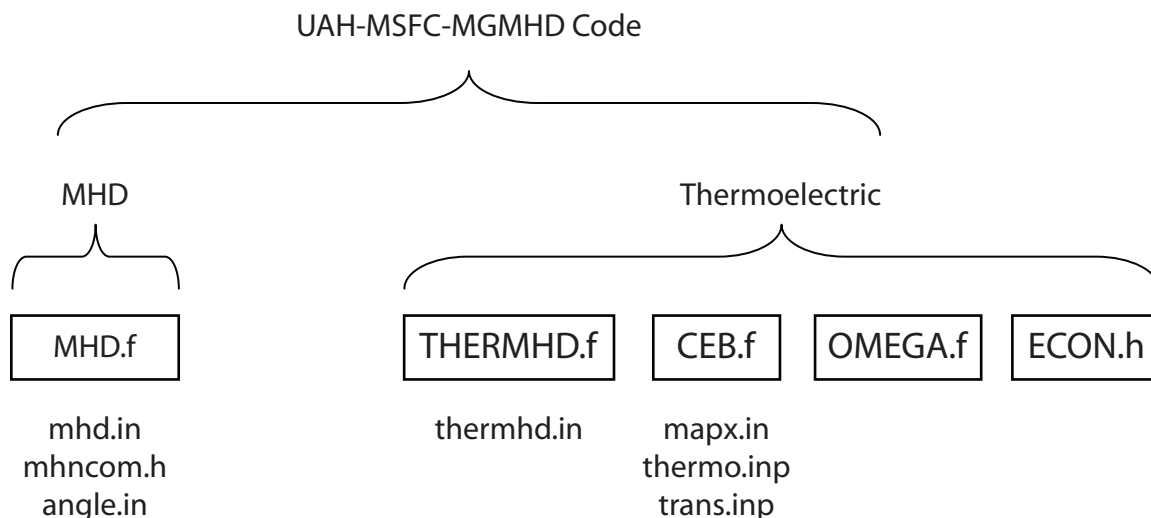
Figure 4.1: The basic code structure of the UAH-MSFC-MGMHD (UMM) numerical model. The UMM code is composed of two basic parts: (1) the MHD modeling section and (2) the thermoelectric modeling section. The boxes represent the individual codes, with their input and required files listed below.

The specific details of each of these sections will be discussed in this chapter. As shown in Figure 4.1, the MHD modeling code consists of a single code—`mhd.f`, the modified MGMHD code—while the thermoelectric model consists of four codes, each of which will be described. The following sections will detail the code structure, modifications, theoretical considerations, assumptions, and limitations of the UMM numerical model. Results (*i.e.*, numerical simulations of the MAPX accelerator) from the UMM code will be presented in Chapter 5.

4.2 Thermodynamic and Electrical Transport Property Models

As detailed in Section 3.4, the MGMHD code does not have an adequate built-in thermodynamic and electrical transport property model, but does allow the user to provide thermoelectric data. In the UMM code, this thermoelectric data input

file is created by thermoelectric numerical models, which are the sum of the thermodynamic and electrical transport property numerical models, and, as shown in Figure 4.1, consists of four programs. Each of these programs is required for the thermoelectric model to function properly; however, they can run independently of the MHD model. For this reason, the thermoelectric code can be thought of as an "independent" numerical model, and will be described first (furthermore, the UMM code actually executes the thermoelectric model before the MHD model).

The program `thermhd.f` manages the other three programs—`ceb.f`, `omega.f`, and `econ.h`—shown in Figure 4.1 (where the ".f" extension denotes a Fortran file and ".h" denotes an include file). The input file for `thermhd.f` is `thermhd.in`, where the user defines the pressure and enthalpy ranges of interest and the step sizes. The primary purpose of the thermoelectric codes is to create a table of thermodynamic and electrical transport property data (temperature, molecular weight, ratio of specific heats, laminar viscosity, electrical conductivity, and total charge at every pressure and enthalpy step) that can used by the MHD numerical model, as described in Section 3.4.4. The thermoelectric models are detailed in the following sections.

4.2.1 Thermodynamic Properties

As stated in Section 2.3.1, the MAPX simulation requires an established equation of state and thermodynamic numerical model, such as the NASA Chemical Equilibrium with Applications (CEA) code [106,107]. For this reason, the NASA CEA code has been modified and integrated into the UMM numerical model. To avoid confusion, this modified CEA code is named `ceb.f`.

The `ceb.f` program has three input files—`thermo.inp`, which automatically creates a library of thermodynamic data (no user input required); `trans.inp`, which automatically creates a library of transport property data (also, no user input necessary); and `maxp.in`, where the user defines the oxidizer/fuel (O/F) species, O/F weight percentages, and initial temperatures. The major difference between the `ceb.f` program and the NASA CEA code is that `ceb.f` has been modified to output an unformatted plot file dimensioned in (at present) 39 variables, which represent the 9 thermodynamic variables and 30 gas species concentrations for which electron-momentum cross-sectional data exists (which are explained in Section 4.2.2.4). It is important to note that all the changes made to the CEA code deal with input/ouput (I/O) and formatting—*i.e.*, none of the thermodynamic equations in the CEA code [106, 107] were altered. The `ceb.f` code runs at every step in the pressure and enthalpy loops (which are defined in `thermhd.in`), the process of which is described in Section 4.2.3.

For every step in the pressure and enthalpy loops, the `ceb.f` code provides the following information to the MHD numerical model:

1. Temperature, T.

2. Molecular weight, MW.

3. Ratio of specific heats, γ.

4. Laminar viscosity, μ_ℓ.

5. Total charge, eN_e.

The CEA code assumes ideal gas and that interactions among phases can be neglected [106]. Based on this assumption (along with the current pressure/enthalpy step and the thermodynamic property tables created by `thermo.inp`), the CEA code can determine a "mixture" of reactants, with which it can determine the number of n moles in the system. From this information, the CEA code can determine mole fractions and species concentrations, and calculate the molecular weight of each species. The CEA code then uses the current enthalpy step and the Gibbs energy equation to determine the current temperature [106]. The ratio of specific heats, γ, is calculated using

$$\gamma = \frac{c_p}{c_v},\tag{4.1}$$

where the specific heat at constant pressure is calculated using [106]

$$c_p = \left(\frac{\partial h}{\partial T}\right)_p,\tag{4.2}$$

and the specific heat at constant volume is [106]

$$c_v = \left(\frac{\partial \acute{u}}{\partial T}\right)_v,\tag{4.3}$$

where $\acute{u}$ is the specific internal energy of the mixture. The total charge is simply the product of the electron number density and the charge of an electron—the electron number density is assumed to be the same as the ion number density, which the CEA code can calculate using the mole fractions and temperatures mentioned above. The value of the current laminar viscosity is calculated using the known transport property

tables (from `trans.inp`) and the current values of the species mole fractions and the total species mixture. For a more detailed explanation of the CEA code equations, please see Gordon and McBride [106].

4.2.2 Electrical Transport Properties

In the UMM numerical model, electrical conductivity is calculated in two parts, based on species collisions, using the `omega.f` and `econ.h` programs. More specifically, `omega.f` is a self-contained (*i.e.*, no input file required) Fortran file which calculates electron-neutral collision integrals for 30 specified species using momentum-transfer collision cross-section data [151, 152]. Charged particle collision integrals are then estimated in `econ.h`. All the collision integrals (along with the species and total number densities mentioned earlier) are then used by `econ.h` (which is an include file called from `thermhd.f`) to calculate the electrical conductivity of the gas mixture, based on a method described by Devoto [153], with the equation

$$\sigma = \frac{e^2 n}{\rho k T} \sum_{j=1}^{\zeta} n_j m_j Z_j D_{1j}, \tag{4.4}$$

where e is the electron charge, n is the total number density, ρ is the total mass density, n_j is the number density of the jth species, m_j is the mass of the jth particle, Z_j is the charge multiple on the jth species, D_{1j} is the multicomponent diffusion coefficient, and j is the the counter, with 1 representing electrons and 2 through ζ being ions (where > 2 means multiple ionic states). The electrical conductivity equation is

explained in detail in Sections 4.2.2.2 and 4.2.2.3 and is calculated at each pressure and enthalpy step, as explained in Section 4.2.3.

4.2.2.1   Kinetic Theory

The behavior of any sufficiently rarified ideal gas can be described by the Boltzmann equation,

$$\frac{\partial f}{\partial t} + \mathbf{v} \cdot \nabla f + \frac{\mathbf{F}}{m} \cdot \frac{\partial f}{\partial \mathbf{v}} = \left(\frac{\partial f}{\partial t}\right)_c, \tag{4.5}$$

for the distribution function, $f(\mathbf{r}, \mathbf{v}, t)$, where $\mathbf{F}$ is the force acting on the particles, the symbol $\partial/\partial\mathbf{v}$ is the gradient in velocity space and $(\partial f/\partial t)_c$ is the time rate of change of f due to collisions [94, 153–155]. The distribution function represents the number of molecules of a species which, at time t, lie in a unit volume element about point $\mathbf{r}$ and have velocities within a unit range about $\mathbf{v}$. The meaning and complexity of the Boltzmann equation becomes clear when one realizes that f is a function of seven independent variables.

Brief outline of the Chapman-Enskog solution procedure.   One solution to the Boltzmann equation is the Chapman-Enskog method (which is rigorously explained and expanded in Hirschfelder, Curtiss, and Bird [154] and Chapman and Cowling [155]) where one assumes that collisions are the driving mechanisms for translational nonequilibrium of the gas and are such that the distribution functions of the various species differ only slightly from a Maxwellian distribution function.

The Chapman-Enskog method uses a perturbation factor,

$$\epsilon = \frac{\lambda}{L} \ll 1, \tag{4.6}$$

based on a scale length of macroscopic quantities, L, and the mean free path between collisions [16],

$$\lambda = \frac{1}{nQ}, \tag{4.7}$$

where Q is the momentum-transfer cross-section and n is the electron number density (note the similarities to Equation 1.16). The distribution function is expanded, order by order, in the small perturbation parameter [155],

$$f(\mathbf{r}, \mathbf{v}, t) = f_0(\mathbf{r}, \mathbf{v}, t) + \epsilon f_1(\mathbf{r}, \mathbf{v}, t) + \epsilon^2 f_2(\mathbf{r}, \mathbf{v}, t) + \cdots, \tag{4.8}$$

where f_0, f_1, and f_2 are assumed to be of the same order of magnitude. If there are no gradients in the composition, velocity, and temperature in the gas, then $f(\mathbf{r}, \mathbf{v}, t)$ reduces to the Maxwellian distribution

$$f_0(\mathbf{r}, \mathbf{v}, t) = n(\mathbf{r}) \left(\frac{m}{2\pi kT} \right)^{3/2} \exp \left(-\frac{m\mathbf{v}}{2kT} \right). \tag{4.9}$$

When the system is not in equilibrium, the distribution function satisfies the Boltzmann integro-differential equation [154].

Typically, one is interested in the properties of gases which are under conditions only slightly different from equilibrium. In fact, it is only under these condi-

tions that the flux vectors are linear in the derivatives and the usual definitions of the transport coefficients apply [154,155]. In this limit, the distribution function is nearly Maxwellian, and the Boltzmann equation can be solved by the Chapman-Enskog perturbation method. The resulting solutions are then used to obtain expressions for the fluxes and the transport coefficients [154, 155].

These expressions show that mass transfer results not only from a concentration gradient, but also from a temperature gradient (*i.e.*, thermal diffusion). Similarly, energy transfer is not only a result of a temperature gradient, but also from a concentration gradient [154]. These and other second-order effects, which cannot be described in terms of simple kinetic theory, emerge quite naturally from the rigorous Chapman-Enskog approach [155].

The final result is that one can express all transfer coefficients in terms of a set of collision integrals, $\Omega_{ij}^{(\ell,s)}$, where ℓ and s are integers whose values depend on the level of approximation used in the Chapman-Enskog method [156]. These integrals will be discussed more thoroughly in the next section, but they explicitly involve the dynamics of a molecular encounter and hence the intermolecular force law. Current knowledge of the nature of intermolecular forces is incomplete, and therefore limits the applicability of the results.

Limitations of the Chapman-Enskog theory. The Chapman-Enskog kinetic theory of gases is based on several assumptions which can limit the applicability of the final results. Since only binary collisions are considered in the Chapman-Enskog approximation, the results are not applicable at densities sufficiently high

where three-body collisions become important [154]. The use of "classical mechanics" excludes the discussion of low temperature phenomena in which quantum effects are significant [155]. The first approximation to the Chapman-Enskog method (which is the one most often used) is only valid for situations in which the gradients of the physical quantities are small (the higher approximations provide corrections for larger gradients) [154]. In the first approximation, the fluxes are proportional to the first derivative of density, velocity, and temperature, and the resulting equations (which describe the change of density, velocity, and temperature with respect to time) are called the Navier-Stokes equations [133]. In the development of the Chapman-Enskog theory, it is assumed that the dimensions of the containing vessel (and any obstacles therein) are large compared to the mean free path [154] (see Equation 4.6). Furthermore, at very low densities, the particles collide more frequently with the walls of the containing vessel than with each other—hence, there is little mechanism for the establishment of a local equilibrium, which is one of the fundamental assumptions of the Chapman-Enskog method; furthermore, in this case, the gas can no longer be approximated as a continuum.

4.2.2.2 Electron-Neutral Collisions

In the thermoelectric numerical model of the UMM code, electrical conductivity, σ, of the partially ionized gas is calculated in two parts—electron-neutral collisions and charged particle collision. Both calculations are based on the same principles, but use different assumptions. Electrical conductivity due to electron-neutral colli-

sions is based on a method described by Devoto [153, 156–160], with the following assumptions:

- Inelastic collisions are neglected.

- The number of ions and electrons is equal.

- There is only one user-defined ion species, which is only singly ionized.

- The temperature of ions and electrons is equal.

- The electron-heavy (electron-neutral, electron-ion) collision terms are neglected in deriving the expression for the ion and atom transport properties (*i.e.*, electrons do not alter the direction, velocity, or momentum of heavy particles).

- The change in the heavy particle perturbation term during a collision will be neglected in obtaining the expressions for the electron transport properties (*i.e.*, when an electron impacts a heavy particle, the perturbation to the heavy particle is insignificant when compared to the electron perturbation).

- The contribution of ions to the electrical conductivity has been neglected (which is consistent with the simplification introduced in solving the linearized electron Boltzmann equation).

The above assumptions result in a simplified form of Equation 4.4, which yeilds in the following "electron-neutral" conductivity equation [158]:

$$\sigma = \frac{e^2 n_1 n m_1}{\rho k T} D_{11}, \tag{4.10}$$

where e is the electron charge, n is the total number density, n_1 is the electron number density (any subscript "1" denotes electrons), m_1 is the mass of an electron, ρ is the total mass density of all particles, k is the Boltzmann constant, T is the fluid temperature, and D_{ij} is the multicomponent diffusion coefficient (here, the subscript "1" is used for both the i and j components because only electron diffusion is considered in the calculation).

The solution of Equation 4.8 for $f_1(\mathbf{r}, \mathbf{v}, t)$ is accomplished through an expansion of the function in a finite series of Sonine polynomials [153], with the level of approximation of the transport coefficients being the number of terms in the expansion series. It has been shown that at least the second-order approximation is required for a reasonable level of accuracy [95, 161]. In the fourth-order approximation, the ordinary diffusion coefficient is given by [158]

$$[D_{11}]_4 = \frac{3n_1\rho}{2nm_1} \frac{\sqrt{2\pi kT/m_1}}{|q|} \begin{vmatrix} q^{11} & q^{12} & q^{13} \\ q^{21} & q^{22} & q^{23} \\ q^{31} & q^{32} & q^{33} \end{vmatrix}, \tag{4.11}$$

where $|q|$ is the determinant of the q^{mn} elements. The q^{mn} elements represent the coefficients to the simplified electron equilibrium Maxwellian distribution function and are dependent on $\bar{Q}_{ij}^{(\ell,s)}$, the Maxwellian velocity-averaged collision cross-section between species i and j. For example, one of the more simple equations for q^{mn} is given by

$$q^{11} = 8\sqrt{2}n_1^2\bar{Q}_{11}^{(2,2)} + 8\sum_i n_1 n_j \left[\frac{25}{4}\bar{Q}_{1j}^{(1,1)} - 15\bar{Q}_{1j}^{(1,2)} + 12\bar{Q}_{1j}^{(1,3)} \right], \tag{4.12}$$

where the equations for q^{mn} become more complex as the values of m and n increase (please see Appendix B for expressions of all the q^{mn} elements from Equation 4.11).

The Maxwellian velocity-average collision cross-section can be calculated through the relation [158]

$$\bar{Q}_{ij}^{(\ell,s)}(T) = \frac{4\,(\ell+1)}{(s+1)!\,[2\ell+1-(-1)^\ell]} \int_0^\infty \exp[-\gamma^2]\gamma^{2s+3}Q_{ij}^\ell(g)\,d\gamma, \tag{4.13}$$

where $\gamma^2 = \mu_{ij}g^2/2kT$, where μ_{ij} is the reduced mass of the colliding species, i and j, and g is the initial relative velocity (before impact). The average collision cross-sections relate to the collision integrals, $\Omega_{ij}^{(\ell,s)}$ with the following equations:

$$\bar{Q}_{ij}^{(\ell,s)} = \pi\sigma_{ij}^2\Omega_{ij}^{(\ell,s)*}, \tag{4.14}$$

where σ_{ij} is the differential cross-section for the i and j species collision. The term $\Omega_{ij}^{(\ell,s)*}$ actually represents the deviation of the particular molecular model from the idealized rigid-sphere model [154], and relates to the collision integral through [154]

$$\Omega_{ij}^{(\ell,s)*} = \frac{[\Omega_{ij}^{(\ell,s)}]}{[\Omega_{ij}^{(\ell,s)}]_{\text{rig sph}}} = \frac{\Omega_{ij}^{(\ell,s)}}{\nicefrac{1}{2}\,(s+1)!\left[1-\frac{1}{2}\frac{1+(-1)^\ell}{1+\ell}\right]\pi\sigma_{ij}^2}. \tag{4.15}$$

The collision integral, $\Omega_{ij}^{(\ell,s)}$ is often used in classic texts [154,155], and is sometimes referred to as the "Omega integrals," where their similarity to Equation 4.13

can be shown by

$$\Omega_{ij}^{(\ell,s)}(T) = \sqrt{kT/2\pi\mu_{ij}} \int_0^\infty \exp[-\gamma^2]\gamma^{2s+3} Q_{ij}^\ell(g) \, d\gamma. \tag{4.16}$$

The value of $Q_{ij}^\ell(g)$ can be calculated with the following equation [154]:

$$Q_{ij}^\ell(g) = 2\pi \int_0^\infty \left(1 - \cos^\ell \chi\right) b \, db, \tag{4.17}$$

where b is the "impact parameter" and $\chi(b,g)$ is the angle of deflection in a binary collision, and can be calculated with [154]

$$\chi(b,g) = \pi - 2b \int_{r_m}^\infty \frac{dr/r^2}{\sqrt{1 - \frac{b^2}{r^2} - \frac{\varphi(r)}{1/2\,\mu_{ij}g^2}}}, \tag{4.18}$$

where $\varphi(r)$ is the intermolecular potential function and r is the distance between the two spheres (particles), with the subscript m representing the center of mass. For a rigorous approach, in order to make calculations of transport coefficients for any potential function, $\varphi(r)$, the angle of deflection in a collision, χ, must be calculated. For rigid spherical molecules, it is relatively easy to write an analytical expression for χ, but for any realistic potential function, as Equation 4.18 shows, numerical methods must be used. Once χ has been evaluated for a large number of values of g and b, the following equation can be evaluated to numerically obtain the collision integral:

$$\Omega_{ij}^{(\ell,s)} = \sqrt{\frac{2\pi kT}{\mu_{ij}}} \int_0^\infty \int_0^\infty \exp\left[-\gamma_{ij}^2\right] \gamma_{ij}^{2s+3} \left(1 - \cos^\ell \chi\right) b \, db \, d\gamma_{ij}. \tag{4.19}$$

Fortunately, it turns out that all of the $\bar{Q}_{ij}^{(\ell,s)}(T)$ terms from Equation 4.13 with $\ell > 1$ have coefficients proportional to a power of m_1/m_j (where $1 =$ electron, and $j \neq 1$), and can be neglected [158]. This leaves only values of Q_{ij}^1, which are the well-known momentum-transfer collision cross-sections [156], which can be experimentally measured as a function of incident electron energy [151, 152], and are given in Appendix A. The integral in Equation 4.13 takes the form of a half-range Gauss-Hermite polynomial, which is a special case of a Gauss-Laguerre integral equation [162], and can be solved using a 16-point Gauss-Laguerre quadrature (which is done in `omega.f`), essentially calculating the values of the average collision cross-section for the selected species. For a numerical analysis, Equation 4.13 is a more advantageous choice than Equation 4.16 or Equation 4.19 because the ℓ and s values are already formatted for a conditional loop, and Equation 4.13 does not use a rigid sphere assumption. From these cross-sectional values, the electrical conductivity (based on electron-neutral collisions) can be calculated from Equations 4.10, 4.11 and 4.12. While it is known that in some gases, the momentum-transfer approximation is not accurate to the 1% level and the angular distributions must be taken into account, for MHD applications, the use of momentum-transfer cross-sections is adequate [163].

4.2.2.3 Charged Particle Collisions

Because the ionization level in MHD devices is so low (on the order of 1-2%), electron-neutral collisions obviously play the dominant role in determining the electrical conductivity of the fluid. However, for completeness, the UMM code has a conductivity model that incorporates charged particle collisions into the global

electrical conductivity of the flow. Charged particle collision integrals are calculated using a method described by Zollweg [164], who modified the Spitzer formula (which is used to calculate the electrical conductivity of fully ionized gases) to permit its application in calculating electrical conductivities of partially ionized gases in the ideal and nonideal plasma regions.

The Spitzer equation for the conductivity of a fully ionized ideal plasma in MKS units without a magnetic field can be written [164]

$$\sigma_{sp} = \frac{\gamma_E T^{3/2}}{38.0 Z \ln \Lambda}, \tag{4.20}$$

where Z is the mean ionic charge multiple, T is the absolute temperature, γ_E is a factor that takes into account electron-electron scattering which has various values depending on the value of the mean ionic charge multiple (*e.g.*, γ_E is 0.582 when $Z = 1$), and Λ is the Coulombic logarithmic term, which (in MKS units) can be written

$$\ln \Lambda = \ln \left(\frac{1.24 \times 10^7 T^{3/2}}{n_e^{1/2}} \right). \tag{4.21}$$

The equation used to approximate the momentum-transfer cross-section for the Spitzer formula is [164]

$$\bar{Q}_{ij}^1 \cong 6\pi \bar{b} \ln \Lambda, \tag{4.22}$$

where $\bar{b}$ is an averaged impact parameter, $\bar{b} = Ze^2/12\pi\epsilon_0 kT$, where ϵ_0 is the permittivity of free space.

The modified form of Spitzer's equation for conductivity is [164]

$$\sigma_{mod} = \frac{\gamma_E T^{3/2}}{38.0 Z \ln\left(1 + 1.4\Lambda_m^2\right)^{1/2}}, \tag{4.23}$$

where Λ_m is a modified Λ, and is calculated by [164]

$$\Lambda_m = \frac{\sqrt{\lambda_D^2 + \lambda_+^2}}{\bar{b}}. \tag{4.24}$$

The Debye length, λ_D is defined as [94]

$$\lambda_D \equiv \left(\frac{\epsilon_0 kT}{ne^2}\right)^{1/2}, \tag{4.25}$$

and λ_+ is the mean ionic radius in terms of the positively charged ion number density (n_+), which can be calculated by [164]

$$\lambda_+ = \left(\frac{4}{3}\pi n_+\right)^{-1/3}. \tag{4.26}$$

As can be seen in Equations 4.20 and 4.23, the difference between the Spitzer and the modified Spitzer equations is the factor which appears after the natural log—the Coulombic logarithmic terms. Essentially, in Equation 4.23, a factor of $(1 + 1.4\Lambda_m^2)^{1/2}$ is substituted for the Λ factor in Equation 4.20. Therefore, in order to determine the charged particle momentum-transfer cross-section for a partially ionized gas, one should substitute a factor of $(1 + 1.4\Lambda_m^2)^{1/2}$ for the Λ in Equation 4.22 [164],

which would give

$$\bar{Q}_{ij}^1 \cong 6\pi\bar{b}\ln(1 + 1.4\Lambda_m^2)^{1/2}. \tag{4.27}$$

Equation 4.27 approximates the momentum-transfer cross-sections for charged particle collisions, which is then used in conjunction with Equations 4.13 and 4.4 to determine the electrical conductivity of the gas due to charged particle collisions.

4.2.2.4 Sequence

Electrical conductivity is calculated in the UMM code using the `omega.f` and `econ.h` programs. Specifically, Equation 4.4 is used to sum the different contributions from the different species interactions. Equation 4.13 calculates a collision integral using two methods, depending on the species involved in the collision:

1. Electron-neutral collisions for the 30 species are calculated using a 16-point Gauss-Laguerre quadrature. The momentum-transfer cross-section data comes from experimental results [151, 152]. See Section 4.2.2.2 for more details.

2. Charged particle collisions are approximated using a method described by Zollweg [164], which is based on a modified Spitzer formula (and assumes ions equal electrons). See Section 4.2.2.3 for more details.

The calculation of the integral cross-section for the charged particle interactions is fairly straight-forward—each cross-section is calculated at the temperature of interest. However, the execution of the Gauss-Laguere quadrature in `omega.f` is slightly more complex. Figure 4.2 is a flowchart representing the processes in

`omega.f`, specifically, the approximations to the Chapman-Enskog method and the Gauss-Laguerre quadrature loop.

The electron momentum-transfer cross-sections for the 30 species are given as a function of incident electron energy, in eV [151, 152]. Please see Appendix A for a table of all 30 gas species with their momentum-transfer cross-sections at various electron energies. Using the Gauss-Laguerre quadrature (which uses abscissa and weight factors, represented by "k" and "m" loops, respectively, in Figure 4.2), for a given species, `omega.f` creates a table of nine "omegas" for each of the 801 temperatures of interest (from 1000 K to 9000 K at 10 K intervals). The term "omegas" is derived from the "Omega integrals" mentioned in Section 4.2.2.2, and physically represent the different ℓ and s values of the average collision cross-section, from Equation 4.13. (Please note that in Figure 4.2, ℓ and s are represented by the sans serif letters "L" and "S," respectively.) The program creates a separate file for each species, containing that species' collision cross-section values, which are later used in the calculation of the q^{mn} elements, such as in Equation 4.12. For each species' cross-sectional table, linear interpolation is used to obtain cross-sections for the parameters of the actual potentials (*i.e.*, the actual temperatures of interest).

The overall electrical conductivity calculation procedure is as follows:

1. `omega.f` calculates the "omega" integrals for electron-neutral collisions, and creates the omega tables (each species has a separate file).

2. `ceb.f` calculates the thermodynamic data (*e.g.*, temperature) and species concentrations (including ions), assuming a single ion species.
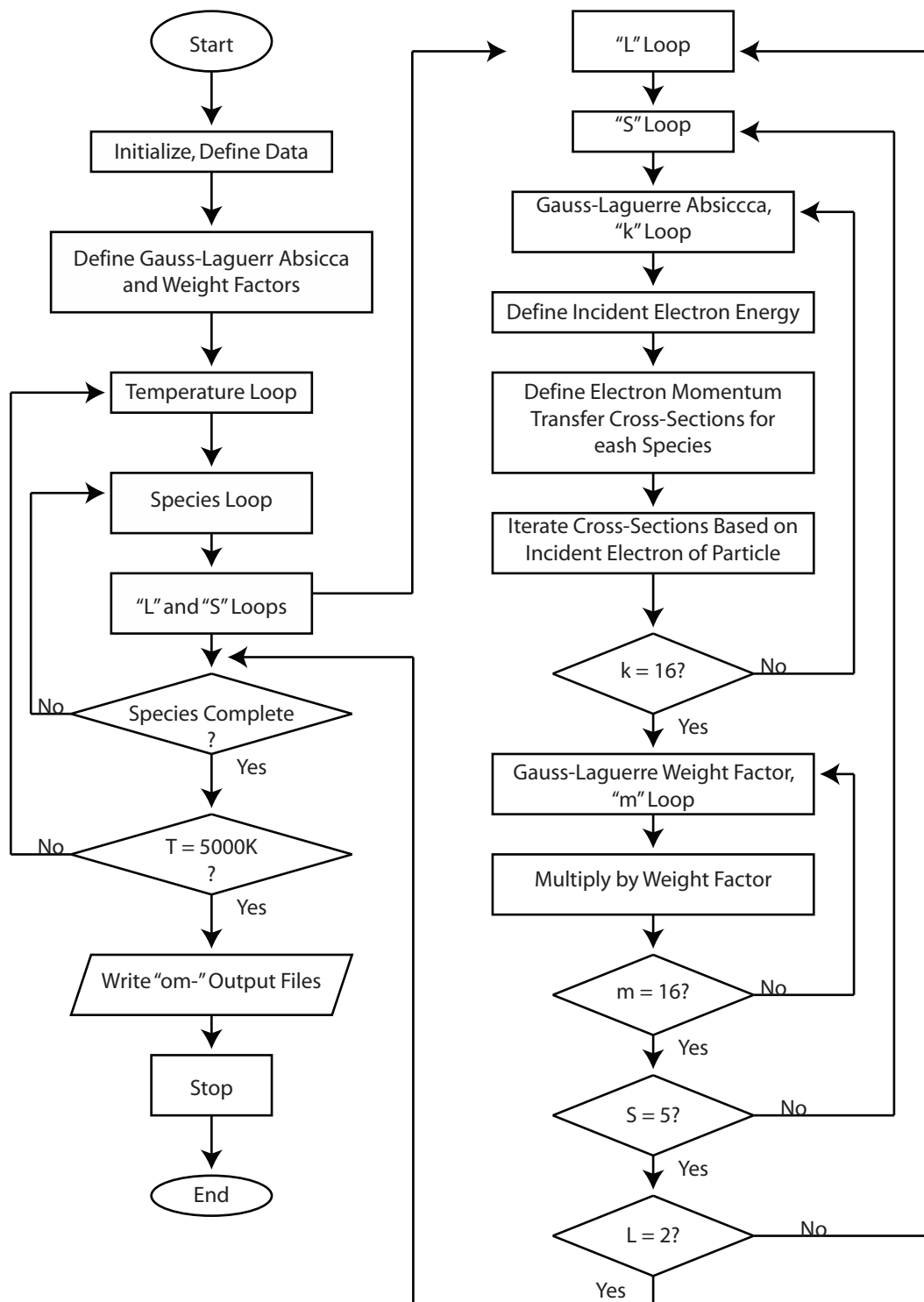
Figure 4.2: Flowchart of the omega.f program. Omega.f creates 30 output files (for the 30 species), each containing collision integrals for 9 levels of approximation, with 801 temperatures at each level.

3. `econ.h` calculates the "omega" integrals for charged particle collisions and interpolates electron-neutral collision cross-sections based on temperatures from `ceb.f`.

4. `econ.h` calculates the total electrical conductivity, based on Equation 4.4.

4.2.3   Implementation

The purpose of the UMM thermoelectric codes is to provide thermodynamic property data (temperature, molecular weight, the ratio of specific heats, laminar viscosity, and total charge) and electrical transport property data (electrical conductivity data) to the MHD numerical model. The thermoelectric codes accomplish this by creating a table which loops in pressure and enthalpy and contains the required thermoelectric data, as shown in Figure 4.3.

As discussed in previous sections, the user specifies to `thermhd.f` (via the input file, `thermhd.in`) the maximum and minimum pressure and enthalpy values, and the number of steps the code should take for the pressure and enthalpy loops. (Note that the code calculates each loop's step size, by taking the difference between the maximum and minimum loop values, and dividing that by the number of steps that should be taken. By making the step size a calculated value, the user is guaranteed that the thermoelectric codes will use their exact minimum and maximum values, and that the step sizes will be constant.) As Figure 4.3 illustrates, for the first pressure step, the thermoelectric codes calculate the required properties at every step in the enthalpy loop; then, the code advances to the second pressure step, calculates all the
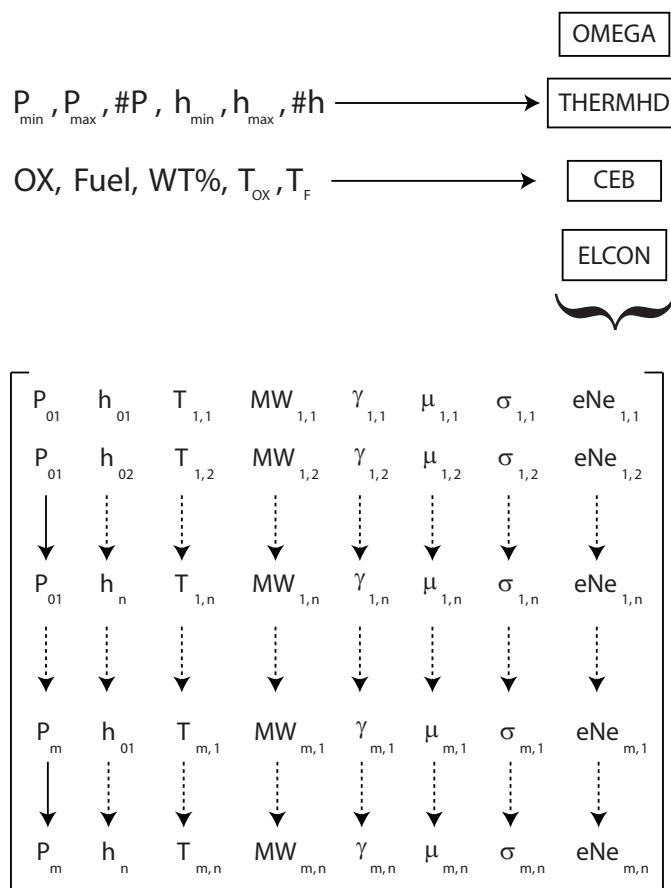
Figure 4.3: The thermoelectric property table created by the thermoelectric numerical model of the UMM code. The thermoelectric codes provide the MHD code with temperature, molecular weight, ratio of specific heats, laminar viscosity, electrical conductivity, and total charge at every pressure and enthalpy step in both loops.

required values at every step in the enthalpy loop, again, and continues to advance in the same manner, until both, the enthalpy and pressure, loops are completed. The current maximum number of pressure and enthalpy steps are 60 and 500, respectively (however, both values can be increased if necessary).

Sections 4.2.1 and 4.2.2 gave detailed descriptions of how the thermoelectric codes calculate each of their specific properties, but did not adequately describe how the codes function together—which is what this section will do. The first of the

thermoelectric codes to run is `omega.f`, which, as previously stated, is self-contained and requires no input from the user and calculates the averaged collision integrals. This program has electron momentum-transfer cross-sectional data as a function of incident electron energy for 30 different gas species—Ar, CO, CO_2, Cs, CsOH, H, H_2, H_2O, He, K, K_2, KCl, KO, KOH, Mg, N, N_2, Na, Na_2, NaCl, NaO, NaOH, Ne, NO, O, O_2, OH, SF_6, SO_2, and Xe— from 0 eV to 50 eV in units of square angstroms (*i.e.*, in 10^{-20} m^2), which is tabulated in Appendix A. When `omega.f` runs, it creates thirty different files (a file for each gas species), within which are the 9 different collision integral values (based on Section 4.2.2.2) at each of the 801 temperatures (from 1000 K to 9000 K at 10 K intervals). These individual files will be referred to as the "omega" files, and later used by `econ.h`.

As previously stated, `thermhd.f` is the "managing" program of the thermo-electric codes. It initiates the thermodynamic and/or electrical transport property calculations, runs the main pressure and enthalpy loops, and controls most of the important I/O, including writing the thermoelectric data output file (illustrated in Figure 4.3) required by the MHD code. Figure 4.4 is a flowchart representing the processes in `thermhd.f`, which include the calculations made by `econ.h` and `ceb.f`, and will be explained in the following paragraphs.

The user defines the pressure and enthalpy ranges/steps in `thermhd.in` which is read by `thermhd.f`. As seen in Figure 4.4, the mass of each particle/atom is calculated in `econ.h` from the product of the atomic mass (in kg/amu) and the molecular weight (in amu). Then, `econ.h` reads in the collision integrals from the omega files, and multiplies them by the appropriate ℓ and s values, from the expression
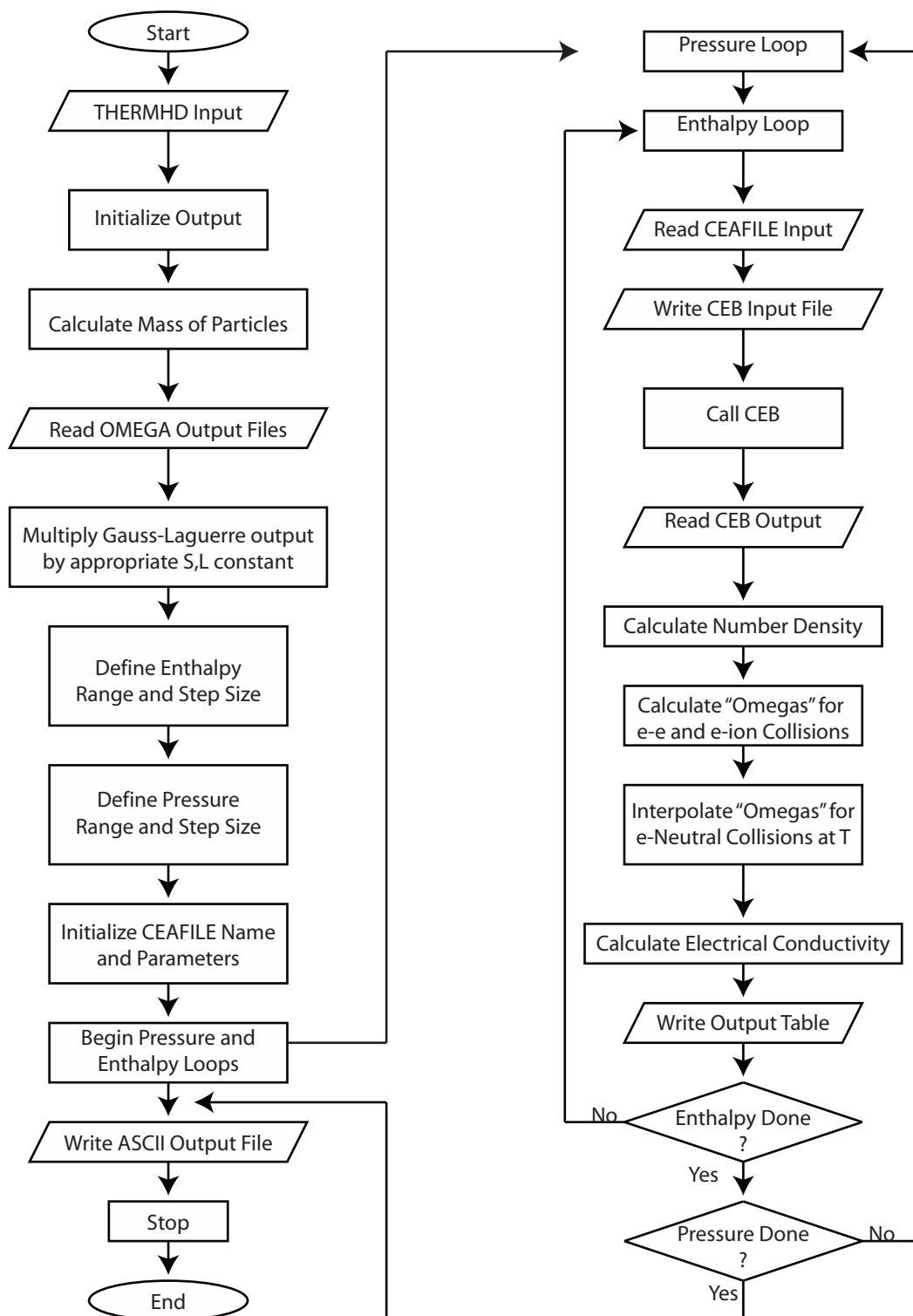
Figure 4.4: Flowchart for the thermhd.f program. This includes the thermodynamic calculations made by ceb.f and the electrical conductivity calculations made by econ.h.

to the left the integral on the right-hand-side of Equation 4.13. The pressure and enthalpy loops are then defined by `thermhd.f`, based on user input, as previously described.

Next, `thermhd.f` initializes what is known as the `CEAFILE`—since the `ceb.f` code needs to run at every step in the pressure and enthalpy loops, it requires a new input file (at every step) to reflect the current enthalpy and pressure. The `thermhd.f` code actually writes a new input file for `ceb.f` at every step in the pressure and enthalpy loops—this input file is based on the original `ceb.f` input file (in this case, `mapx.in`), the original `thermhd.f` input file (known as `thermhd.in`), and the current enthalpy and pressure steps. Only after `thermhd.f` has written a new input file, does it call `ceb.f` to run.

After `ceb.f` runs, the `thermhd.f` code reads its output which is used to calculate the number density of each species (including ions and electrons, which equal). A call is then placed to `econ.h` to calculate the collision integrals for charged particle collisions (electron-electron and electron-ion, described in Section 4.2.2.3) and to interpolate for the correct electron-neutral collision integral (based on the current thermodynamic values given by `ceb.f` at the current pressure and enthalpy step, described in Section 4.2.2.2). With this information, `econ.h` calculates the electrical conductivity (see Equations 4.4 and 4.10) of the gas mixture at the current thermodynamic conditions, and `thermhd.f` writes all the current thermoelectric conditions to the output table, as illustrated in Figure 4.3.

This process continues if the enthalpy and pressure loops are not done. After the enthalpy and pressure loops are complete (and the main thermoelectric output

file is completely filled in), `thermhd.f` writes summary output data in ASCII (text) format. At this point, the UMM thermoelectric codes have completed their processes, and the MHD numerical model is executed.

4.3   MHD Numerical Model Modifications and Improvements

As discussed in Section 3.6, the original form of the MGMHD code is inadequate for the proper modeling of the NASA MSFC MAPX diagonal accelerator, and thus requires modifications and additional features. The resulting numerical model is referred to as the UAH-MSFC-MGMHD (UMM) code, which is divided into two main parts, as illustrated in Figure 4.1. This section will detail the modifications and additions to original MGMHD code, which (in modified form) is the program `mhd.f` (with the input files `mhd.in`, `mhncom.h`, and `angle.in`), the MHD portion of the UMM code.

4.3.1   Accelerator Mode

As illustrated in Figures 1.2 and 1.3, for a given MHD channel, the primary difference between generator and accelerator modes is the direction of the J_y current. The reversal of the J_y current from generator mode to accelerator mode is typically accomplished with an applied current—an external power supply is used to overpower the naturally occurring J_y current, which stems from the $\mathbf{u} \times \mathbf{B}$ Lorentz force, described in Section 1.2.1.1. This applied J_y current results in a $J_y B$ Lorentz force which accelerates the flow in the positive $\mathbf{u}$ direction, as outlined in Section 1.2.1.2. Furthermore, in an MHD accelerator, since the user applies/specifies the J_y current

(instead of one being induced by the interaction of the moving particles and the magnetic field), it can alter the solution procedure for the problem.

The following sections explain how the MGMHD code was modified to achieve MHD accelerator operation in the respective configurations (Faraday, diagonal, and Hall). In all cases, even where potentials and currents are calculated in different ways, these modifications were additions to the MGMHD code—*i.e.*, the original MGMHD code is still intact and operational. It is also important to note that when running the UMM code in any MHD accelerator configuration, the user should always double-check the output to ensure the proper orientation of the J_y current. As explained in Chapter 5, in accelerator mode, the J_y current, under certain circumstances, sometimes reverses direction, essentially changing the accelerator to generator mode.

4.3.1.1 Faraday

Section 3.3.1.1 describes how the MGMHD code simulates a Faraday generator condition. In the case where `IOPT` is equal to 1, the Faraday channel potential difference is calculated by a load factor, K, using Equation 3.47, where standard generator load factors are $0 < K < 1$. The same basic theory is used in MHD accelerators—the main difference being that, since the J_y current must flow in the opposite direction, the potential at $y = 0$, ϕ_0, must be greater than the potential at $y = H$, ϕ_H. Rewriting Equation 3.47 results in

$$\phi_0 - \phi_H = K\langle u \rangle BH. \tag{4.28}$$

Just as the generator case, the short- and open-circuit values of K are 0 and 1, respectively. Therefore, ϕ_0 must overcome the naturally occurring potential value of uBH, which means that, for an MHD Faraday accelerator, the load factor, K, must be greater than 1. Just as with the generator mode, the user can specify the accelerator load factor at different locations along the channel, and the code will average between specified points.

Further modifications were also necessary to enable Faraday accelerator operation. Similar to the MHD generator case where boundary conditions are defined by external loading and resistance, the MGMHD code was modified to allow the user to specify the J_y current value, when operating in MHD Faraday accelerator mode. A new input parameter, IOPT3, is a switch (*i.e.*, IOPT3= 1 enables this option) which allows the user to specify the J_y current (in A/m^2) via another new input variable, ZJCNT.

In practice, one models an MHD Faraday accelerator similarly to how one builds an MHD Farday accelerator. As seen in Section 1.2.2.2, a Faraday accelerator has independent loading and power supplies—*i.e.*, each individual pair of electrodes is powered such that the J_y current is oriented correctly. In the UMM code, the user can set loading parameters to different values along the channel to ensure that J_y maintains proper orientation. Furthermore, the user can specify the J_y current to be used along the channel length (just as one can specify the current from the power supplies). The UMM code offers someone modeling a Faraday accelerator the same basic options someone building a Faraday accelerator has.

4.3.1.2 Diagonal

The primary goal of this research is to numerically model a diagonal MHD accelerator, therefore the majority of the modifications to the MGMHD code deal with facilitating the simulation of a diagonal accelerator. The additions mentioned in this section will deal strictly with enabling the MGMHD code to model a diagonal accelerator. Subsequent sections will detail other complementary changes/additions to the MGMHD code—*e.g.*, varying diagonal angle, power takeoff, and axial neutralized current.

It is important to note that the governing equations and assumptions outlined in Section 3.3.1 are true in this derivation. As explained in Section 3.3.2, the physical difference between a diagonal accelerator and generator is the diagonal link between the electrodes. Therefore, for an MHD accelerator, a new set of oblique coordinates must be defined, and for the purposes of this derivation, a new diagonal angle, α_d will be used. The details of this are located in Appendix C, but from these new oblique coordinates and α_d, the electric potential can be defined as

$$\psi = - \left(x + y \cot \alpha_d \right) E_x + \phi(y, z), \tag{4.29}$$

where, just as Equation 3.34, $\phi(y, z)$ is a two-dimensional potential and where the relationship between α_d and θ_d is

$$\alpha_d = 180 - \theta_d. \tag{4.30}$$

Note that Equation 3.34 is recovered when Equation 4.30 is substituted into Equation 4.29. Substituting Equation 4.29 into Equations 3.29, 3.30 and 3.31, results in the following equation for the two dimensional function $\phi(y, z)$,

$$\frac{\partial}{\partial y}\left(\sigma_n \frac{\partial \phi}{\partial y}\right) + \frac{\partial}{\partial z}\left(\sigma \frac{\partial \phi}{\partial z}\right) = E_x \frac{\partial}{\partial y}\left[(\beta + \cot \alpha_d)\sigma_n\right] - \frac{\partial}{\partial y}\left[\sigma_n B\left(u - \beta v\right)\right], \quad (4.31)$$

where, just as in Equation 3.35, Equation 4.31 is linear in ϕ and a decomposition of the potential is permitted (which, because of similarities to Section 3.3.1 and the derivation in Appendix C, will not be detailed here).

As in the generator case, both ϕ_1 and ϕ_2 are independent of E_x, which is determined by the external connection and loading of the accelerator. Applying Ohm's Law, the current densities are as follows:

$$J_x = E_x \sigma_n \left(1 - \beta \cot \alpha_d + \beta \frac{\partial \phi_1}{\partial y}\right) + \sigma_n \left[(\beta u + v) B + \beta \frac{\partial \phi_2}{\partial y}\right], \quad (4.32)$$

$$J_y = E_x \sigma_n \left(\beta + \cot \alpha_d - \frac{\partial \phi_1}{\partial y}\right) - \sigma_n \left[(u - \beta v) B + \frac{\partial \phi_2}{\partial y}\right], \quad (4.33)$$

and

$$J_z = -E_x \sigma \frac{\partial \phi_1}{\partial z} - \sigma \frac{\partial \phi_2}{\partial z}. \quad (4.34)$$

Just as in Section 3.3.1, using the cross-sectional spatial average, $\langle f \rangle$, the cross-sectional average current densities can be represented as follows:

$$\langle J_x \rangle = E_x \left[\langle (1 - \beta \cot \alpha_d)\, \sigma_n \rangle + \langle \sigma_n \beta \frac{\partial \phi_1}{\partial y} \rangle \right] + \langle \sigma_n \beta \frac{\partial \phi_2}{\partial y} \rangle + B \langle \sigma_n \left(\beta u + v \right) \rangle, \quad (4.35)$$

and

$$\langle J_y \rangle = E_x \left[\langle (\beta + \cot \alpha_d)\, \sigma_n \rangle - \langle \sigma_n \frac{\partial \phi_1}{\partial y} \rangle \right] - \langle \sigma_n \frac{\partial \phi_2}{\partial y} \rangle - B \langle \sigma_n \left(u - \beta v \right) \rangle. \quad (4.36)$$

For the boundary conditions of a diagonal connection (`IOPT`= 3 or 4) outlined in Section 3.3.1, the axial electric field is determined by the equation

$$E_x = \frac{J_{ld} - \langle \sigma_n \left(\beta - \cot \alpha_d \right) \left(\phi_{2_y} + uB \right) \rangle - B \langle \sigma_n \left(1 + \beta \cot \alpha_d \right) v \rangle}{(1 + \cot^2 \alpha_d)\, \langle \sigma_n \left(\beta - \cot \alpha_d \right) \phi_{1_y} \rangle}. \quad (4.37)$$

The purpose of this brief derivation (which is detailed in Appendix C) was to show the differences and similarities in the generator and accelerator cases. A quick comparison of Equations 3.35 and 4.31, Equations 3.40 and 4.32, Equations 3.41 and 4.33, Equations 3.42 and 4.34, and Equations 3.62 and 4.37 (respectively) shows that the only difference between the generator and accelerator cases is the sign preceding the cotangent of the angle (θ_d for generator and α_d for accelerator). Here, it is important to note one of the the properties of cotangent—the cotangent of an angle is equal to the negative value of the cotangent of the supplement of that angle (*e.g.*, when Equation 4.30 is substituted into one of the α_d equations in this section, the generator and accelerator equations are identical). In other words, if one uses

an obtuse diagonalization angle, $180 > \theta_d > 90$, the result would be the same as if one used the angle α_d, described in this section. Therefore, in order to modify the MGMHD code to run in accelerator mode, one needs only to define the diagonalization angle in terms of the obtuse angle, θ_d (as illustrated in Figures 3.3 and 3.4). As the MHD part of the UMM numerical model (*i.e.*, `mhd.f`), the MGMHD code has been altered to accept obtuse diagonalization angles (which the user inputs in `mhd.in`). This was the only required modification to enable modeling of MHD accelerators; however, other modifications (which improve the accelerator modeling accuracy) are described in subsequent sections.

4.3.1.3   Hall

The Hall generator configuration was not independently mentioned as an option in the original MGMHD manual [125]. However, since a Hall generator/accelerator is simply a special case of a diagonal generator/accelerator (where $\theta_d = 90.0$) [90], the addition of a Hall configuration was relatively simple. However, because of the numerical processes in the MGMHD and UMM codes, defining $\theta_d = 90.0$ would result in numerical instability.

Therefore, to model a Hall configuration (in generator or accelerator modes) without introducing numerical instabilities, one should set the value of `IOPT` to 3 (the case for a diagonal configuration, with insulating sidewalls), and set the value of θ_d to 89.9 or 90.1 degrees, for generator or accelerator, respectively. The value of the diagonalization angle, θ_d, is the input parameter `ANGLE` in the file `mhd.in`. These

angles, even though not exactly 90.0 degrees, can accurately model a Hall generator or accelerator [165, 166].

4.3.2   Integration of Thermodynamic and Electrical Property Models

This section describes how the UMM thermoelectric codes are integrated into the MHD code. The thermoelectric data used by the UMM MHD code are temperature, molecular weight, ratio of specific heats, laminar viscosity, electrical conductivity, and total charge (the product of electron charge and electron number density), as a function of user-specified pressure and enthalpy. Section 4.2 details the UMM thermodynamic and electrical transport property codes—including their output files, which are structured in such a way as to work most efficiently with the MHD code.

Figure 4.3 shows the structure of the UMM thermoelectrical data table, while Figure 4.5 illustrates how this thermoelectrical data is used by the MHD code in three-dimensional calculations. As described in Section 3.5 and detailed in the MGMHD manual [125], the UMM MHD code solves for pressure at each axial location using the value of static pressure at the previous axial station and the pressure gradient from the momentum equation, and solves for enthalpy in each cell at each axial position using the energy equation (see Section 3.2.1) [125]. Similarly, using the momentum equation and mass continuity equation, the UMM MHD code solves for the value of axial velocity in each cell at each axial location [125]. For each cell, at each axial location, the UMM MHD code interpolates for the values of temperature (T), molecular weight (MW), ratio of specific heats (γ), laminar viscosity (μ_ℓ), electrical conductivity (σ), and total charge (eN_e) using the calculated values of pressure and
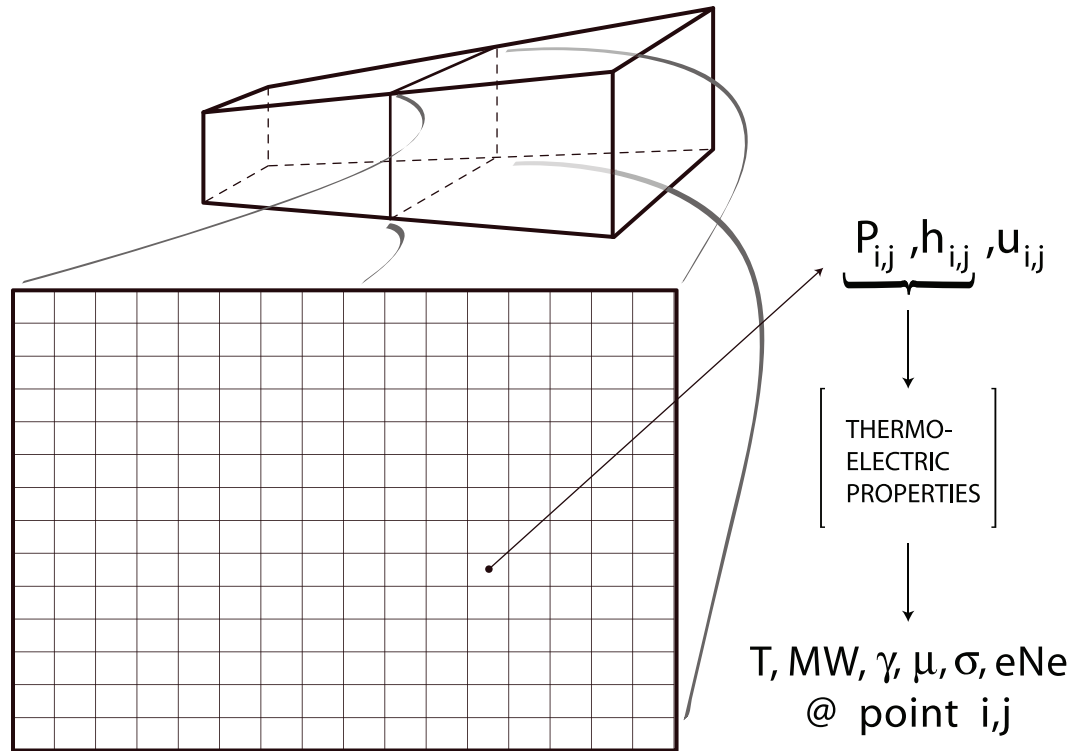
Figure 4.5: How the UMM MHD code uses the thermoelectrical data in three-dimensional calculations.

enthalpy and the values of pressure and enthalpy in the thermoelectrical data table. With this information (and the aforementioned axial velocity measurements), the UMM MHD code can calculate virtually any required magnetohydrodynamic value—*e.g.*, gas constant, sonic speed, Mach number, total pressure, and Hall parameter. In the `mhd.f` program, the tabular data look-up occurs in subroutine `PROPT`, with the two-dimensional interpolation carried out by a function called `TERP2`, and the calculation of the thermoelectrical data at every point in the cross-sectional plane occurs in subroutine `PROPS`.

It is worth noting that because the MGMHD code was modified to accept tabular values of laminar viscosity—instead of calculating viscosity with Equation 3.73—

the UMM MHD code can only operate in an `IPROP`= 4 condition (as outlined in Section 3.4.4). That is, the UMM MHD code can only operate in the "Variable Fluid and Electrical Properties using Fourth-Order Interpolation Polynomials" condition— it cannot operate in any constant fluid and/or electrical property conditions (*i.e.*, the UMM MHD code cannot operate in an `IPROP`= 1, 2, or 3 condition). This could be viewed as a modification that removed features from the original MGMHD code; however, since the thermoelectrical codes are so tightly integrated into the UMM MHD code, the loss of functions that used inferior methods of calculating thermoelectrical properties is a nonissue.

4.3.3   Varying Diagonal Angle

The original MGMHD code allowed the user to input a constant diagonal angle for modeling diagonal MHD generators. This is an adequate, albeit practically inaccurate, representation of real-world diagonal MHD channels (both generators and accelerators). Allowing a variable diagonal angle in the UMM code would give the user much more flexibility when designing a diagonal MHD device, and offer another tool for modeling real-world systems [44]. Therefore, the UMM code was modified to allow for variable diagonal angles.

In practice, this involved adding an input file to the `mhd.f` code. In the file `angle.in`, the user enters an axial distance (in meters, measured from the entrance of the channel) and a diagonalization angle, θ_d, in degrees. The user can enter as many locations/angles as necessary (as long as they are within the pre-defined boundaries of the MHD channel), and the `mhd.f` code linearly interpolates the angle between

entries. The user tells the `mhd.f` code to use the varying angles in `angle.in` by entering a value larger then 360 for `ANGLE` (which is the constant angle input value, in degrees) in the file `mhd.in`.

4.3.4 Axial Current Neutralized

As discussed in Section 1.2.2, MHD accelerators operate more efficiently when the axial, J_x, current density is at a minimum. An increase in the J_x current can effectively reduce the J_y current (and, therefore, reduces the axial Lorentz force term, $J_y B$), induce flow in the cross-section, and cause instabilities in the flow. The segmented Faraday configuration (Section 1.2.2.2) is designed to eliminate the J_x current, while the diagonal configuration (Section 1.2.2.3) seeks to minimize the J_x current with the use of a diagonal angle. Therefore, it would be advantageous for the user if the UMM code could output the angles that would effectively neutralize the axial current in the diagonal accelerator mode. (Note, in some texts [72,73], this is referred to as the "Hall Current Neutralized" mode of operation.)

As detailed in Section 3.3.2, the electric field angle is defined as $\tan \theta = E_y/E_x$. In accelerator mode, the diagonalization angle, θ_d, is related to the electric field angle by $\theta_d = \theta + \pi/2$ (please see Figure 3.3), which, when used with the trigonometric relationship $\cot \vartheta = \tan(\pi/2 - \vartheta)$, results in

$$\cot \theta_d = -\frac{E_y}{E_x}. \tag{4.38}$$

In Appendix C the x and y components of Ohm's Law are isolated, and result in the following equations:

$$J_x = \sigma_n \left[E_x - \beta E_y + (v + \beta u)\, B \right] \tag{4.39}$$

and

$$J_y = \sigma_n \left[E_y + \beta E_x + (\beta v - u)\, B \right], \tag{4.40}$$

which are also alternate forms of Equations 1.24 and 1.25. By definition, in an axial current neutralized case, $J_x = 0$; therefore, (using Equation 4.38) Equation 4.39 can be rewritten as

$$E_x = -\frac{(v + \beta u)\, B}{1 + \beta \cot \theta_d}. \tag{4.41}$$

Using Equation 4.41, Equation 4.40 can be expressed as

$$J_y = \sigma_n B \left[\frac{(v \cot \theta_d - u)\,(1 + \beta^2)}{1 + \beta \cot \theta_d} \right]. \tag{4.42}$$

Substituting Equation 4.42 into Equation 3.61 (recalling that $J_x = 0$) results in

$$J_{ld} = -\sigma_n B \left[\frac{(v \cot \theta_d - u)\,(1 + \beta^2)}{1 + \beta \cot \theta_d} \right] \cot \theta_d. \tag{4.43}$$

Here, given that the v-velocity (in the cross-plane) is much less than the u-velocity (in the axial direction), the v-velocity term can be neglected from Equation 4.43. Recalling that $\sigma_n = \sigma/(1 + \beta^2)$, Equation 4.43 can be rewritten as

$$\cot \theta_d = \frac{J_{ld}}{\sigma \beta u - \beta J_{ld}}. \tag{4.44}$$

Equation 4.44 allows the UMM MHD code to solve for the appropriate accelerator diagonalization angle for an axial current neutralized ($J_x = 0$) condition [72, 73]. It is important to note, however, that the axial current neutralized mode operates on the cross-sectional averaged values for J_x—that is, local non-zero values for J_x will exist, but all the values of J_x integrated over the cross-section will result in a zero value. Since the resulting diagonal angle is applied over the entire cross-section, it is logical that cross-sectional values of J_x are used in the calculation. A switch (the input parameter `IOPT4`) was added to `mhd.in`, which when activated (`IOPT4= 1`), tells the MHD code (in subroutine `MAXCF`) to recalculate the value of the angle using Equation 4.44. The MHD code recalculates the angle at every step as it marches down the accelerator channel. This calculated angle tells the user which angles (and at which axial positions) should result in the most efficient diagonal accelerator operation.

4.3.5   Power Takeoff

Power takeoff (PTO) is a means to locally control the current in end regions of an MHD channel where connections are made to a load or power supply [166]. In the end regions of an MHD channel, where the magnetic field is attenuating, the PTO electrodes help reduce the eddy current loss [121]. Power takeoff is necessary but treated differently for generators and accelerators, which will be explained below.

4.3.5.1   Basic Theory

In an MHD generator, the key issue related to power takeoff is that the load should not demand more current out of an electrode than the generator can de-

liver [166]. The maximum current that a generator can deliver is the local short circuit current [166, 167]. Asking for more current than the local short circuit value can result in a reversal of the axial electric field and the MHD channel will run in accelerator mode at that location [166–168].

Wu [108] defines the axial electric field of an MHD generator as follows:

$$E_x = \frac{(1 - \beta^2)I - A\sigma uB(\beta + \varphi)}{\sigma A(1 + \varphi^2)}. \tag{4.45}$$

In generator mode, the short circuit current is defined as [108]

$$I_s = \frac{\sigma AuB(\beta + \varphi)}{1 + \beta^2}, \tag{4.46}$$

where combining Equations 4.45 and 4.46 yields

$$E_x = \frac{1 + \beta^2}{\sigma A(1 + \varphi^2)} (I - I_s). \tag{4.47}$$

It is clear from Equation 4.47 that to assure the channel operates in generator mode, the local current, I, required of the electrode must be less than the local short circuit current, I_s.

The opposite issues apply to an MHD accelerator power takeoff scheme. In general, enough potential must be applied across each PTO electrode to ensure that they are being powered. Otherwise, just as in the generator case, the local electric field will reverse, which will cause the channel to effectively run in a local generator mode [166].

Litchford [90] defines the axial electric field in an MHD accelerator as follows:

$$E_x = \frac{(1 + \beta^2)\, I + A\sigma uB\,(\varphi - \beta)}{\sigma A\,(1 + \varphi^2)}, \qquad (4.48)$$

where the differences between Equations 4.45 and 4.48 result from the definition of the electric field angle, θ (as explained in Section 3.3.2), and its relationship to the electric field direction, φ. In accelerator mode, the zero power current (also called short circuit current) is defined as [90]

$$I_z = \frac{\sigma AuB(\beta - \varphi)}{1 + \beta^2}, \qquad (4.49)$$

where combining Equations 4.48 and 4.49 yields

$$E_x = \frac{1 + \beta^2}{\sigma A(1 + \varphi^2)}\,(I - I_z)\,. \qquad (4.50)$$

It is clear from Equation 4.50 that to assure the channel operates in accelerator mode, the local applied current, I, must be greater than the local zero power current, I_z (which is why it is referred to as the zero power current).

However, there are other factors to consider when designing a power takeoff region. The current in an MHD channel excites the electrons in the flow, which in turn, increase the internal energy (*i.e.*, temperature) of the flow through collision with atoms and other particles. This temperature increase is known as "Joule heating," which (as described by Rayleigh flow [169]) tends to drive the flow to a choke condition (*i.e.*, $Mach = 1$) [166]. In an accelerator, if the heat addition term overpowers

the Lorentz J_yB acceleration term, the flow could be driven to choke (which would decelerate a supersonic flow). Furthermore, the increase in local temperature could increase the local pressure gradient, which could, if it exceeds the local boundary layer shape parameter, cause the flow to separate from the wall [166]. The flow separation can cause a recirculation region, which will cause the UMM code to terminate (because the MGMHD and UMM codes, due to the parabolic assumption, cannot handle any kind of flow reversal).

Therefore, it is absolutely necessary to control the local current in the end regions of an MHD channel. In a generator, the local current must be less than the local short circuit current. In an accelerator, the local current must be greater than the local zero power current, but not so high as to cause a Rayleigh flow choke and/or flow separation. In the **B** field fringe regions (where the J_yB Lorentz term is not as powerful), it is important that the local current behave in a manner that is consistent with the desired global operation of the MHD device.

4.3.5.2 Diagram and Analysis of Power Takeoff Scheme

The power takeoff scheme in the UMM numerical model was designed to give the user the necessary control over the specified current in the magnetic-field-attenuated (*i.e.*, end) regions of the MHD channel. In the UMM code, the power takeoff scheme is controlled by six user-defined input parameters (which are illustrated in Figure 4.6):

- `AJLIN` is the load/applied current, in Amperes (depending on whether generator/accelerator mode is chose, respectively). This parameter name was changed from `AJL` in the MGMHD code.
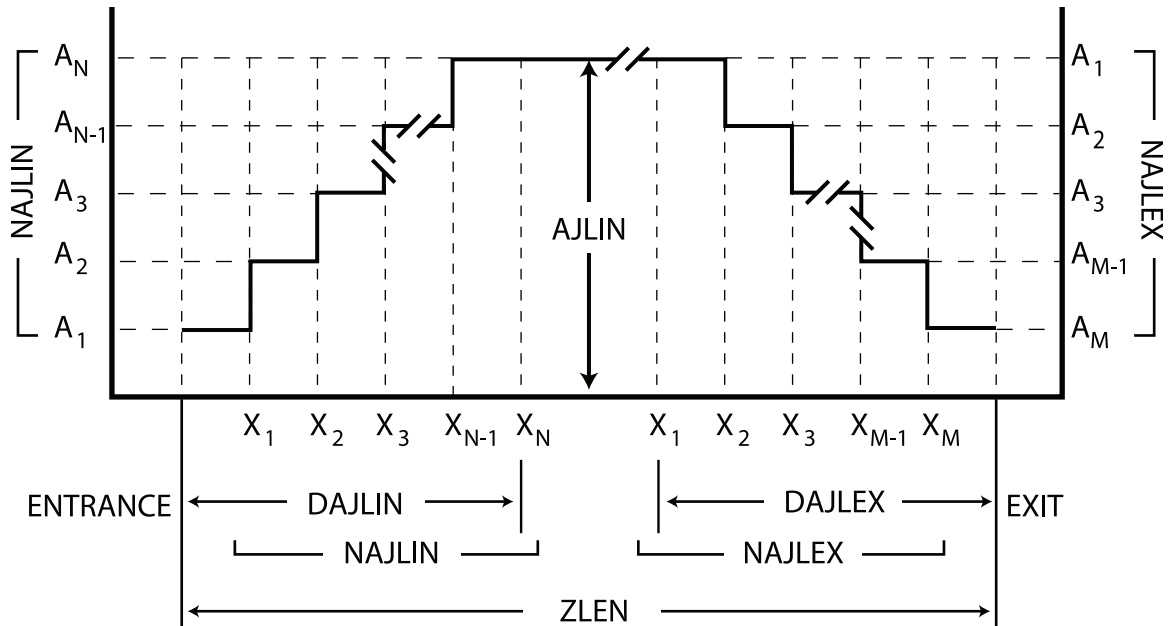
Figure 4.6: Illustration of power takeoff scheme used in the UMM numerical model.

- ZLEN is the total length of the MHD channel (in meters).

- DAJLIN is the length of the entrance PTO region. This value is given as a decimal, and represents a percentage of the total length (ZLEN) of the channel.

- NAJLIN is the number (integer value) of "steps" in the entrance PTO region. In both distance and current value, the code will step NAJLIN number of times until it reaches the end of the PTO region and 100% load/applied current value.

- DAJLEX is the length of the exit PTO region, given as a decimal (percentage) value of ZLEN.

- NAJLEX is the number of steps in the exit PTO region, given as an integer.

Figure 4.6 illustrates the meaning of the six power takeoff parameters (where AJLIN and ZLEN are from the original MGMHD code, and the other four are added

modifications). There are some obvious limitations to the parameters: (1) all values must be positive or zero, and (2) the sum of `DALJIN` and `DAJLEX` must be less than or equal to 1.0. The values of `NAJLIN` and `NAJLEX` can be set to lower number (*e.g.*, 4 or 5) for the PTO region to represent a step function, or they can be set to higher values (*e.g.*, 100) to approximate a linear distribution. The PTO scheme offered in the UMM code simulates a resistive- or power-electronics type of external circuit to control current distribution, which is standard technology for real-world MHD PTO applications [121, 166, 167].

4.3.6 Electrical Efficiency

The electrical efficiency of an MHD accelerator, as defined in Section 1.2.1.2, is simply the ratio of the of the push power to the applied power [90]

$$\eta_a = \frac{P_p}{P_{app}} = \frac{\mathbf{u} \cdot (\mathbf{J} \times \mathbf{B})_x}{\mathbf{J} \cdot \mathbf{E}}, \tag{4.51}$$

where the push power associated with the streamwise Lorentz force at any given cross-section is given by [90]

$$P_p = \mathbf{u} \cdot (\mathbf{J} \times \mathbf{B})_x, \tag{4.52}$$

and the total applied electrical power is

$$P_{app} = \mathbf{J} \cdot \mathbf{E}. \tag{4.53}$$

An alternate form of the total applied power is [90]

$$P_{app} = P_p + P_d, \tag{4.54}$$

where P_d is the power dissipated due to Joule heating over the entire cross plane, given by

$$P_d = \frac{\mathbf{J} \cdot \mathbf{J}}{\sigma} + \mathbf{J} \cdot \mathbf{E}_d. \tag{4.55}$$

The dissipated power in the core flow region is given by $\mathbf{J} \cdot \mathbf{J}/\sigma$, and $\mathbf{J} \cdot \mathbf{E}_d$ is represents the dissipated power in the electrical boundary layer [90]. The equivalent electric field, $\mathbf{E}_d$ that accounts for the nearby voltage drop, V_d, is given by $E_d = V_d/h_c$. The electrode voltage drop, V_d, is detailed in Section 3.3.1.2.

Therefore, Equation 4.55 can be rewritten as

$$P_d = \frac{\mathbf{J} \cdot \mathbf{J}}{\sigma} + J_y \frac{V_d}{h_c}, \tag{4.56}$$

where h_c is the channel height. Now, Equation 4.51 can be rewritten as

$$\eta_a = \frac{J_y u B}{J_y u B + \frac{\mathbf{J} \cdot \mathbf{J}}{\sigma} + J_y \frac{V_d}{h_c}}. \tag{4.57}$$

Because of the availability of the parameters, Equation 4.57 is used by the UMM code to calculate the efficiency of an MHD accelerator. Push power and core flow dissipation are calculated and output as three-dimensional variables, and cross-sectionally averaged in subroutine PSTPR. In that same subroutine, the electrode voltage drop is

calculated, and all the parameters are assembled into Equation 4.57 to calculate the electrical efficiency of the accelerator.

4.3.7 Total Pressure

Section 4.3.2 describes how the UMM code calculates and interpolates certain flow parameters at every cell as it marches down stream. Specifically, the UMM code has values for pressure, enthalpy, temperature, molecular weight, ratio of specific heats, viscosity, and total charge at every cell in a cross-sectional plane. With this information, the UMM code first calculates the specific gas constant, as a three-dimensional variable

$$gasK_{i,j} = \frac{8314.34}{MW_{i,j}}, \tag{4.58}$$

where 8314.34 is the value of the gas constant, R, in J/kg mol K. The speed of sound is calculated next, as a three-dimensional variable, using

$$a_{i,j}^2 = \gamma_{i,j}\, gasK_{i,j}\, T_{i,j}. \tag{4.59}$$

The Mach number is calculated as a three-dimensional variable using the following equation:

$$Mach_{i,j} = \frac{u_{i,j}}{\sqrt{a_{i,j}^2}}, \tag{4.60}$$

where $u_{i,j}$ is the three-dimensional velocity. Therefore, the three-dimensional total pressure can be calculated with

$$P_{0_{i,j}} = P \left(1 + \frac{\gamma_{i,j} - 1}{2} \, Mach_{i,j}^2 \right)^{\frac{\gamma_{i,j}}{\gamma_{i,j} - 1}}, \qquad (4.61)$$

where $\gamma_{i,j}$ is the ratio of specific heats at every point in the cross-sectional plane. Note that Equation 4.61 does use the parabolic assumption of the UMM (and MGMHD) code, that the static pressure is constant across a cross-sectional plane in the channel. Furthermore, Equation 4.61 assumes isentropic conditions and that the value of γ at a in a given cell i, j is constant from the value of the static pressure, P, to the value of the total pressure, P_0. An MHD accelerator should increase the total pressure of the flow as it it travels down the channel.

CHAPTER 5

MAPX PRE-TEST ANALYSIS

> *No amount of experimentation can ever prove me right; a single experiment can prove me wrong.*

—Albert Einstein

5.1 Overview

This chapter presents the results of the three-dimensional numerical study of the NASA MSFC MAPX diagonal accelerator, with analysis and interpretation of the critical physical phenomena inside the MHD channel. Section 5.2 details the physical characteristics and flow properties of the MAPX facility that will influence the numerical model—this includes the physical specifications of the MAPX accelerator and the thermoelectric properties used in modeling the channel. Section 5.3 discusses the major parameters with which the MAPX accelerator can be optimized, and outlines initial modeling case studies based on those parameters. Section 5.4 expands on Section 5.3 by fine-tuning the baseline MAPX test configuration in an attempt to determine the most appropriate setup for the MAPX testing. This section also explains some of the critical physical processes that occur within a diagonal magnetohydrodynamic accelerator. Section 5.5 details the magnitude of influence that

specific input parameters have on certain important output parameters. This section quantifies how changes in certain input variables will influence the output of the UMM numerical model and test conditions of the MAPX accelerator. Section 5.6 offers a recommendation for the test setup of the MAPX accelerator, given the restrictions of the MAPX accelerator/facility, the goals of the MAPX project, and the known physical quantities at the time of this writing.

5.2 Experimental Setup

This section details the aspects of the MAPX experiment considered as "fixed" quantities for this dissertation. These fixed quantities include the design and dimensions of the MAPX accelerator (excluding the applied current and diagonal angle), the flow properties over the regime of interest to the MAPX project, and the magnetic field distribution from the 2 T electromagnet. Most of these quantities are outlined in Chapter 2; however, this section details how these characteristics are integrated into the UMM code. The optimization parameters of concern to this dissertation—the applied current and the diagonal angle between electrodes—are analyzed in Section 5.3.

5.2.1 MAPX Channel Configuration

Section 2.1.2.2 and Table 2.2 detail the physical design, dimensions, and specifications of the MAPX accelerator. The UMM numerical model requires that the user define certain physical characteristics of the MHD channel, namely,

- The channel inlet and exit dimensions.

- The overall length of the powered section of the channel. (Note: in this dissertation, the UMM code will only model the powered section of the MAPX channel.)

- The manner in which the cross-sectional area of the channel varies (*i.e.*, constant cross-section, symmetric expansion, or asymmetric expansion).

- The electrode pitch.

The MAPX physical specifications are detailed in Figure 5.1. Recall from Table 2.2 that the MAPX accelerator is 99.5 cm in total length, which consists of 66 total electrode-insulator pairs plus one extra insulator (*i.e.*, the MAPX channel begins and ends with an insulator). The powered region of the MAPX accelerator consists of only 60 electrode-insulator pairs, for a length of 90.5 cm (again, beginning and ending with an insulator). The channel entrance height and width is 1.56 cm × 1.56 cm while the exit is 3.64 cm × 3.64 cm—however, at the end of the powered region, the dimensions are 3.46 cm × 3.46 cm. Given these entrance and exit dimensions and the user-defined symmetric expansion, the UMM code calculates the cross-sectional dimensions for every step in the axial direction—the user needs not define the divergence angle.

Also note in Figure 5.1 that the entrance electrodes have an approximate surface area of 1.56 cm^2, while the exit electrodes are approximately 3.46 cm^2. Because of electrode erosion, it is recommended that the current density in the power take-off (PTO) regions not exceed 15 A/cm [165, 170]. These conditions dictate that the entrance PTO should be spread over 5 electrodes, while the exit PTO would only
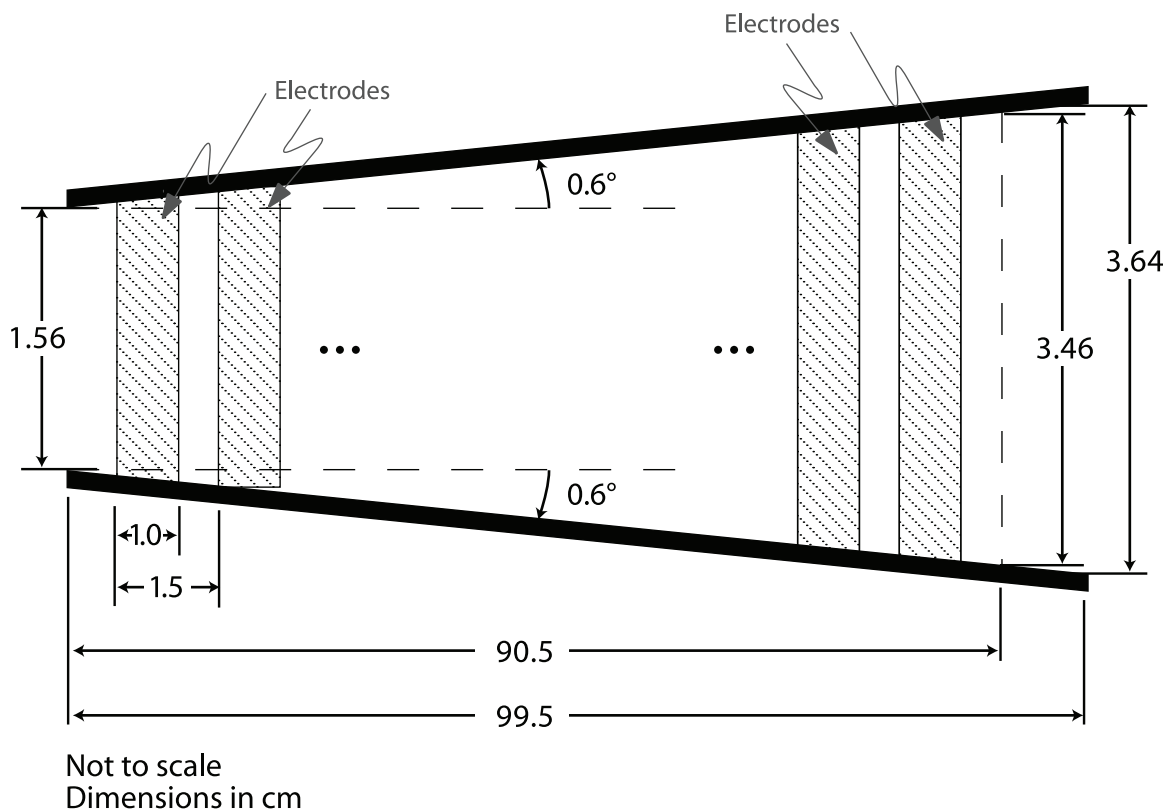
Figure 5.1: The physical characteristics of the MAPX accelerator. Note: (1) even though electrodes are represented in the illustration, because the MAPX accelerator has a square cross-section, these dimensions describe both the insulator sidewalls and electrode walls, and (2) the powered length of the channel is 9 cm shorter than the total length.

require 2 electrodes (assuming an applied current of 100 A). Unfortunately, the infinite segmentation assumption of the MGMHD and UMM codes prohibits the proper implementation of an exit PTO—*i.e.*, when the code gets to the end of the channel, it simply terminates calculation. Therefore, an exit PTO is not modeled with the UMM code at this time; however, preliminary analysis shows that in order to avoid the 15 A/cm upper boundary, only 2 electrodes would require PTO at the MAPX exit. At the entrance, however, the code can simulate a proper PTO region, therefore a 5-electrode entrance PTO is used in the calculations.

5.2.2 Flow Parameters for the MAPX Regime

As described in Section 4.2, the purpose of the thermoelectric portion of the UMM numerical model is to provide the MHD portion of the code with a property table, consisting of thermodynamic and electrical transport data, as illustrated in Figures 4.3 and 4.5. The thermoelectrical table provides temperature, molecular weight, ratio of specific heats, viscosity, electrical conductivity, and total charge at the specified pressure and enthalpy points. The electrical conductivity of the fluid is calculated using a method developed by Devoto [153] while the other thermodynamic parameters are calculated using a modified version of the NASA CEA code [106, 107].

For the purposes of this dissertation, the thermoelectric input parameters will be thought of as "fixed." This is not to say that the thermoelectric flow parameters are not allowed to vary inside the MAPX accelerator—on the contrary—however, all of the user-defined input parameters to the thermoelectric codes will remain constant during the MAPX numerical analysis. The pressure range, enthalpy range, oxidizer, fuel, weight percentages, and fuel/ox temperatures are all predetermined and outside the control of the MAPX accelerator. (Please note that the NASA CEA code uses the terms "fuel" and "oxidizer" in the input file and manuals [106, 107] to describe the two parts of the flow. Even though no combustion occurs in the MAPX channel, when referring to the CEA code, this dissertation will call the working fluid the "oxidizer" and the seed material the "fuel" to avoid confusion with the actual input files. The terms oxiziser/fule, or O/F, are used for consistency with the CEA program, and is not meant to imply that there is any form of combustion occurring.) Therefore, the same

Table 5.1: Thermodynamic flow parameters presented exactly as they are for the UMM numerical model input.

Characteristic	Value
Oxidizer, N_2 (weight %)	100.0
Oxidizer Temperature (K)	2700
Fuel, Na (weight %)	22.0
Fuel, K (weight %)	78.0
Fuel Temperature (K)	300
Seed (Fuel) Percentage (% NaK)	1.0
Pressure Range (bar)	$0.001 - 5.0$
Pressure Steps	60
Enthalpy Range (J/kg)	$7.0 \times 10^5 - 3.5 \times 10^7$
Enthalpy Steps	500

thermoelectric data table can be used (and is used) for all of the MAPX numerical modeling and analysis, in order to maintain consistency. The UMM thermoelectric input files are given in Appendix D, and a summary of the thermodynamic input parameters is given in Table 5.1.

Before the flow parameter graphs are presented, it is important to understand the limiting factors and ranges used in these simulations. All of the inlet parameters listed in Table 2.4 are defined by "upstream" conditions—*i.e.*, these conditions are defined by the current capabilities of the MAPX laboratory and the Aerotherm archeater (all of which are described in Chapter 2). Furthermore, the `mapx.in` input parameters—where the user defines the oxidizer/fuel (O/F) species, the O/F weight percentages, and the initial temperatures—are determined by the capabilities of the NaK feed system. The minimum/maximum pressure and enthalpy and their loop step sizes are defined by the user in `thermhd.in`, and will remain constant throughout the

MAPX numerical analysis. All calculated values for static pressure and enthalpy fall within the range presented in Table 5.1.

The pressure loop (used in `thermhd.f` and defined by the user in `thermhd.in`) uses static pressure values for calculations (both in the `ceb.f` and `mhd.f` codes). Since the total pressure $(P_{0_{i,j}})$ in `mhd.f` is calculated using Equation 4.61 and since the static pressure of the flow decreases inside the accelerator, the inlet static pressure value of the MAPX accelerator represents the highest static pressure expected in the channel. To be conservative, the pressure range defined in `thermhd.in` is from 0.001 bars to 5.0 bars (or, 0.00098 atm to 4.9 atm). The UMM code is capable of modeling a larger pressure range (the pressure range is only limited by the NASA CEA code), but for the MAPX accelerator, a larger range is not necessary.

The enthalpy values defined in `thermhd.in` translate directly to the range of temperatures the UMM code can model. The electron-neutral momentum-transfer cross-sections (in `omega.f`) are the temperature limiting factor in the UMM numerical model—currently, for the 30 specified species, incident electron energy data exist up to 50 eV [151, 152], which converts to a flow temperature of approximately 8500 K. This temperature is approximately twice the maximum temperature seen in the MAPX accelerator (as future graphs will show), and should be sufficient for most future MHD modeling needs. However, should higher temperatures be required, one only needs to update the cross-section data in `omega.f` to include higher incident electron energies. Based on this maximum temperature of 8500 K, the enthalpy range defined in `thermhd.in` (and looped in `thermhd.f`) is from 7.0×10^5 J/kg to 3.5×10^7 J/kg.
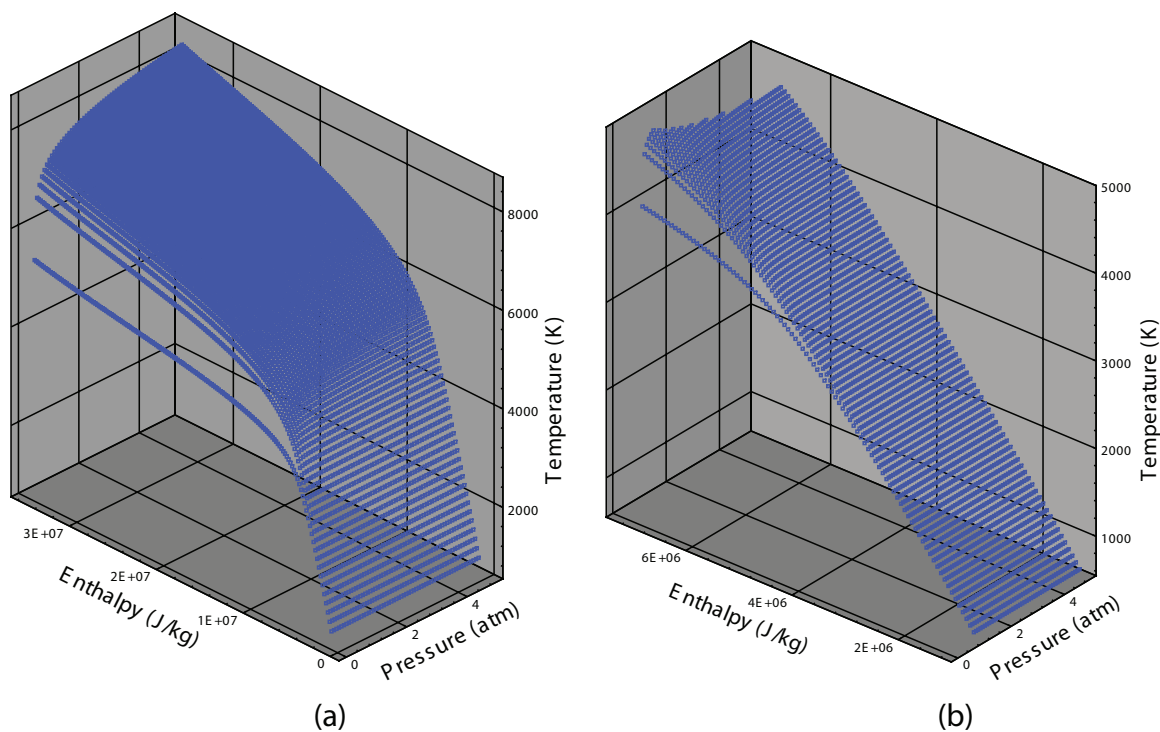
Figure 5.2: Temperature as a function of pressure and enthalpy, as calculated by the UMM thermoelectric codes: (a) over the entire regime of which the UMM code is currently capable and (b) over the regime of interest to the MAPX project.

As previously stated in Sections 3.2 and 4.2.1, the UMM thermoelectric model calculates six parameters as a function of pressure and enthalpy—one of these parameters is temperature. Figure 5.2 shows temperature as a function of both pressure and enthalpy—part (a) of the figure shows the temperature plotted for the entire enthalpy range over which the UMM code is currently valid, and part (b) shows the temperature range that is of interest to the MAPX project. Inside the MAPX regime, the temperature curves are essentially linear in both pressure and enthalpy, which is what one would expect from the ideal gas assumptions of the NASA CEA code [106].

For the following graphs, the more familiar "temperature-pressure" plots will be employed when displaying the other thermoelectric properties (even though tem-
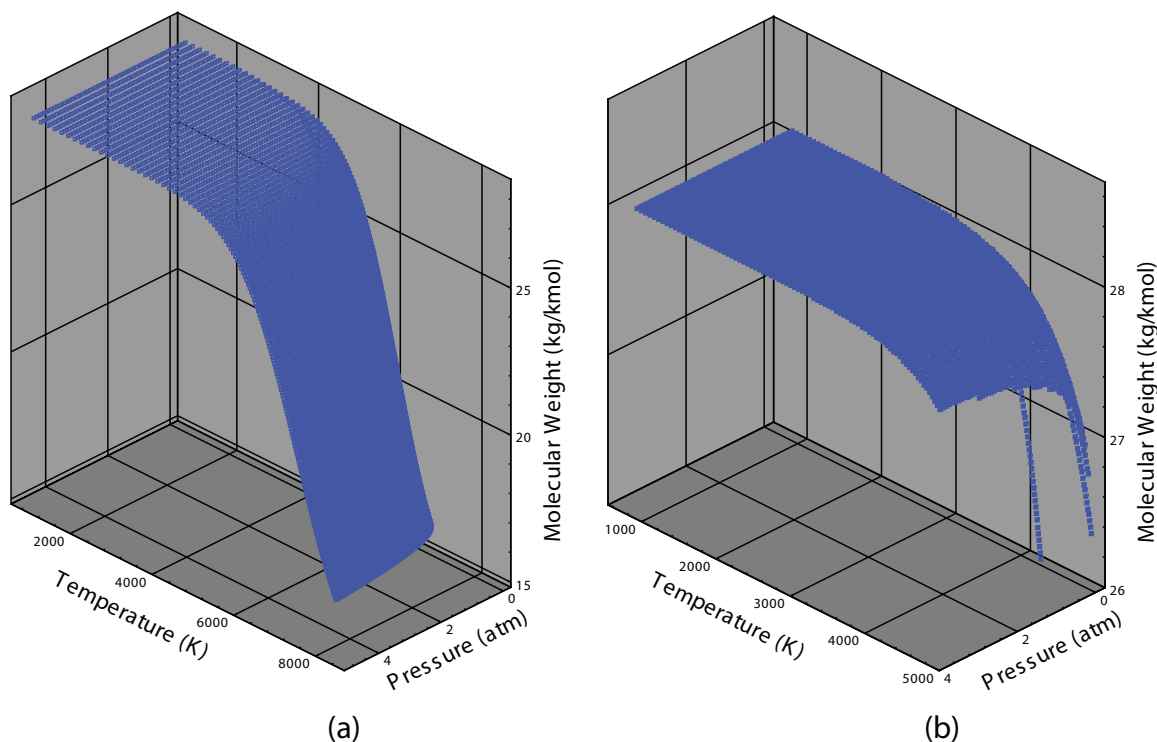
Figure 5.3: Molecular weight as a function of temperature and pressure, as calculated by the UMM thermoelectric codes: (a) over the entire regime of which the UMM code is currently capable and (b) over the regime of interest to the MAPX project.

perature is a calculated value). Section 4.2.1 and Gordon and McBride [106] describes how the UMM and NASA CEA codes calculate molecular weight. Figure 5.3 shows molecular weight of the MAPX gas mixture (N_2 with 1% NaK by weight) as a function of temperature and pressure, over the entire UMM modeling regime and over the MAPX regime. As is evident from the graph, the molecular weight remains fairly constant throughout the MAPX regime. There is a slight decrease in molecular weight at the higher temperature range, but this drop of less than 1 kg/kmol will be insignificant when the gas constant is calculated from molecular weight, as in Equation 4.58.
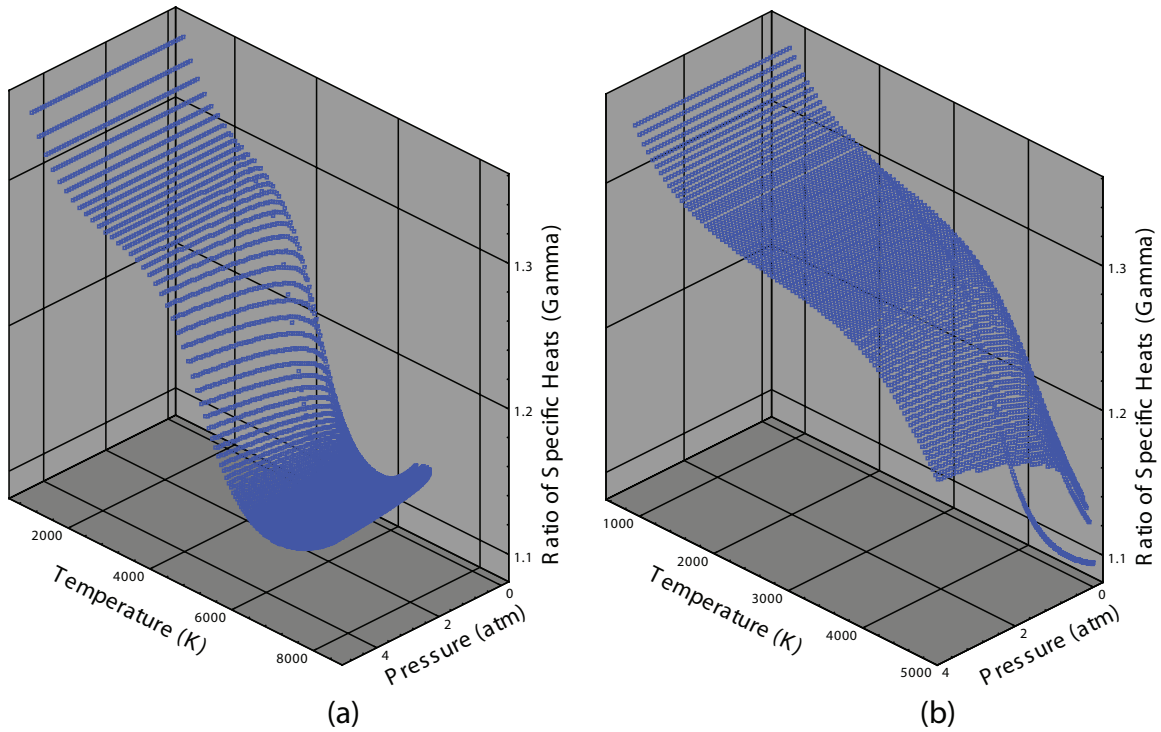
Figure 5.4: Ratio of specific heats as a function of temperature and pressure, as calculated by the UMM thermoelectric codes: (a) over the entire regime of which the UMM code is currently capable and (b) over the regime of interest to the MAPX project.

Figure 5.4 shows the ratio of specific heats (γ, often simply called "gamma") as a function of temperature and pressure, which reveals that gamma has a much greater dependence on temperature than it does pressure. While the variation in gamma over the MAPX regime appears to be large, the change in the values of gamma is actually quite small. Though, as Equation 4.61 shows (since the ratio of specific heats is used in the exponent), a small change in gamma could result in a very large change in the calculation of total pressure. However, a close inspection of part (b) in Figure 5.4 shows that there is little variation in gamma from $2000 - 3000\,\mathrm{K}$, the temperature
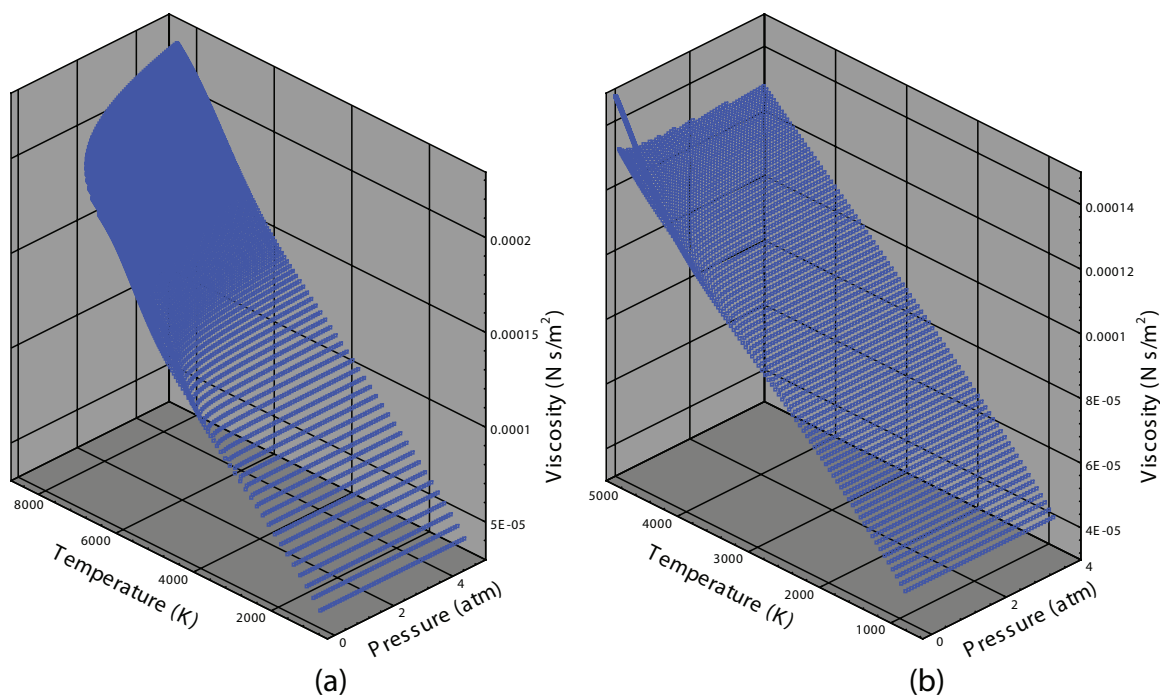
Figure 5.5: Laminar viscosity as a function of temperature and pressure, as calculated by the UMM thermoelectric codes: (a) over the entire regime of which the UMM code is currently capable and (b) over the regime of interest to the MAPX project.

range within which most of the MAPX flow field falls (please see Figure 5.13 for the MAPX temperature as a function of axial distance).

Figure 5.5 illustrates the laminar viscosity as a function of temperature and pressure. As the plots show, laminar viscosity appears to be linear—in both temperature and pressure—over the MAPX regime of interest. Also note that (as described in Sections 4.2.1 and 4.3.2) the laminar viscosity is calculated using the UMM numerical model (with a more detailed description in Gordon and McBride [106]), instead of using the second order polynomial function shown in Equation 3.73. Using the UMM codes to calculate the laminar viscosity is more accurate than using Equation 3.73, especially in regimes where the data is not so easily approximated.
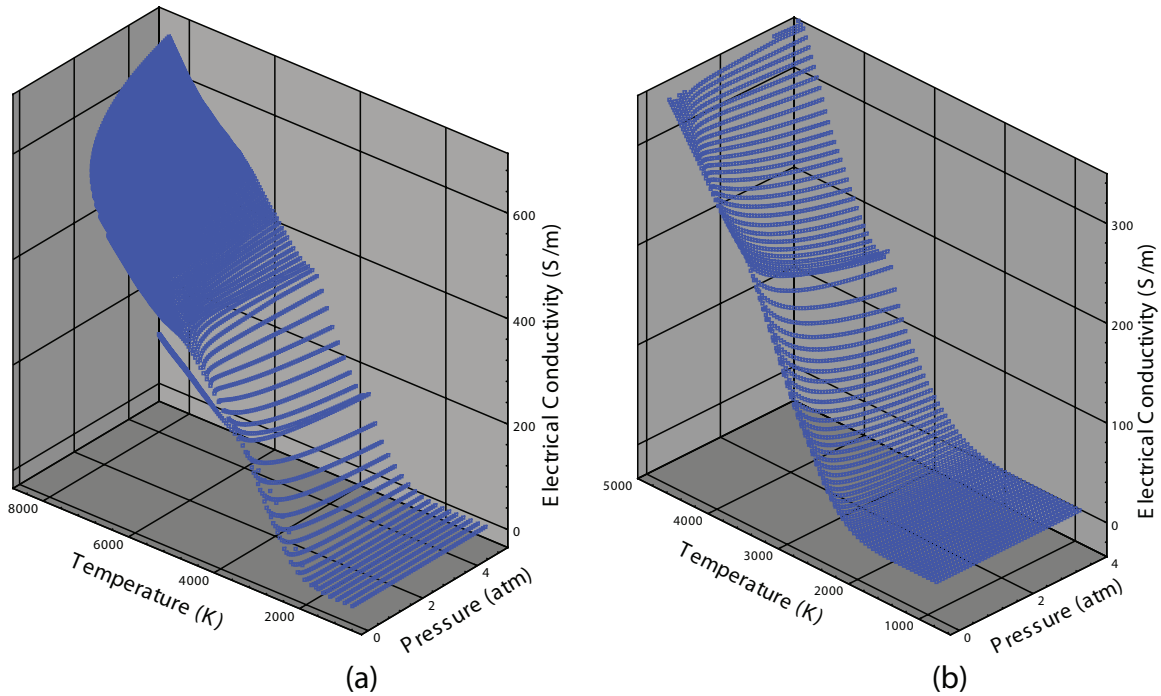
Figure 5.6: Electrical conductivity as a function of temperature and pressure, as calculated by the UMM thermoelectric codes: (a) over the entire regime of which the UMM code is currently capable and (b) over the regime of interest to the MAPX project.

The electrical conductivity of the flow regime as a function of temperature and pressure is shown in Figure 5.6. The UMM numerical model calculates electrical conductivity is as described in Section 4.2.2, using momentum-transfer collision cross-sections and a numerical integration method developed by Devoto [153]. As expected, the electrical conductivity increases greatly with increasing temperature; and for a given temperature, decreases with increasing pressure. This is logical because the increased temperature excites more electrons, while increasing pressure impedes the electron motion. Furthermore, is it important to note that electrical conductivity is virtually nonexistent until the flow reaches 2000 K (which should not be an issue for the MAPX flow, as the inlet temperature is 2700 K).
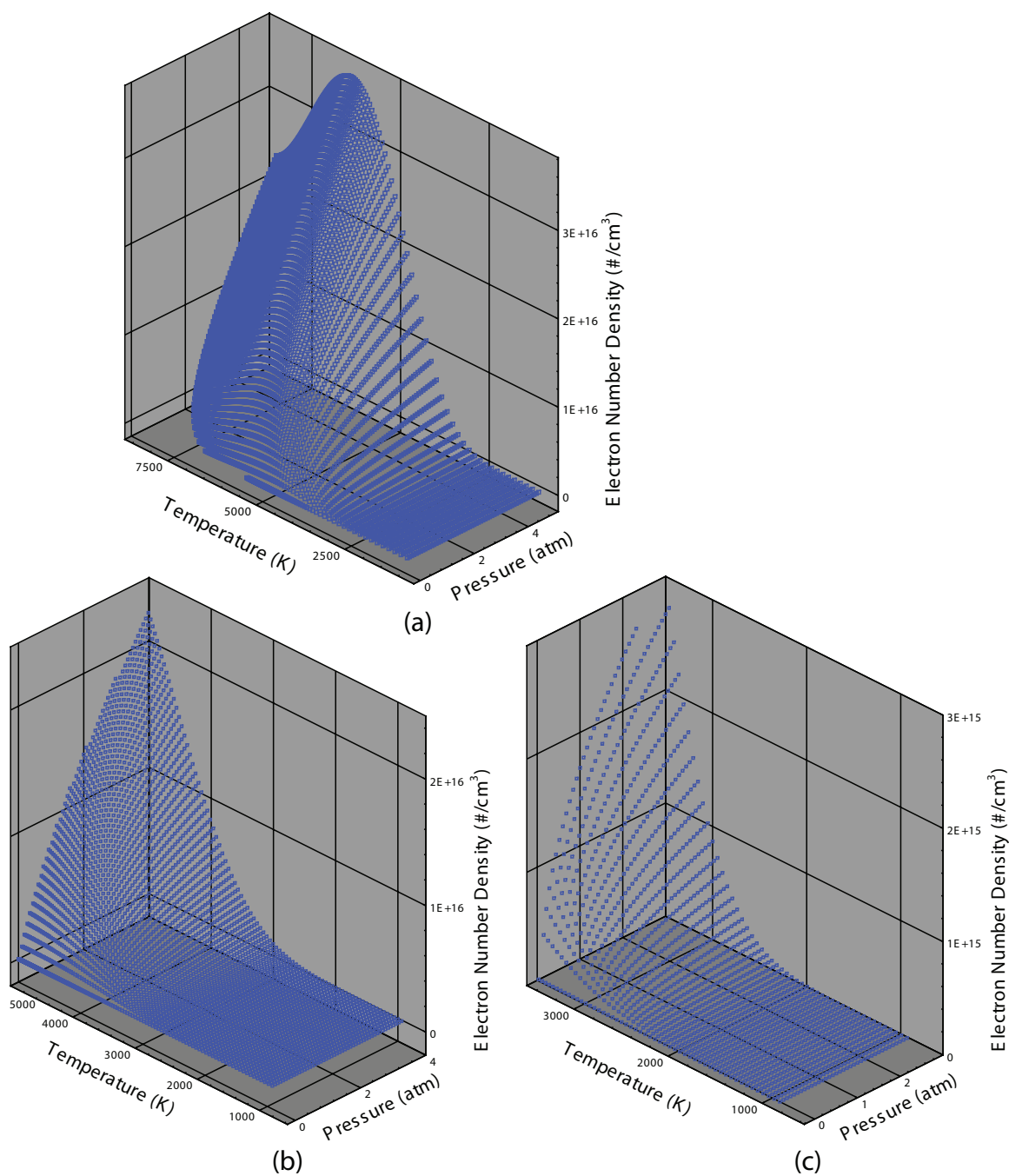
Figure 5.7: Electron number density as a function of temperature and pressure, as calculated by the UMM thermoelectric codes: (a) over the entire regime of which the UMM code is currently capable, (b) over the regime of interest to the MAPX project, and (c) a close-up of the temperature regime seen by most of the MAPX flow-field.

Figure 5.7 shows the electron number density as a function of temperature and pressure. As described in Section 4.2.1, the electron number density is calculated by the UMM numerical model from the total number of moles in the gas mixture and the concentrations of each individual species, as in the NASA CEA code [106]. As Figure 5.7 shows, there is great variation of the electron number density within the MAPX regime—with the increasing number density showing a greater dependence on increasing pressure than on increasing temperature. This is logical because the number density is only a measure of particles per unit volume—increasing the pressure effectively adds more particles to the system. Furthermore, just as in Figure 5.6, the electron number density is virtually zero until approximately 2000 K (which is also logical—without free electrons there would be no electrical conductivity).

Another useful electrical transport property is electron mobility, μ_e, which is used to describe the relation between the electron drift velocity, v_d, and the applied electric field:

$$\mu_e = \frac{v_d}{E}.$$ (5.1)

When a single charge carrier is dominant, the electrical conductivity of the gas is directly proportional to the mobility of that charge carrier—in this case, electrons are the charge carrier, and the electron mobility can be calculated with the following relations:

$$\mu_e = \frac{e}{m_e}\tau = \frac{\sigma}{eN_e} = \frac{\beta}{B}.$$ (5.2)

The electron mobility for the MAPX gas mixture is plotted as a function of temperature and pressure in Figure 5.8. Electron mobility increases as pressure decreases
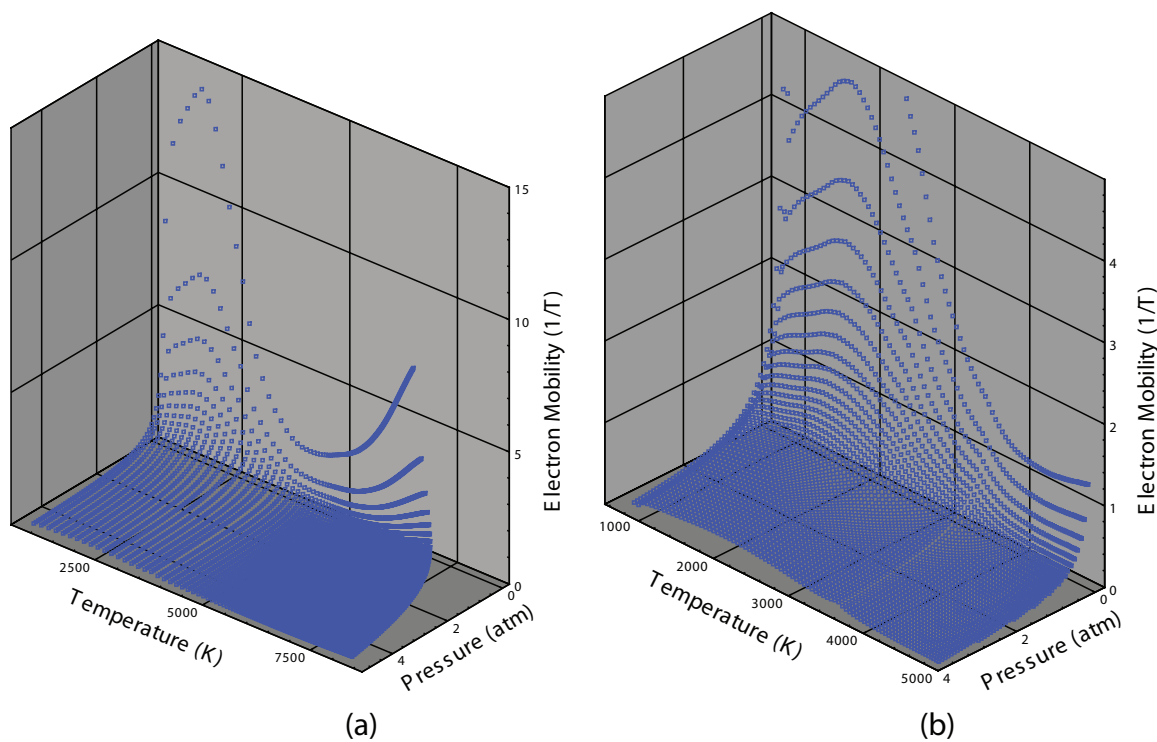
Figure 5.8: Electron mobility as a function of temperature and pressure, as calculated by the UMM thermoelectric codes: (a) over the entire regime of which the UMM code is currently capable and (b) over the regime of interest to the MAPX project.

and decreases as temperature increases (after an initial rise in mobility beginning at 500 K). This stands to reason—from Equation 5.2 and Figures 5.6 and 5.7, electrical conductivity decreases as pressure increases and increases as temperature increases; however, electron number density (which is inversely proportional to electron mobility) drastically increases as temperature increases, and increases with increasing pressure. As the name would suggest, electron mobility is also directly proportional to the electron diffusion coefficient, related through electrical conductivity in Equations 5.2 and 4.4. Electron mobility in the UMM numerical model (plotted in Figure 5.8) is calculated using the equation $\mu_e = \sigma/eN_e$, which relates to the electron

diffusion coefficient through Equations 4.4 and 4.10, with the assumptions listed in Section 4.2.2.2.

5.2.3   MAPX Electromagnet Magnetic Field Distribution

The MAPX electromagnet is described in Section 2.2.2, with details in Table 2.3. All preliminary analysis of the MAPX facility/accelerator (described in Section 2.2.2) assumed a constant 2 Telsa magnetic field distribution over the entire MAPX accelerator channel. Since that time, Thompson Mechanical and Electrical Technologies recorded detailed measurements of the magnetic field strength inside the MAPX electromagnet [171]; these measurements were integrated into the UMM numerical model (specifically, into `mhd.in`). Figure 5.9 shows both the measured magnetic field data points (with blue circles) and the magnetic field approximation used in the UMM code (with a red line). Please note that the magnetic field data was approximated for the UMM code only for the powered region of the channel (as marked in the figure). The UMM code does not model the non-powered region of the MAPX accelerator, and therefore no magnetic field approximation was implemented. The powered region begins at the entrance of the MAPX channel, and ends 9 cm before the MAPX channel exit, as shown in Figure 5.1.

Figure 5.9 shows many interesting aspects of the magnetic field distribution that are not captured using the 2 T assumption from Table 2.3. First, one notes that the magnetic field never actually reaches 2 T—instead only reaching a maximum of 1.86 T. Second, there is heavy attenuation of the magnetic field in the downstream half of the MAPX channel. From the entrance to 70 cm, the magnetic field is fairly
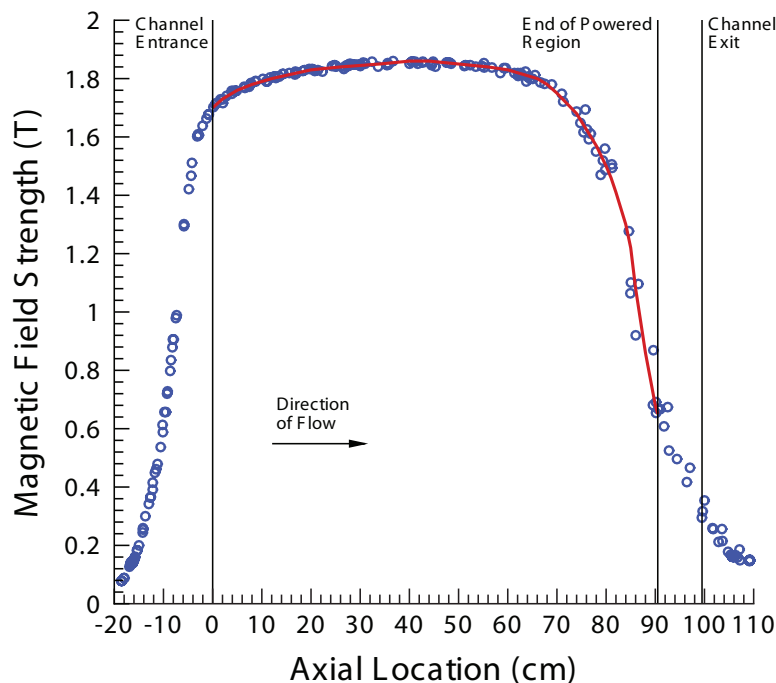
Figure 5.9: Magnetic field distribution of the MAPX electromagnet. The measured data points are represented by blue circles, while the magnetic field approximation used by the UMM code is represented by the red line. The channel entrance, flow direction, end of powered region, and channel exit are given in their respective positions on the graph.

stable—beginning at 1.70 T and ending at 1.75 T (at 70 cm), with a maximum at 42 cm of 1.86 T. However, after 70 cm, the magnetic field begins to fall rapidly, at an accelerating rate. At 80 cm, the magnetic field is 1.50 T; and at 90 cm, the magnetic field is 0.68 T.

This rapid decline of the magnetic field can be explained with Figure 5.10, where one sees that the poles in the downstream portion of the MAPX electromagnet have been widened with flares, effectively "spreading out" the magnetic flux, and thus decreasing the intensity of the magnetic field in the region where the MAPX channel resides. As one might expect, this rapid attenuation of the magnetic field will

(a) (b)

Figure 5.10: Close-up photographs of the MAPX electromagnet, showing the increasing surface area of the magnetic poles, which effectively lowers the intensity of the magnetic field in the downstream region of the MAPX channel. Part (a) is the view of the poles from the upstream end of the magnet, while (b) is the downstream view. The white lines/arrows show the poles divergence in each photo.

have an effect on MAPX accelerator performance—most notably, the Hall parameter (Equation 1.17), which is directly proportional to the magnetic field intensity. Furthermore, as discussed in Section 1.2.1, the $\mathbf{u} \times \mathbf{B}$ Lorentz force term attempts to create a field which opposes the externally applied field/voltage (which pushes the flow in the positive downstream direction). This opposing current should be lessened as the intensity of the magnetic field falls. However, the $J_y B$ "pushing" Lorentz force term also depends on the intensity of the magnetic field, and will therefore decline with the magnetic field. The interplay of the decreasing magnetic field intensity with the different components of the Lorentz force provides for interesting phenomena, and will be discussed in the following sections.

Finally, the lower magnetic field strength will help alleviate concerns of flow deceleration in the non-powered region of the MAPX accelerator. As described in Section 1.2.1, the $\mathbf{u} \times \mathbf{B}$ Lorentz force effectively decelerates the flow in an MHD channel. In the non-powered region, with no applied current to push the flow, a high speed flow and high magnetic field would result in an intense force opposing the direction of the flow. However, the 0.25 T magnetic field, in the 9 cm non-powered region of the MAPX channel, should have a minimal effect on the exit flow velocity of the MAPX accelerator.

5.3 Exploratory Analysis of Parameter Space

This section discusses some of the parametric studies used in determining the test configuration for the MAPX accelerator. The full parametric test matrix consists of 182 simulations: varying the applied current from 0.0 A to 300 A (at 25 A intervals) for the axial current neutralized mode (Section 4.3.4) and for every diagonalization angle (θ_d), from 90° to 150° at 5° intervals (which translates to accelerator electric field angles, θ, of 0.0° to 60° at 5° intervals—see Section 3.3.2). Showing results from all 182 numerical models is extraneous and unnecessary, so this section focuses on the more realistic and pertinent test cases, with interpretations of the underlying physical phenomenon.

In all of the graphs in this parametric analysis, some parameter, Y, is plotted on the ordinate as a function of axial distance (in cm, on the abscissa) of the MAPX channel. As stated, only the powered region is modeled by the UMM code, therefore the last axial distance in each graph is 90.5 cm. On many of the graphs, several

Table 5.2: Entrance input parameters presented exactly as they are for the UMM MHD numerical model.

Characteristic	Value
Flow Rate (kg/s)	0.130
Flow Temperature (K)	2700
Wall Temperature (K)	1000
Static Pressure (Pa)	3.24240×10^5
Velocity in $\hat{\mathbf{y}}$ (m/s)	0.0
Velocity in $\hat{\mathbf{z}}$ (m/s)	0.0
Wall Roughness (m)	0.0
Axial Pressure Gradient (Pa/m)	0.0
Electrode Pitch (m)	0.015
PTO Length (% of total length)	0.083
PTO Steps	5

different levels of applied current (from 0.0 to 300 A) are shown. (Note: the applied current is the user-defined input parameter `AJLIN`, located in `mhd.in`.) In these cases, the applied current level is labeled with a number (*e.g.*, 25, 100, 250) which represents that line's level of applied current in amperes (A). The case marked "Hydro" has no applied current or magnetic field, which differs from the "0.0" case which has no applied current (0.0 A), but does have a magnetic field as defined in Figure 5.9. Some texts refer to the "0.0" case as an "open circuit" case, because the magnetic field and electrodes exist, but no current is allowed to flow outside the channel. In many graphs, a cross-sectional averaged parameter, Y, is given—this parameter is averaged in both the x and y directions, across the entire cross-section at a given axial plane. The plots marked as "Center-Line" simply give the value of a parameter, Y, at the center-point of that cross-sectional plane, at that particular axial distance.

Table 5.3: Levels of applied current and their associated line color, used in exploratory parametric analysis.

Level of Applied Current (A)	Line Color
Hydro	Yellow
0.0	Purple
25.0	Red
50.0	Green
75.0	Cyan
100.0	Red
125.0	Blue
150.0	Yellow
175.0	Purple
200.0	Green
250.0	Blue
300.0	Cyan

The UMM magnetohydrodynamic input file (`mhd.in`) is given in Appendix D, with a summary of the important inlet parameters given in Table 5.2. As discussed, most of the input parameters remain constant throughout this MAPX analysis (*e.g.*, MAPX channel physical characteristics, thermodynamic characteristics, and flow characteristics at the channel entrance). The parameters listed in Table 5.2 are constant throughout the parametric analysis in the subsequent sections. Other "constants" used in the UMM MHD code are the magnetic field distribution (discussed in Section 5.2.3) and the diagonal angles used in the MAPX accelerator (discussed in Section 5.3.1). Sections 5.3.2 and 5.3.3 study the fluid dynamic and electromagnetic parameters, respectively, of the MAPX accelerator, for different levels of applied current. For each graph in these sections, the levels of applied current are represented by

a specific colored line, listed in Table 5.3. Because of the limited number of available colors, one specific color represents more than one level of applied current; however, care was taken to avoid confusion.

5.3.1   Diagonal Angle

To determine the ideal diagonal angle for the MAPX experiment, the axial current neutralized mode of the UMM numerical model was utilized. As discussed in Section 4.3.4, MHD accelerators typically operate more efficiently when the axial, J_x, current is at a minimum [172]. An increase in the J_x current can effectively reduce the J_y current (and, therefore, reduce the axial Lorentz force term, $J_y B$), induce secondary flow in the cross-section [126], cause asymmetries in the axial flow [173], and even cause flow separation [120]. Please note that the axial current neutralized mode is sometimes referred to as the "Hall Current Neutralized" mode of operation [72, 73, 120].

Figure 5.11 shows the diagonalization angle, θ_d, as a function of axial distance in the MAPX accelerator when the UMM numerical model is run in axial current neutralized mode, with an applied current of 100 A. For most of the accelerator channel, the diagonaliztion angle falls between 140 and 150 degrees (which gives an accelerator electric field angle, θ, range of 50 to 60 degrees). The erratic behavior of the angle at the entrance of the MAPX accelerator is due to "entrance phenomenon"— namely, the combination of a slower-moving bulk flow with the gradually increasing applied current inside the power takeoff (PTO) region. Notice that near the 7 cm mark, where the PTO is almost at full power, the angle distribution function becomes
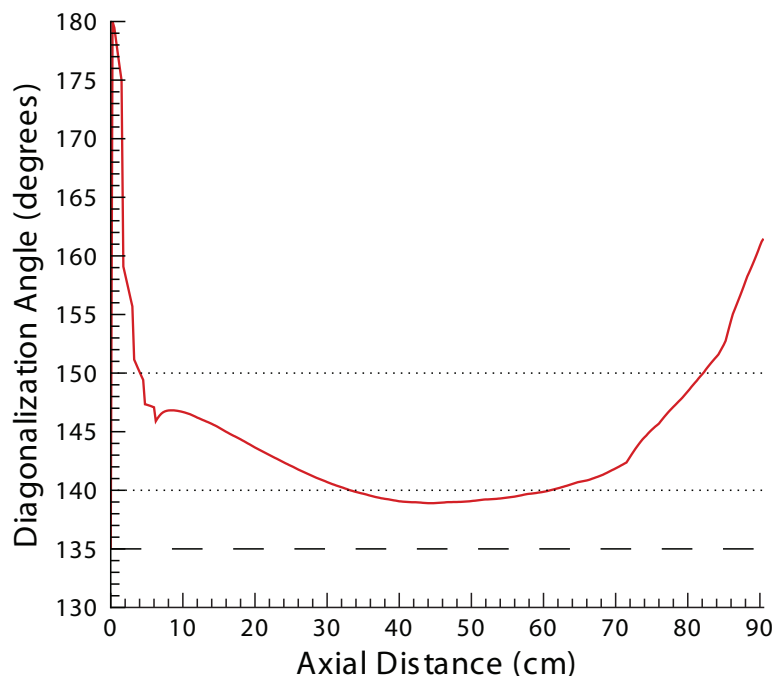
Figure 5.11: Diagaonalization angle, θ_d, as a function of axial downstream distance when the UMM numerical model operates in "axial current neutralized" mode, at 100 A applied current.

less erratic. Near the exit of the MAPX accelerator, the rise in the diagonalization angle is due to the attenuation in the magnetic field, as shown in Figure 5.9.

According to the axial current neutralized test (at 100 A), the optimum angle throughout the MAPX accelerator is $\theta = 55$ degrees. Unfortunately however, a 55 degree electric field angle is unreasonable for the MAPX channel—from a physical standpoint, the greatest achievable diagonalization angle is 135 degrees (or, $\theta = 45$ degrees) [166], which is shown with a dashed line in Figure 5.11. Therefore, because anything greater is not physically possible in the MAPX accelerator, a diagonalization angle of 135 degrees (electric field angle of $\theta = 45$ degrees) is chosen as the optimum angle for the MAPX accelerator and is used in all of the subsequent MAPX paramet-

ric studies. MHD generator studies have shown that power output from a diagonal generator is within 10% of the power output from an axial-current-neutralized generator [100], so the difference in angle should have a minor affect.

5.3.2 Fluid Dynamic Parameters

The primary fluid dynamic parameters included in this study are axial velocity, temperature, Mach number, static pressure, density, total pressure, and friction loss factors. Velocity and total pressure are obviously important parameters when designing an MHD accelerator—one would expect both velocity and total pressure to increase over the length of the MHD accelerator. Analysis of the Mach number allows one to understand the relationship between the axial velocity and the temperature of the flow, and the tradeoffs between the two. Temperature is also an important parameter in MHD channel analysis—runaway temperature increases can push the flow toward the sonic value, and high near-wall temperatures can result in reversal of the positive J_y current density flow (which effectively turns an MHD accelerator into a generator).

5.3.2.1 Axial Velocity

Figure 5.12 shows the axial velocity as a function of axial distance in the MAPX accelerator, at various levels of applied current—where part (a) shows the cross-sectional averaged velocity and part (b) shows the velocity at the center-line. On initial inspection, Figure 5.12 shows two important things—(1) for each case, the centerline velocity exceeds the cross-sectional averaged velocity (2) and the 125 A case
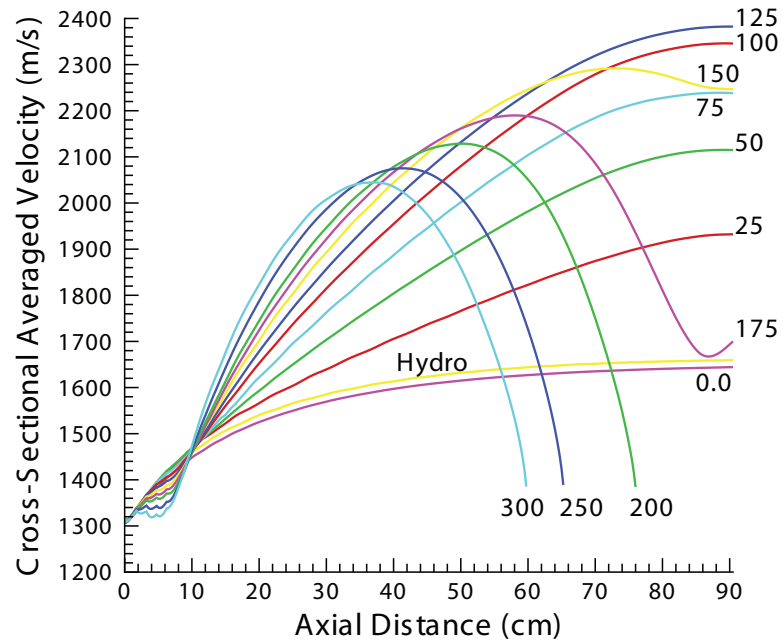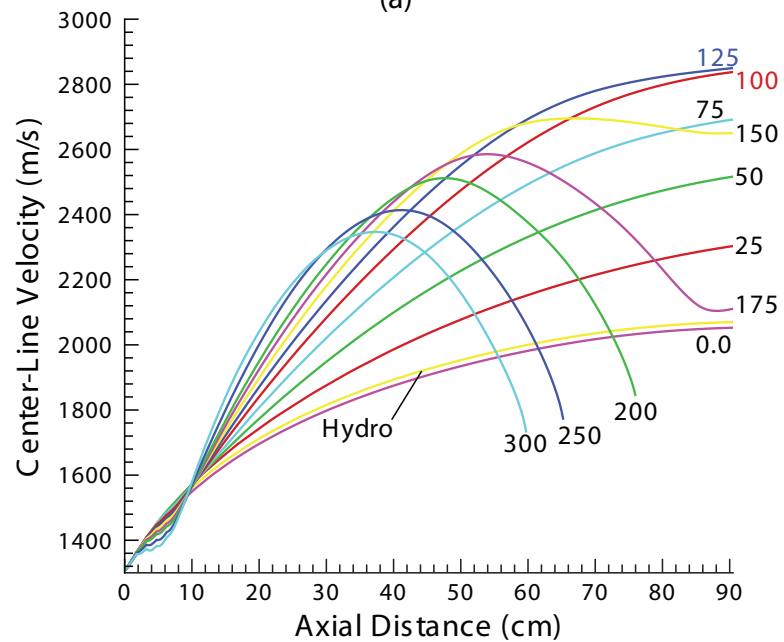
Figure 5.12: Axial velocity, u, as a function of axial distance for various applied levels of current: (a) The axial velocity averaged across the entire cross-sectional plane, and (b) the axial velocity at the center-line of the cross-sectional plane.

yields the highest exit velocity (both cross-sectional averaged and center-line cases). MHD flows typically exhibit "velocity overshoot" in the near-wall regions [14,20,109], which is why a higher center-line velocity is unique. Also important is the fact that for all the applied current levels above 125 A, the axial velocity declines at some point in the channel. The deceleration of the flow in the cases with a higher applied current is due to the excessive heat, as shown in Figure 5.13, pushing the flow toward a Mach 1 condition (*i.e.*, Rayleigh flow). Furthermore, for some cases (typically, the three highest applied current levels) numerical modeling stops before the flow reaches the exit of the MAPX channel because, at the point where modeling stopped, the UMM code detected some sort of flow reversal or a high opposing pressure gradient (which means that flow reversal is near). In short, based on Figure 5.12 alone, the 125 A case is the best choice.

5.3.2.2   Temperature

Figure 5.13 depicts the temperature of the flow as a function of the axial distance in the MAPX accelerator, for various levels of applied current. Part (a) shows the cross-sectional averaged temperature, while part (b) gives the temperature at the center-line of the channel. First, it is important to note that in parts (a) and (b), the temperature levels from the 200 to 300 A cases increase rapidly without any recovery. This implies that the majority of the applied current simply serves to enhance Joule heating of the flow. Furthermore, excessive heat along channel walls will increase electrode and sidewall erosion. Second, for each of the cases below the 200 A applied current level, the cross-sectional averaged temperature is greater than the
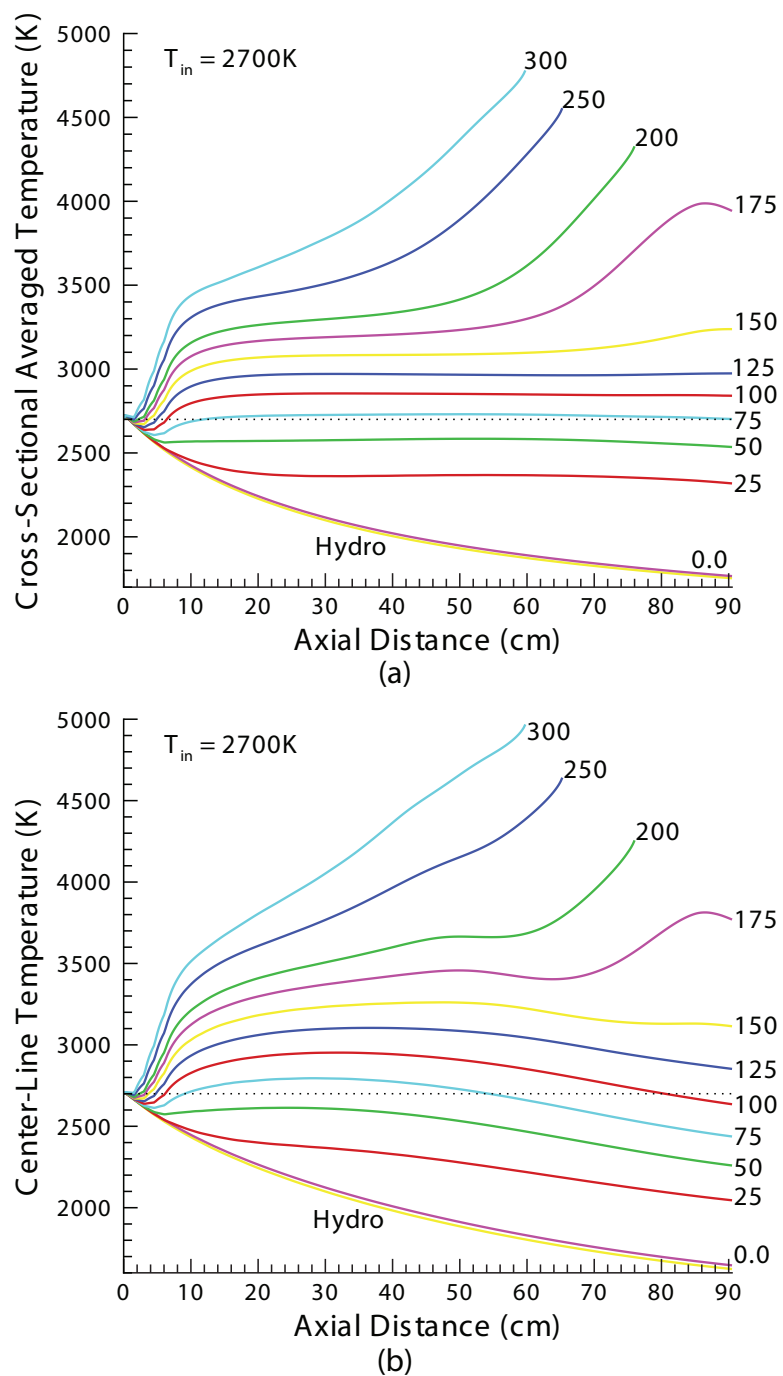
Figure 5.13: Temperature, T, as a function of axial distance for various applied levels of current: (a) The temperature averaged across an entire cross-sectional plane, and (b) the temperature at the center-line of the cross-sectional plane.

respective center-line temperature. This indicates that, as expected, the electrode and insulator sidewalls are much hotter than the core of the flow. Higher sidewall temperatures are consistent with previous MHD studies [174] and—from a purely hydrodynamic standpoint—lower velocities in the near-wall regions, as seen in Figure 5.12. Finally, it is important to note that for the two cases with the highest axial velocities, 100 A and 125 A, after an initial increase in the entrance PTO region, the cross-sectional averaged temperatures remain approximately constant throughout the channel, which indicates that excessive heating is not occurring within the channel. It is true though, that the decreasing center-line temperatures shown in part (b) of Figure 5.13, combined with the constant cross-sectional temperatures shown in part (a) indicate that the near-wall temperatures are increasing with increasing downstream distance. However, because the 150 A case shows an increasing cross-sectional averaged temperature as the flow progresses downstream, the 125 A case represents the highest level of applied current that maintains a constant cross-sectional averaged temperature.

5.3.2.3 Mach Number

Figure 5.14 shows the flow Mach number as a function of axial distance—part (a) gives the cross-sectional averaged Mach number while (b) gives the center-line values for Mach number. Recall that in the UMM numerical model, Mach number is calculated using Equation 4.60—basically, Mach number is proportional to the axial velocity and inversely proportional the square root of gamma, the gas constant, and temperature. In the UMM code, Mach number is calculated as a three-dimensional
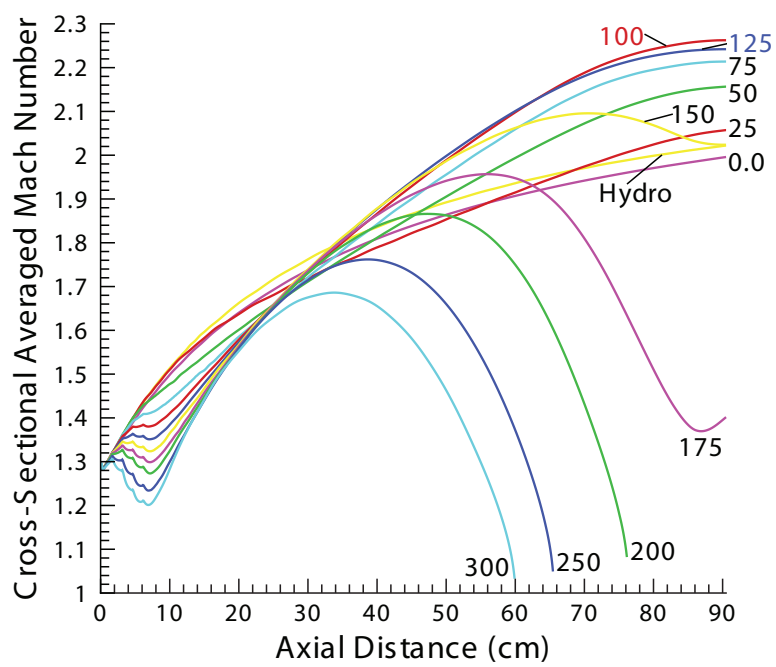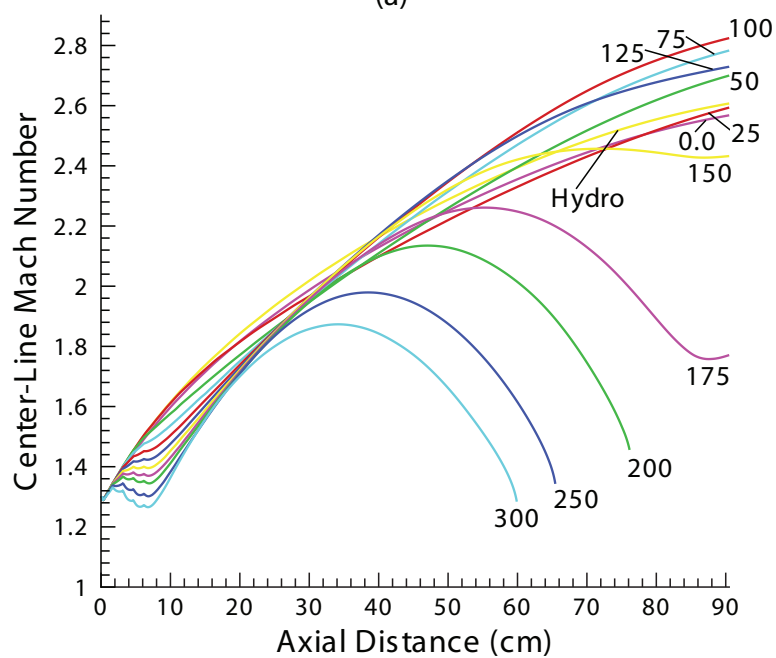
Figure 5.14: Mach number as a function of axial distance for various applied levels of current: (a) The Mach number averaged across an entire cross-sectional plane, and (b) the Mach number at the center-line of the cross-sectional plane.

variable (*i.e.*, at every single point in the cross-sectional plane). From this, the cross-sectional values are calculated, and the center-line values are extracted.

The Mach number plots in Figure 5.14 show the relative influence of temperature on the flow velocity, at the different levels of applied current. In the entrance PTO region, the Mach number for the 300 A applied current case drops drastically, while the cross-sectional averaged axial velocity for that applied current in that same entrance region declines only slightly. This sharp decline in Mach number shows the adverse effects of high temperature (*i.e.*, too much current) in the entrance region of an MHD accelerator, where the velocity is relatively low and static pressure relatively high. As has been mentioned, heat addition will drive a flow to a Mach 1 condition—which is known as Rayleigh flow [133]. On the downstream side, the heat addition from the higher levels of applied current irreparably slows the flows, driving them to a Mach 1 condition. The 250 and 300 A cases terminate calculation before the magnetic field attenuates (see Figure 5.9), while the 200 A case terminates calculation at approximately 76 cm, shortly after the magnetic field intensity begins to fall.

The Mach number for the 175 A current level case, however, does begin to turn around, just before the exit of the MAPX channel. That local minimum value in Figure 5.14 matches the local minimums in Figures 5.12 and 5.13—all occurring at approximately 86 cm downstream. From Figure 5.9, the value of the magnetic field at that point is approximately 1 T; furthermore, from Figure 5.12, the axial velocity for the 175 A case peaks at approximately 60 cm, and drops to approximately 75% of that peak value by 86 cm. Taking into account the dropping velocity and the declining magnetic field, the retarding $\mathbf{u} \times \mathbf{B}$ electric field becomes very weak, allowing the

pushing $\mathbf{J} \times \mathbf{B}$ Lorentz force to dominate. As discussed in Section 1.2.1, the $\mathbf{u} \times \mathbf{B}$ transverse deflection induces an electric field and current in the negative $\hat{\mathbf{y}}$ direction (*i.e.*, negative J_y direction), which opposes the positively applied electric field and J_y accelerating current. As the velocity and magnetic field decrease, this negative electric field also decreases, allowing for the positive electric field to dominate (which will be shown in the the following section). This, in turn, allows for the positive $J_y B$ Lorentz force term to regain influence over the flow, resulting in acceleration, as shown in the 175 A case, and to some extent, in the 150 A case.

Figure 5.14 also shows that the Mach number for the 100 A case is higher than the 125 A case, even though the 125 A case has a higher overall velocity. Furthermore, part (b) shows a large difference in center-line Mach number (which stems from a smaller difference in center-line velocity, as seen in Figure 5.12, and a larger difference in center-line temperature, as seen in Figure 5.13). The lower Mach number for the 125 A case indicates that most of the additional 25 A (above the 100 A applied current value) simply serves to increase Joule heating in the flow. This will be studied further in the following sections.

5.3.2.4   Static Pressure

Figure 5.15 shows the static pressure of the flow as a function of axial distance. Since the UMM code assumes that the static pressure is constant across the cross-section, only a single plot is required. The curves in Figure 5.15 are as one would expect for accelerating flow—the static pressure drops with increasing axial velocity. The "Hydro" (hydrodynamic) case results in the lowest static pressure (approximately
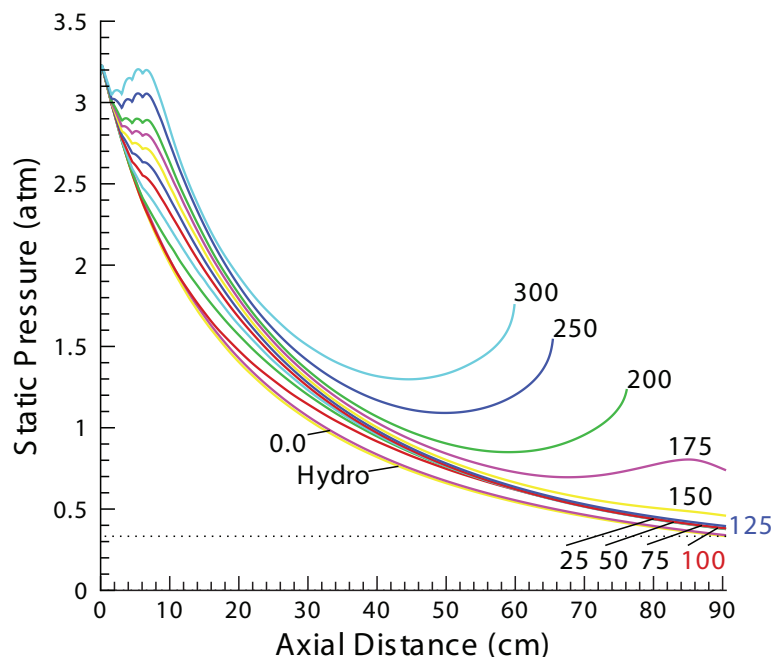
Figure 5.15: Static pressure as a function of axial distance. Recall that in the UMM code, static pressure is assumed constant across the cross-section.

0.33 atm), though it is virtually identical to the 0.0 A case. In both cases, no current was added to the flow; therefore, there was no heat addition. From the ideal gas law, temperature is directly proportional to static pressure; therefore, even though the velocities of the 25, 50, 75, 100, and 125 A cases are much higher than the no-applied-current cases, the heat addition (from the applied current) resulted in a slightly higher static pressure at the exit. Also as expected, the highest applied current levels resulted in the highest static pressures—those cases resulted in the lowest axial velocities and had the most heat addition. Furthermore, from Figure 5.16, cases with the highest levels of applied current have the lowest density levels at the entrance regions of the channel; however, as the static pressure increases, so does density.
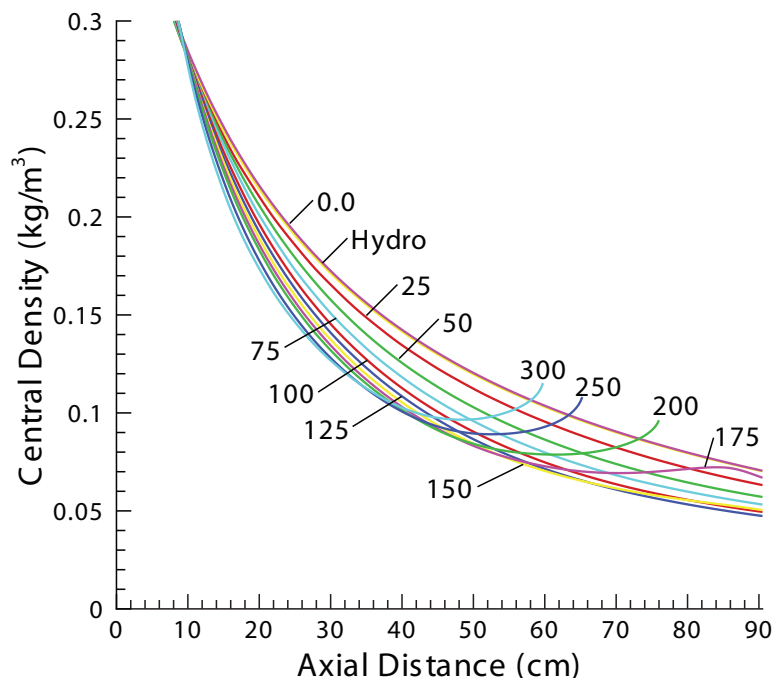
Figure 5.16: Central density as a function of axial distance.

Also interesting in Figure 5.15, is that the static pressure raises in the entrance PTO region, in the 300 A case. This phenomena is sometimes called "MHD compression" [73], and results from excessive current density at the entrance of an MHD channel—the current heats the slow moving fluid (Joule heating effect), lowering the velocity of the plasma even further (Rayleigh flow) while increasing the back-pressure (through the equation of state). This can sometimes result in flow reversal within the first few centimeters of the channel. Preventing such a situation is one of the reasons for implementing a power takeoff region, and as Figure 5.15 shows, it would require only a small amount of extra current at the entrance of the MAPX accelerator to excessively heat the flow as it enters the channel, thus causing flow reversal and termination of modeling calculations.

5.3.2.5 Total Pressure

Figure 5.17 shows the total pressures of the flows as functions of axial distance in the MAPX channel. Total pressure (sometimes referred to as "stagnation pressure") is calculated using Equation 4.61 in Section 4.3.7, as a function of static pressure, Mach number, and the ratio of specific heats. Even though static pressure is assumed constant across the entire cross-section, total pressure is calculated at every point in the cross-sectional plane (as are Mach number and the ratio of specific heats), and can therefore be plotted as a three-dimensional output. Three-dimensional plots are presented in Section 5.4, but the cross-sectional averages in Figure 5.17 are calculated directly from the three-dimensional data.

The results of the cross-sectional averaged total pressure, in part (a), are unexpected for an MHD accelerator, given the one-dimensional results from Figure 2.9. The center-line total pressure values, in part (b) of Figure 5.17, more closely resemble the one-dimensional graphs in Figure 2.9, however not at the same levels of applied current. (Recall that the single-dimensional plots in Section 2.2.2 are based on an applied current of 300 A. Furthermore, the one-dimensional numerical model uses air as a working fluid, and assumes a constant 2 T magnetic field.) Lower total pressures at the sidewall are indicative of frictional losses, while higher sidewall temperatures, as seen in Figure 5.13, also indicate entropy production.

Figure 5.17 does suggest that the MAPX accelerator experiences large losses at the walls. For the applied current levels between 50 A and 125 A, the center-line total pressure increases from the entrance to the exit of the channel. However, in all

Figure 5.17: Total pressure as a function of axial distance for various applied levels of current: (a) The total pressure averaged across an entire cross-sectional plane, and (b) the total pressure at the center-line of the cross-sectional plane.
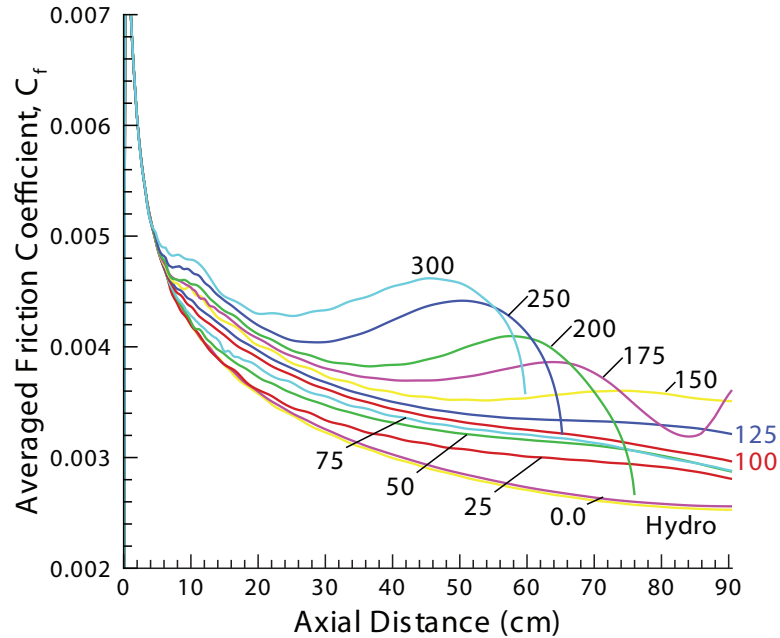
Figure 5.18: Averaged friction coefficient, C_f, for the MAPX channel as a function of axial location. Note that this friction coefficient is averaged over the electrode and insulator sidewalls.

cases, the cross-sectional averaged total pressure decreases from entrance to exit—this indicates that friction forces are dominating in the near-wall regions. Figure 5.18 shows the averaged friction coefficient as a function of axial location. The UMM code defines friction coefficient just as White [133]:

$$C_f = \frac{\tau_{wall}}{1/2\,\rho u^2},$$

$$(5.3)$$

where τ_{wall} is the shear stress, ρ is the gas density, and u is the axial velocity of the gas. Studies have also shown that, under constant velocity, the coefficient of friction in MHD channels decreases with increasing magnetic field and/or J_y current density [110]. The concept of "electromagnetic roughness" was formulated by Deme-

triades, which states that, because of current flow into and out-of the electrodes, the averaged coefficient of friction is substantially enhanced by the sidewall boundary layer [175]. Even in cases where smooth walls were assumed (which is the case for the MAPX accelerator, where the wall roughness height, `RHGT`, is assumed to be zero), the net result of the averaged skin friction distribution along the channel is substantially enhanced due to the insulating sidewalls [176]. Furthermore, studies of MHD generators have shown that the anode typically has the lowest skin friction [126] (because velocity of the flow in generators is typically higher near the cathode [140]), and is therefore most prone to flow separation [129].

The general form of Figure 5.18 is as expected—the curve is inversely proportional to the square of axial velocity. Consistent with the decreasing total pressure values seen in Figure 5.17, the values for coefficient of friction are higher than those seen in other MHD channels [110]. From Equation 5.3, with increasing velocity, from Figure 5.12, comes a decreasing friction coefficient. However, for the four highest applied current levels (300, 250, 200, and 175 A), the friction coefficient begins to rise, and then declines sharply. The rise is due to a decline in velocity at these upper levels of applied current, seen in Figure 5.12; while the decline is due to the increase in density, shown in Figure 5.16, and a drop in averaged shear stress, shown in Figure 5.19.

In the UMM code, the shear stress is calculated using the near-wall equation set described in Section 3.2.3. Total shear force, from Figure 5.20, is the sum of the product of shear stress and node length at each node location along the wetted surface area (electrode and insulator sidewalls) in the channel, and at each axial step
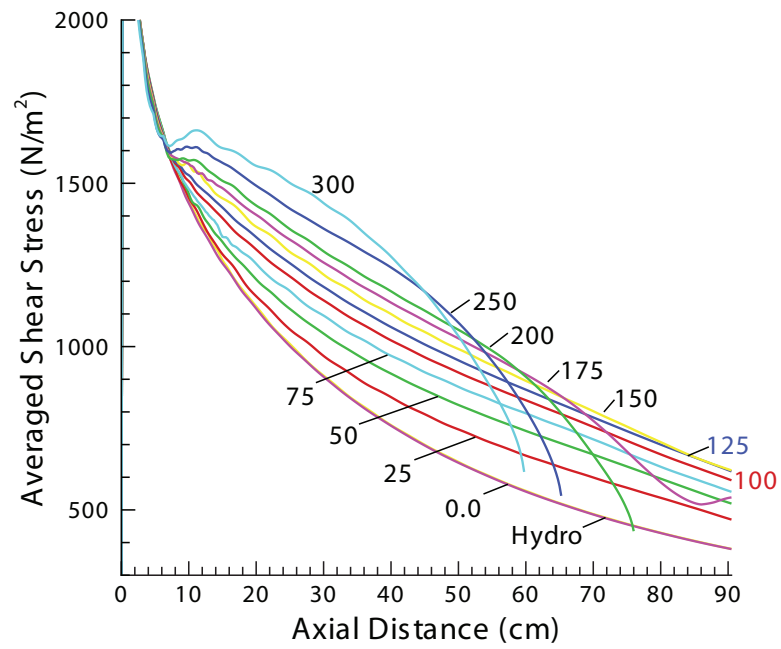
Figure 5.19: Averaged shear stress as a function of axial distance.
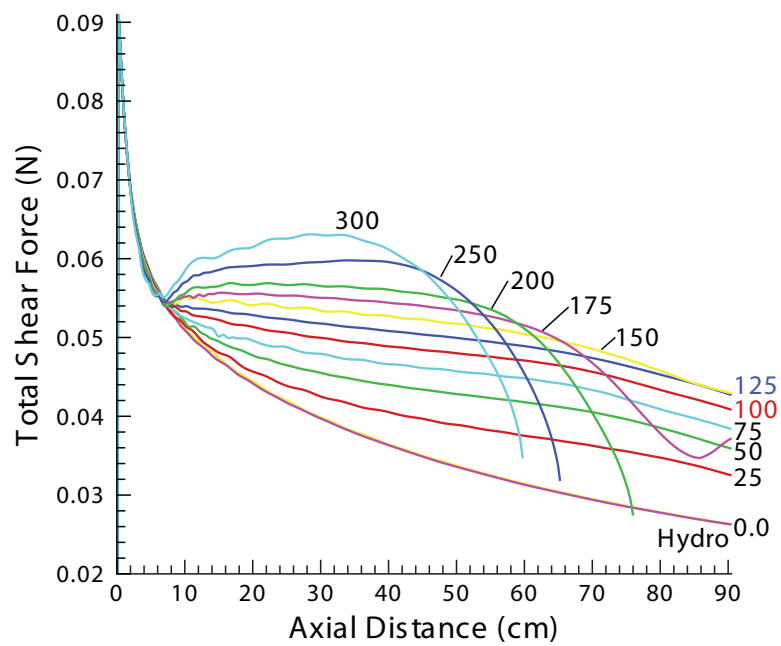
Figure 5.20: Total shear force as a function of axial distance.

location. For computational efficiency, in the UMM code, the averaged shear stress is calculated by dividing the total shear force by the total wetted surface area of that axial location. The general shapes of Figures 5.18, 5.19 and 5.20 are similar, with rapid declines for the highest levels of applied current because of increased static pressure and density.

From the fluid dynamic parameters presented in this section, it appears that the ideal applied current level for this 45 degree MHD accelerator case is either 125 A or 100 A. The 125 A applied current case resulted in the highest overall velocity, while the 100 A case yielded a higher Mach number and total pressure. Entropy production (*i.e.*, wall losses in the form of heat and friction) shows to be a severe detriment to the performance of this MHD accelerator. The surface to volume ratio of the MAPX accelerator seems to be too high—*i.e.*, the cross-section of the MAPX accelerator appears to be too small for its overall length (which is a design constraint resulting from the internal dimensions of the electromagnet).

Even more problematic is the fact that these losses do not remain in the near-wall regions of the flow—in the cases with the highest levels of applied current, it is obvious to see how the wall losses influence the entire flow. Furthermore, at approximately 60 cm downstream, the wall losses begin to impede the center-line values for the 125 A case. Figure 5.12, part (b), shows a definite change in slope of the center-line velocity at 60 cm, even with a decreasing center-line temperature, as shown in Figure 5.13. Until the 60 cm mark, the center-line Mach numbers for the 100 and 125 A current cases follow the same line, however after that point, the 125 A case takes a lower slope. This deviation in Mach numbers at 60 cm is accentuated

(and squared) in Figure 5.17, where the center-line total pressure for the 125 A case crosses the 100 A line as it begins the decline to its exit value. A subsequent drop in the 100 A center-line total pressure also occurs, but to a much lesser degree. The friction coefficient, C_f, shown in Figure 5.18, displays this same type of displacement between the 100 and 125 A cases at 60 cm. At the entrance of the channel, Joule heating (Figure 5.13) causes most of the flow losses—typically, these losses can be mitigated through the proper use of an entrance power takeoff. However, as the flow travels downstream, the frictional losses migrate from the near-wall regions to impede the core flow, which in the end, is detrimental to the entire cross-sectional area flow, as seen in Figures 5.14 and 5.17. Besides a redesign of the entire MHD channel, these frictional losses cannot be mollified.

5.3.3   Electromagnetic Parameters

The primary electromagnetic parameters included in this study are electrical conductivity, electron mobility, the Hall parameter, current densities (J_x and J_y), electric fields (E_x and E_y), power levels, efficiencies, and the dimensionless voltage drop. In an MHD accelerator, power levels and efficiencies are important for obvious reasons; however, these parameters are directly dependent on the current densities, Hall parameter, mobility, and electrical conductivity. Equation 3.33 shows that the electric field is the negative gradient of the electric potential. The dimensionless voltage drop incorporates all voltage losses associated with the electrode boundary layer [90], and is approximately linearly dependent on the transverse current density (J_y) [90, 108]. The transverse current density, J_y, is obviously a very important parameter in MHD

accelerators—the accelerating Lorentz force, J_yB, is directly dependent on J_y, which arises from the user-defined applied current.

5.3.3.1 Electrical Conductivity

Electrical conductivity as a function of axial distance is presented in Figure 5.21, with part (a) showing the cross-sectional averaged electrical conductivity, and part (b) showing the center-line values. The electrical conductivity distribution plots are very similar to the temperature plots in Figure 5.13, which is as expected from the temperature-pressure-electrical conductivity plots in Figure 5.6. While temperature is in the denominator in Equation 4.4 for electrical conductivity, electron number density is listed in the numerator. As shown in Figure 5.7, electron number density has a strong dependence on temperature—basically, as the temperature increases, more electrons are given the energy to break free from their atomic/molecular orbits. This increases electron number density, which increases electrical conductivity.

The conductivity distributions in Figure 5.21 show the same behavior as the temperature distributions. The strange behavior at the beginning of the channel is an entrance effect—where the steadily increasing current density inside the PTO region meets the relatively slow moving flow. For all but the two highest applied current levels, at the beginning of the channel, the center-line electrical conductivity is higher than the cross-sectional averaged conductivity. However, at distances farther downstream, the cross-sectional averaged electrical conductivity surpasses the value of the center-line conductivity—indicating that, just like temperature, the near-wall values of electrical conductivity are higher than the central values. Increased conductivity
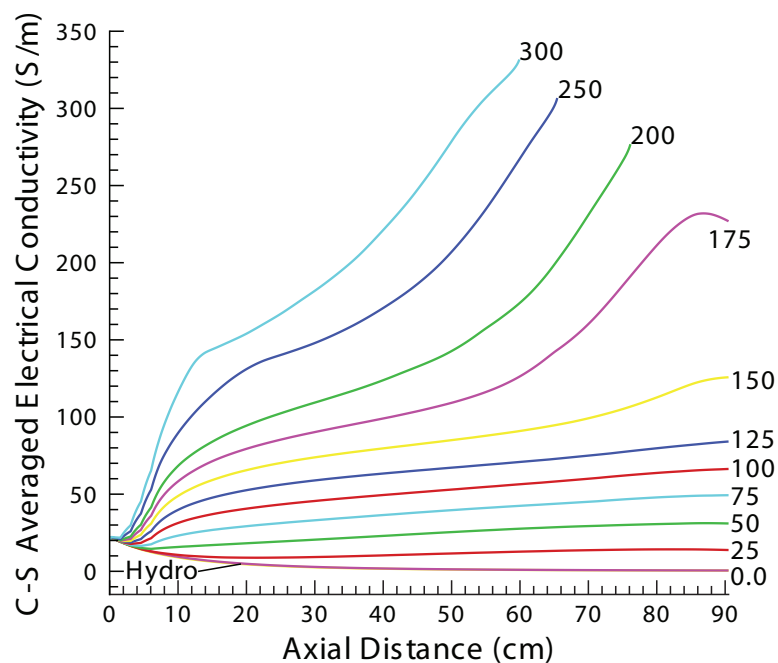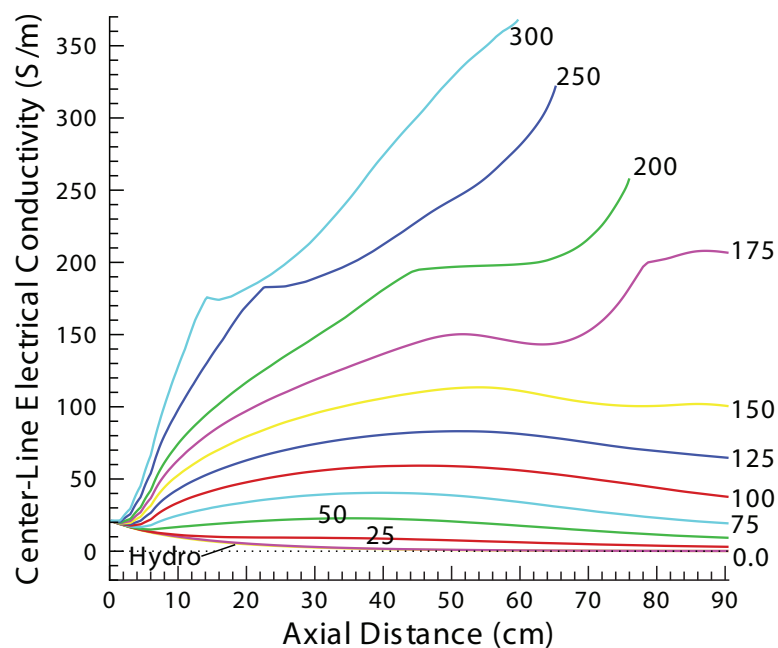
Figure 5.21: Electrical conductivity as a function of axial distance for various applied levels of current: (a) The electrical conductivity averaged across an entire cross-sectional plane, and (b) the electrical conductivity at the center-line of the cross-sectional plane.

in the side-wall regions also suggests an appropriate decline in electric field intensity in those same regions. Typically, increased sidewall conductivity translates to increased current density, and therefore, increased J_yB Lorentz force, which results in velocity overshoots at the sidewalls. However, it seems as though frictional forces are hampering this MHD effect.

The "dips" in the center-line conductivity curves for the 200 A and 150 A applied current cases at approximately 50 cm are also seen in the center-line curves for temperature, in Figure 5.13. Recall that the near-wall losses impinged on the 125 A flow at approximately 60 cm, so it stands to reason that for higher levels of applied current, this distance would be closer to the entrance of the channel. Figure 5.12 shows how the center-line and cross-sectional averaged velocities for the 175 A and 200 A cases begin to decrease at approximately 50 cm, which would explain the drop in conductivity, as the electrical conductivity is related to the colliding velocity of the gas through the diffusion coefficient, in Equation 4.11. After this saddle point at 50 cm, the electrical conductivity begins to increase again due to excessive heating of the flow, as seen in Figure 5.13; and, the final inflection point seen in the 175 A applied current case is due to the attenuation of the magnetic field, which, as already shown, has an effect on virtually all the other parameters as well.

5.3.3.2 Electron Mobility

Figure 5.22 shows the electron mobility of the gas as a function of axial distance for the cross-sectional area (a), and for the center-line values (b). Electron mobility was defined in Equations 5.1 and 5.2, where mobility is directly proportional to the
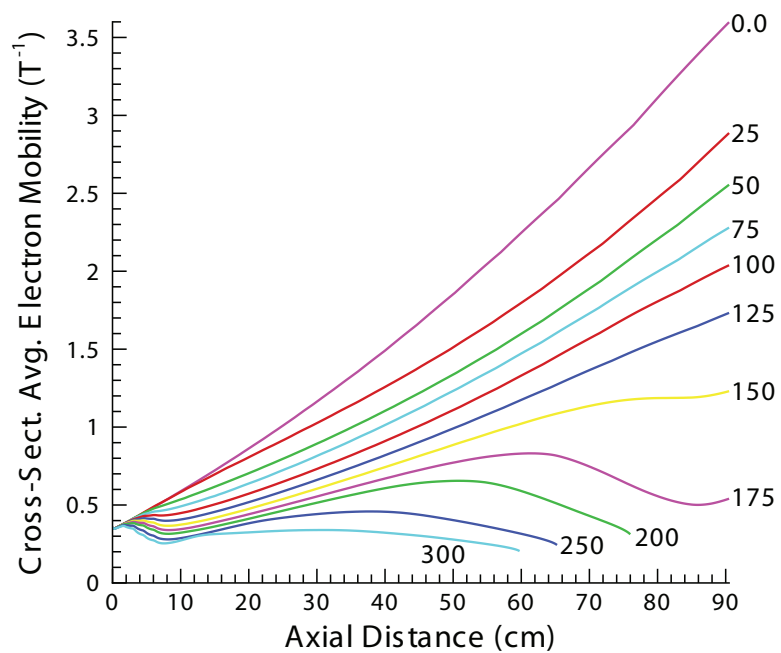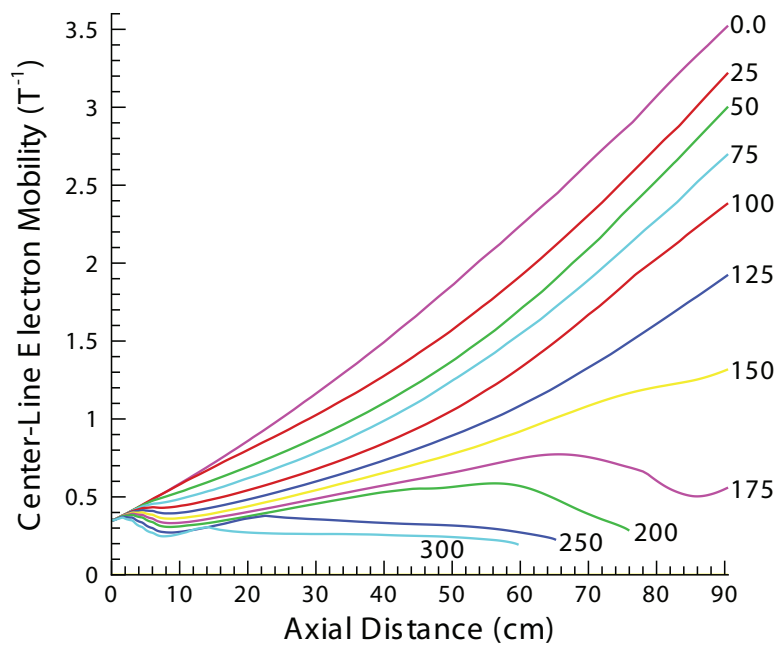
Figure 5.22: Electron mobility as a function of axial distance for various applied levels of current: (a) The electron mobility averaged across an entire cross-sectional plane, and (b) the electron mobility at the center-line of the cross-sectional plane.

drift velocity and inversely proportional to the electric field. Electron mobility is also directly proportional to the Hall parameter, and inversely proportional to the magnetic field strength (which is actually canceled out by the B in the equation for Hall parameter, shown in Equation 1.17). The dependence of mobility on the Hall parameter is the reason that the cases with the lower levels of applied current have a higher electron mobility—as shown in Equation 1.17, the Hall parameter is inversely proportional to the electron mean random thermal velocity, c_e (which is directly related to the level of applied current and temperature). As the mean random thermal velocity increases, the Hall parameter and electron mobility decrease.

Furthermore, Figure 5.22 shows that for the 0.0, 200, 250, and 300 A levels of applied current, the cross-sectional averaged electron mobility is greater than the center-line value, while for the $25 - 150$ A applied current levels, the cross-sectional averaged mobility is lower than the center-line value. This behavior is directly related to the temperature and conductivity of the flows—as previously stated, the conductivity is effectively inversely proportional to the electric field, and where, from Equation 5.1, the electron mobility is also inversely proportional to the electric field. Therefore, in the cases where the flows experience runaway heating (the highest levels of applied current), and where the central electrical conductivity is higher than the cross-sectional values, the central electron mobility will also be higher than the cross-sectional averaged values. The opposite is true for the cases where the center-line electron mobility is less than the cross-sectional value—with higher temperatures in the near-wall regions, and therefore higher conductivity, comes a higher electron mobility in those same regions.

5.3.3.3 Hall Parameter

Figure 5.23 shows the Hall parameter as a function of axial distance for (a) the averaged cross-section and (b) the center-line values, at various levels of applied current. Note, as there is no applied magnetic field, the "Hydro" case has a zero Hall parameter for both the cross-sectional averaged and center-line values (even though center-line is not shown). The relationship between the level of applied current and the intensity of the Hall parameter was explained in the previous paragraphs—as Equation 1.17 shows, the Hall parameter is inversely proportional to the electron mean random thermal velocity, which is directly proportional to the level of applied current and temperature. Note, however, that as the applied magnetic field declines (see Figure 5.9), so does the Hall parameter. This behavior was not seen in the electron mobility graphs, as the magnetic field variable in the Hall parameter calculation is canceled by the magnetic field variable is Equation 5.2. Otherwise, the same line trends that are seen in the electron mobility are seen in the Hall parameter—the higher levels of applied current have higher cross-sectional averaged values while the lower levels of applied current (excluding the 0.0 case) have higher center-line values.

5.3.3.4 Transverse, J_y, Current Density

The J_y current density for all levels of applied current is shown in Figure 5.24, with part (a) showing the cross-sectional averaged values for J_y, and part (b) showing the center-line J_y values. Upon inspection, at all current levels it is clear that little variation exists between the center-line and cross-sectional values, which indicates
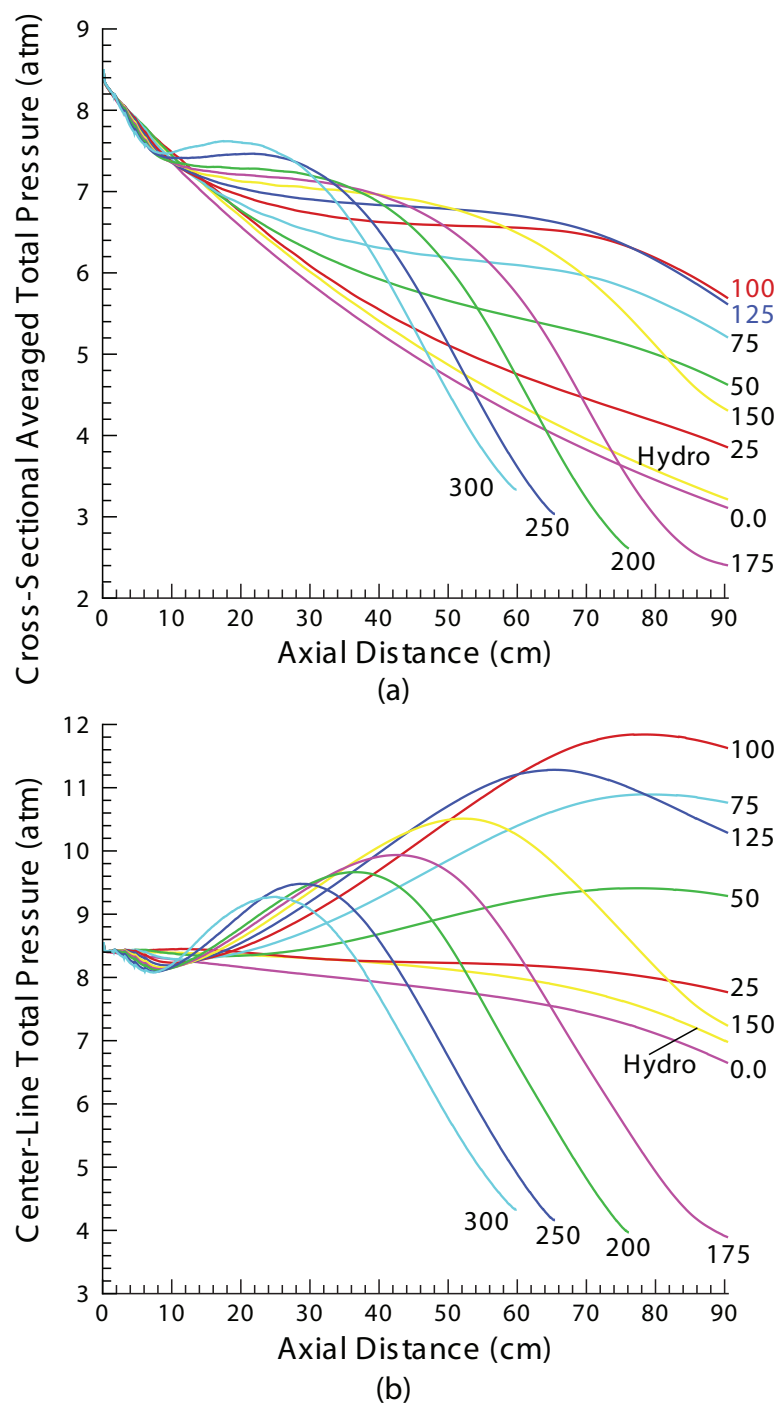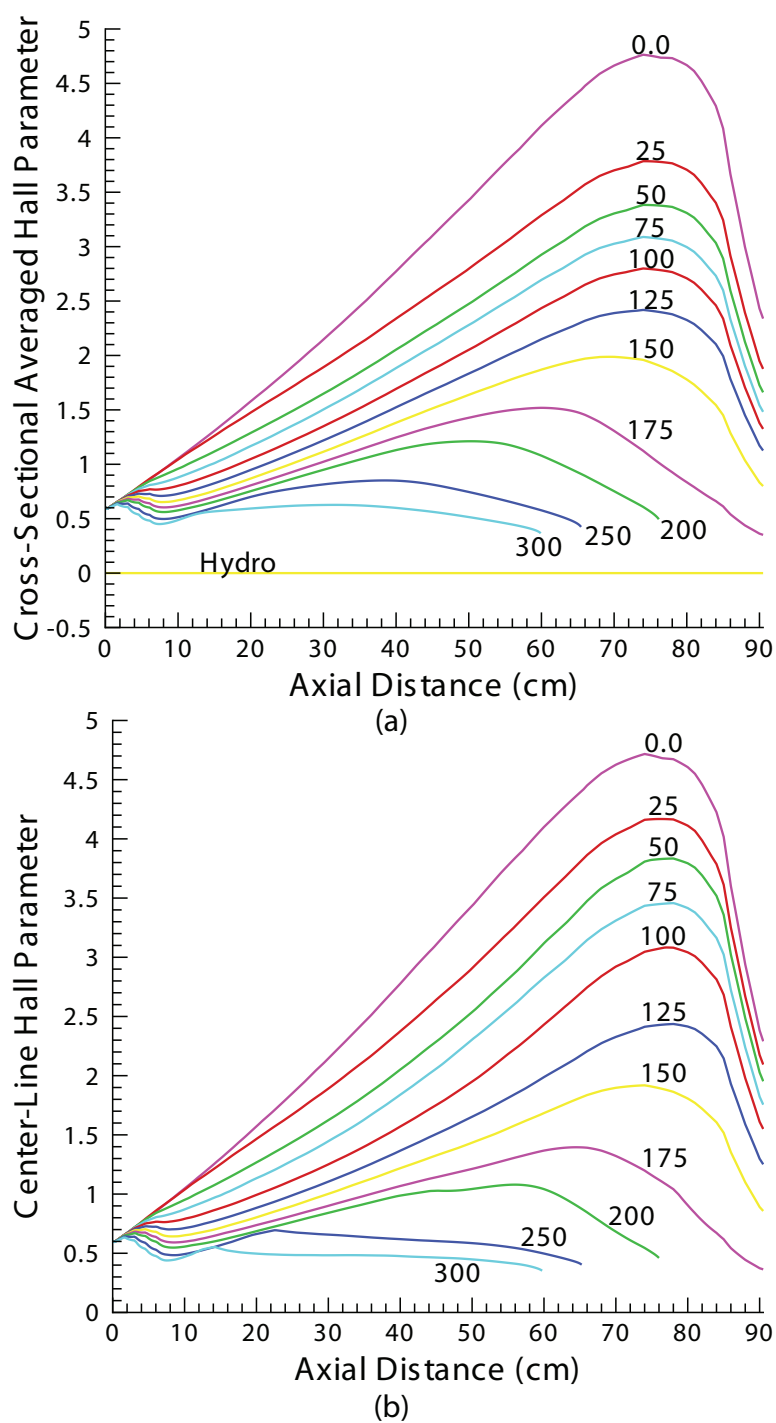
Figure 5.23: Hall parameter as a function of axial distance for various applied levels of current: (a) The Hall parameter averaged across an entire cross-sectional plane, and (b) the Hall parameter at the center-line of the cross-sectional plane.
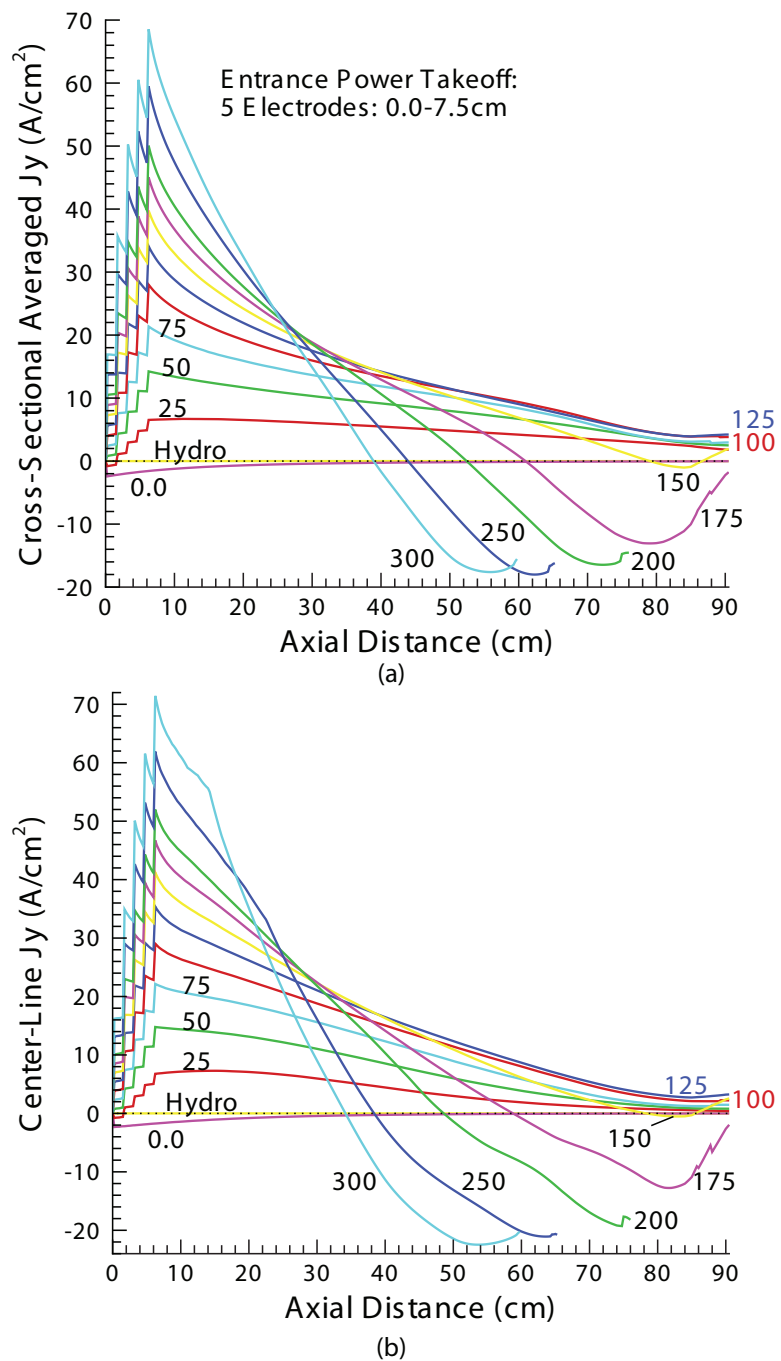
Figure 5.24: The J_y current density as a function of axial distance for various applied levels of current: (a) J_y averaged across an entire cross-sectional plane, and (b) J_y at the center-line of the cross-sectional plane.

that the J_y current is approximately uniform across the cross-section. In all cases, the center-line J_y current density is higher at the entrance (just after the PTO region) and lower near the channel exit than the corresponding cross-sectional value in the same regions—this indicates a slightly higher J_y current density at the center-line in the entrance region, and a slightly higher near-wall value for J_y in the exit region. This behavior is consistent with the higher temperatures and conductivities in the downstream near-wall regions shown in previous graphs.

Most notable, however, is the fact that J_y seems to be decreasing as the flow travels downstream. As stated in Section 1.2.1, J_y is a very important element in an MHD accelerator because it "powers" the $\mathbf{J} \times \mathbf{B}$ Lorentz force which accelerates the flow. As stated, the $\mathbf{u} \times \mathbf{B}$ transverse deflection induces an electric field in the channel, which (if the top and bottom electrodes were connected through an external load) would allow a current to flow in the negative $\hat{\mathbf{y}}$ direction (in the MAPX orientation), which would serve to decelerate the flow. In an MHD accelerator, an opposing external electric field is applied (via an external power supply) to the flow, which attempts to force a current to flow in the positive $\hat{\mathbf{y}}$ direction (in the MAPX orientation). This positive J_y current would serve to accelerate the flow. The "resulting" $\hat{\mathbf{y}}$ current (seen in Figure 5.24) arises from the net electric field, which is the difference between the induced electric field and the externally applied field [166]. Therefore, as the flow velocity increases (as seen in Figure 5.12), the $\mathbf{u} \times \mathbf{B}$ transverse deflection increases, which increases the induced electric field. If the applied electric field is constant—as it is with the MAPX accelerator—the resulting net electric field will tend to increase in the direction of the induced electric field (or, decrease in the direction of the externally

applied electric field). The net decrease in the direction of the applied electric field will result in a net decrease in current in that same direction—total current, however, is conserved. The E_y electric fields are shown in Figure 5.25. As seen in the graphs, the E_y electric field does decrease in magnitude in the positive $\hat{\mathbf{y}}$ direction, just as predicted by the behavior of the J_y current density. It is also important to realize that J_y is a measure of current density—not simply a measure of current value. Therefore, as the cross-sectional area of the channel increases, the current density will naturally decrease, while the velocity (of a supersonic flow) will naturally increase. However, based on the results presented in Figure 5.24, the 100 A and 125 A current cases maintain the highest levels of J_y current density through most of the MAPX channel, and are therefore the optimum levels of applied current.

Also noteworthy in Figure 5.24 are the cases with higher levels of applied current ($150 - 300$ A), where, at some point in the MAPX channel, the J_y current density becomes a negative value. Section 1.2.1 explains that a negative J_y current density dictates that the channel will operate in a generator mode, which would cause the flow velocity to decrease. Each of the decelerations for the higher levels of applied current in Figure 5.12 is preceded by a change in sign of the J_y current density in Figure 5.24. In two of the cases—150 A and 175 A—the current density changes direction near the end of the channel, tending to a more positive value. This results from a lowering of the induced electric field (to a level where it is once again overcome by the applied electric field), which results from a combination of the lowering axial velocity and the attenuating magnetic field, shown in Figure 5.9. The result of this current-change can be seen in Figure 5.12, where the velocity decelerations decrease,
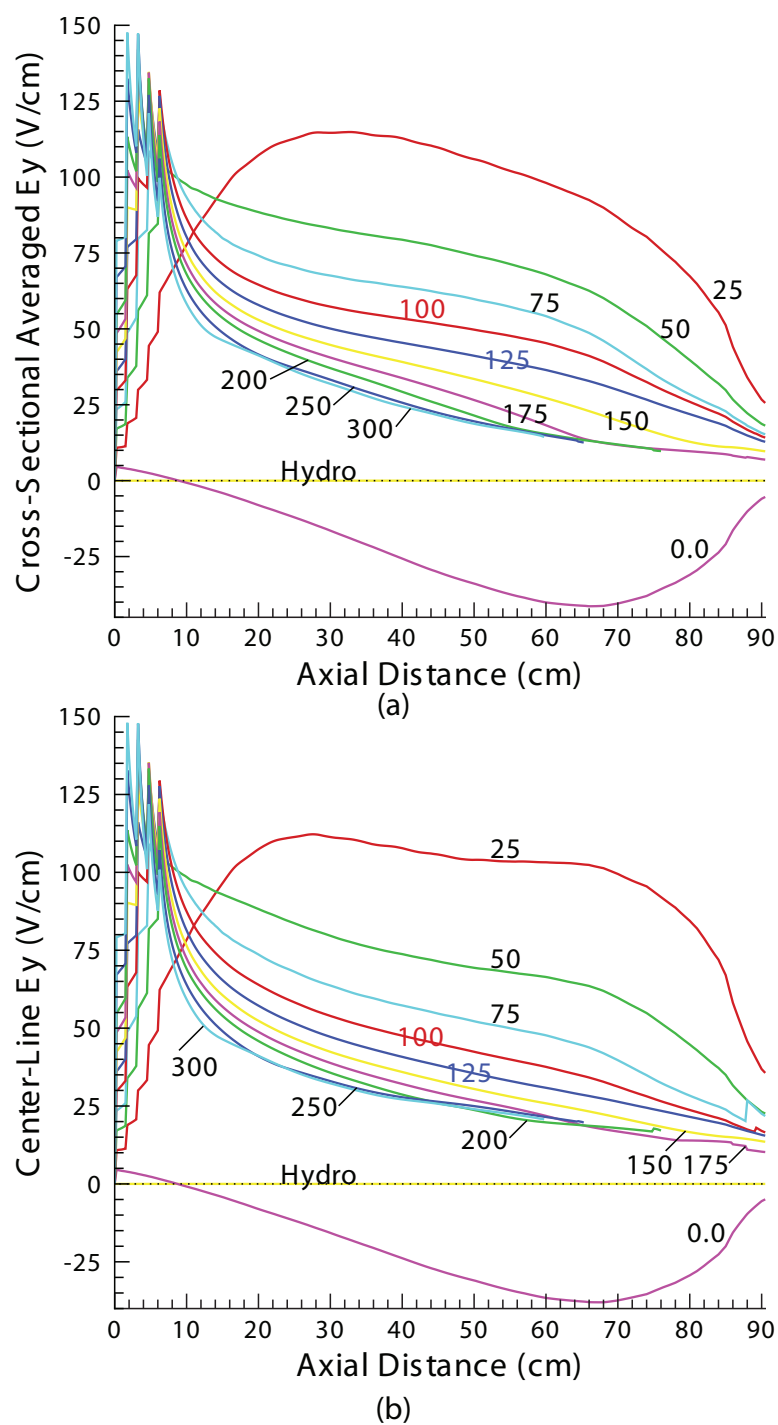
Figure 5.25: The E_y electric field as a function of axial distance for various applied levels of current: (a) E_y averaged across an entire cross-sectional plane, and (b) E_y at the center-line of the cross-sectional plane.

and even begin to accelerate. (However, as stated in the previous section, there are many factors, besides the J_y current, that can influence the velocity of the flow—*e.g.*, temperature, frictional losses, and channel divergence.)

It is important to realize, however, that the cases where the J_y current density becomes a negative value are not representative of the "real world." An actual MHD accelerator would have physical/electronic devices which would prevent current from flowing in the generator direction (*e.g.*, a diode). In a real MHD accelerator, current flowing in the generator direction, besides being detrimental to the intended goal of the accelerator, could result in damage to the external power supply. However, for this dissertation, the current densities are allowed to pass into the negative regime in order to study the overall effects and outcomes of the current density reversals.

5.3.3.5 Axial, J_x, Current Density

Figure 5.26 shows the axial current density, J_x, as a function of axial distance— part (a) showing the cross-sectional average J_x values, and part (b) giving the center-line values for J_x. The differences between the cross-sectional averaged and center-line axial current densities are great—the cross-sectional averaged current densities are all less than $0.05\,\mathrm{A/cm^2}$, while the center-line values for J_x are as high as $70\,\mathrm{A/cm^2}$. The large values of the center-line current densities coupled with the very small cross-sectional averaged values indicates that inside each cross-sectional plane, there are upstream and downstream axial currents of approximately the same magnitude.

Recall that the axial current neutralized mode described in Section 4.3.4 uses the cross-sectional averaged values of J_x to calculate the appropriate angle. The
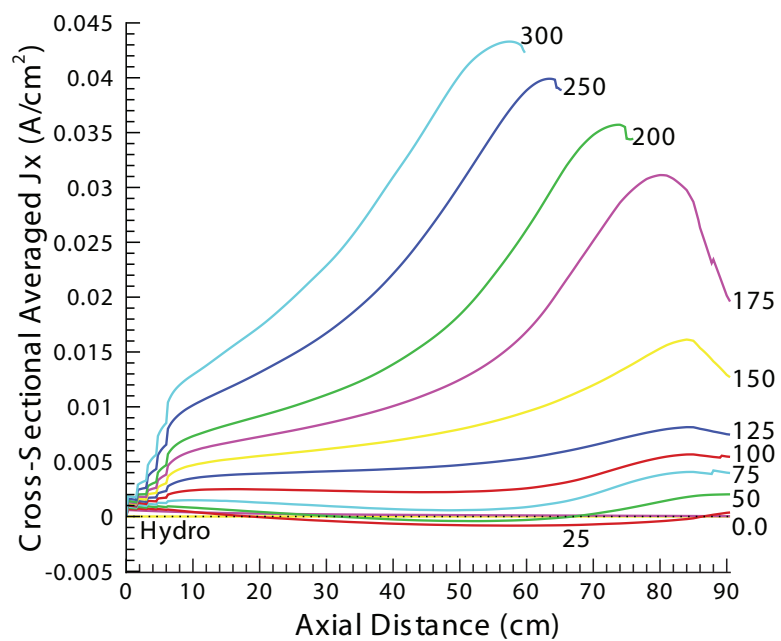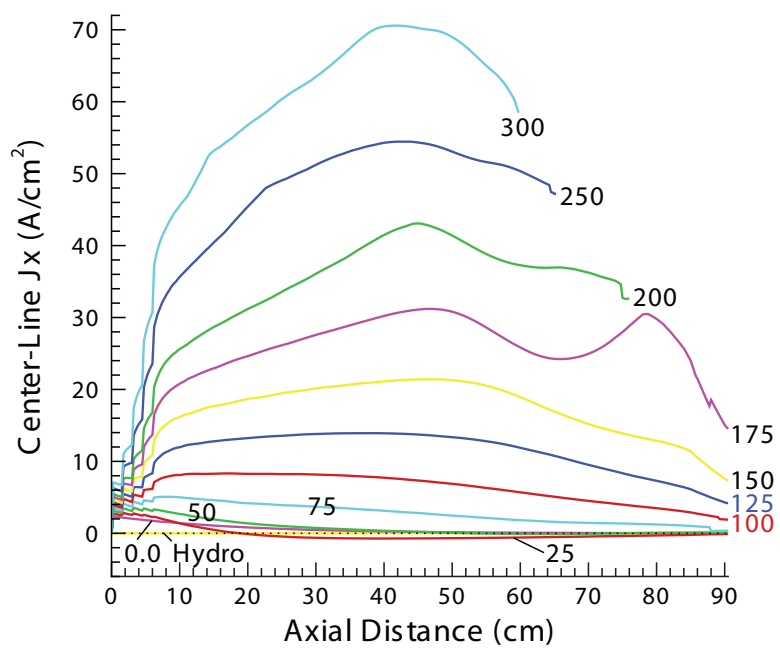
Figure 5.26: The axial current density (J_x) as a function of axial distance for the various levels of the user-defined applied current: (a) J_x averaged across an entire cross-sectional plane, and (b) J_x at the center-line of the cross-sectional plane.

diagonal angle is applied across the entire cross-section; therefore, it is appropriate for the algorithm to use the cross-sectional values of J_x. The non-zero values for cross-sectional averaged J_x in Figure 5.26 are a result of the physical limitations of the diagonal angle configuration—*i.e.*, because the recommended axial current neutralized angle of 55 degrees (see Figure 5.11) is not physically possible, a 45 degree angle is used; therefore, the cross-sectional averaged values for J_x are small and non-zero. The axial current neutralized mode does, however, allow for localized non-zero values of J_x—and as Figure 5.26 shows, the local values can be quite large. Furthermore, recall that in the MGMHD and UMM numerical models, the axial electric field, E_x (shown in Figure 5.27), is assumed to be a constant value across the cross-section [125] (see Section 3.3 for more details). Therefore, the cross-sectional averaged value for E_x is the only value for E_x, which means that the variations in the J_x current density must be explained through other avenues. Also, from the definition for electric field angle in Equation 1.46, it is no surprise that for a 45 degree accelerator angle, the axial electric field, E_x, shown in Figure 5.27, is exactly equal to the cross-sectional averaged E_y electric field, shown in Figure 5.25.

However, the significance of Figure 5.26 should not be missed. First, it shows the importance of a proper three-dimensional numerical model when analyzing MHD flows. While it is true that neither of the graphs in Figure 5.26 is three-dimensional, the center-line values of J_x were extracted from the center points of the three-dimensional data (which will be shown in the following section). The cross-sectional averaged values—which is how a typical one-dimensional numerical model calculates—completely misses the magnitude and variations of the local J_x values,
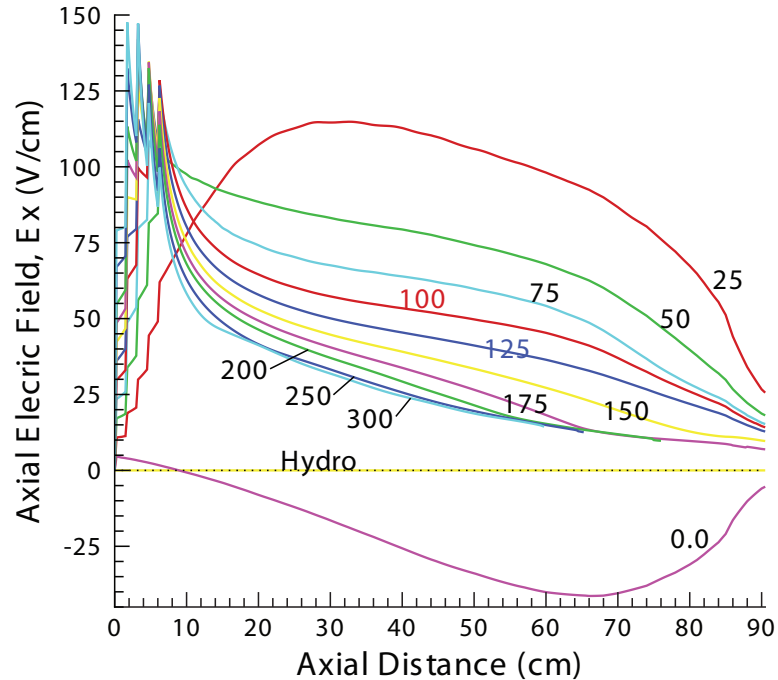
Figure 5.27: The axial electric field, E_x, as a function of axial distance. Recall that the UMM code assumes E_x is a constant over the entire cross-section.

which gives a very inaccurate representation of the axial current in the channel. Second, the large, but approximately equal, upstream and downstream axial currents indicate high Joule dissipation losses in the channel. In an MHD accelerator, the axial current is not beneficial—it only serves to heat [165] and cause asymmetries in the flow [93, 120, 172, 173]. Therefore, high axial currents—especially in the near-wall regions, which Figure 5.26 suggests—indicate that much of the applied current is not being used to accelerate the flow, but instead, to heat the flow. Lastly, the 100 A level of applied current appears to perform best in Figure 5.26. After the initial rise in center-line axial current in the entrance PTO region, the center-line values for J_x fall throughout the length of the channel. A rising cross-sectional averaged axial current at 70 cm does indicate increased near-wall axial current and heating, but the
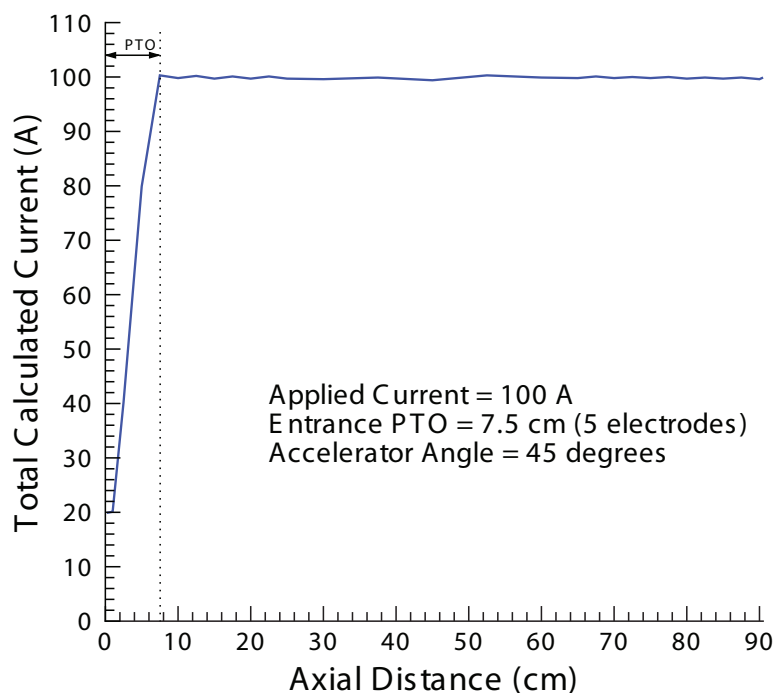
Figure 5.28: Proof of conservation of current in the UMM numerical model.

overall values are comparatively low, coupled with the high exit values for velocity and center-line total pressure.

5.3.3.6 Conservation of Current

It is important for a numerical model to conserve current throughout the MHD channel. This ensures that the code is free of current sources or sinks, which would give unrealistic results during a simulation. Current conservation is especially important for the MAPX accelerator, with the apparently decreasing J_y current density and the high opposing values of J_x. Figure 5.28 shows the total current in the MAPX channel, as calculated by the UMM code for the 100 A level of applied current. The total current is calculated from the three-dimensional current data, using the follow-

ing method. First, for every cell in the cross-sectional plane, the current densities are summed:

$$\mathbf{J}_{j,k} = J_{x_{j,k}} + J_{y_{j,k}} + J_{z_{j,k}}. \tag{5.4}$$

Then, the area of each cell, $A_{j,k} = dydz$, is multiplied by the total current density in that cell to determine the total current, $I_{j,k}$, in that cell:

$$I_{j,k} = \mathbf{J}_{j,k} A_{j,k}. \tag{5.5}$$

The sum of the $I_{j,k}$ values in each cross-sectional plane is I, the total current in that cross-sectional plane. As Figure 5.28 shows, current conservation inside the UMM numerical model does exist. Immediately after the entrance PTO region, the total current in the cross-sectional plane equals the total applied current, 100 A. Therefore, there are no current sources or sinks in the UMM code which would distort its results.

5.3.3.7 Total Power

Power levels (which are calculated as shown in Section 4.3.6) are also of great importance when designing an MHD accelerator. Figure 5.29 shows the total cumulative power that the MHD accelerator (at various levels of applied current) delivers to flow. Note that, as they have no applied current, the Hydro and 0.0 A cases show no power delivered by the MHD channel. Also note that, for the cases that did not terminate prematurely, there is a diminishing rate of return for increasing levels of applied current. For example, from 75 A to 100 A, the difference in total cumulative power is approximately 68 kW; while, from 100 A to 125 A, the difference in total
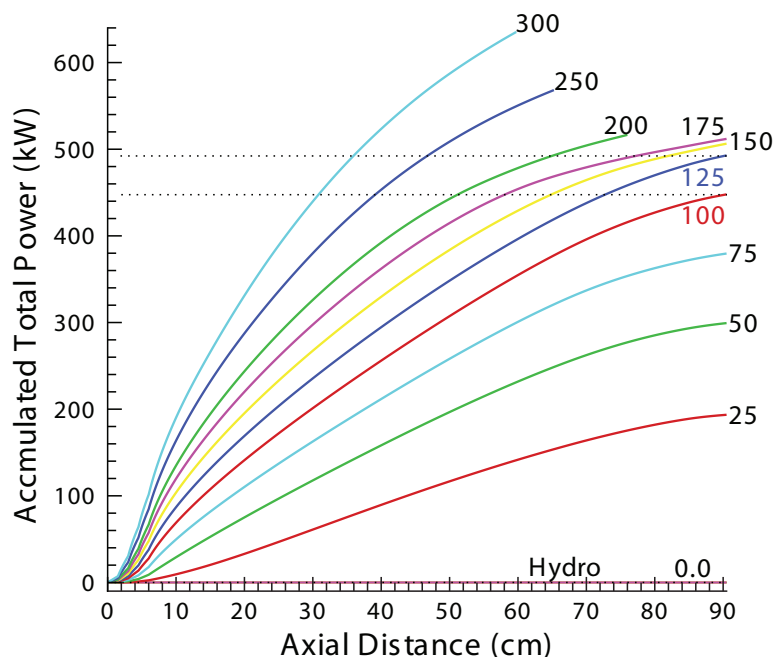
Figure 5.29: The total power consumed by the flow, accumulated along the length of the channel.

cumulative power is approximately 45 kW. And, as can easily be seen on the plot, the increase in total power diminishes for each 25 A increment above that (for the cases that did not terminate calculation before the end of the channel). Since this graph shows a rate of diminishing total power with increased applied current, one would assume that there is an optimum level of applied current, above which losses would dominte.

5.3.3.8 Push Power

The total cumulative power delivered to the flow, shown in Figure 5.29, either serves to accelerate the flow or heat the flow. Figure 5.30 shows the amount of total power delivered to the flow that was used to accelerate, or "push," the flow,
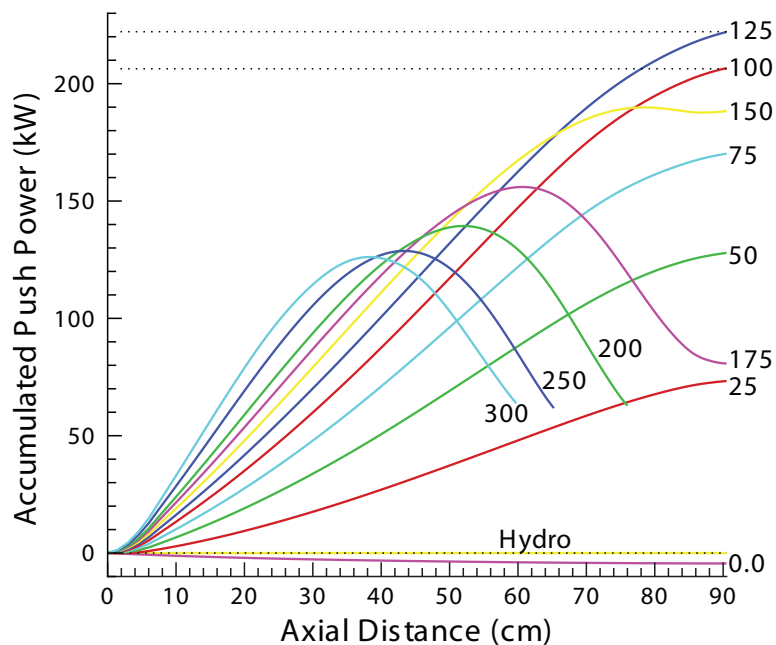
Figure 5.30: The push power used by the flow, accumulated along the length of the channel.

accumulated over the length of the MAPX accelerator. This graph shows the same diminishing returns on push power as were seen for total power in Figure 5.29; however, in this case, the 150 A and 175 A cases show push power drop-offs in the downstream portion. Note, however, that from 75 A to 100 A, the difference in push power is approximately 36 kW, while the difference in push power from 100 A to 125 A is only about 15 kW. So, while the 125 A level of applied current does represent the highest level of accumulated push power, the difference from the previous level of applied current is less. It is also interesting to note that the 0.0 A case shows a small, but negative, push power. This is consistent with having no applied current, but allowing the magnetic field to induce a small, internal negative J_y current (even though this is an open-circuit case).
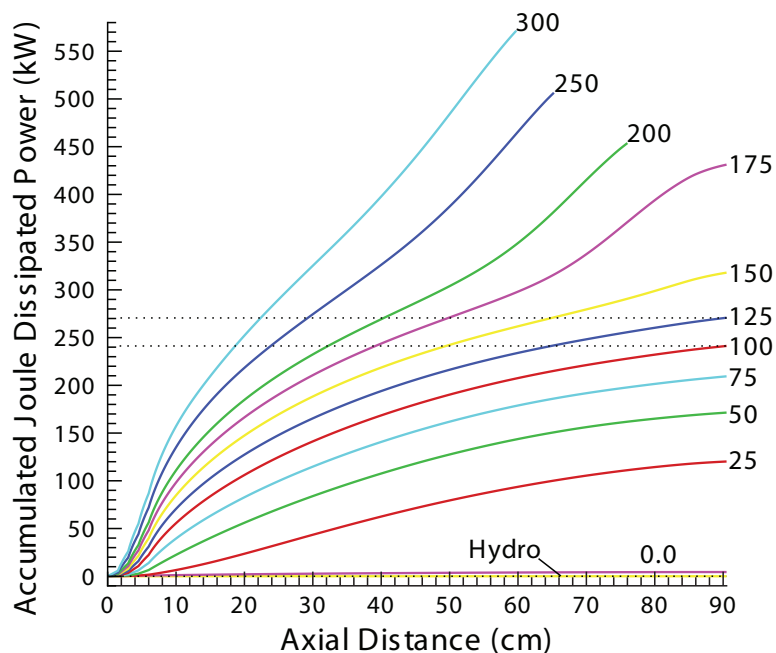
Figure 5.31: The power delivered to the flow that is used exclusively for Joule heating, accumulated along the length of the channel.

5.3.3.9   Joule Dissipated Power

Aside from acceleration, the total applied power can serve to heat the flow—this is known as Joule heating or Joule dissipation. Figure 5.31 shows the amount of the total power that was used to heat the flow, thus providing no propulsive benefits whatsoever. The graph shows a similar "diminishing returns" phenomenon that was seen in Figures 5.29 and 5.30, however the 150 A and 175 A cases show enormous, and increasing, jumps in Joule dissipated heat losses (which is to be expected, as they saw large drops in Figure 5.30). Furthermore, the difference between the 75 and 100 A and 100 and 125 A is almost negligible—from 75 to 100 A, the difference is approximately 32 kW, while the difference from 100 to 125 A is approximately 30 kW. Also note that

the 0.0 A case shows a small, positive Joule dissipated heat loss—equal and opposite to push power in Figure 5.30, so the sum is zero, as shown in Figure 5.29.

Figures 5.29, 5.30 and 5.31 tell an important story. While it is true that the 125 A case has the highest accumulated push power level, one should note that of the 45 kW of added total power (above the 100 A case), only 15 kW of that went toward accelerating the flow. The other 30 kW—twice the push power value—went into Joule dissipative losses (*i.e.*, heat). So, while only ⅓ of the "added" total power (from 100 to 125 A), was used to accelerate the flow at the 125 A level, approximately 52% of the added total power (from the 75 to 100 A current level) was used for acceleration in the 100 A case. That is, while the 125 A case does give higher total and push power values, more of the total applied power (above the 100 A case) is used to heat the flow than to accelerate the flow.

5.3.3.10   Electrical Efficiency

The differences in the push and applied power levels can best be explained through the electrical (or global) efficiency, shown in Figure 5.32 (the calculation of which is explained in Section 4.3.6). This graph clearly shows that, from a power standpoint, the 100 A case is superior to the 125 A case. Furthermore, since the 75 A and 125 A cases are so near to each other (and both approximately equidistance from the 100 A case), the 100 A case seems to represent the highest electrical efficiency, at 46%, for this MAPX accelerator (with this given configuration). While a 46% accelerator efficiency is not very impressive, and nowhere near the 61% predicted in Table 2.4, recall that the MAPX channel was designed and the performance
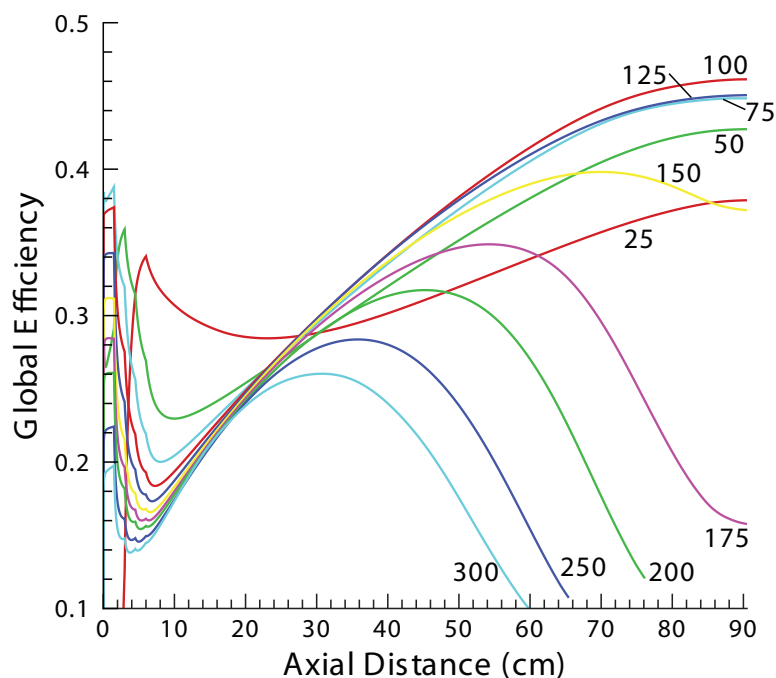
Figure 5.32: The electrical/global efficiency of the MAPX accelerator at various levels of applied current.

predictions were calculated using a one-dimensional numerical model (described in Section 2.2.1), which could not have captured the sidewall and channel losses that have already been seen in this and the previous section. It should also be noted that the initial decrease in global efficiency in Figure 5.32 is due to the low current levels in the power takeoff region. In short, for an MHD accelerator which would be used as an onboard propulsive device, efficiency is paramount—and the 100 A level of applied current gives the best efficiency for the MAPX accelerator.

5.3.3.11 Dimensionless Voltage Drop

Another useful electrical parameter is the dimensionless voltage drop, Δ, defined as [90, 108]

$$\Delta = \frac{E_d}{uB} = \frac{V_d}{uBh_c}, \tag{5.6}$$

where E_d is the equivalent electric field (defined in Section 4.3.6) and V_d is the near-electrode voltage drop (defined in Section 3.3.1.2). The dimensionless voltage drop is basically a lump loss term, which incorporates all voltage losses associated with the electrode boundary layer [90]—including, but not limited to, plasma nonuniformities (boundary layer), sheath drop and emission losses, current concentrations, as well as possible current leakage and shorts [108]. In this manner, the dimensionless voltage drop can be used to determine whether an MHD channel is operating in generator (positive Δ) or accelerator (negative Δ) mode, or how well the channel is operating in that particular mode.

Figure 5.33 shows the dimensionless voltage drop, Δ, as a function of axial distance down the channel for (a) all the levels of applied current, and (b) only the 100 A case. In accelerator mode, the dimensionless voltage drop should be a negative value, however one notes that, even for the most efficient (100 A) case, there are positive regions near the entrance and exit of the channel. (It is important to note, however, that the dimensionless voltage drop for the 100 A case does remain negative longer than any other level of applied current.) However, from Figure 5.24, it is obvious that for the 100 A case, the J_y current density remains positive (and hence, in accelerator mode) throughout the length of the MAPX channel—so why, exactly,
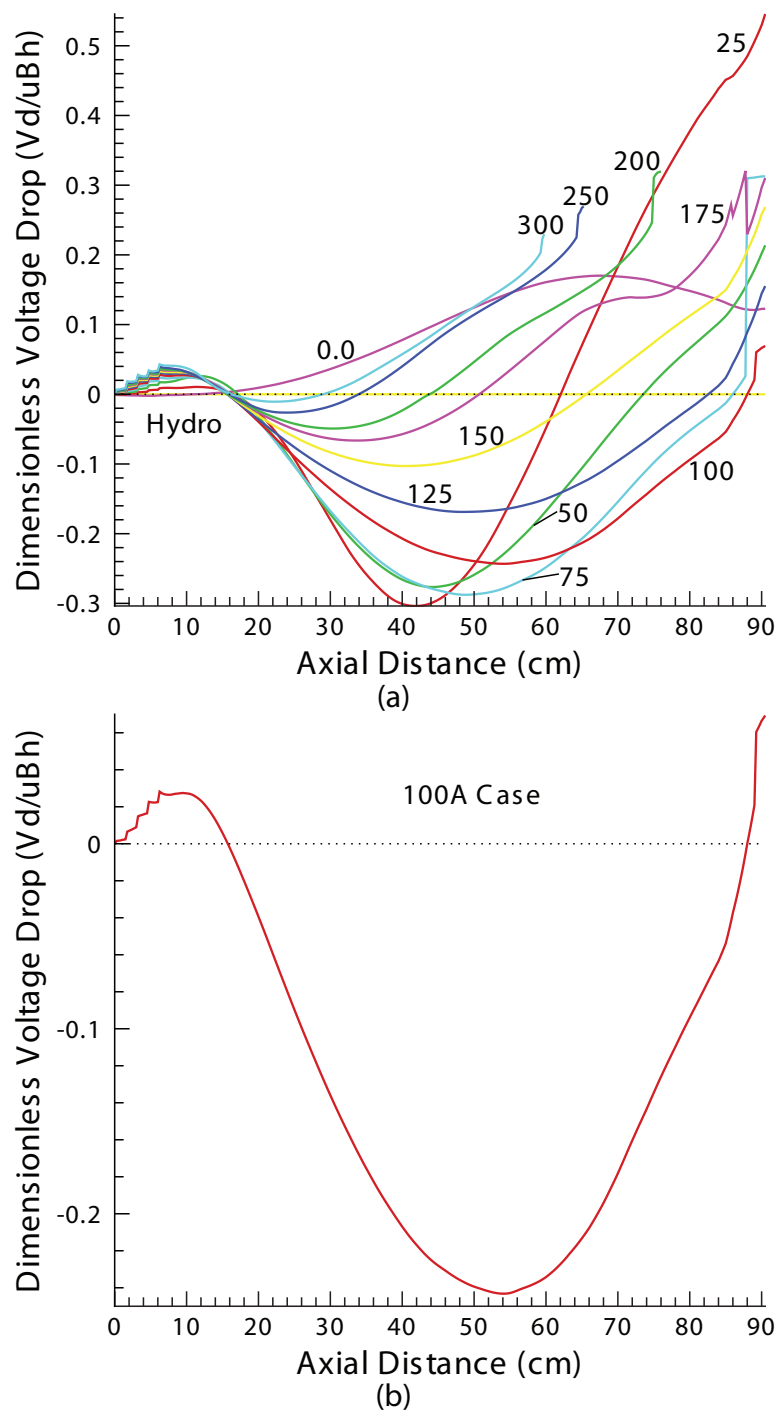
Figure 5.33: The dimensionless voltage drop, Δ, as a function of axial distance: (a) Δ for all levels of applied current, and (b) a close-up Δ of only the 100 A case.

are there positive regions near the ends of the channel and why does the dimensionless voltage drop change directions near the mid-point of the channel?

The calculation of the dimensionless voltage drop in the MGMHD numerical model makes certain assumptions. Recall from Equation 3.70 in Section 3.3.1.2, that V_d is the sum of the anodic (V_{d_a}) and cathodic (V_{d_c}) voltage drops (Equations 3.68 and 3.69, respectively). The anodic and cathodic voltage drops are basically the integrals of the difference of the E_y electric field evaluated at the center of the channel, $H/2$, and at some other location less than $H/2$ (for each half of the channel, respectively). The dimensionless voltage drop is typically a measurement of the losses in the electrical boundary layer (*i.e.*, close to the anode or cathode walls); however, the MGMHD code uses the center-line of the channel as the reference point, which captures more losses than would normally be included in the dimensionless voltage drop which was calculated using a reference point closer to the electrode walls. Therefore, the Δ calculation in the MGMHD code can be shifted (to a positive or negative value) or the individual values can be intensified. Furthermore, recall from Figure 5.28 that the power takeoff (PTO) region covers the first 7.5 cm of the entrance, and from Figure 5.9, that the magnetic field attenuates in the latter half of the MAPX channel. Note in part (b) of Figure 5.33, that the positive portion at the entrance of the MAPX channel peaks as the entrance PTO ends (which is where the J_y current density is strongest), then promptly declines into negative territory. Therefore, while the dimensionless voltage drop in the UMM numerical model, shown in Figure 5.33, uses an assumption that can shift or magnify its value, the calculation of Δ still offers

(via the slope) a good indication of the regions in the MAPX channel where the $J_y B$ Lorentz force is most intense.

The behavior of the dimensionless voltage drop in Figure 5.33 can be better explained through the graphs in Figure 5.34, where the E_y electric field (which is used to calculate anodic and cathodic voltage drops, and therefore, V_d, in the UMM code), is plotted against the height of the channel sidewall, y (sometimes referred to as h_c or H). Each of the six graphs in Figure 5.34 is a two-dimensional plot at a particular cross-sectional plane, normal to the primary flow, in the MAPX channel. Therefore, the 100 A case in Figure 5.33 can be explained using Figure 5.34 in the following manner. As the relatively slow-moving and cold supersonic flow enters the expanding channel, it comes into contact with the even colder electrode walls (see Table 5.2), while the applied current begins to slowly increase to its maximum value. In this entrance region, where the J_y current is relatively low, heating still occurs, but hydrodynamic forces dominate, and the core flow begins to accelerate due to the area expansion, therefore decreasing the flow temperature near the center-line of the channel. The E_y electric field is inversely proportional to temperature, which explains the convex shape of the central curve and the positive value for Δ at the 10 cm location in Figures 5.34 and 5.33, respectively. Furthermore, the 1000 K electrode walls maintain a very cold boundary layer temperature (and very high E_y), and therefore cause a relatively large temperature and E_y gradient across the channel. Some two-temperature MHD models have shown that because of the large electric field in the boundary layer, the electron temperatures remain high, which is the main
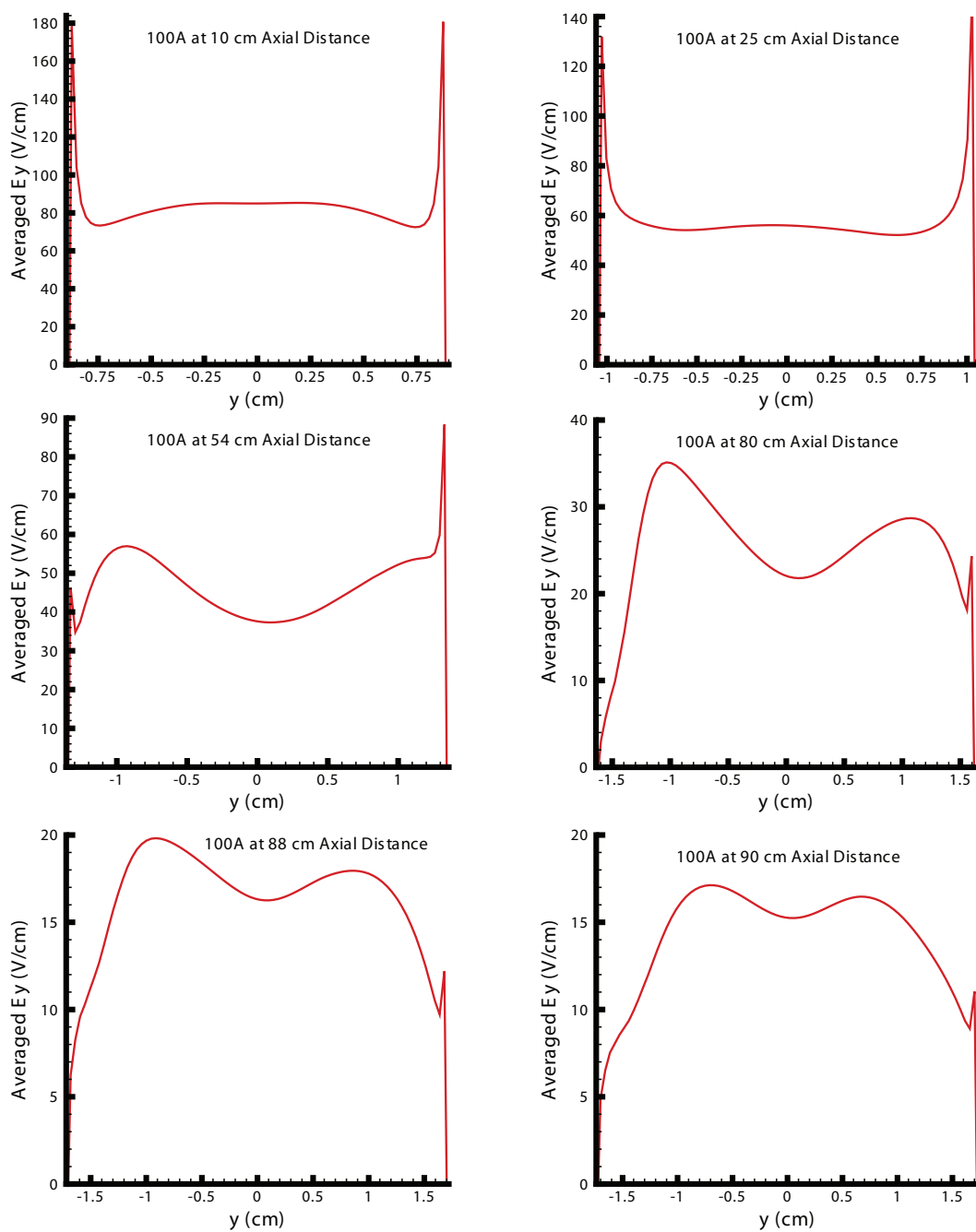
Figure 5.34: The E_y electric field of the 100 A level of applied current as a function of sidewall height, y, at six specific downstream locations—10 cm, 25 cm, 54 cm, 80 cm, 88 cm, and 90 cm. Accelerator, J_y, current flow is from negative y to positive y, or left-to-right on the page.

source of conduction across the boundary layer [100]; but the UMM numerical model assumes a single temperature fluid, therefore some of this resolution is lost.

Furthermore, from Figure 5.33, one notes that the dimensionless voltage drop for the 0.0 A case is slightly negative in the first few centimeters of the channel. In this case, the flow is initially hydrodynamically accelerated via the duct divergence. It is not until the magnetic field begins to influence the flow (as the 0.0 A case is basically an open-circuit MHD generator) at approximately 15 cm, that the value for Δ becomes positive. This behavior is seen in Figure 5.12 where the 0.0 A case has very high initial acceleration, which begins to level off as the flow moves downstream (some of which is also due to frictional forces). The opposite happens for the cases with nonzero applied current—as they enter the channel, even though the applied current is relatively low, heating does occur (see Section 2.3.1 on MHD compression). The core of the flow accelerates due to channel divergence, but the Joule heating around the core combined with the cold electrode walls causes the rest of the cross-sectional velocity to lag behind, as seen in Figure 5.12. It is not until the end of the PTO region, where the full applied current and cross-sectional flows have helped to normalize the flow temperature (excluding the boundary layer), that the dimensionless voltage drop begins to fall into negative territory.

At 25 cm in Figure 5.34, electromagnetic forces have taken over (and cross-sectional flow has helped to equalize the temperature), J_y has heated the flow (and reduced E_y throughout the cross-section), even while the boundary layer remains relatively cold (recall, the wall temperature is held constant at 1000 K). At this downstream location, the dimensionless voltage drop is a negative value and steadily

decreasing. The 54 cm point marks the lowest negative dimensionless voltage drop seen for the 100 A level of applied current. Figure 5.34 shows that, at this location, the electron-collecting electrode is seeing a very low E_y, which implies a large increase in boundary layer temperature (recall that, in Figure 5.34, current flow is from negative y to positive y, or left to right on the page). The core flow has also experienced an increase in temperature, while the electron-emitting electrode remains relatively cold.

At 80 cm downstream, the "hot spot" which developed in the boundary layer of the negative-y electrode at 54 cm, has grown and begun to push away from the wall. The core flow remains hot, and the positive y boundary layer has finally succumbed to the intense heat in the channel. At this point, the dimensionless voltage drop is still negative, but with a positive slope. At 88 cm downstream, the hot, negative y boundary layer has pushed farther into the core flow, while E_y at the positive y boundary layer has dropped to almost half its value from the previous plot. This implies great heat losses at the electrode walls, which is consistent with the zero value of the dimensionless voltage drop at this location. Finally, at 90 cm, the dimensionless voltage drop is a high positive value. Note that the E_y electric field in the negative y electrode boundary layer has diminished to approximately 5% of its value at 10 cm, implying huge heat losses at the sidewalls. Furthermore, while the central portion of the E_y curve is concave, the overall shape across the entire cross-section is convex, similar to the shape at 10 cm, and consistent with a positive value for Δ.

The intense attenuation of the magnetic field in the downstream portion of the MAPX channel did not, in and of itself, cause the negative-to-positive transformation of the dimensionless voltage drop; however, as clearly seen in Equation 5.6, a lower

magnetic field will increase the magnitude of the value for Δ. Hence, the value for the dimensionless voltage drop at 90 cm is exacerbated by the low magnetic field—which is more obvious in the 25 A case in Figure 5.33. Therefore, while the sign changes in Figure 5.33 do not indicate that the MAPX accelerator switched to generator mode for the 100 A case, the sign of the dimensionless voltage drop combined with the slope of the curve, when used in conjunction with E_y graphs (as in Figure 5.34), do indicate areas in the MAPX accelerator where the acceleration is most efficient, and where losses tend to dominate. Furthermore, the slopes seen in Figure 5.33 are consistent with the efficiency slopes seen in Figure 5.32.

5.3.4 Design Point Selection

The previous sections outline the parametric studies used in determining the test configuration for the MAPX accelerator. Section 5.3.1 shows that the ideal diagonal angle for the MAPX accelerator is not physically possible; therefore, the closest physically viable angle was chosen—a $\theta = 45$ degree accelerator angle ($\theta_d = 135$ degrees). Section 5.3.2 shows that, while frictional losses are detrimental in all cases, the 125 A case has the highest axial velocity at the exit, while the 100 A case has the highest center-line total pressure. Lastly, Section 5.3.3 shows that neither the 125 A or 100 A case experiences a negative J_y current density, but the 100 A case offers better overall efficiency because of the Joule dissipative losses seen in the 125 A case.

As previously stated, for propulsion applications, efficiency is typically the deciding factor—therefore, the design point selected for the MAPX accelerator is a 100 A

applied current with an accelerator angle of 45 degrees (using the thermodynamic flow parameters from Section 5.2.2). A more detailed three-dimensional analysis of the MAPX design point is presented in the following sections.

5.4   Three-Dimensional Numerical Study of Design Point

This section presents a three-dimensional analysis of the MAPX baseline design point—specifically, the MAPX MHD accelerator described in Sections 2.1.2 and 5.2 and depicted in Figures 2.4, 2.5, 2.6 and 5.1, with a 45 degree accelerator angle and a 100 A applied current. The information in this section gives a more detailed view/analysis of the information presented in Section 5.3; therefore, the same flow and entrance parameters—those presented in Tables 5.1 and 5.2—still apply. The full UMM thermodynamic input file (`thermhd.in`) and magnetohydrodynamic input file (`mhd.in`) for this particular case is given in Appendix D. Whenever possible, an interpretation/analysis of the underlying physical phenomenon will accompany the three-dimensional graphs.

5.4.1   Data Representation

There are three general types of graphs presented in this section—mesh, contour, and vector. The mesh plots are three-dimensional structures at a given cross-sectional plane in the MAPX channel, in which information is given via the overall size and shape of the structure. The contour graphs are also given at various cross-sectional planes, but the information is flattened into two-dimensions and the third dimension is represented by lines and/or colors. Finally, the vector plots represent

cross-sectional flows of some kind (*e.g.*, cross-sectional current density or flow velocity). The vectors are drawn in the well-known "arrow" format, with the length of the vector representing a relative magnitude.

In this section, the cross-sectional planes are represented such that the center-line of the MAPX channel is at the origin, (0,0), of the cross-section. Therefore, each plot will have some negative values for height and width in the (y,z) plane. Furthermore, the entrance of the MAPX channel will have the dimensions $-0.78\,\mathrm{cm}$ to $0.78\,\mathrm{cm}$; and the exit of the channel will have dimensions $-1.82\,\mathrm{cm}$ to $1.82\,\mathrm{cm}$. This was done to facilitate finding the center-point of each plot—simply locating the (0,0) point in each cross-section gives its center-point.

In an MHD accelerator, the applied current should flow in the direction which provides a $J_y B$ Lorentz force in the direction of the primary flow—*i.e.*, an accelerating force. Throughout this dissertation, "accelerating" current flow is defined in the positive $\hat{\mathbf{y}}$ direction (with the magnetic field defined in the positive $\hat{\mathbf{z}}$ direction, and the primary flow defined in the positive $\hat{\mathbf{x}}$ direction), as shown in Figures 1.3, 1.4, 1.6, 1.7 and 1.8. In this section, because the center-point of each cross-section is defined as the origin, the accelerating current flow (positive current flow) will occur from the electrode with a negative y value to the electrode with a positive y value. Visually, these electrodes are at the bottom (negative) and top (positive) of the MAPX channel. Many texts refer to these electrodes as the anode and cathode, respectively (the current leaves the anode and travels to the cathode). However, as seen in Figure 5.24, because of current reversal in the accelerator, the electrode which sends or receives the current is not necessarily a constant in the MAPX channel (*e.g.*,

at 70 cm downstream, the anode for the 100 A case is the cathode for the 175 A case).
Furthermore, referring to the electrodes as the "positive-" or "negative-" y (based on
their relationship to the center-line, (0,0), of the channel) can also cause confusion
as one might mistake the negative/positive label as an indication of that electrode's
charge (which, with positive current flow, is actually the opposite of the truth).

Therefore, the electrodes will be referred to by their visual-physical placement
in the channel, as shown in Figure 1.8. The negative y electrode (the anode when
positive current flow exists) will be referred to as the "bottom" electrode, and the
positive y electrode (the cathode, under positive current flow), will be referred to as
the "top" electrode. However, note—per the definition of current flow [91]—while
positive current flow in the MAPX channel is from the bottom to the top electrode,
electrons (the more mobile of the charge carriers) flow in the opposite direction.

5.4.2 Results and Analysis

5.4.2.1 Velocity

In Section 5.3.2, Figure 5.12 shows the axial velocity, u, as a one-dimensional
function of the axial distance for all the levels of applied current. Figures 5.35
and 5.36 show the axial flow velocity, u (in m/s), at various locations along the
MAPX channel—specifically at 2 mm, 10 cm, 25 cm, 60 cm, 80 cm, and 90.5 cm (the
channel exit). Figure 5.35 shows the axial velocity as a three-dimensional mesh plot,
where one can see the formation of the "bullet-shaped" velocity profile from entrance

to exit. The contour plots in Figure 5.36 reveal that the velocity distribution is not evenly distributed in the cross-sectional plane.

The MGMHD and UMM codes treat the axial velocity at the entrance as a "plug" profile; therefore, the profile at the 2 mm mark is still constant across the cross-section, with a no-slip condition imposed at the wall, which is shown in both Figures 5.35 and 5.36. Typically, uniform entrance flows require a much shorter entrance length [177]. Recall that in the UMM code, inlet velocity is calculated from the inlet parameters such as flow rate, area, and density—the inlet velocity is not a user-defined input. Therefore, at 2 mm, the UMM code calculates the velocity to be 1313 m/s across most of the channel, which is very close to the inlet value used in Table 2.4. At 10 cm, the velocity profile remains fairly flat, with entrance perturbations (*i.e.*, wavy lines) being seen in the three-dimensional mesh plot (the contour plot lacks the precision to show these small deviations). Note, however, that both the contour and mesh plots show the large velocity losses in the corners of the channel. At 25 cm, the entrance perturbations have equalized, and the velocity profile is still quite flat across most of the cross-section. The contour plot in Figure 5.36 shows a peak velocity in the center of the channel, with all velocity levels displaying symmetry about the center-line of the channel.

The axial velocity profile at 60 cm is no longer symmetrical. Not as noticeable in Figure 5.35, Figure 5.36 shows that the core flow in the channel has started to push toward the bottom electrode. The no-slip condition is maintained at the wall, with the same low-velocity corner-regions seen at 10 cm. At 80 cm, the velocity profile has pushed farther toward the bottom electrode. The high-velocity core flow is increasing

Figure 5.35: Three-dimensional axial velocity, u, plots at 0.2, 10, 25, 60, 80, and 90.5 cm along the MAPX channel. The last position is the channel exit. The positive J_y current flows from the bottom electrode (in the background) to the top electrode (in the foreground), which is out of the page.

Figure 5.36: Contour plots of axial velocity, u in m/s, at 0.2, 10, 25, 60, 80, and 90.5 cm along the MAPX channel. The last position is the channel exit. The bottom and top electrodes are oriented correctly, with the positive J_y current density flowing up in each graph.

in size (as is the channel cross-sectional area). Near the top electrode wall, a concave feature, possibly due to secondary flow (see Figure 5.37), is beginning to form in the medium-speed velocity regions—this is visible in both the mesh and contour plots. At the channel exit, the high-velocity core flow is very near the bottom electrode wall. There is a large velocity gradient near the bottom electrode—within 3 or 4 mm, the velocity profile goes from zero (at the wall) to approximately 2300 m/s. The peak velocity, approximately 2700 m/s, occurs farther away from the bottom electrode, but on the negative side of the center-line. The indentation near the top electrode in the medium-speed velocity sections has increased in intensity and size, and small velocity-profile indentations (curves in the lines) are now visible in Figure 5.35 along the insulator walls. The causes of the asymmetry in the axial velocity profile will be discussed shortly.

Figure 5.37 shows the contour plots of the axial velocity at 2 mm, 10, 25, 60, 80, and 90.5 cm, but with a vector overlay representing the secondary velocities, v and w, at these locations. MHD effects tend to increase the amount of secondary flow in a channel—while normal turbulence can cause secondary flows with, typically, 3% of the mean axial flow velocity, MHD channels have seen $\hat{\mathbf{z}}$ directed flows of 11% and $\hat{\mathbf{y}}$ flows of more than 20% of the mean axial velocity [129]. Secondary flows in MHD channels usually result from axial, J_x, currents [126, 129]. The plots at 2 mm and 10 cm, show what one might expect for entrance flow in an expanding duct [126]—flow primarily in the axial direction and expanding into the walls, with no overriding secondary direction. Shear at the wall retards the near-wall flow, and thereby directs flow toward the center. At 25 cm, the secondary flow shows some
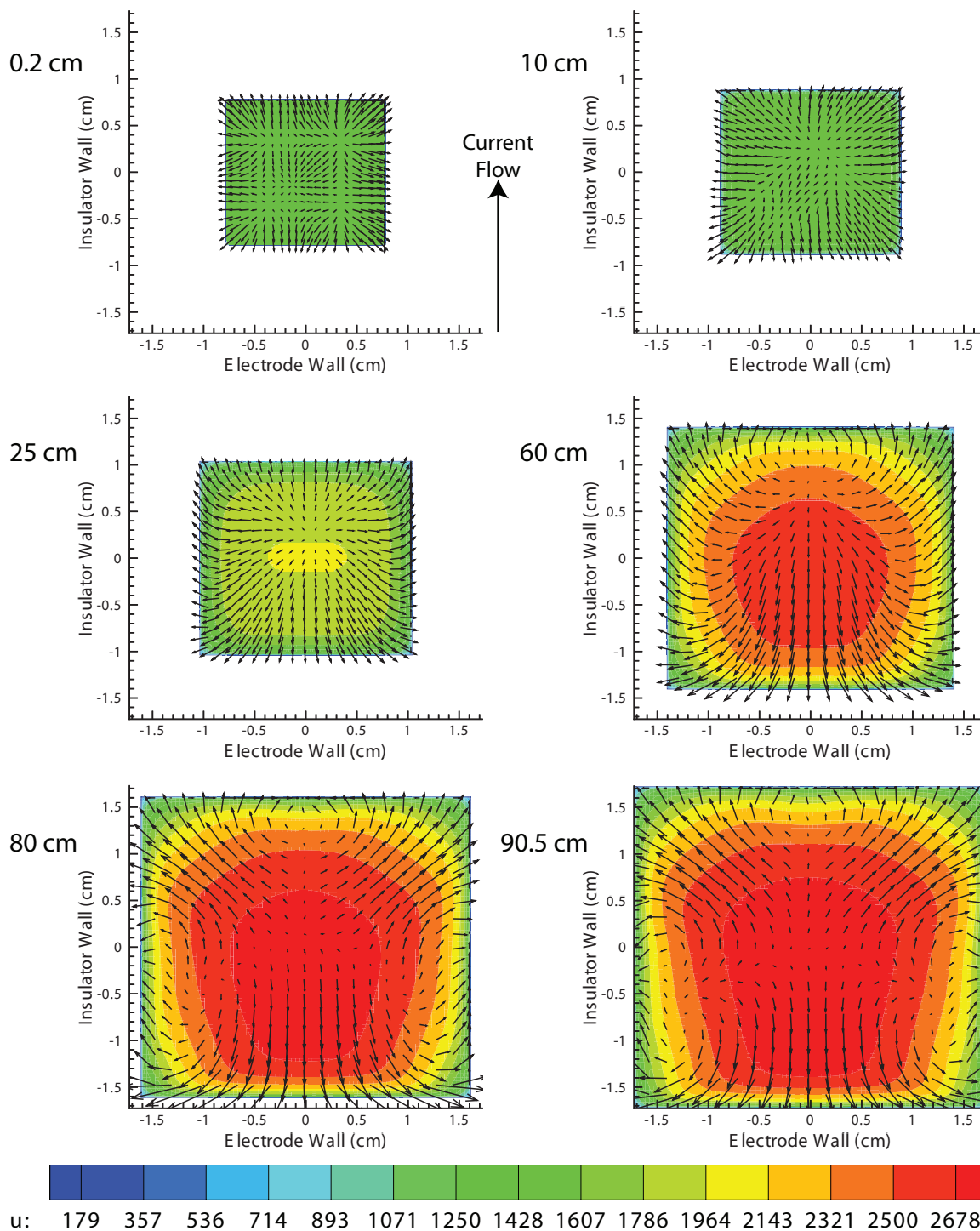
Figure 5.37: Vector plots of secondary velocity flow, v and w, in the cross-section with the axial velocity, u, in m/s, as a contour background. The bottom and top electrodes are oriented correctly, with the positive J_y current density flowing up in each graph. The length of the vector represents a relative intensity.

group behavior, with currents beginning to flow from just above the center-line to the bottom electrode, and smaller amount of flow curving into the upper corners of the channel. At 60 cm, strong secondary currents are accelerating from a high velocity region above the center-line to low-velocity regions at the bottom electrode wall. At the top electrode wall, a recirculation region has formed in the middle of the channel. At 80 cm downstream, the center of the secondary flow has shifted downward in the channel, just as the core axial velocity. Strong secondary currents now flow into the top corners of the channel and directly downward into the bottom electrode, as seen in previous research [126]. Strong recirculation regions are located at the center of the top electrode and along the lower portions of the sidewalls, causing concave regions in the axial core flow. Most of the secondary flow structures have intensified at 90.5 cm downstream. The "center" of the secondary flow has shifted farther downward in the channel cross-section, corresponding with the downward shift of the axial core flow. The secondary flow from the center to the upper corners of the channel is stronger, and is causing the axial flow to spread in that direction. This accentuates the concave regions caused by the secondary recirculation at the center of the top electrode. The recirculation regions at the sidewalls also spread the axial flow toward the walls in some areas, and cause concavities in other areas.

Generally, the secondary flow seems to be driving the axial core flow toward the bottom electrode. The "center" of the secondary flow—which actually seems to be a source for the flow, feeding off of the higher-velocity regions in the primary axial flows—progresses downward in the channel as the flow progresses downstream. This behavior has been seen in MHD channels before [126]. The upward secondary flow

regions seem to be pushing the axial flow into the upper corners of the cross-section, while simultaneously pushing the flow away from the center of the top electrode. This causes a concave region at the top of the axial profile, which, if allowed to develop further, might cause a separation in the core flow field.

5.4.2.2 Temperature

After approximately $10\,\mathrm{cm}$, Figure 5.13 shows a that the $100\,\mathrm{A}$ case maintains a constant cross-sectional averaged temperature, with a slight (approximately $300\,\mathrm{K}$) drop in center-line temperature. This indicates a slight increase in the near-wall (or non-center-line) temperature profile, which is an understatement, as Figures 5.38 and 5.39 show. Both the mesh and contour profiles show huge variations in temperature as the flow progresses downstream, much more than indicated by the one-dimensional plots in Section 5.3.2. Note, also, that the user-defined inlet temperature is $2700\,\mathrm{K}$.

Much like the inlet velocity profile, the inlet temperature profiles in Figures 5.38 and 5.39 are mostly flat across the cross-section. As described for Figure 5.34, the temperature spikes near the walls and in the corners at $2\,\mathrm{mm}$ are real (not a numerical anomaly), and a result of the slow-moving flow being Joule heated by the sudden application of the current (even though, because of the power take-off, the applied current at $2\,\mathrm{mm}$ is $20\,\mathrm{A}$). The wall temperature remains a constant $1000\,\mathrm{K}$ (as defined by the user), and the sharp near-wall temperature spikes remain until approximately $2.5\,\mathrm{cm}$ downstream (not shown). At $10\,\mathrm{cm}$, the flow temperature has somewhat equalized (thanks in part to the secondary flow [129, 140]), but

0.2 cm   10 cm   25 cm

60 cm   80 cm   90.5 cm
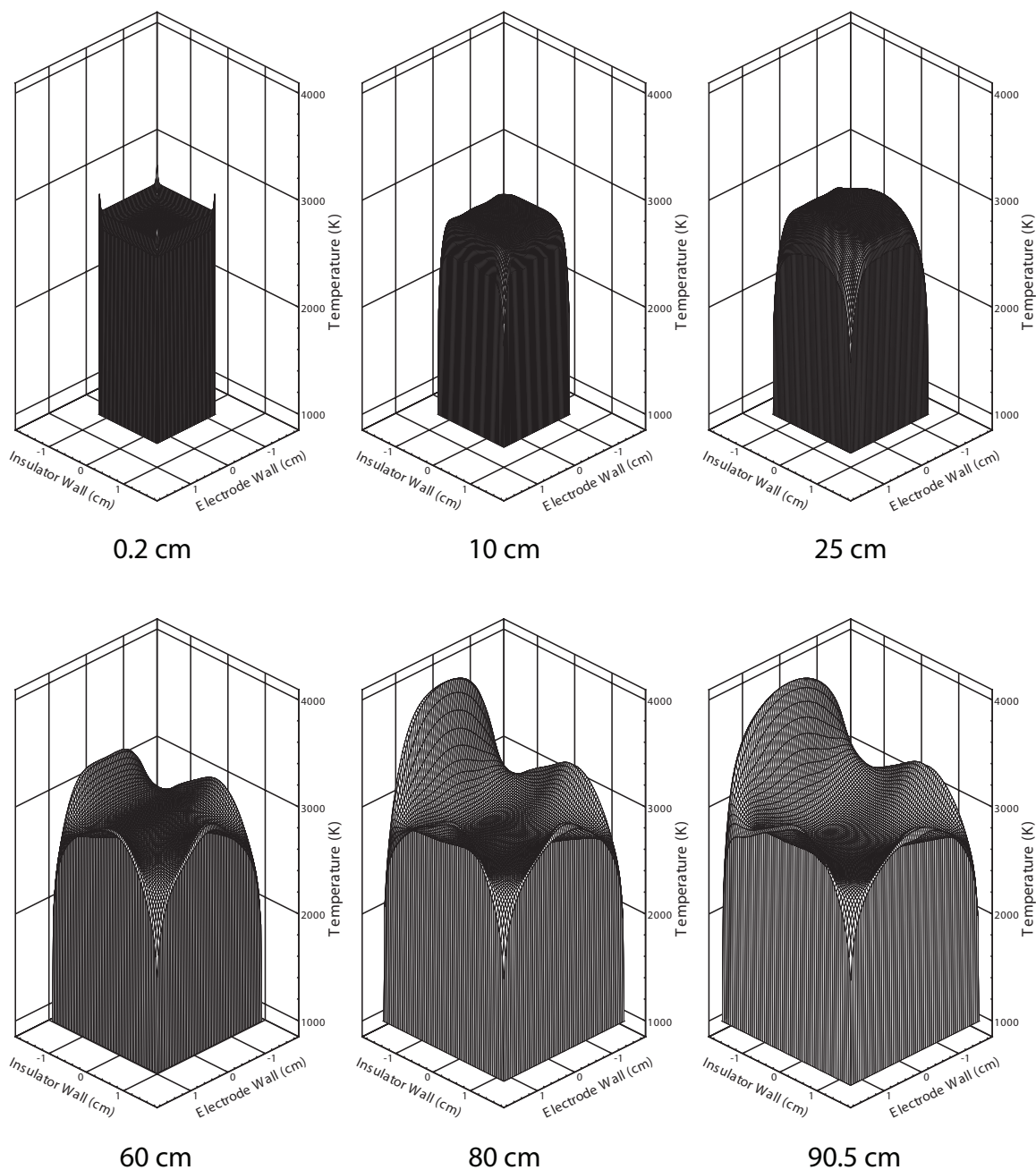
Figure 5.38: Three-dimensional temperature plots at 0.2, 10, 25, 60, 80, and 90.5 cm along the MAPX channel. The last position is the channel exit. The positive J_y current flows from the bottom electrode (in the background) to the top electrode (in the foreground), which is out of the page.
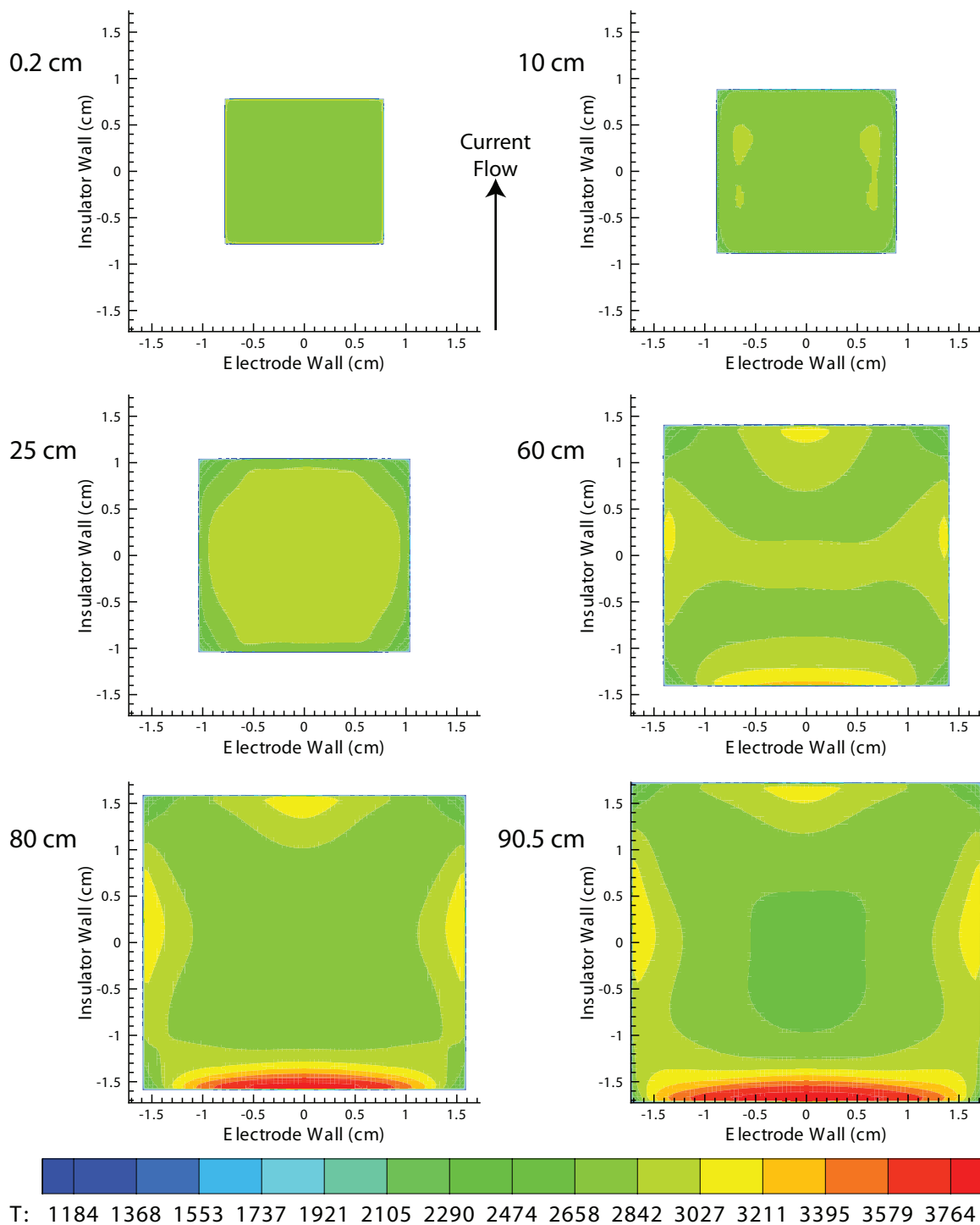
Figure 5.39: Contour plots of channel temperature, T in K, at 0.2, 10, 25, 60, 80, and 90.5 cm along the MAPX channel. The last position is the channel exit. The bottom and top electrodes are oriented correctly, with the positive J_y current density flowing up in each graph.

two higher-temperature regions remain along the insulator walls (which coincide with current flow from the bottom to the top electrode). At 25 cm, the high-temperature region has grown to encompass most of the core flow, excluding the corner regions. The two hot insulator sidewall regions from 10 cm are still slightly warmer than the rest of the flow (as shown in Figure 5.38), but the highest temperature increases are found near the center of the electrode walls.

There is much more variation in the temperature profile at 60 cm downstream. The hottest region is near the center of the bottom electrode, just outside the cold-electrode region. Other hot areas are found at the centers of the electrode walls and sidewalls, with the bottom electrode having the largest region. Cooler regions surround these near-wall regions, and even connect the sidewalls through the center-line of the channel. The coldest regions are found just above and below the center-line of the cross-section, and in the corners of the channel. At 80 cm downstream, the bottom electrode has developed a large "hot spot" just outside the cold-electrode boundary layer. The centers of the other walls (top electrode and sidewalls), remain approximately the same temperature as they were at 60 cm. The central portion of the flow has lowered in temperature, while the corners remain the coldest. At 90.5 cm, the hot spot at the bottom electrode has intensified and grown to cover almost the entire electrode. The other walls remain at the same temperature, while the center of the flow actually decreases in temperature (as seen in Figure 5.13).

The high-temperature region near the bottom electrode corresponds with the downward shift of the axial core flow, depicted in Figures 5.35 and 5.36, and is consistent with previous MHD research [140]. Figure 5.40 shows the three-dimensional
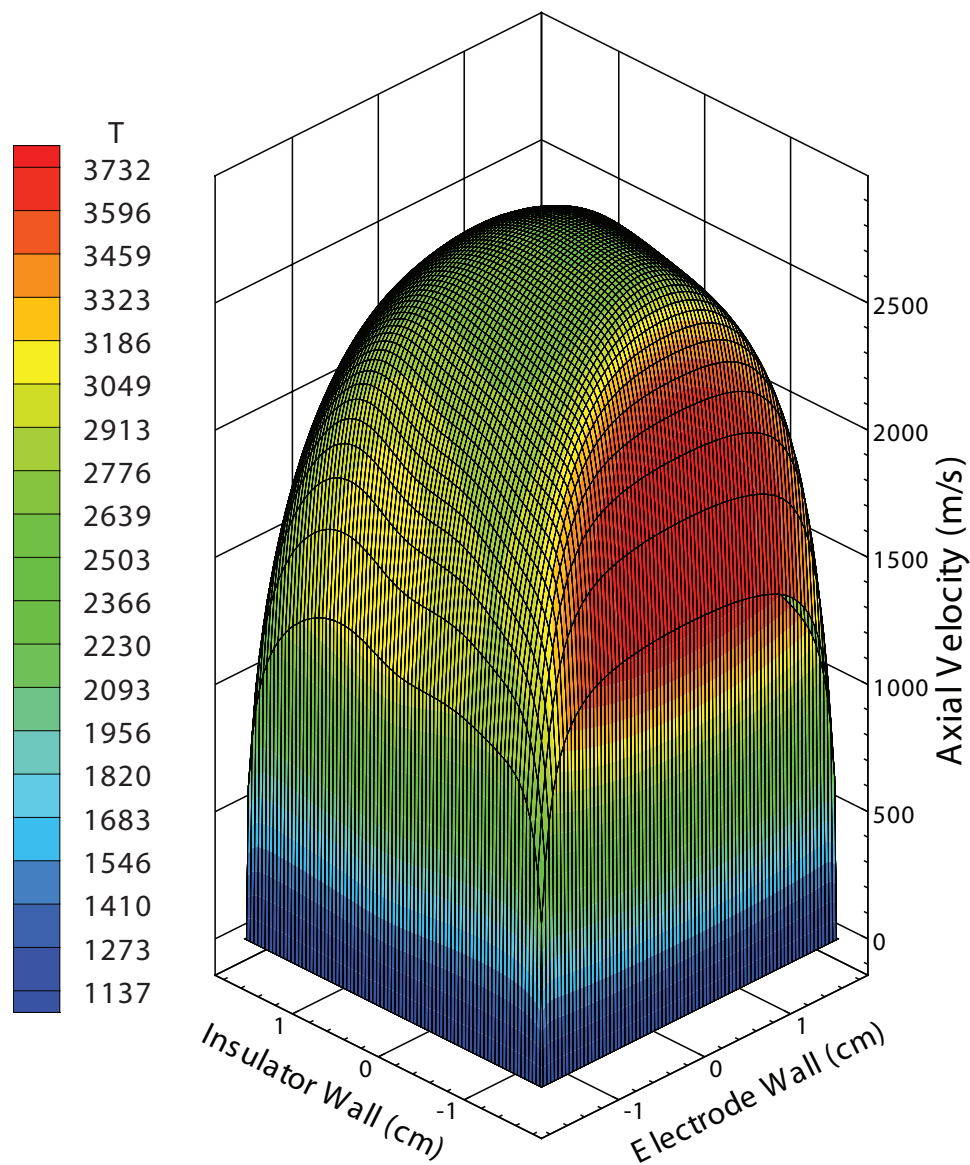
Figure 5.40: Three-dimensional axial velocity plot with a temperature (units of K) overlay at the exit of the MAPX accelerator. Positive J_y current density flows from the bottom electrode in the foreground, to the top electrode, which is obscured in the background.

axial velocity profile with a temperature overlay at the exit of the MAPX channel. (Note that this velocity profile has been rotated $180\,^{\circ}$ from those in Figure 5.35, so that the bottom electrode is in the foreground and the top electrode is obscured in the background—*i.e.*, current flows diagonally right to left into the page.) In MHD channels, one cause of the high-temperature regions is current flow, which (when one recalls that electrons flow from the top electrode to the bottom electrode) corresponds with the large downward secondary flows seen in Figure 5.37. Notice, however, that the highest velocity regions, just below the center-line of the cross-section, correspond with some of the lowest temperature regions. Furthermore, the high-temperature near-wall regions do not correspond with the highest velocity near-wall regions. This is consistent with normal hydrodynamic duct flow (where, as the velocity increases, temperature decreases), but since it appears that the high-speed core flow is attracted to the near-wall hot spot, one might draw the conclusion that the two are related—this, however, does not seem to be the case. Instead, it seems as though the secondary flow, which is somehow related to the temperature profile, is driving the core flow toward the bottom electrode.

5.4.2.3   Mach Number

As shown in Figure 5.14 and Equation 4.60, the Mach number shows the relative influence of temperature on the flow velocity. Figure 5.41 shows three-dimensional Mach number graphs at $2\,\mathrm{mm}$ and at 10, 25, 60, 80, and $90.5\,\mathrm{cm}$ downstream in the MAPX channel. As expected, the high-temperature area close to the near-wall high-velocity regions serves to "equalize" the Mach number profiles across the cross-section

0.2 cm   10 cm   25 cm

60 cm   80 cm   90.5 cm
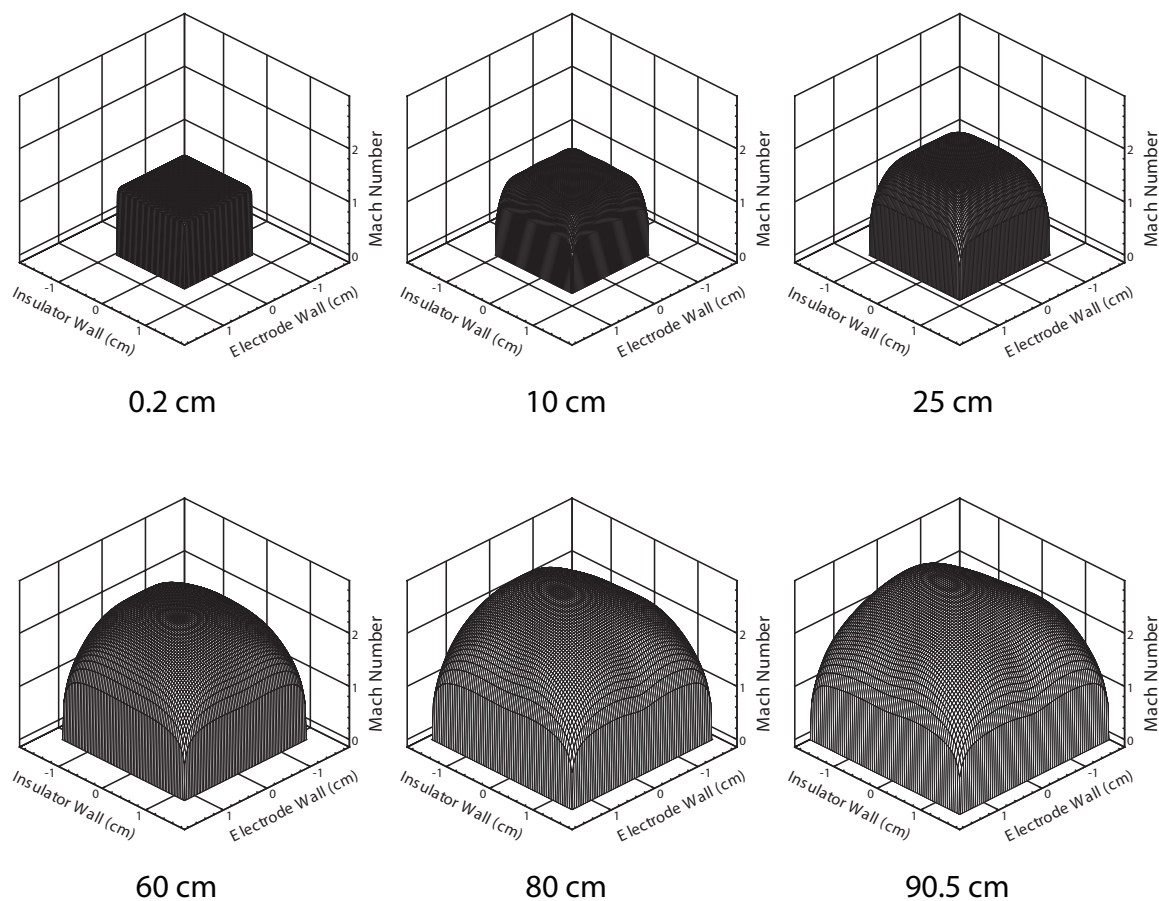
Figure 5.41: Three-dimensional axial Mach number plots at 0.2, 10, 25, 60, 80, and 90.5 cm along the MAPX channel. The last position is the channel exit. The top electrode is in the foreground with the bottom electrode obscured in the background—*i.e.*, positive J_y current flows diagonally from left to right, out of the page.

of the channel. At 2 mm, 10 cm, 25 cm, and even 60 cm, the Mach number is fairly

consistent and centered across the cross-section, becoming less flat-topped as the flow

travels downstream. At 80 cm, one can see that the Mach profile is pushing slightly

toward the bottom electrode wall, while a small concave region forms near the top

electrode wall, consistent with the primary and secondary velocity profiles. At the

channel exit, the Mach profile still has only a slight favoring toward the bottom

electrode (just as at the previous axial station), but the concave region at the top

electrode wall has become more pronounced (just as with the velocity profiles). The region with the highest Mach number is near the center of the channel—a combination of the high-speed and low temperature flow. Because of the extremely high temperatures near the bottom electrode wall (as seen in Figure 5.39), the Mach number is proportionally lower in this region than the overall flow velocity. This translates into a Mach number profile that is more "centered" in the channel than the velocity profile. Furthermore, the low temperature regions between the mid-line and the insulator walls effectively "spread out" the Mach number profile across the width of the channel, with the Mach number lowering in the higher-temperature and lower-velocity sidewall regions.

5.4.2.4 Total Pressure

In Figure 5.17, the cross-sectional averaged total pressure falls while the center-line total pressure increases, for the $100\,\mathrm{A}$ case. This indicates that there should be a large difference between the center-line total pressure and the near-wall total pressure. Figures 5.42 and 5.43 show exactly that—the total pressure in the central portion of the MAPX channel increases, while the total pressure outside the central region decreases. Total pressure in the UMM code is calculated using Equation 4.61, where one should recall that, because of the parabolic assumption in the MGMHD and UMM codes, the static pressure, P, is assumed to be constant across a cross-sectional plane in the channel. Also recall that the inlet static pressure is a user-defined input—which for this MAPX case (as shown in Table 5.2) is $3.24240 \times 10^5\,\mathrm{Pa}$ (or, $3.2\,\mathrm{atm}$).
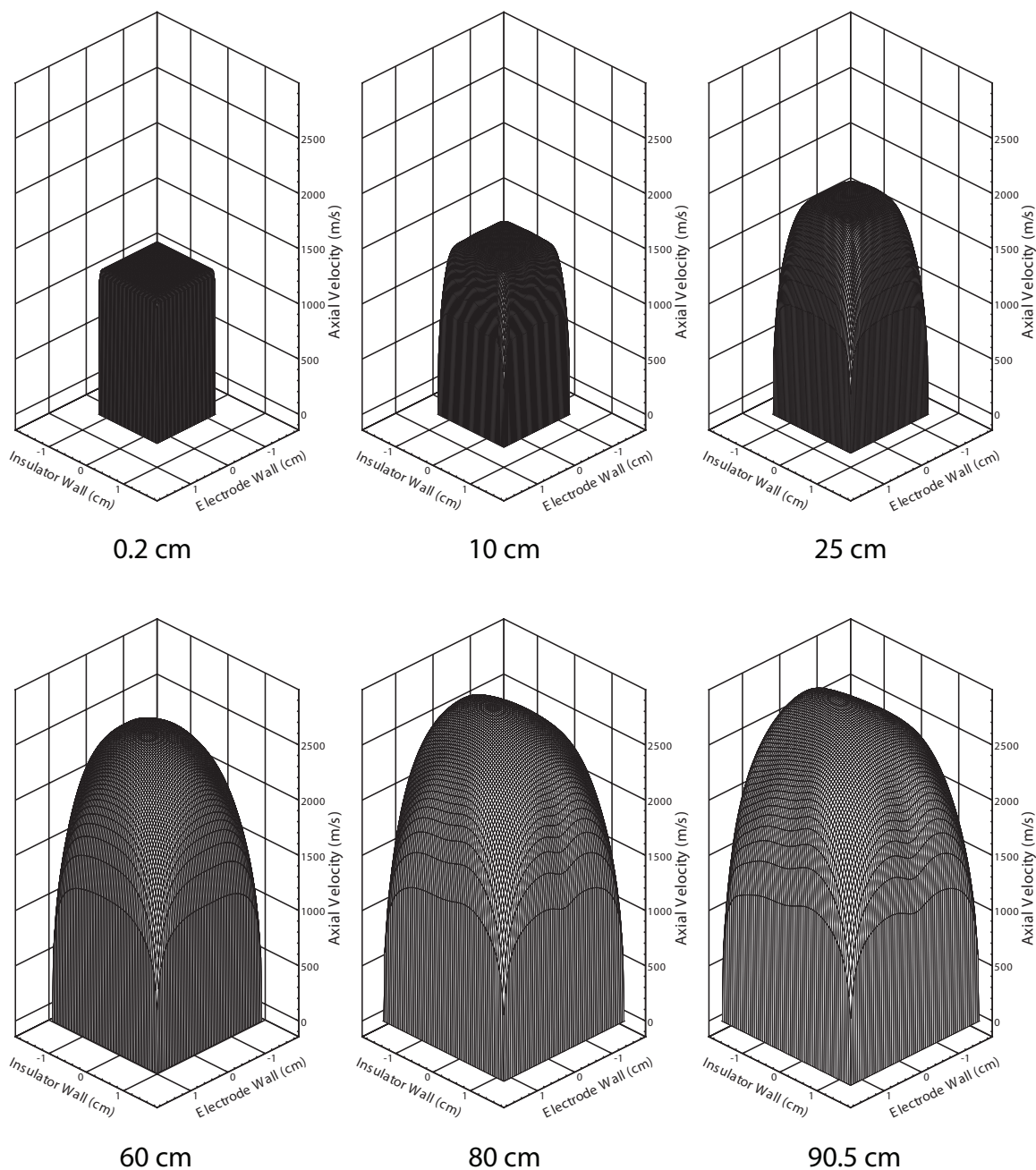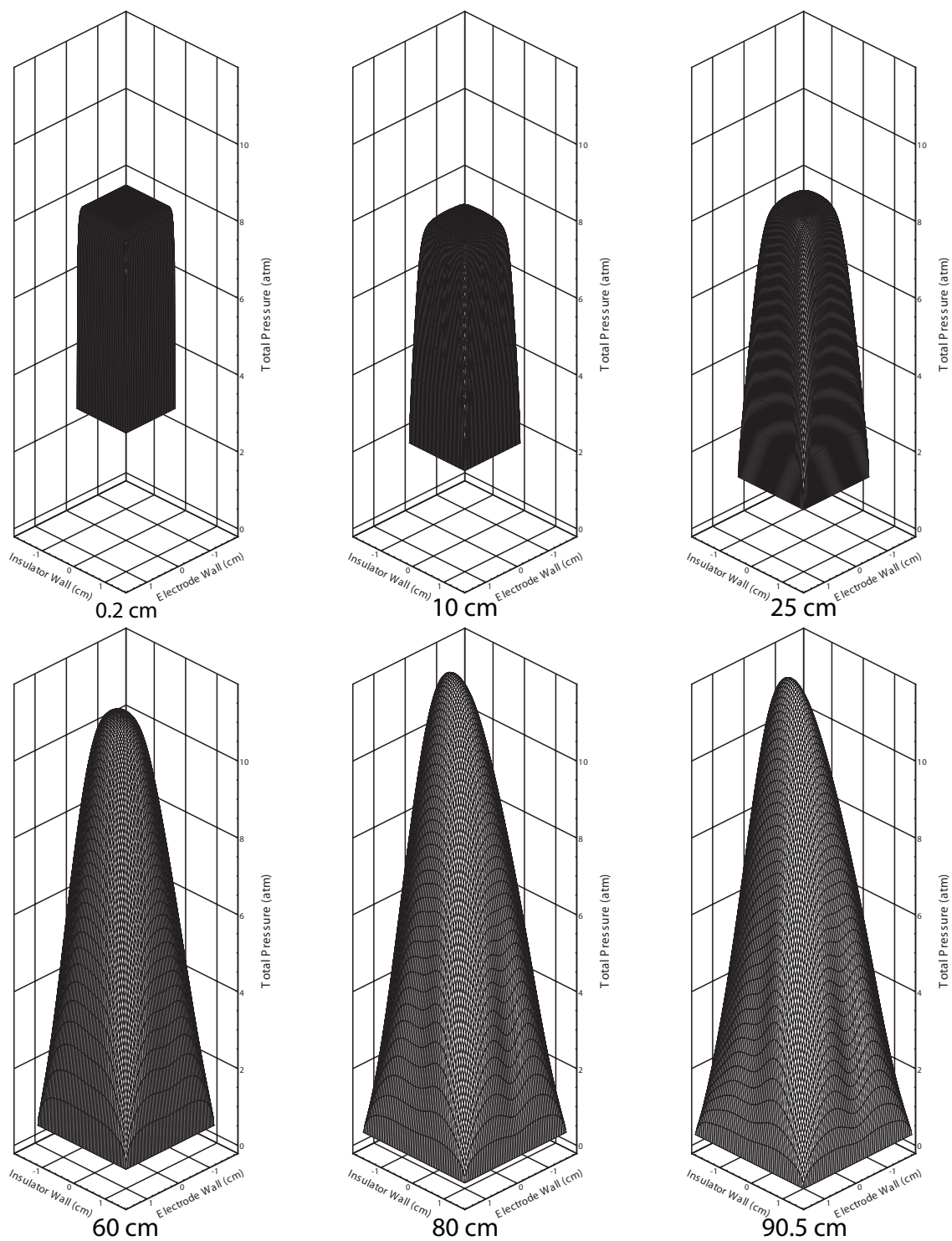
Figure 5.42: Three-dimensional total pressure plots at 0.2, 10, 25, 60, 80, and 90.5 cm along the MAPX channel. The last position is the channel exit. The positive J_y current flows from the bottom electrode (in the background) to the top electrode (in the foreground), which is out of the page.
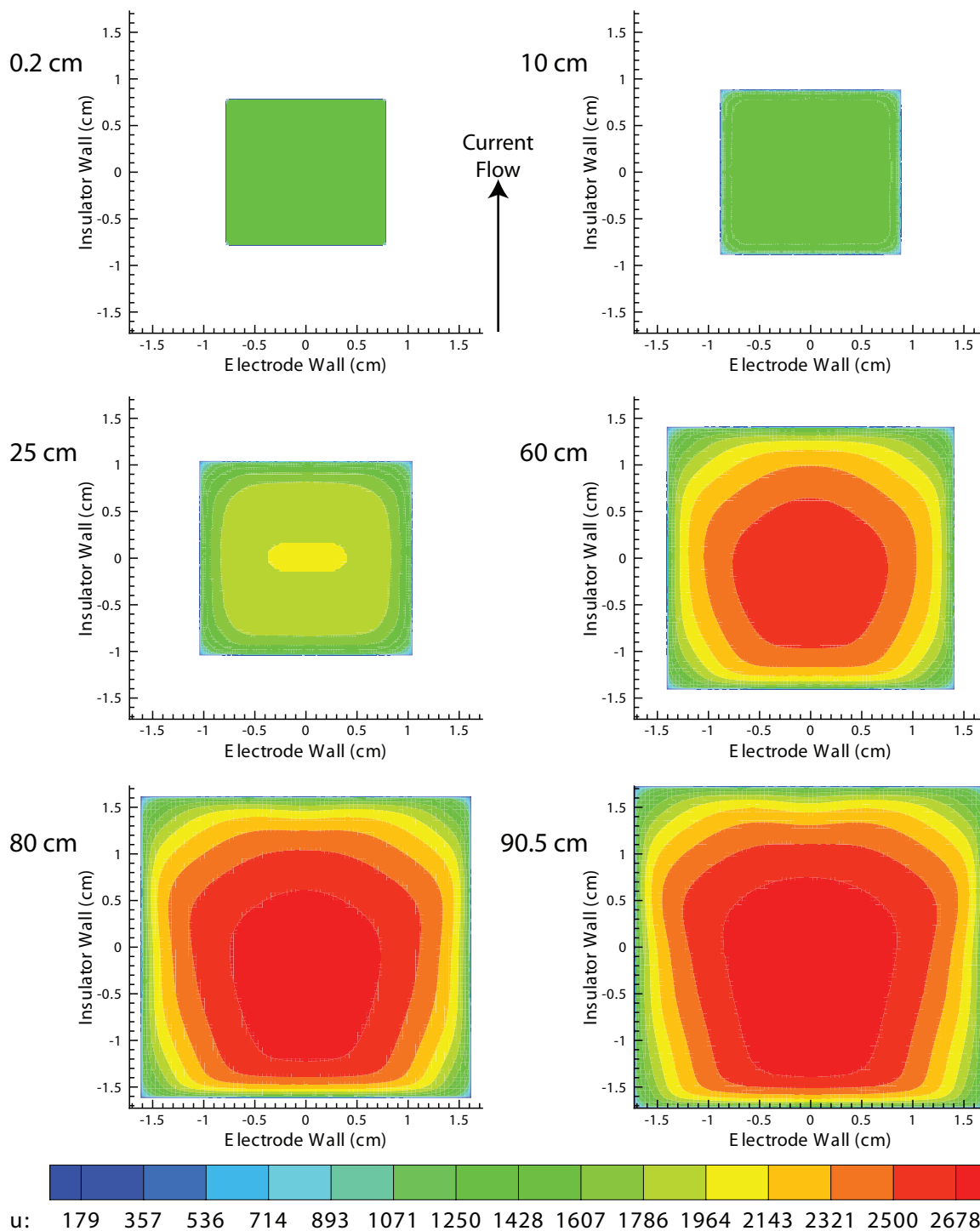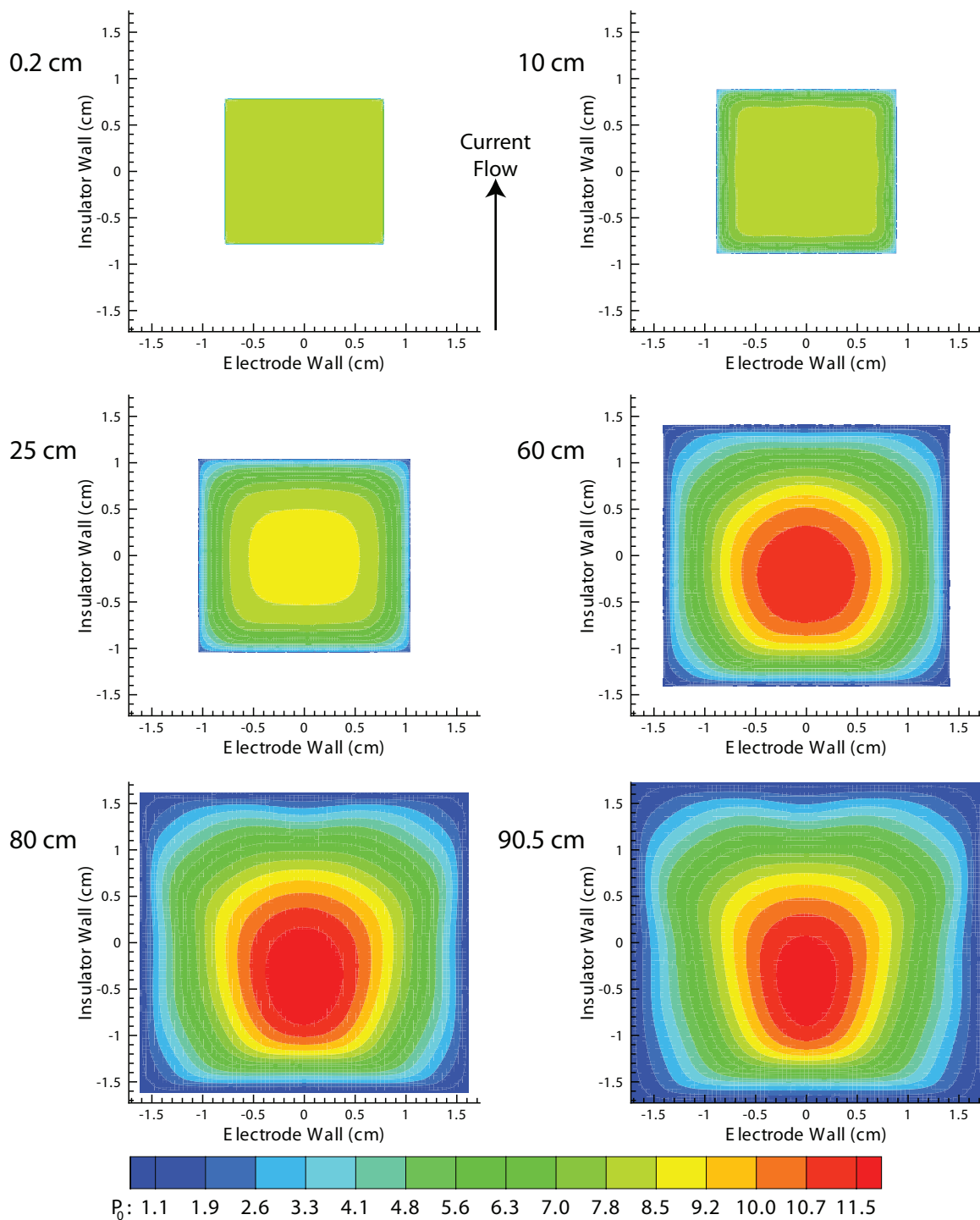
Figure 5.43: Contour plots of total pressure, P_0, in atm, at 0.2, 10, 25, 60, 80, and 90.5 cm along the MAPX channel. The last position is the channel exit. The bottom and top electrodes are oriented correctly, with the positive J_y current density flowing upward in each graph.

Just as with Mach number and velocity (and because the static pressure is assumed to be constant across a cross-sectional plane in the channel), the total pressure profile at 2 mm in Figures 5.42 and 5.43 is also a constant. At 10 cm, the flow is undergoing some entrance fluctuations (as seen by the wavy lines in both Figures 5.42 and 5.43), and the profile still remains constant across most of the channel. Figure 5.43 shows that the pressure near the walls has already fallen by a couple atmospheres, but more interesting is that the core flow has also fallen slightly from the entrance level, as Figure 5.42 shows. This is most likely due to a rapid decline in the static pressure (see Figure 5.15), combined with a slow increase in velocity (and therefore Mach number). It is not until approximately 25 cm that the central flow finally recovers to its entrance total pressure value. At this location, however, the near-wall flow has fallen very low—the boundary layer is below 2 atm, while just outside the boundary layer the total pressure is just above 3 atm.

At 60 cm, the total pressure profile has become very steep—the core flow has reached to approximately 10 atm, while the near-wall flow has fallen to approximately 1 atm. Notice also that the total pressure profile in Figure 5.43 is beginning to lean towards the bottom electrode wall, just as the velocity profile. The total pressure profile at 80 cm downstream has shifted farther toward the bottom electrode. The core flow has increased in intensity, approximately 11.5 atm, but it has also decreased in overall size. There is very high pressure gradient between the core flow and the bottom electrode, and concave regions—just as with the velocity profile—are beginning to form. When the flow reaches the exit of the MAPX channel, according to Figure 5.42, the total pressure of the core flow has actually decreased slightly. Figure 5.43 shows

that the highest-total pressure region has decreased in size yet again, and concave regions along the top electrode and insulator sidewalls have become more pronounced.

From Equation 4.61, it is logical for the total pressure to display the same profile characteristics as the velocity depicted in Figures 5.35 and 5.36, especially when one considers that the static pressure is a constant across a cross-sectional plane. Through the Mach number, total pressure is directly related to axial velocity. Therefore, it is logical to assume that the total pressure is influenced by some of the same parameters that influence axial velocity—namely, that secondary flows push the core flow (and highest total pressure region) toward the bottom electrode, creating a very steep total pressure gradient near that wall. However, a simple inspection of Figures 5.35 and 5.42 shows that the total pressure falls victim to more near-wall losses than does axial velocity. It is obvious from Figures 5.35 and 5.36 that frictional forces dominate the total pressure profile in the channel—the surface to volume ratio inside the MAPX accelerator is much too high.

5.4.2.5   Electrical Conductivity

Just as the electrical conductivity functions in Figure 5.21 follow the temperature functions in Figure 5.13, the contour plots of electrical conductivity in Figure 5.44 are very similar to the contour plots of temperature in Figure 5.39. As previously stated, an increase in temperature causes a dramatic increase in electron number density, which is directly proportional to the electrical conductivity of the flow.

At 0.2 and 10 cm, the electrical conductivity is low, and basically a constant across the cross-section. It is not until 25 cm that the contour plot begins to indicate
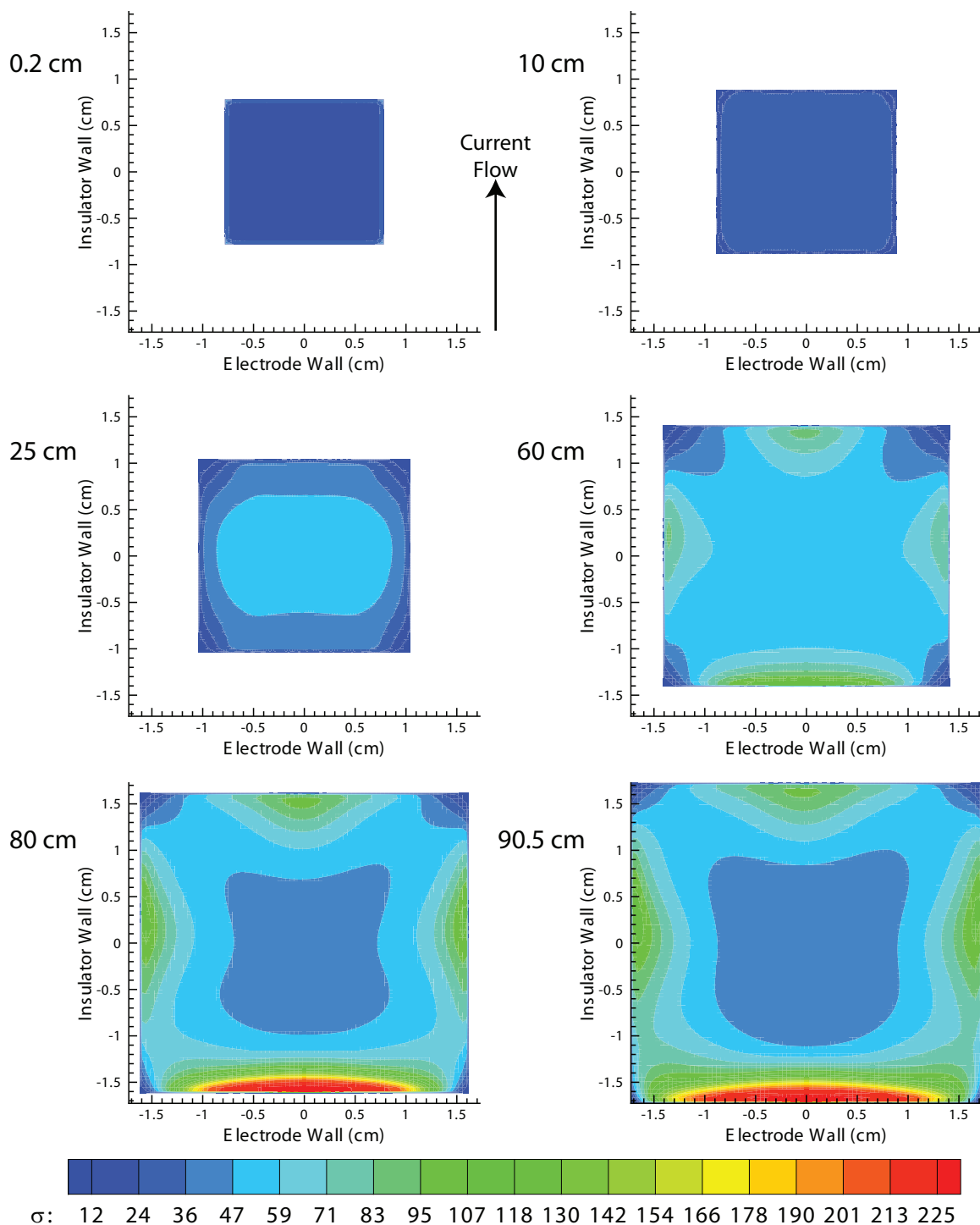
Figure 5.44: Contour plots of cross-sectional electrical conductivity, σ, in S/m, at 0.2, 10, 25, 60, 80, and 90.5 cm along the MAPX channel. The last position is the channel exit. The bottom and top electrodes are oriented correctly, with the positive J_y current density flowing upward in each graph.

some difference in the profile across the channel. The conductivity profile at 25 cm has the same basic form of the temperature at that same point—the central region has the highest values, with the corners having the lowest. At 60 cm, the mid-points of the near wall regions have the highest conductivity values (just as with temperature), with the core flow having lower conductivity, and the corners still having the lowest. At 80 cm, a very high electrical conductivity region has formed at the bottom electrode, matching the "hot spot" seen in Figure 5.39. The mid-points of the other walls also retain descent conductivity, with the conductivity of the core flow lowering with the temperature. Finally, at the exit of the MAPX channel, the high-conductivity region near the bottom electrode has grown in both intensity and size, just as the high-temperature region at the same location. The mid-points of the other walls remain at their previous conductivity levels, while the electrical conductivity of the core flow falls further. However, the corners remain the areas of lowest conductivity.

Generally speaking, in MHD channels (generators and accelerators), regions of high temperature (*e.g.*, near the walls) have regions of high conductivity, which is seen here. However, in most cases, regions of high conductivity are regions of high current density, which translates to regions of high Lorentz force, and therefore high velocity (assuming that the current flow promotes flow acceleration). However, while the velocity profiles in Figures 5.35 and 5.36 do show that the velocity is higher in the lower half of the accelerator, there are no velocity overshoots in the high-temperature and high-conductivity region—on the contrary, the axial flow velocity actually slows slightly as it enters this region of the channel. As seen in Figures 5.42 and 5.43, frictional forces play a large roll in the flow development in the accelerator; therefore,

these sources of entropy might be one of the factors preventing velocity overshoots at the bottom electrode.

5.4.2.6 Hall Parameter

The Hall parameter, β, has an interesting profile, shown in Figure 5.45. In the UMM code, the Hall parameter is calculated using Equation 3.77, which leads one to believe that the Hall parameter is directly proportional to the electrical conductivity. However, substituting Equations 4.10 and 4.11 for conductivity and diffusion coefficient, respectively, gives a different story. Perhaps the best way to visualize the Hall parameter is through Equation 1.17, where β is inversely proportional to electron number density and electron mean random thermal velocity—which basically implies that the Hall parameter is inversely proportional to temperature, which can be seen by comparing Figures 5.39 and 5.45. Physically, the Hall parameter can be thought of as a ratio of the electron's gyro frequency to its collision frequency—therefore, a high β indicates that the electron is influenced by the magnetic field more than it is by particle collisions.

In Figure 5.45 at 2 mm and 10 cm, just like most parameters, the Hall parameter is at a low level and constant across the entire cross-sectional plane. At 25 cm, the central flow has a lower Hall parameter than the corner and wall regions of the flow—the inverse of temperature. As the flow progresses to 60 cm, the Hall parameter in the central region (and most of the cross-section) has increased to approximately 2.5, while the region near the bottom electrode has the lowest Hall parameter of approximately 1.6. The corners remain the regions of highest Hall parameter, with
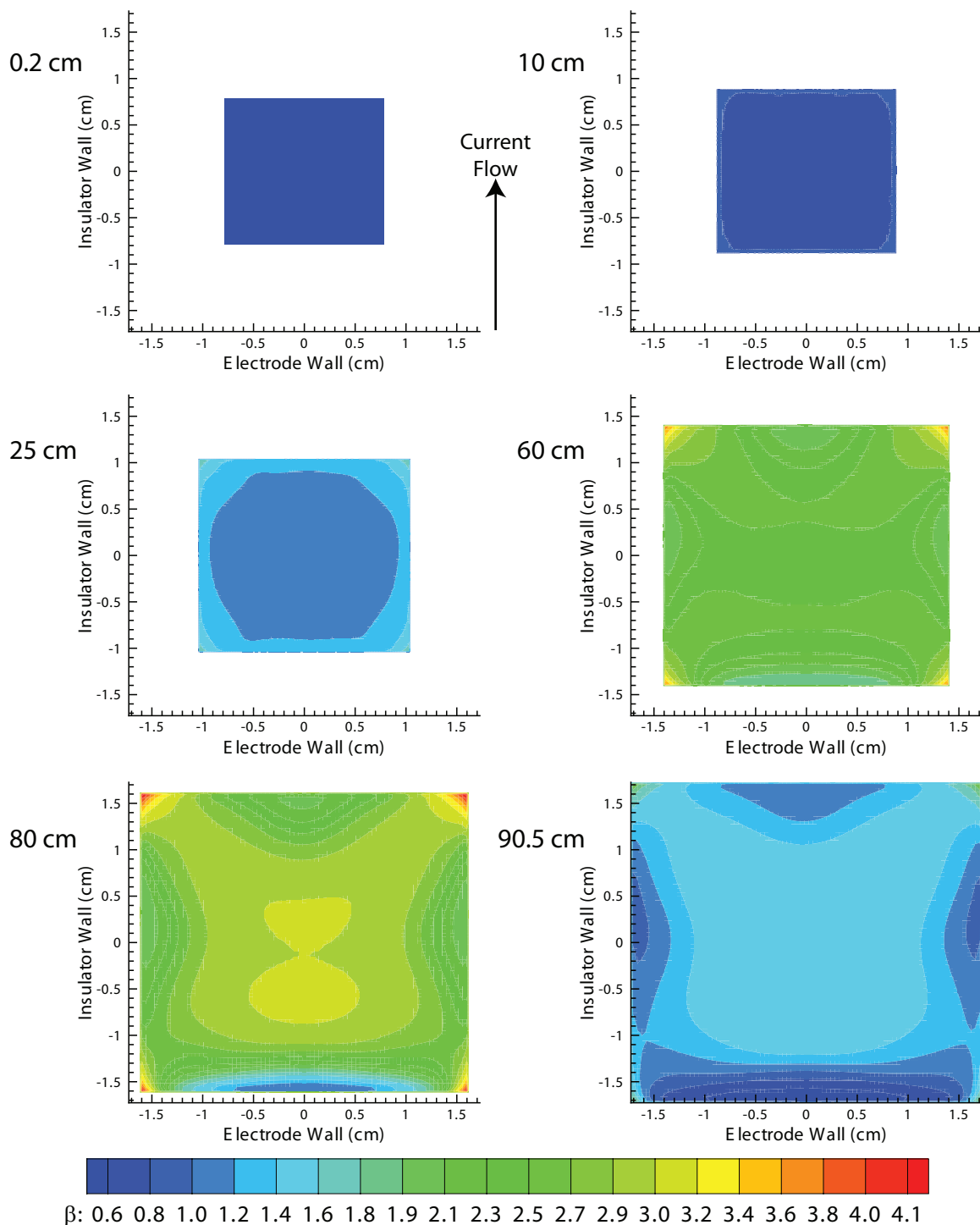
Figure 5.45: Contour plots of cross-sectional Hall Parameter, β, at 0.2, 10, 25, 60, 80, and 90.5 cm along the MAPX channel. The last position is the channel exit. The bottom and top electrodes are oriented correctly, with the positive J_y current density flowing upward in each graph.

values as high as 4, with bands of moderately high Hall parameter (that correspond to areas of low temperature) connecting the corners. At 80 cm, the corner regions (especially near the top electrode) have increased in Hall parameter value and size. The core flow, corresponding to areas of lower temperature, have moderately high Hall parameters. The near wall regions, with their higher temperatures, have low Hall parameters, and the lowest Hall parameters are seen at the bottom electrode, corresponding with the hot spot seen in Figure 5.39. At the exit, the Hall parameter has dropped over the entire cross-section. Recall from Figure 5.9, that the magnetic field attenuates at the exit of the MAPX channel. From Equations 1.17 and 3.77, the Hall parameter has a strong dependence on the magnetic field inside the channel. However, even with the sharp drop in magnetic field, the same profile still exists at the exit of the channel. The lowest Hall parameter is at the bottom electrode (where the temperature is highest), with the mid-points of the other walls also having low Hall parameters. The core flow region has slightly higher Hall parameter values, with the top corners of the MAPX accelerator having the highest Hall parameters. Fluctuations in the Hall parameter, such as those seen in the MAPX accelerator, can destabilize the acoustic waves in the magnetic field [178].

5.4.2.7 Electric Potential

Because the UMM and MGMHD codes utilize Maxwell's steady state equations, the electric field can be defined as the negative of the gradient of potential, ψ, as in Equation 3.33. The electric potential is a scalar quantity, but should not be confused with potential energy, which is a completely different parameter. Since the

electric field defines the direction of the current flow, the gradient of the potential can also be used to determine which direction the current will flow. Note, however, that because the electric field is the negative of the gradient of the electric potential, positive current will flow from areas of low (or negative) potential to areas of higher (or positive) potential.

Figure 5.46 shows the electric potential at 0.2, 10, 25, 60, 80, and 90.5 cm along the MAPX channel. Near the entrance of the channel, the potential results from the externally applied current (which, in practice, is a voltage, or potential, applied across the channel). The first location in Figure 5.46, 2 mm, is near the channel entrance and still inside of the power takeoff (PTO) region. Therefore, the externally applied current/field is not at full power, which is why only a small potential difference is seen. At 10 cm, the flow is past the PTO region; therefore, a negative potential has developed along the bottom electrode and a positive potential along the top. Farther downstream, at 25 cm, the rather intense negative and positive potentials have developed along the sidewalls near the bottom and top electrodes, respectively. At 60 cm these potential locations have migrated toward the center-line of the channel, with potentials of the opposite sign developing in the wake of their movement (at the top and bottom electrodes). The potential distribution at 80 cm has become less intense, now with a high potential at the bottom electrode and a lower potential near the top electrode (and an area of low potential in between). At the channel exit, the potential has essentially reversed from the forward end of the channel. There is an area of lower potential near the top electrode and an area of higher potential near the
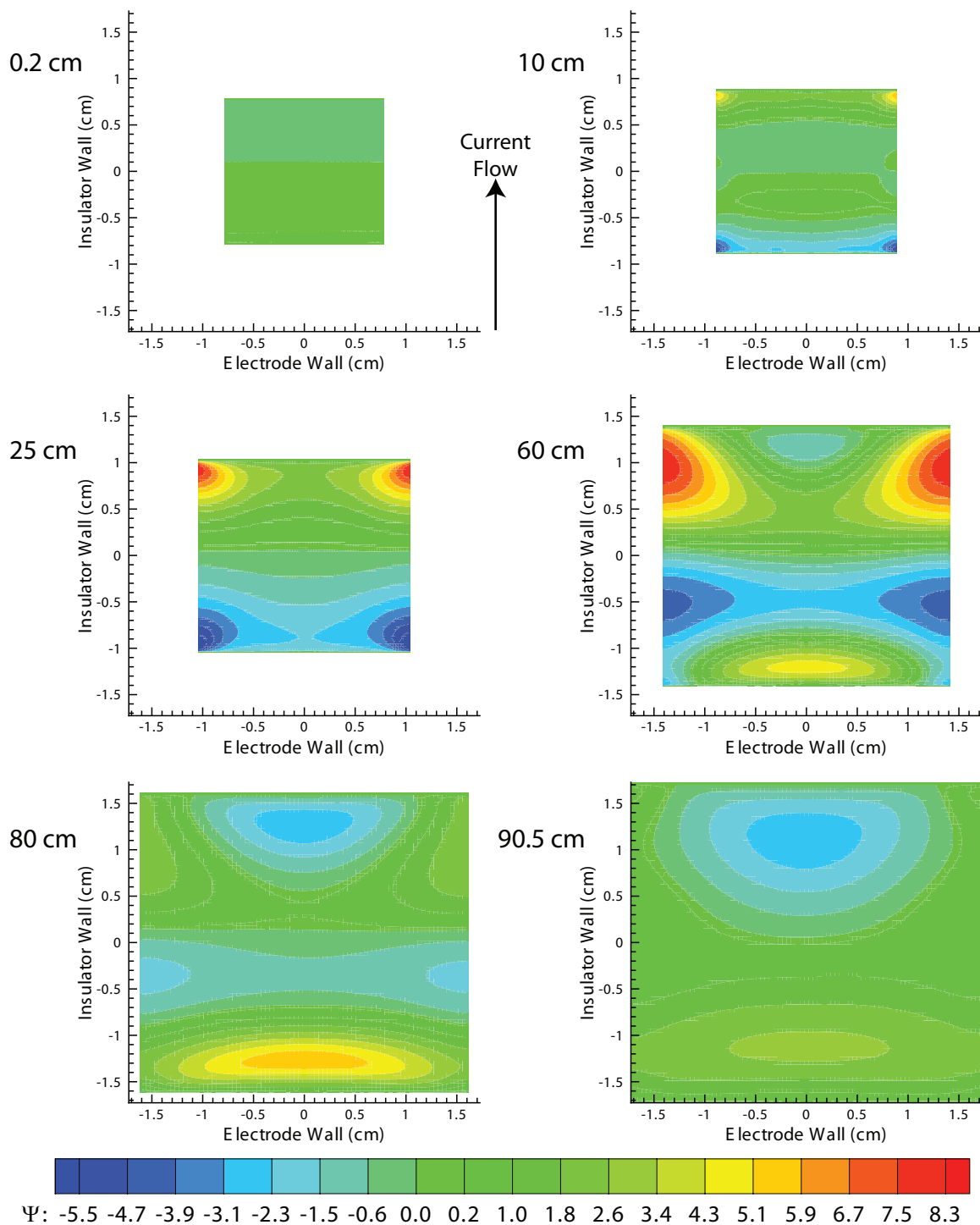
Figure 5.46: Contour plots of cross-sectional potential, ψ, in V, at 0.2, 10, 25, 60, 80, and 90.5 cm along the MAPX channel. The last position is the channel exit. The bottom and top electrodes are oriented correctly, with the positive J_y current density flowing upward in each graph.

bottom. Furthermore, the difference between the two potential zones, or the gradient between them, is not high.

When viewing Figure 5.46, it is important to remember that while the electric potential is a scalar quantity (a single number without direction), the gradient of that potential is a three-dimensional vector with magnitude and direction. Therefore, it is important to look at the potential as it changes from one axial location to the next. For instance, along the bottom of the channel, the potential starts positive and becomes increasingly negative from $2\,\mathrm{mm}$ to $10\,\mathrm{cm}$ to $25\,\mathrm{cm}$, which would set up an electric field in the negative axial direction, and may cause an axial current, J_x, to flow in the negative direction. Furthermore, from 25 to 60 to $80\,\mathrm{cm}$, the potential near the bottom electrode becomes a higher value, which would set up an electric field in the positive axial direction, and should result in an axial current flowing in the positive axial direction. The same can be said for the top electrodes—at $60\,\mathrm{cm}$, there is a very high potential located near the corners at the top electrode wall, but at $80\,\mathrm{cm}$, that area has lowered in potential. From this, it can be assumed that an electric field would exist in the negative axial direction, which could cause a negative axial current to flow. Moreover, notice how the high potential regions at $25\,\mathrm{cm}$ are much closer to the upper corners than the high potential areas are at $60\,\mathrm{cm}$. Therefore, in the small area around the top corners, there should be a negative E_x field which would result in a negative J_x current density.

As discussed in Section 5.3.3, areas of high current are generally areas of low electric field. Since current and temperature are directly related, and since electric field and potential are directly related (excluding the sign change), it can be assumed

that with higher temperature comes a lower gradient in the potential, and vice versa. Figure 5.47 shows the temperature contour, as in Figure 5.39, but with an electric potential overlay—solid lines represent positive lines of potential and dashed lines represent negative lines of potential, with more intense gradients being represented by lines that are closer together. Furthermore, since the 2 mm location is not particularly interesting (for temperature or potential), it is excluded, and the 45 cm location is shown.

Looking at Figure 5.47 (and Figure 5.46) since the 10 cm location seems to have a low gradient in potential, one would expect high current. The temperature at that location is not relatively high, but one must remember that it is near the entrance of the channel. At 25 cm, the potential has grown somewhat, but still rather low—the temperature has increased over most of the core of the channel, meaning that one should still expect to see descent levels of current flow. The areas of low temperature in the upper corners at 45 cm correspond with the areas of high gradients in potential, as one would expect. The same is true at 60 cm, where the upper corners have high potential gradients, but low temperature. Also, note the early development of the "hot spot" region near the bottom electrode. At this location, the temperature is not yet very high; therefore, the gradient in potential is higher. The high-temperature region at the bottom electrode has formed at 80 cm, and the gradient in potential at that location has decreased. Note, the value of the potential at the bottom electrode increased from 60 cm to 80 cm, but the gradient at that cross-section (the inverse of the distance between the lines) decreased. At the channel exit, the gradient in potential is low, and the hot area near the bottom electrode has increased in size.
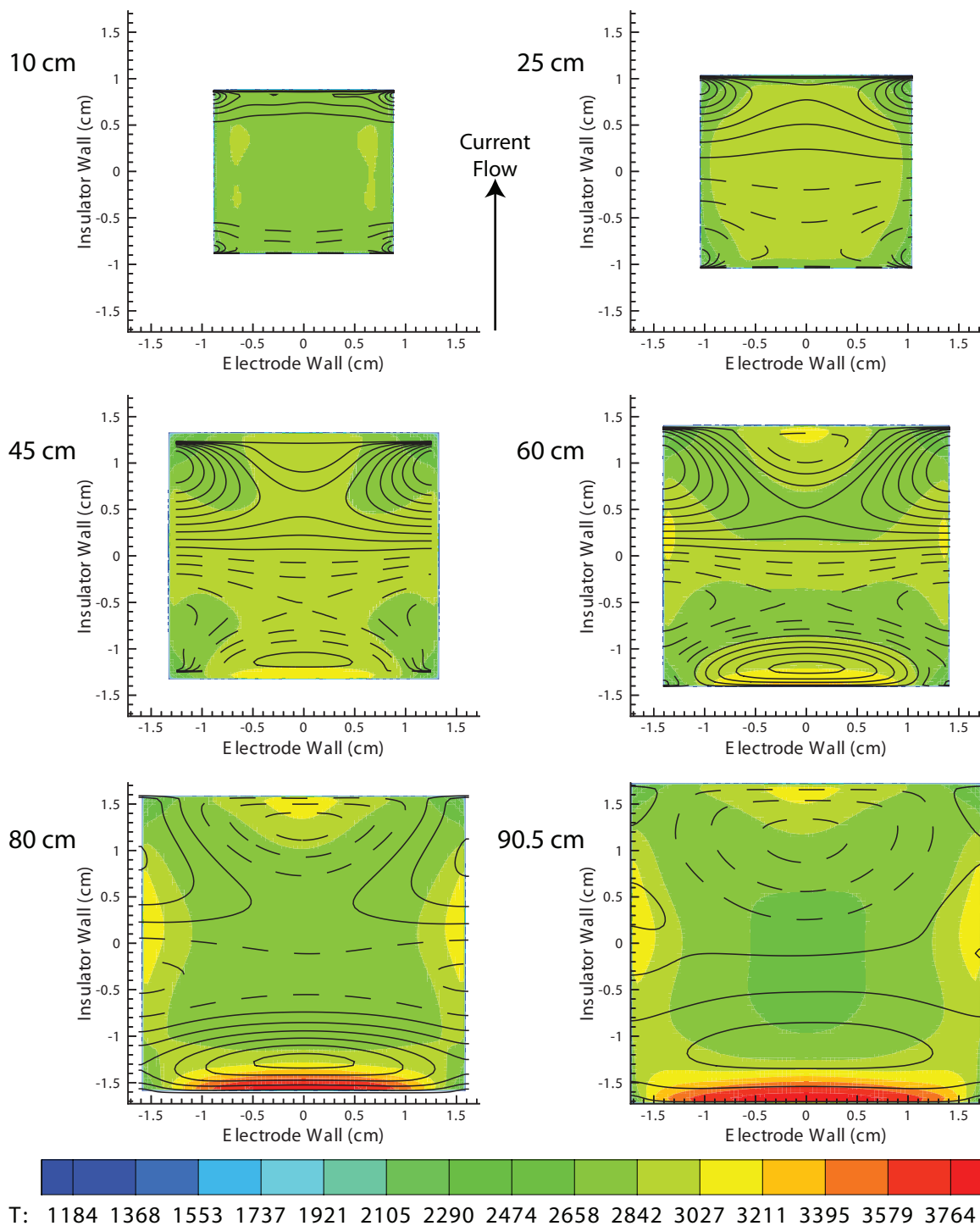
Figure 5.47: Contour plots of potential, ψ, with a temperature, T in K, overlay, at 10, 25, 45, 60, 80, and 90.5 cm along the MAPX channel. J_y current flows upward (bottom to top) when in accelerator mode. For the potential, the dashed lines represent negative values, while the solid lines represent positive values.

5.4.2.8   Transverse, J_y, Current Density

The J_y current density is sometimes referred to as the "pushing" current in MHD accelerators (as it provides the current for the J_yB accelerating Lorentz force). Figure 5.24 shows the J_y current density as a function of axial location (for cross-sectional averaged and center-line values). The graphs show that, after the PTO entrance region, the J_y current density steadily declines as the flow travels downstream. As explained, this is due to an opposing electric field which is set-up in the negative $\hat{\mathbf{y}}$ direction (opposes the externally applied electric field), which results from the $\mathbf{u} \times \mathbf{B}$ Lorentz force. It is also important to note that in Figure 5.24, the J_y current density for the $100\,\mathrm{A}$ case seems to remain positive over the length of the channel (as opposed to, for example, the $175\,\mathrm{A}$ case, which becomes negative just after $60\,\mathrm{cm}$).

Figure 5.48 shows the three-dimensional contour plots of the J_y current density at various locations. Obviously, since it is inside the PTO region, the J_y current density at $2\,\mathrm{mm}$ is low. The current density at $10\,\mathrm{cm}$ has the highest magnitude of any location in the channel. This is consistent with the graphs in Figure 5.24, and with the low gradient in potential in Figure 5.46. Furthermore, the two most intense regions (centered on the center-line, and equidistance from the mid-line, near the insulating sidewalls) are consistent with the two higher-temperature regions in Figure 5.39 at the same location. Higher J_y current density in the core flow region has been seen in previous research, and stems from current shunting in the colder boundary layer and current transfer to-and-from the sidewalls [140]. The current density at $25\,\mathrm{cm}$ is
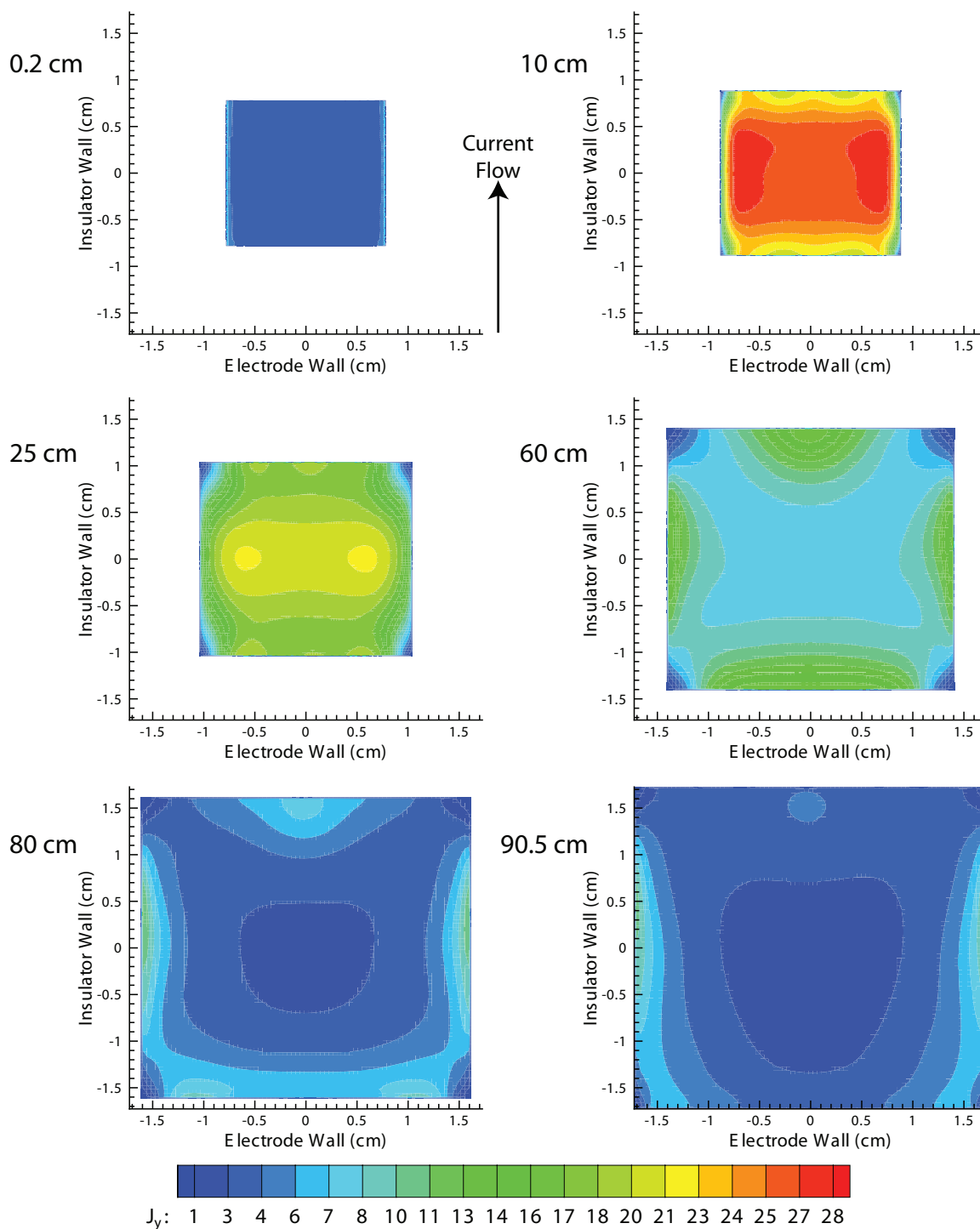
Figure 5.48: Contour plots of current density, J_y in A/cm^2, at 0.2, 10, 25, 60, 80, and 90.5 cm along the MAPX channel. The last position is the channel exit. The bottom and top electrodes are oriented correctly, with the positive J_y current density flowing upward in each graph.

of the same form as the last location, however with lower intensity, as expected. At 60 cm, the areas of higher J_y coincide with the areas of higher temperature at that same location (the reverse is also true). The current density at 80 cm is quite low, as predicted in Figure 5.24, even near the walls. Therefore, the "hot spot" (high-temperature region) near the bottom electrode in Figure 5.39, is not due to the J_y current density. At the channel exit, the J_y current density has fallen drastically, but remains positive. The highest areas are along the sidewalls, and at the center of the top electrode. Large current fluctuations like those seen in the MAPX channel cause uneven acceleration and flow fluctuations [105], such as those seen in Figures 5.35 and 5.36.

Because J_y and J_z flow in the cross-sectional plane, they can be visualized just as the secondary fluid flow in Figure 5.37. Figure 5.49 shows the J_y and J_z current density vectors at the various cross-sectional planes. Ideally, an MHD accelerator would be designed such that the J_y current would flow straight from the bottom electrode to the top electrode, essentially eliminating J_z. When the current deviates from straight-up-and-down, it will tend to accumulate in one area on the electrode, which increases temperature and the chances of electrode erosion. Impurities and erosion on the surface of electrodes can actually, in the short term, emit electrons easier than normal [100]; however increased current flow due to erosion quickly escalates until the electrode suffers irreparable damage. Furthermore, an ideal MHD accelerator would have a strong positive J_y current through the length of the channel, feeding the $J_y B$ Lorentz force.
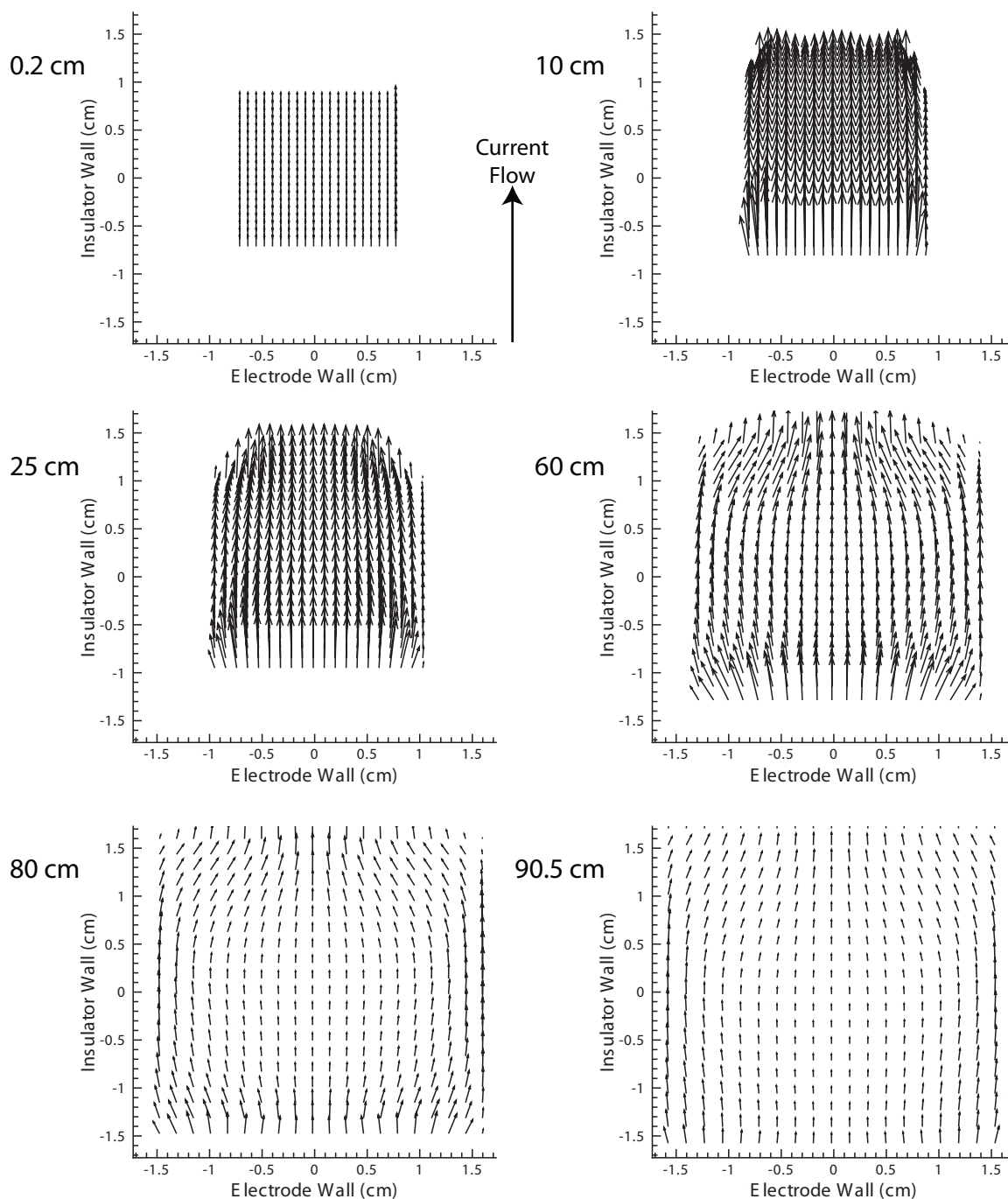
Figure 5.49: Vector plots of current flow, J_y and J_z, in the cross-section at 0.2, 10, 25, 60, 80, and 90.5 cm along the MAPX channel. The last position is the channel exit. The bottom and top electrodes are oriented correctly, with the positive J_y current density flowing upward in each graph. The length of the vector represents a relative intensity.

The J_y current density in the MAPX accelerator represented in Figure 5.49 accomplishes one of those goals—for most of the channel, the current is essentially straight-up-and-down, with very little deviation in the $\hat{\mathbf{z}}$ direction, and very little accumulation. At 2 mm, the current is low because of the PTO entrance region. As shown in Figure 5.48, at 10 cm the J_y current has its greatest magnitude, which is echoed in Figure 5.49. At 25 cm, the current density has lowered, in part due to the increase in cross-sectional area. One can also see that the current is bending toward the center of the electrodes (away from the lower-temperature corners). The current density at 60 cm looks as one would expect from Figure 5.48—leaving the central region of the bottom electrode, traveling mostly along the sidewalls, and entering the central portion of the top electrode. If the magnitude of the current density were higher, erosion might be a problem, but as Figure 5.48 shows, the current density is approximately 15 A/cm². This same current formation exists at 80 cm, with a lower magnitude; which is also true at the channel exit.

Even though the magnitude of the J_y current density falls as a function of downstream distance, as Figure 5.49 shows, the direction of the current remains positive through the entire length of the channel. This is very important for an MHD accelerator, because current flowing in the negative direction results in a generator mode of operation. It is true that most "real world" MHD accelerators would have physical mechanisms in place to prevent current from flowing in a negative direction through the external circuit; however, current can flow in a negative direction inside the channel, as shown by the 0.0 A case in Figure 5.24. The current flow seen in Figure 5.49 is not very intense in the downstream regions of the MAPX channel, but

its direction and distribution are almost ideal for a square channel with insulating sidewalls [179]. Furthermore, having some positive J_y current flow, even as little as at the exit of the 100 A case, is better than having no positive J_y current flow at all.

Take, for example, Figure 5.50, which is the J_y and J_z current density vector plots for the 175 A case. (Note: the J_y and J_z current density vector plots for the first 40 cm of the MAPX channel are very similar to those of the 100 A case, and are therefore not shown.) Notice that at 45 cm, the current vectors are mostly in the positive $\hat{\mathbf{y}}$ direction, as they should be. At 60 cm, (where, according to Figure 5.24, the cross-sectional averaged current density is near zero), large areas of current circulation emerge just below the center-line of the channel. The current begins to flow in the negative direction at 65 cm, with small amounts of current flowing in the positive direction near the top electrode. At 70 cm, all of the J_y current density is now pointed in the negative direction—flowing from the top electrode to the bottom electrode, which is the generator mode of operation (actually, at 60 cm, most of the channel is acting like a generator). The negative current density increases at 80 cm downstream, with large amounts of current flowing from the top to bottom electrode. From Figure 5.24, one notices that the 175 A J_y current density tries to recover, pushing toward positive numbers. This can be seen at the channel exit in Figure 5.50. So, for the 100 A case, the lower magnitude of the J_y current density in the downstream portions of the channel is not ideal, but it is better than cases where larger amounts of current are applied externally to the channel, resulting in negative current flow in the downstream locations.
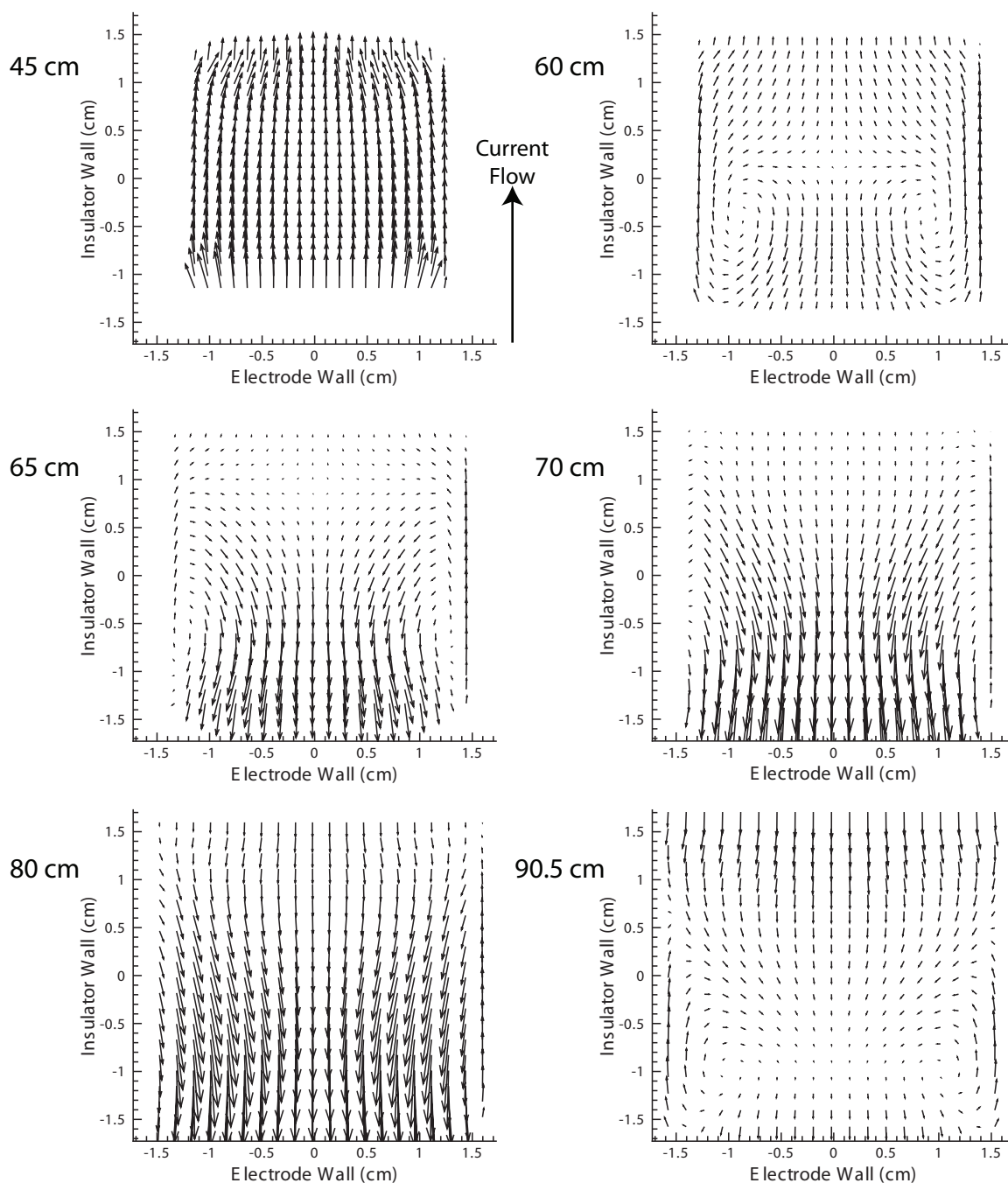
Figure 5.50: Vector plots of current flow, J_y and J_z, for the 175 A case, in the cross-section at 0.2, 10, 25, 60, 80, and 90.5 cm along the MAPX channel. The last position is the channel exit. The bottom and top electrodes are oriented correctly, with the positive J_y current density flowing upward in each graph. The length of the vector represents a relative intensity.

5.4.2.9 Axial, J_x, Current Density

The graphs in Figure 5.26 show a cross-sectional averaged axial current density, J_x, which is very close to zero, but a center-line axial current density with values as high as $70\,\mathrm{A/cm^2}$ for the $300\,\mathrm{A}$ case and $10\,\mathrm{A/cm^2}$ for the $100\,\mathrm{A}$ case. These graphs imply that there are strong opposing axial currents in the MAPX accelerator. Figures 5.51 and 5.52 show exactly that—the axial current density, while close to zero when integrated across the entire cross-section, does have very large differences and peaks. The plots show, for the $100\,\mathrm{A}$ case, that there are large opposing currents in the same cross-section, and these shift in magnitude and placement as the flow travels downstream.

Figure 5.51, at $2\,\mathrm{mm}$, shows high peaks in the axial current density in the boundary layer regions. This is a real effect, following the peaks in the temperature at that same location. At that position, the core flow is still relatively cold, and the low applied current has only had time to heat the region near the walls, thus producing J_x flow along the walls, in the positive axial direction. This behavior continues until approximately $2.5\,\mathrm{cm}$ downstream (not shown). At $10\,\mathrm{cm}$, Figures 5.51 and 5.52 show a flat, approximately $7\,\mathrm{A/cm^2}$, current density profile across much of the core flow, with negative axial current in the near-electrode regions, as was seen by Vanka and Ahluwalia [126]. Remember, averaged across the entire cross-section, the axial current density is approximately $0.002\,\mathrm{A/cm^2}$ at this location (according to Figure 5.26), which seems quite unbelievable, until one realizes that the intensity of the negative current density near the electrodes is in excess of $-10\,\mathrm{A/cm^2}$. The reason

for the negative current near the electrodes is explained using the electric potential, in Figure 5.46, and the positive current density of the core flow can be explained through the simple diagram in Figure 1.8—the external current/voltage, even though it is transferred through the electrodes on the top and bottom of the channel, is applied over the length of the channel. Therefore, there is actually a large voltage, or potential, applied from end-to-end over the MAPX channel. Hence, local axial currents are unavoidable. The same profile is basically repeated at 25 cm; however, here, the peaks in the positive current profile are closer to the insulator sidewalls, where, at 10 cm, the peaks are closer to the electrode walls. Figure 5.52 shows an increase in the size/area of the negative current flow, at the electrodes. Furthermore, 25 cm is also where the core flow is at its hottest temperature, with the peaks along the insulator walls, and the current density is reacting appropriately.

By 60 cm in Figures 5.51 and 5.52, the current density profile is much different. There is now substantial positive current flow along the bottom electrode wall, with more positive current flow in the center of the top electrode wall, and in a band across the center-line of the channel, which coincides with the high-temperature regions seen in Figures 5.38 and 5.39. Strong negative current flow now exists in the corners of the channel, which is consistent with the movement and evolution of the electric potential values in those regions. At 80 cm, there is a huge spike in the positive axial current density along the bottom electrode. This is consistent with the high-temperature region seen at that same position. Positive current density regions also still exist at the centers of the sidewalls and the center of the top electrode—also consistent with regions of higher temperature. Finally, at the exit of the MAPX accelerator, a strong,
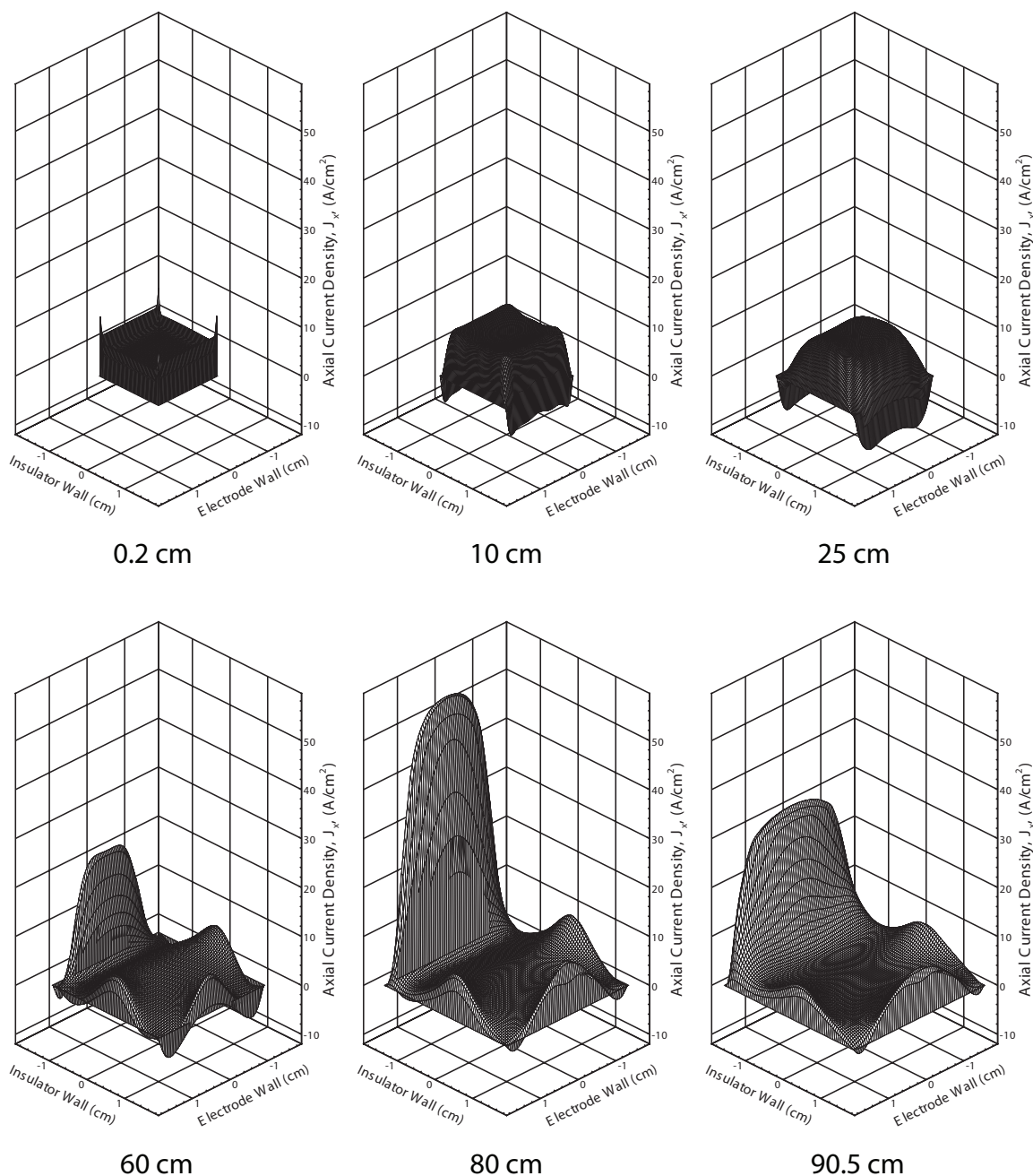
Figure 5.51: Three-dimensional axial current, J_x, plots at 0.2, 10, 25, 60, 80, and 90.5 cm along the MAPX channel. The last position is the channel exit. The positive J_y current flows from the bottom electrode (in the background) to the top electrode (in the foreground), which is out of the page.
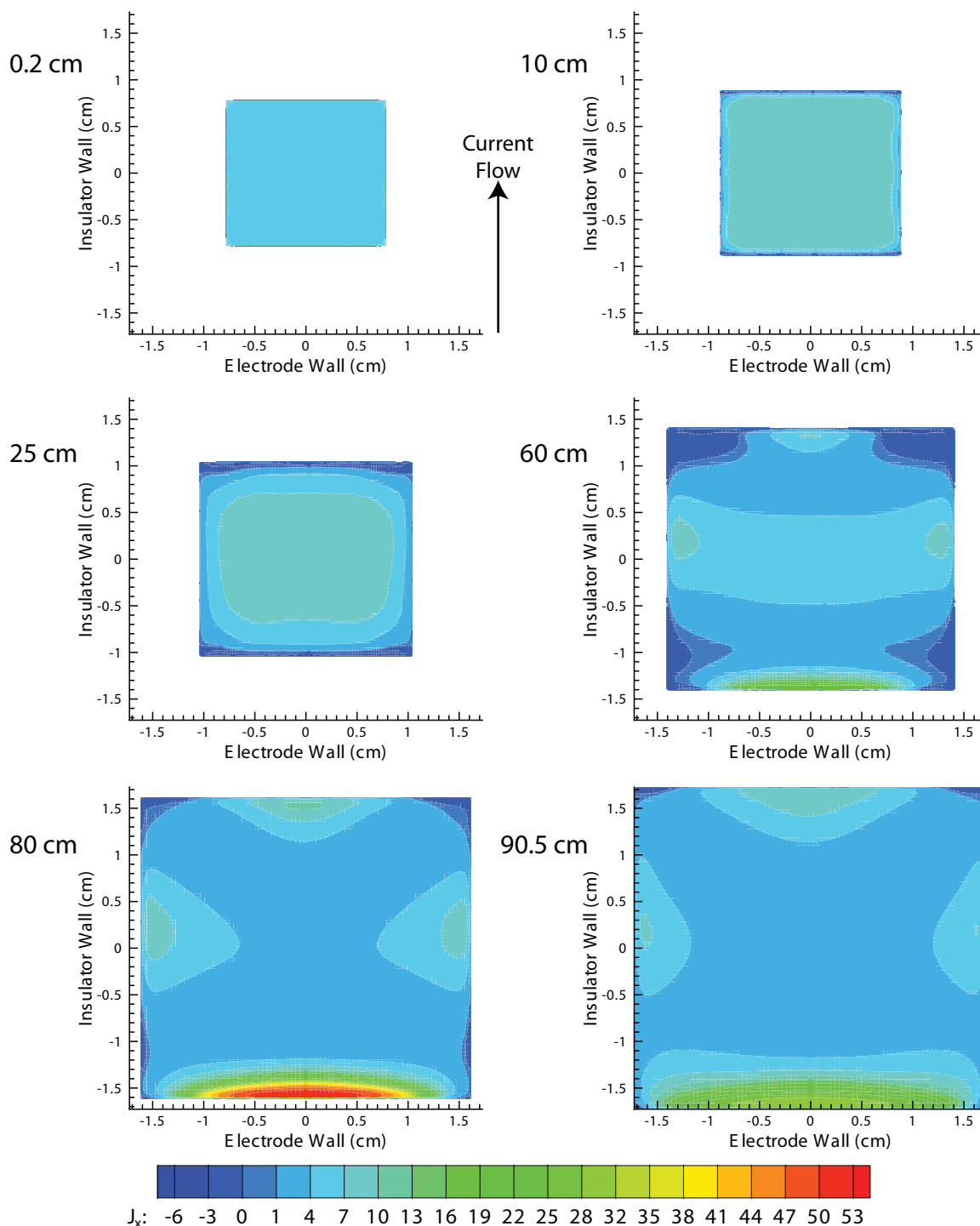
Figure 5.52: Contour plots of axial current density, J_x in A/cm^2, at 0.2, 10, 25, 60, 80, and 90.5 cm along the MAPX channel. The last position is the channel exit. The bottom and top electrodes are oriented correctly, with the positive J_y current density flowing upward in each graph.
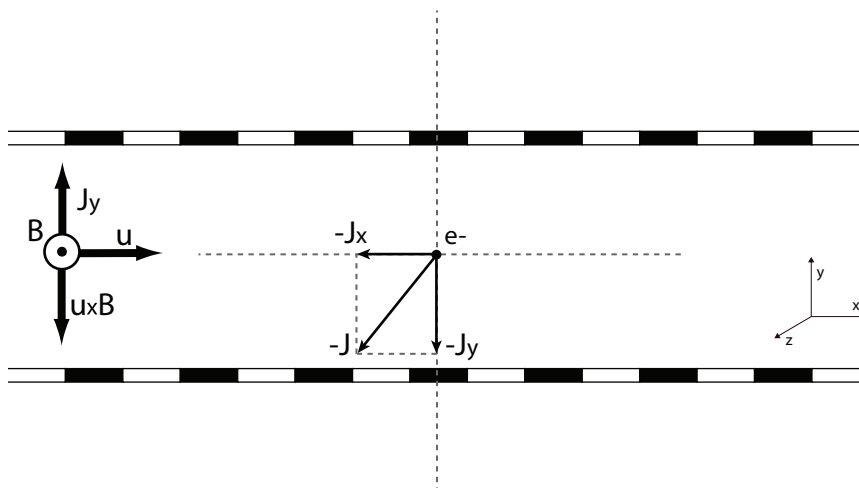
Figure 5.53: The resultant negative current (the direction an electron would flow) for the sum of $-J_y$ and $-J_x$.

but less intense, positive current density region still exists at the bottom electrode, with positive current density at the centers of the other walls. This is consistent with the higher-temperature regions, and the drop in potential seen at the end of the channel.

The physical ramifications of the axial current density are many. As the slow-moving flow enters the MAPX channel, it is influenced by the two primary current densities—J_x and J_y. (Note that, as shown in Figure 5.49, the J_z current density—into and out-of the insulating sidewalls—is very small and considered negligible). Therefore, the electrons in the flow (the more mobile of the charged particles by several orders of magnitude) are forced in a negative $\hat{\mathbf{y}}$ direction, and a negative $\hat{\mathbf{x}}$ direction. From Figures 5.48 and 5.52, it is evident that in the first half of the MAPX channel, the intensity of J_y is twice that of J_x, therefore the resultant "electron current" is two parts negative $\hat{\mathbf{y}}$, and one part negative $\hat{\mathbf{x}}$, as illustrated in Figure 5.53. Furthermore,
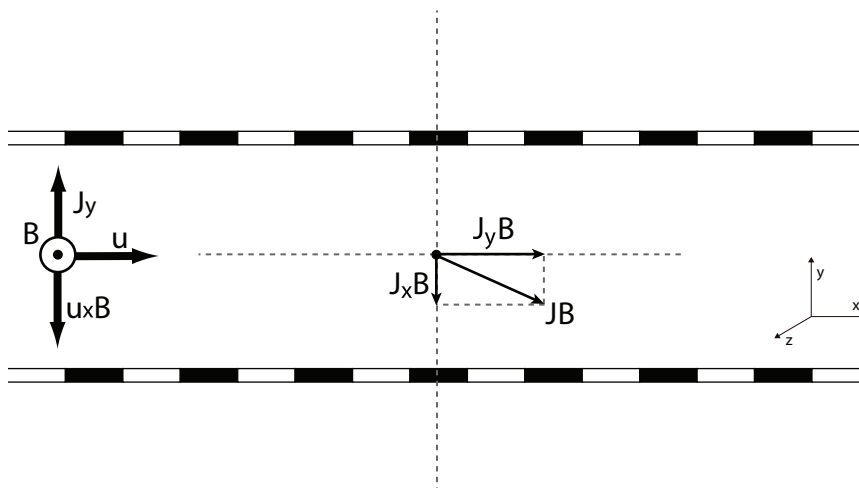
Figure 5.54: The resultant of the sum of the J_yB and J_xB Lorentz forces.

recall that the bulk of the flow is accelerating downstream, while the electrons are essentially being "held back" and pushed toward the bottom electrode by the positive axial and transverse current densities in the bulk of the flow. This results in a higher electron density, and therefore higher conductivity, near the bottom electrode.

The flow is accelerating primarily due to the expansion of the MAPX channel, and the pushing of the Lorentz force. In the entrance region of the channel, the J_y current density is high, as seen in Figure 5.48, and the magnetic field strength is high, as seen in Figure 5.9. This results in a high J_yB Lorentz force in the first half of the MAPX accelerator. However, the J_xB Lorentz force also influences the flow. In the core flow, the J_xB Lorentz force (with a positive J_x) would essentially push the flow in the negative $\hat{\mathbf{y}}$ direction. The $\hat{\mathbf{y}}$ directed velocities are acted on by the J_xB Lorentz force, just as the axial velocity is acted on by the J_yB Lorentz force [126]. As stated, in the entrance region, the J_y current density is approximately twice that of J_x; therefore, the result of the J_yB and J_xB forces would direct the

total flow approximately 30 degrees below a flat, positive $\hat{\mathbf{x}}$ path, as illustrated in Figure 5.54. The result of this is obvious—Figures 5.35 and 5.36 show that as the flow progresses downstream, the core is essentially pushed by the secondary (v) flow, seen in Figure 5.37, in the direction of the bottom electrode, because of the J_xB force [93, 126, 173].

Therefore, the electrons in the flow experience a Lorentz force that is approximately 30 degrees below the positive $\hat{\mathbf{x}}$ direction, and a current attraction that is approximately 30 degrees behind a negative $\hat{\mathbf{y}}$ direction. While these two influences cannot be directly added, the overall result is an abnormally high density of electrons along the bottom of the channel, which results in a higher level of conductivity (by reducing resistance). This higher level of conductivity allows for more current density to flow in this region of the channel, because the current wants to take the path of least resistance (as seen in Figures 5.48 and 5.52). The higher current density in this region increases the Joule heating of the flow in that area, which, in turn, further increases conductivity, which allows for more current to flow, which increases the temperature, and so on. Basically, as temperature rises, more current can flow; and as more current flows, the temperature rises [19, 126]. Once this process begins, and there are no external influences that try to halt it, it can snowball into what is seen in Figures 5.38 and 5.39 and Figures 5.51 and 5.52—runaway heating combined with abnormally high current density at the bottom electrode [126]. Nonuniform J_x current densities can also cause the Lorentz force to have a rotational component [93], which can result in vorticity near the sidewalls [126, 137].

The detrimental effects of this runaway heating and excessive current density can be seen in Figure 5.50, where the positive J_y current flow actually reverses direction, essentially turning the MHD accelerator into an MHD generator. Furthermore, Figure 5.24 shows that for every applied current level above 125 A, J_y current flow reversal occurs somewhere in the MAPX channel. Everything described in the previous paragraphs (the J_x current density, which uses the secondary flow to push the electrons toward the bottom electrode, resulting in increased heating and current flow) occurs sooner and with more intensity when a higher level of external current is applied to the MAPX channel. Figure 5.55 shows the temperature contours of the 175 A case. Notice how much higher the internal temperature of the flow is, and how much sooner the "hot spot" develops along the bottom electrode.

As stated, current prefers the path of least resistance, and at 60 cm, as the bottom half of the MAPX channel passes 3500 K, the positive J_y current begins to recirculate and reverse flow toward the bottom electrode (as seen in Figure 5.50). Just as runaway temperature and J_x current density are seen in the 100 A case, the 175 A (and above) cases exhibit runaway temperature and negative J_y current flow. As shown in Figure 5.55, at 70 cm, the high-temperature region has pushed toward the top electrode, causing the J_y current across the entire cross-section to flow in the negative $\hat{\mathbf{y}}$ direction (as seen in Figure 5.50). At 80 cm, basically the entire flow field is in excess of 3200 K, with most of the flow above 3700 K, resulting in a high negative J_y current density. At the exit of the MAPX channel, the temperature profile of the 175 A case exhibits runaway heating across the entire cross-section. (Note, however, that the drop in the negative J_y current density at 90.5 cm for the 175 A case is due to
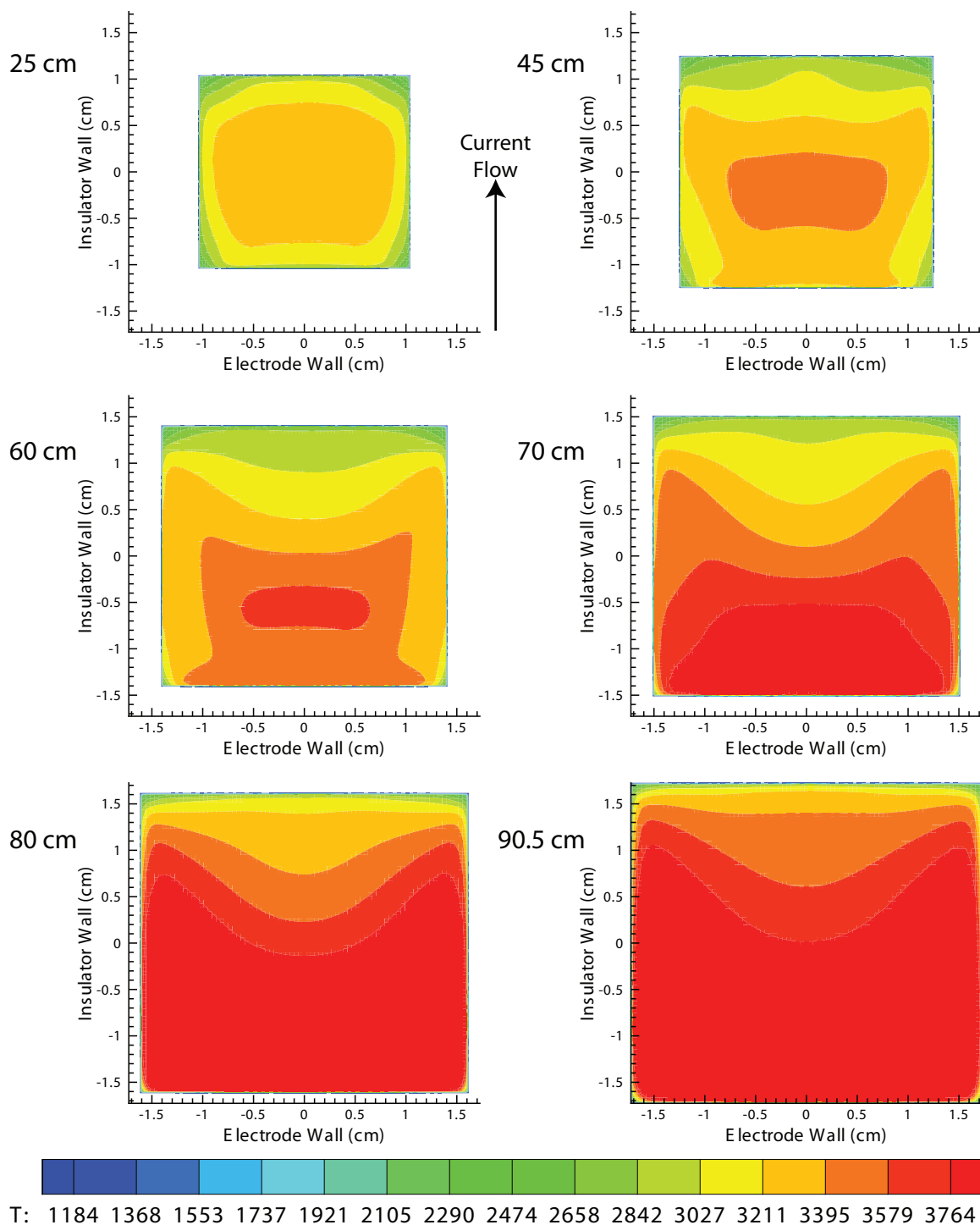
Figure 5.55: Contour plots of the temperature, T, in K, at 25, 45, 60, 70, 80, and 90.5 cm along the MAPX channel for the 175 A case. The last position is the channel exit. The bottom and top electrodes are oriented correctly, meaning that, in accelerator mode, positive J_y current should flow upward on the page.

the attenuating magnetic field.) The contours in Figure 5.55 (and the graphs of the higher applied current cases in Sections 5.3.2 and 5.3.3) show the detrimental effects of the axial current density, J_x, when combined with a high level of applied current.

5.4.2.10   Lorentz Force

The purpose of an MHD accelerator is to use a cross-field J_y current density and a magnetic field, B, to accelerate a fluid flow through a channel. This J_yB pushing force is known as the Lorentz force, and can be measured in units of force. Figure 5.56 shows the three-dimensional profile of the Lorentz force as the flow travels downstream (with units of $10^{-5}\,\mathrm{N}$). As expected from Figures 5.9 and 5.48, the flow experiences the highest Lorentz force in the first half of the channel, with the core-flow force lessening mid-way down the channel, and finally, very little J_yB force at the channel exit. This drop in Lorentz force is primarily due to two reasons: (1) the attenuation of the magnetic field, as seen in Figure 5.9, in the latter half of the MAPX accelerator, and (2) the decrease in the effective positive J_y current density, seen in Figures 5.24 and 5.48. The attenuation of the magnetic field is due to the physical widening of the poles of the MAPX electromagnet, shown in Figure 5.10, and the decrease in the effective J_y current density is due to the $\mathbf{u} \times \mathbf{B}$ induced electric field.

It is interesting to note that the J_yB profile, as the flow progresses downstream, is consistent with the dimensionless voltage drop, Δ, profile, seen in Figure 5.33. In the areas where the J_yB force is greatest, the dimensionless voltage drop has its most negative slope. However, in the areas where the J_yB force is diminishing (where the channel is experiencing less than optimum pushing Lorentz force), the slope of Δ
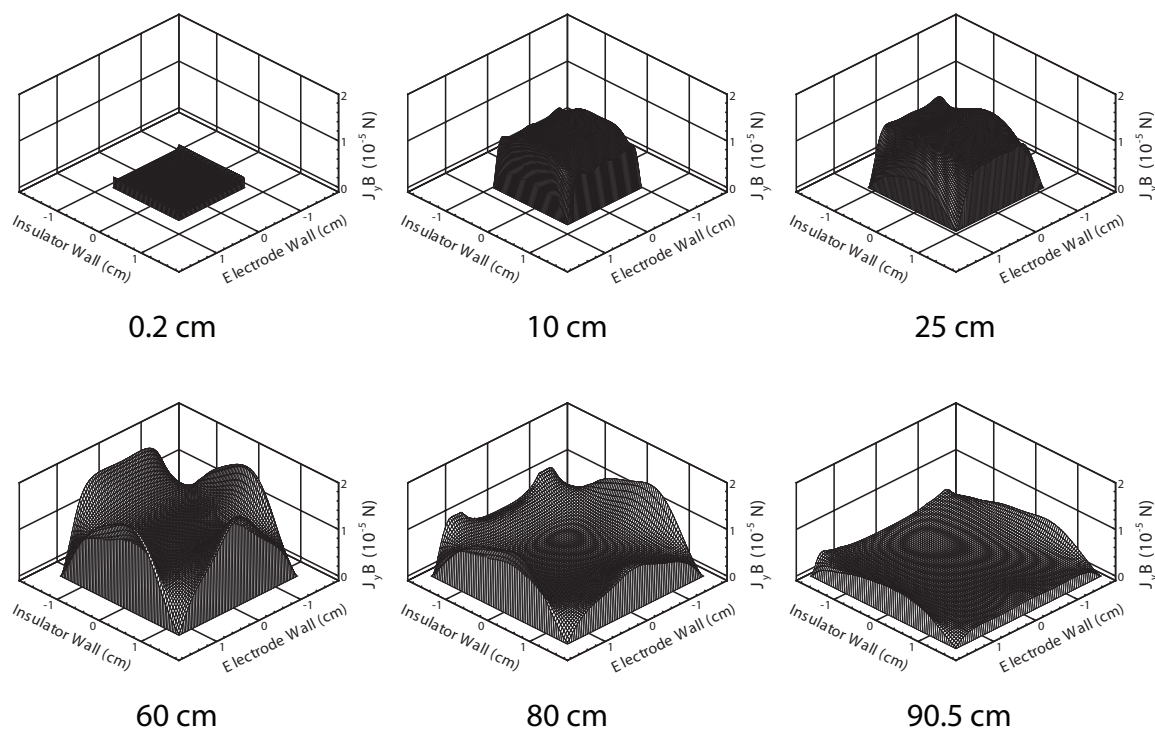
Figure 5.56: Three-dimensional axial Lorentz force (J_yB) plots at 0.2, 10, 25, 60, 80, and 90.5 cm along the MAPX channel. The last position is the channel exit. The positive J_y current flows from the bottom electrode (in the background) to the top electrode (in the foreground), which is out of the page.

becomes positive. This is not to say that the dimensionless voltage drop knows where the highest J_yB forces exist in the channel, and adjusts its slope accordingly—that would require that Δ has knowledge of upstream conditions, which is impossible with the parabolic solution procedure in the UMM code. However, at each cross-section, the slope of dimensionless voltage drop does seem to coincide with the performance of the accelerator (and the intensity of the J_yB Lorentz force).

5.5   Sensitivity Analysis

To determine the most appropriate configuration for the initial MAPX testing, it is advantageous to know the relative influence of certain input (*i.e.*, user-defined) variables on important exit parameters. To accomplish this analysis, uncertainty magnification factors (UMF), as described by Coleman and Steele [180], are calculated for the relationship of ten input variables to each of three exit parameters. This section gives an overview and the results of the UMF analysis—please see Appendix E for more details of the baseline, perturbation, and difference values.

Generally, the UMF for a given input variable indicates the influence of the uncertainty in that variable on the uncertainty in the result. Since the UMF values are squared when used in the general uncertainty equation, values greater than 1 indicate that the influence of the uncertainty in the variable is magnified [180]. However, since this is a numerical model and overall uncertainty is not calculated here, the UMF values can be used to indicate which input variables have more influence on the overall value of an exit parameter. This information will be helpful when comparing the MAPX experimental results to the results of the UMM numerical model—*i.e.*, if the experimental exit value for a parameter X differs excessively from the value predicted by the UMM numerical model, researchers will know which inlet values/variables are more "important" and can devote more time/energy/money to decreasing the experimental uncertainty in that measurement to provide a more accurate input value for the UMM code. The opposite is also true—if a UMF value

Table 5.4: Exit parameters used in sensitivity (UMF) analysis.

Exit Parameter	Symbol	Dissertation Section
Total Pressure	P_{0e}	Section 4.3.7
Exit Velocity	u_e	Section 3.2.1
Electrical Efficiency	η_a	Section 4.3.6

is consistently low for all exit parameters, the accuracy of the measurement of this variable is not as important as variables with higher UMF values.

As an initial analysis, only cross-sectional averaged values/parameters are used to determine the UMF values. Table 5.4 shows the three exit parameters used in this sensitivity analysis, where velocity and total pressure are their cross-sectional averaged values. Electrical efficiency is, by nature, a single value for a given cross-sectional plane. Therefore, this analysis could be considered one-dimensional in nature, and, as such, appropriate input variables are used. For example, as seen in Appendix D, values for secondary-flow velocities and wall roughness height are user-defined input variables, but, as they are highly three-dimensional in nature, they will be excluded from this analysis.

The ten user-defined input values studied in this sensitivity analysis are defined in Table 5.5, with their input-file variable names given for cross-referencing with Appendix D. Note that two variables—wall temperature and arcing temperature—do deal with wall and "three-dimensional" effects; however, their treatment in the MGMHD code is essentially one-dimensional in nature, as described in Section 3.4.3. Furthermore, recall that, as described in Section 5.2.1, the channel divergence angle

Table 5.5: Input variables used in sensitivity (UMF) analysis.

Input Variable	Symbol	Input File Name
Inlet Temperature	T	TIN
Static Pressure	P	PIN
Mass Flow Rate	$\dot{m}$	FLOW
Diagonal Angle	θ_d	ANGLE
Applied Current	I	AJLIN
Channel Divergence	H,W	HGTH,WDTH
Wall Temperature	T_{wall}	TWAL
Arcing Temperature	T_{arc}	TARC
Magnetic Field	B	BFLD
NaK Seeding %	NaK	FUEL

is calculated using the overall channel length combined with the inlet and exit dimensions (height/width). However, for the purposes of this analysis, the divergence of the channel is treated as a single variable—details are located in Appendix E.

5.5.1 UMF Results

In order to determine the UMF values for the different exit parameters, each of the ten input variables was individually perturbed by 1% of its baseline value while all other input variables were held at their baseline values. Three "perturbed exit parameter" values were obtained for each of the ten tests, and the corresponding partial derivatives needed for the UMF values were calculated by comparing the perturbed exit values to the baseline exit values. A more detailed description of the UMF calculations can be found in Appendix E, with the theory and method explained

Table 5.6: Uncertainty magnification factors (UMF) for the cross-sectional exit values of total pressure, axial velocity, and global efficiency; based on the 1.0% perturbation of the input variables listed.

Perturbation Variable	UMF Value		
	P_{0e}	u_e	η_a
Inlet Temperature	0.2780	0.0256	0.7326
Static Pressure	0.7793	0.1876	0.9494
Mass Flow Rate	1.6660	0.1791	0.3099
Diagonal Angle	1.1259	0.1833	0.7283
Applied Current	0.1654	0.1279	0.0173
Channel Divergence	0.2164	0.5329	0.2991
Wall Temperature	0.2445	0.0512	0.0650
Arcing Temperature	0.0000	0.0000	0.0000
Magnetic Field	0.6228	0.1833	0.3836
NaK Seeding %	0.0457	0.0298	0.0065

in Coleman and Steele [180]. Table 5.6 gives all thirty UMF values—ten values for each of the three exit parameters.

5.5.1.1 Total Pressure

Figure 5.57 gives a graphical representation of the cross-sectional averaged exit total pressure UMF values for each of the ten input variables. As Equation 4.61 indicates, static pressure would naturally have a considerable influence on the total pressure of the flow, and since the $\mathbf{J} \times \mathbf{B}$ Lorentz force provides the acceleration for the flow, it is logical that the magnitude of the magnetic field would also be influential. Since the diagonal angle ultimately controls the balance between the J_x and J_y current densities, as described in Section 4.3.1.2, its influence over the total pressure should be, and is, relatively high. Finally, since by definition, the total (stagnation) pressure
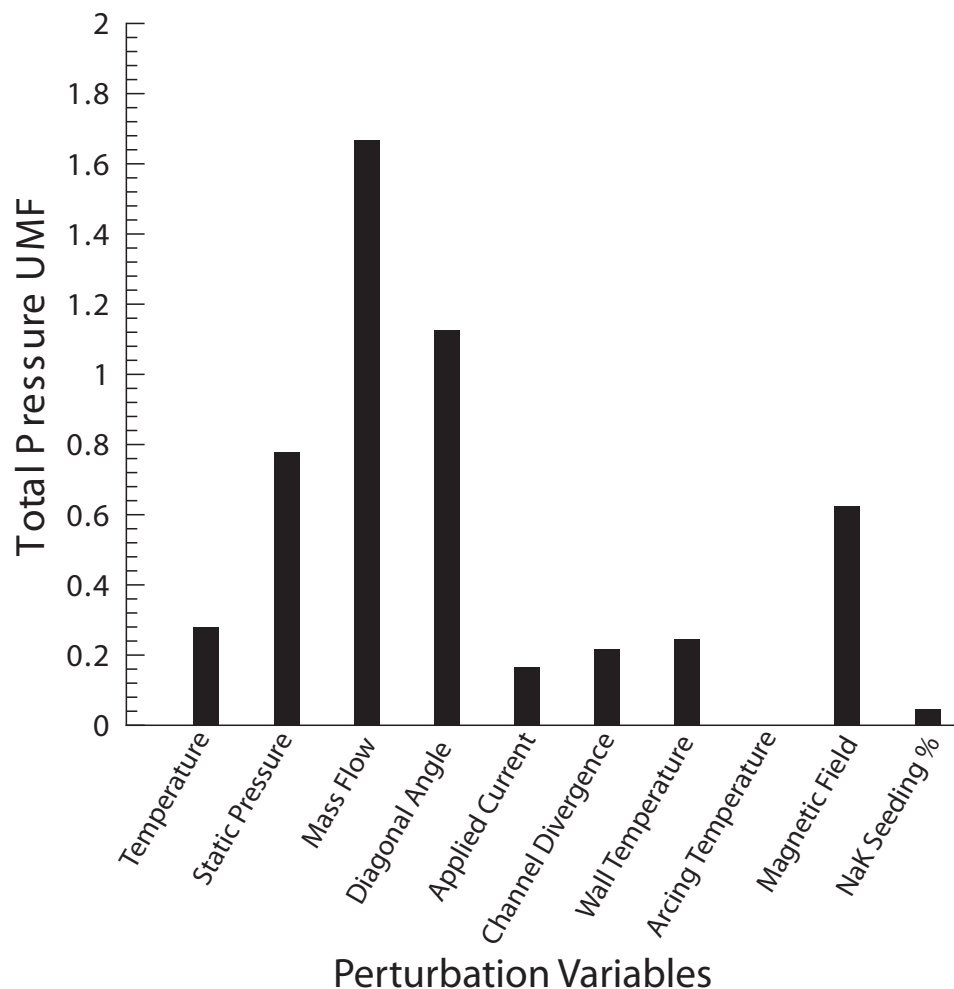
Figure 5.57: Presentation of the uncertainty magnification factor (UMF) results for cross-sectional averaged total pressure at the exit of the MAPX channel, based in the 1.0% perturbation of ten user-defined input variables from their baseline values.

of a flow is the sum of the components of static and dynamic pressure, the velocity of the flow should have great influence of the total pressure, especially at the flow velocities seen in the MAPX channel. This velocity-total pressure connection can easily be seen in Figures 5.35 and 5.42. Since the UMM code calculates velocity from the value of mass flow rate, its UMF value is understandably high.
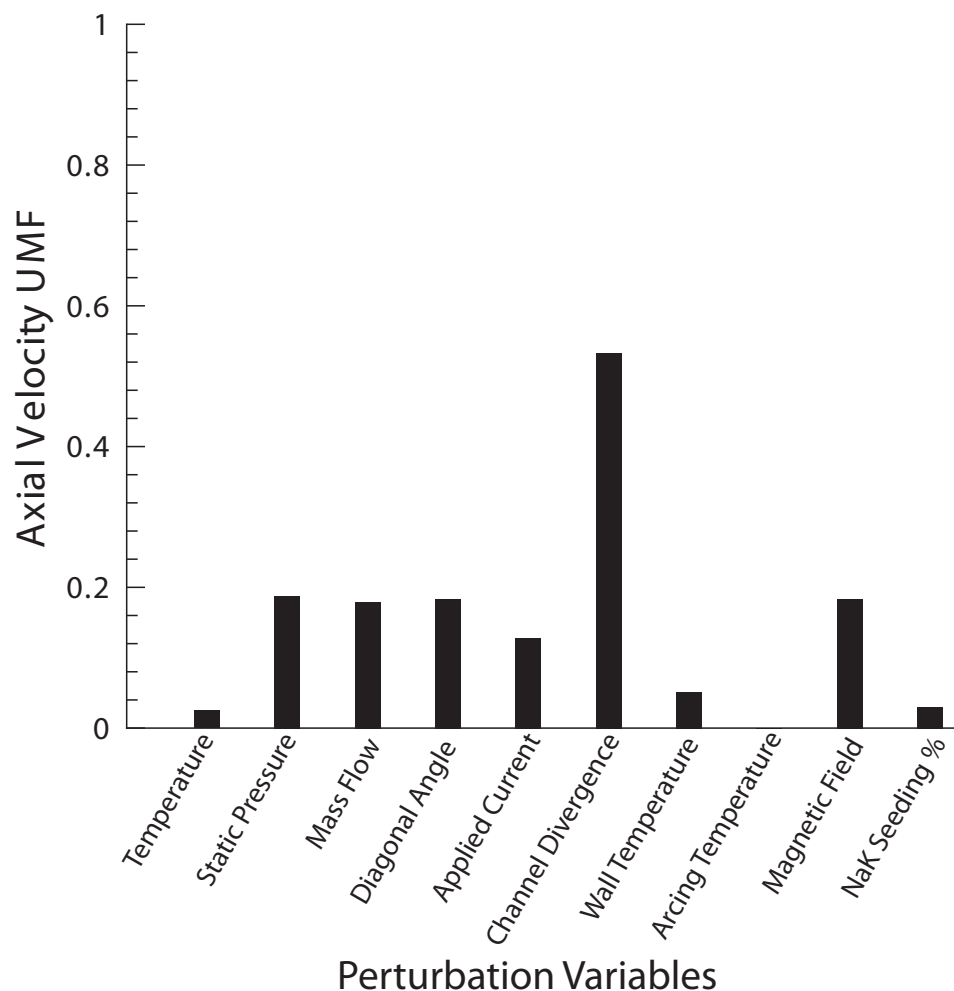
Figure 5.58: Presentation of the uncertainty magnification factor (UMF) results for cross-sectional averaged axial velocity at the exit of the MAPX channel, based in the 1.0% perturbation of ten user-defined input variables from their baseline values.

5.5.1.2 Axial Velocity

Figure 5.58 gives a graphical representation of the cross-sectional averaged axial velocity UMF values at the channel exit for each of the ten input variables. The figure shows that the UMF values for static pressure, mass flow rate, diagonal angle, and magnetic field strength are very close, which is as one would expect for a generic MHD accelerator. Static pressure influences the back-pressure and pressure gradient

that the flow must overcome as it marches downstream; the UMM code uses mass flow rate to calculate velocity, so that relationship is obvious; as previously stated, the diagonal angle effectively controls the amounts of J_x and J_y current densities in the flow; and the magnetic field (along with the J_y current density) accelerate the flow through the channel. However, the influence of the channel divergence on the exit velocity for the MAPX accelerator could be abnormally high, when compared to another MHD accelerator. As shown in Sections 5.3 and 5.4, the MAPX accelerator has an unfavorably low volume to area ratio (*i.e.*, friction effects have a huge influence over the flow). Therefore, a 1% increase in the divergence of the MAPX channel would have a noticeable difference in the friction losses through the channel, which would translate to an abnormally high UMF value for channel divergence. (Note that while this analysis is, essentially, one-dimensional in nature, the cross-sectional averaged values are calculated at each step in the simulation using the full cross-sectional plane. Therefore, wall losses will be captured in these values.)

5.5.1.3 Electrical Efficiency

The electrical efficiency, defined in Section 4.3.6, is the ratio of the push power to the total applied power. Figure 5.59 gives a graphical representation of the electrical efficiency (or global efficiency) UMF values at the MAPX channel exit for each of the ten input variables. As the equations in Section 4.3.6 show, the global efficiency of an MHD accelerator has a heavy dependence on the axial velocity. As shown in Figure 5.15, the static pressure quickly decreases with increasing axial velocity, which explains its high influence on global efficiency. Furthermore, density has a similar
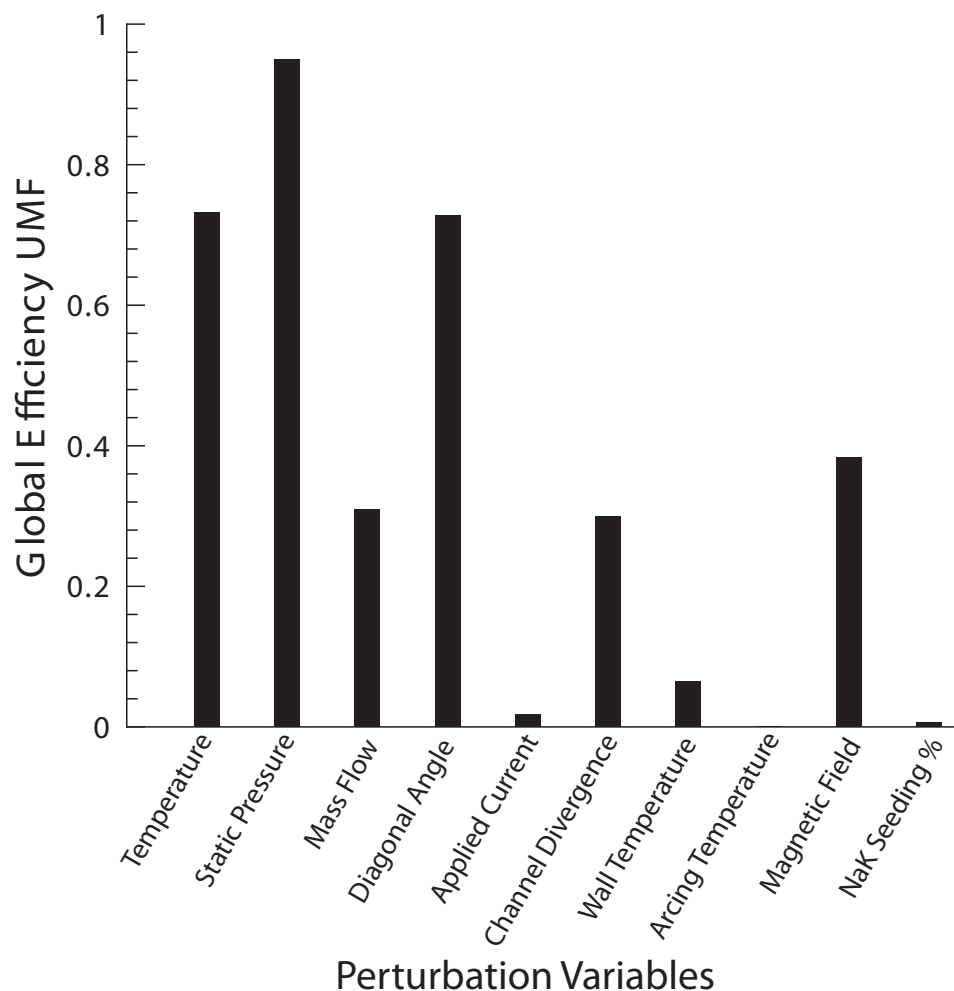
Figure 5.59: Presentation of the uncertainty magnification factor (UMF) results for electrical/global efficiency at the exit of the MAPX channel, based in the 1.0% perturbation of ten user-defined input variables from their baseline values.

dependence on axial velocity, as shown in Figure 5.16, which cancels out the overall influence that mass flow rate would have on electrical efficiency. The influence of temperature and diagonal angle on electrical efficiency is obvious—temperature is closely related to electrical conductivity and current density (as explained in the previous sections), and the diagonal angle essentially controls the relative levels of $\hat{\mathbf{x}}$ and $\hat{\mathbf{y}}$ current density in the flow. Since efficiency is a measure of how well the flow

converts applied power to push power, the UMF values for temperature and diagonal angle are as high as one would expect. While magnetic field strength is an important part of Equation 4.51, current density plays a much larger roll—this would explain why the UMF value for magnetic field is almost half that of temperature and diagonal angle. Furthermore, since channel divergence deals more with the hydrodynamic aspects of the flow, even though it does serve to offer acceleration to supersonic flows, its mid-range UMF value is as expected.

5.5.2 UMF Results Analysis

Overall, the UMF values from Figures 5.57, 5.58 and 5.59 show that no single input variable dominates all the exit parameters. The dominant UMF variable for total pressure is mass flow rate; for axial velocity, it is channel divergence; and static pressure has the most influence over electrical/global efficiency. It is, however, also no surprise that mass flow rate, magnetic field strength, static pressure, and diagonal angle seem to be either very, or at least somewhat, influential in all categories, as those input parameters are important in defining the basic characteristics of the inlet flow and MHD channel.

The "good news" from Figures 5.57, 5.58 and 5.59 is that applied current, wall temperature, arcing temperature, and NaK seeding percentage have relatively small UMF values—meaning that they have a relatively small impact on the flow exit parameters (at least the exit parameters discussed here). All of these variables are difficult to measure and/or maintain at a constant level during an experiment. The applied current is relatively simple to measure, but difficult to maintain at a

constant level across the entire MHD channel. The wall temperature is very difficult to measure without disturbing the flow or compromising integrity of the channel. The arcing temperature—which is typically just an estimation—has, apparently and fortunately, a zero UMF value in all cases discussed here, which is consistent with previous research that shows that arcs are not the main source of current conduction through the boundary layer [100]. Lastly, the NaK seeding percentage, which is the most difficult input variable to maintain at a constant level and accurately measure in the MAPX experimental apparatus, has a very small UMF value in all cases, and therefore has little influence on the overall flow exit parameters. (Note, however, that this small UMF value for NaK seeding assumes that the flow already has sufficient ionization. Insufficient NaK seeding, and therefore insufficient flow ionization, would result in a much higher UMF value.)

5.6   Recommended Test Configurations

The previous sections in this chapter present single-dimensional and multi-dimensional analyses of the NASA MSFC MAPX accelerator, under different levels of applied current. Due to exit velocity, total pressure, and electrical efficiency, in Section 5.3, the case using 100 A of applied current with a diagonal angle of $\theta = 45$ degrees ($\theta_d = 135$ degrees) is chosen as the "baseline" configuration. This configuration is explored in three-dimensional space in Section 5.4, where it is shown that viscous effects dominate the flow, and the J_x current density causes non-uniform flow fields resulting in excessive spot-heating in the channel.
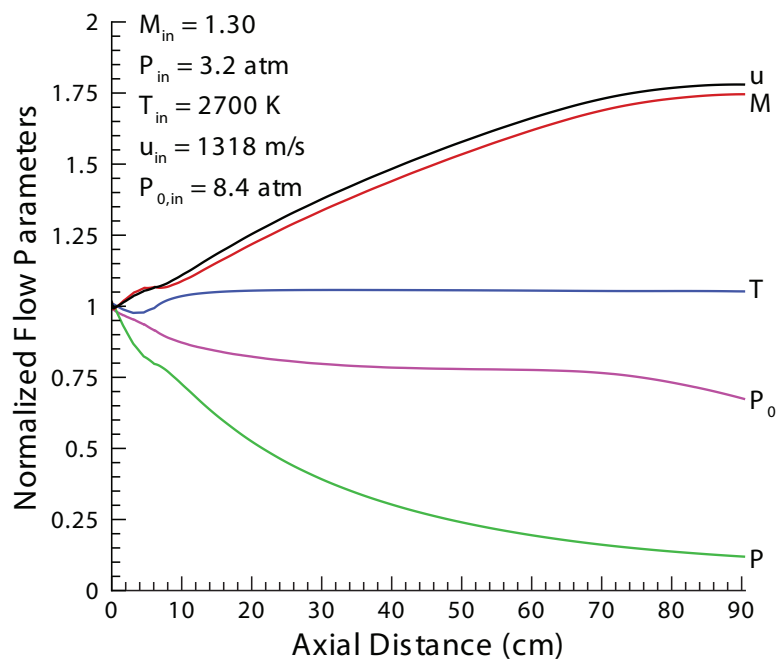
Figure 5.60: Normalized flow parameters for the baseline case.
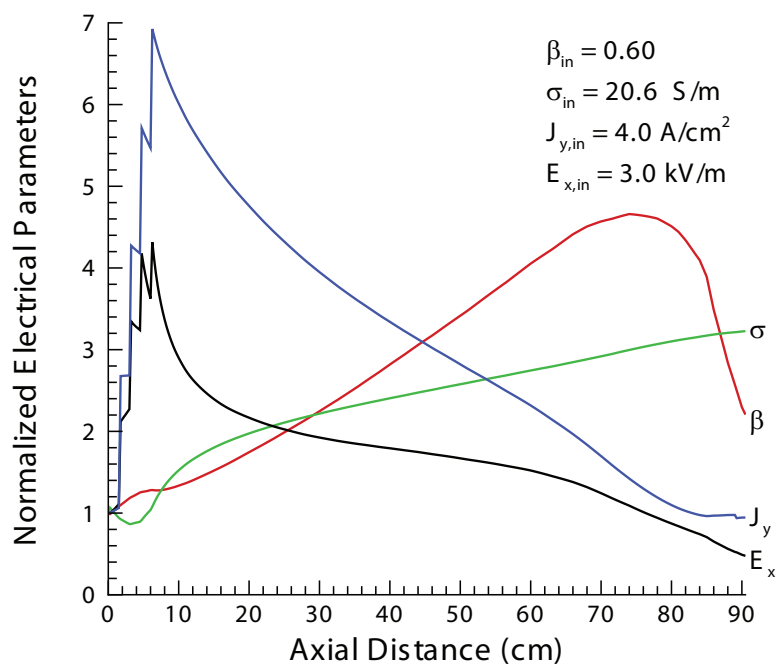
Figure 5.61: Normalized electrical parameters for the baseline case.

As a comparison to the original MAPX one-dimensional predictions in Figures 2.9 and 2.10, normalized flow and electrical parameters of the baseline configuration, as predicted by the UMM numerical model, are shown in Figures 5.60 and 5.61. These normalized parameters were calculated using cross-sectional averaged values—just as one would calculate with a one-dimensional code. The primary difference between Figure 2.9 and Figure 5.60 is the total pressure prediction—Figure 2.9 predicts an increasing total pressure and Figure 5.60 predicts a decreasing total pressure. While the magnitudes of axial velocity and Mach number differ, recall that Figure 2.9 assumes a 300 A applied current.

The differences between Figure 2.10 and Figure 5.61 are not as pronounced, and most can be explained through the level of applied current and the magnetic field distribution. Recall that Figure 2.10 assumes a constant 2 T magnetic field; however, Figure 5.61 uses the measured magnetic field from Figure 5.9, where attenuation in the baseline magnetic field causes the Hall parameter to fall after 70 cm. The J_y current density and axial electric field, E_x, have the same general shapes in Figures 2.10 and 5.61, with differences attributed to applied current levels.

5.6.1 Exploration of Alternate Configurations

Figure 5.32 shows that 100 A is the most appropriate level of applied current for the MAPX accelerator. Anything less does not deliver the most current and acceleration to the flow, and anything more only serves to heat the flow—which results in runaway heating, as seen in Figure 5.55. Furthermore, even though the MAPX channel has a low volume to surface ratio, redesigning and remanufacture is not an

option. There are, however, a some possible alternate experimental configurations that require little work and should be briefly explored. First, the "flare-sections" affixed to the downstream half of the poles of the electromagnet, seen in Figure 5.10, could be removed. This would, in theory, prevent the attenuation of the magnetic field seen in Figure 5.9, and the subsequent effects. Also, even though the axial current neutralized case, explained in Section 4.3.4 and plotted in Figure 5.11, calculates that the MAPX accelerator should use the largest possible angle (which is 45 degrees), the effects of smaller angles on the MAPX channel should be briefly visited. As shown in Figure 2.6, the MAPX accelerator is designed such that changing the diagonal angle is not troublesome. The following sections will explore these variations on the baseline case.

5.6.1.1   Magnetic Field Profiles

Section 5.2.3 gives a detailed description of the MAPX electromagnet, with photos of the physical magnet and a graph of the magnetic field distribution. Figure 5.10 shows the flares on the downstream portion of the MAPX electromagnet, and Figure 5.9 shows how these flares affect the magnetic field distribution. In this section, it is assumed that the magnet pole flares are removed, and that that magnetic field from the first half of the MAPX channel is identical (but mirrored) on to the second half of the MAPX channel, resulting in the magnetic field distribution seen in Figure 5.62. This magnetic field distribution peaks at $1.86\,\mathrm{T}$ at the center of the channel ($45.25\,\mathrm{cm}$), with the lowest B field intensities being $1.7\,\mathrm{T}$ at either end.
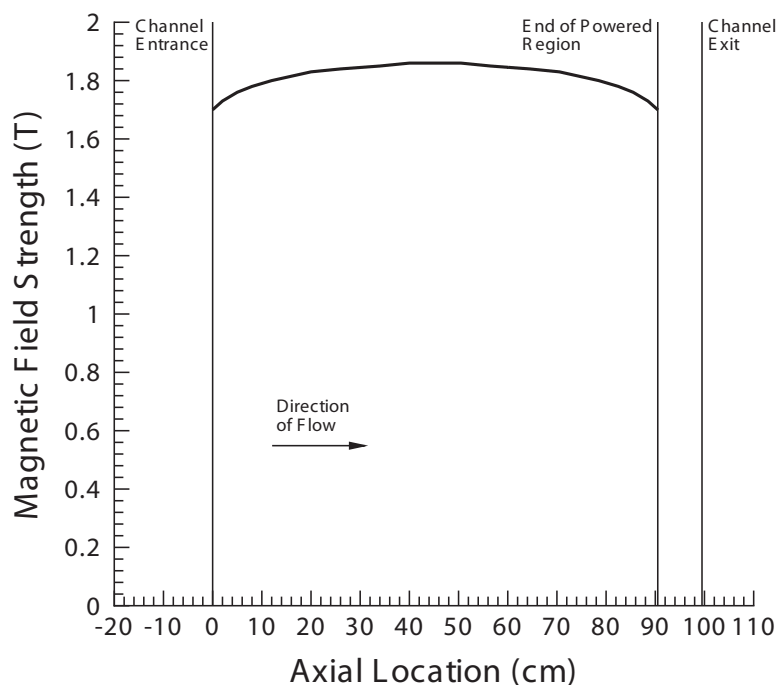
Figure 5.62: Magnetic field distribution, assuming the flares are removed from the downstream portion of the MAPX channel, and the magnetic field in the first half of the channel is reflected on to the second half.

Recall, that the UMM code only models the powered portion of the MAPX channel, therefore the magnetic field was mirrored only over that portion.

For most MHD accelerators, an increase in the temperature or magnetic field will allow for a reduced accelerator length [181]. However, the results of this magnetic field reflection can be seen in Figures 5.63 and 5.64. There is virtually no difference in the normalized flow parameter between the baseline case and the reflected magnetic field case, Figures 5.60 and 5.63. There are slightly higher exit values for axial velocity and Mach number in the reflected magnetic field case, but the differences are small enough to be considered negligible. Furthermore, the shapes (slopes) of all the curves
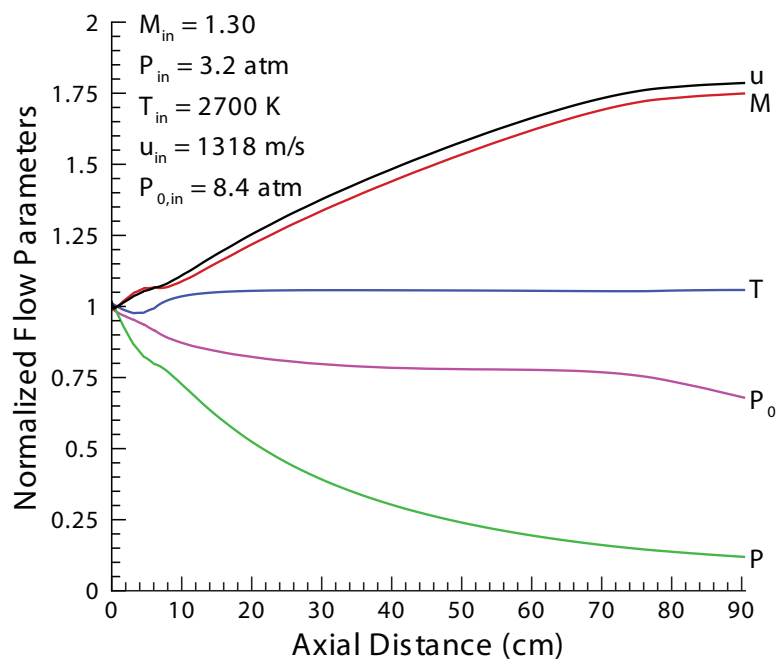
Figure 5.63: Normalized flow parameters, where the magnetic field over the first half of the MAPX baseline channel was reflected onto the second half of the channel.
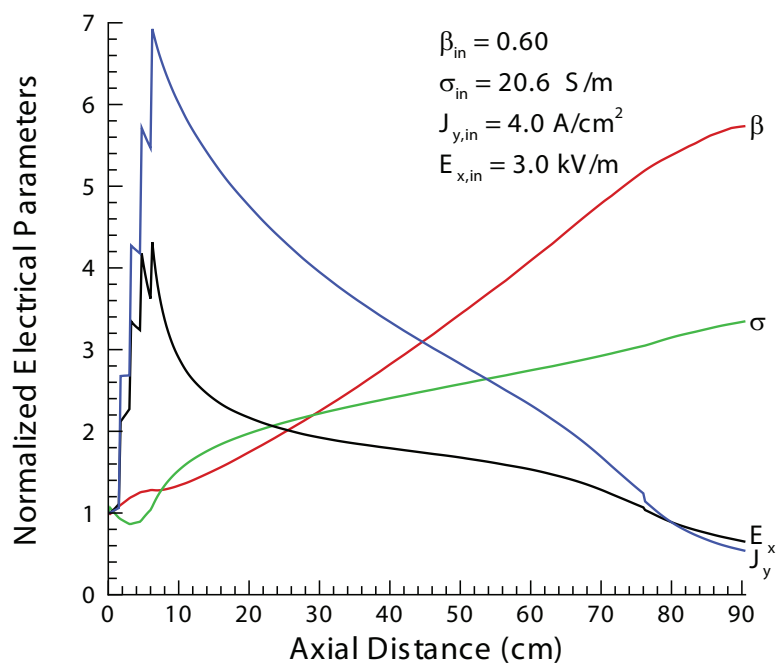
Figure 5.64: Normalized electrical parameters, where the magnetic field over the first half of the MAPX baseline channel was reflected onto the second half of the channel.

are the same—this begs the question, does the magnetic field attenuation have an effect on the flow?

The differences between the baseline and reflected magnetic field cases can, however, be seen in Figures 5.61 and 5.64. The Hall parameter shows the greatest difference, as expected—the baseline case shows a declining Hall parameter following the profile of the attenuated magnetic field, while the reflected case shows a Hall parameter rising to the end of the channel. There is virtually no change in electrical conductivity and the axial electric field between these two cases. However, there is a small, but meaningful change in the cross-field, J_y, current density.

In Figure 5.61, the J_y current density stays just above unity, and the slope over the last $10 \, \mathrm{cm}$ begins to flatten—$i.e.$, the decline in the J_y current begins to decrease near the end of the MAPX channel. However, the J_y current density in the reflected magnetic field case, Figure 5.64, actually continues to decline throughout the MAPX channel, with a sharp drop at approximately $85 \, \mathrm{cm}$. The final J_y current density is approximately $12 \, \mathrm{A/cm^2}$ (only 60% of its entrance value of $20 \, \mathrm{A/cm^2}$).

The dropping J_y current density could explain why there is negligible difference between the exit Mach number and axial velocity in the baseline and reflected magnetic field cases. Normally, one would expect that for a given J_y current density, increasing the magnetic field would result in a larger Lorentz "pushing" force, $J_y B$, which would accelerate the flow further. However, as seen in Figure 5.64, the J_y current density does not remain the same—it, in fact, decreases—resulting in no difference in the exit velocity of the flow. The decrease in the J_y current density could be explained through an increase in the $\mathbf{u} \times \mathbf{B}$, opposing Lorentz force. In the down-

stream portion of the channel, where the axial velocity of the flow is relatively high, increasing the B field results in an increase in the E_y field that opposes the externally applied (*i.e.*, accelerating) electric field, which reduces the positive, accelerating, J_y current density.

In other words, the magnetic field contributes to two competing "forces" (for lack of a better word). On the one hand, the magnetic field helps to accelerate the flow using the $J_y B$ Lorentz force, but, on the other hand, the magnetic field contributes to the opposing electric field, via the $\mathbf{u} \times \mathbf{B}$ Lorentz force, which indirectly serves to slow the flow. This phenomenon has been seen in previous studies [105], and how the magnetic field influences the flow depends, therefore, not just on the intensity of the magnetic field, but on the axial velocity of the flow at that point. The fact that the magnetic field contributes to both accelerating and decelerating the flow, depending on the velocity and J_y current density of the flow at that point, implies that one could "design" an optimized magnetic field distribution of a given MHD channel. This, however, is beyond the scope of this dissertation and cannot be accomplished with existing MAPX equipment.

To confirm this interplay of the magnetic field intensity with the axial velocity and J_y current density, two more tests were performed using constant $2.0\,\mathrm{T}$ and $2.5\,\mathrm{T}$ magnetic fields, Figures F.1 and F.2 and Figures F.3 and F.4 respectively. The results, seen in Appendix F, show that the higher magnetic fields improve acceleration in the first half of the MAPX channel, but impede acceleration in the second half of the accelerator. Both cases show flat Mach number and velocity profiles, with sharper decreases in the total pressure, in the latter part of the channel. This effect is,

obviously, exacerbated in the 2.5 T case, where the velocity profile peaks at 45 cm, and actually declines slightly as it continues to the end of the channel. Both cases also show very large drops in J_y current density in the second half of the channel, as expected. In the 2.5 T case, the J_y current density actually experiences a large decline at 45 cm, and continues to fall asymptotically toward zero at the exit of the MAPX channel. These two tests are further confirmation that increasing the intensity of the magnetic field is not always the best solution.

5.6.1.2 Diagonal Angles

The axial current neutralized case, explained in Section 4.3.4 and plotted in Figure 5.11 calculates that the MAPX accelerator should use a diagonal accelerator angle of $\theta \approx 55$ degrees throughout the channel. An angle this steep is, however, physically impossible in an MHD accelerator [166], so the largest physically-possible angle, $\theta = 45$ degrees, is used for the baseline analysis. For completeness, however, the effects of lesser angles should be explored. Appendix F shows two tests of the baseline MAPX accelerator configuration with different diagonal angles—Figures F.5 and F.6 show the results of a $\theta = 15$ degrees test and Figures F.7 and F.8 show the results of a $\theta = 30$ degree test.

The results are clear—lesser angles result in poorer MHD accelerator performance. For the 15 degree angle case, total pressure drops almost linearly, axial velocity and Mach number peak at approximately 50 cm and decline until flow reversal occurs (and the code actually stops calculating) at 77 cm. The J_y current density becomes negative at approximately 46 cm, which causes the subsequent drop in axial

velocity. The 15 degree angle allows for too much axial, J_x, current density to flow through the channel, which effectively "steals" applied current away from the useful J_y current density, and heats the flow (as seen in Figure 5.55).

The case with the 30 degree diagonal angle is only slightly better. Figure F.7 shows that the axial velocity and Mach number achieve only 1.5 times their entrance values, as opposed to 1.75 seen in the baseline case. Subsequently, total pressure is also lower at the exit of the 30 degree case. The J_y current density briefly reverses to a negative value at approximately 80 cm, but quickly recovers to a positive value, as seen in the 175 A case in Figure 5.24. Simply put, the 30 degree diagonal angle also allows for too much J_x current density and is too small for this accelerator.

5.6.1.3 Comparisons

The previous sections discuss minor alterations in the MAPX configuration, and their influences on the overall exit parameters of the flow. Figure 5.63 shows that removing the pole flares on the MAPX electromagnet offer virtually no benefit to exit velocity or total pressure. Figures F.5 and F.7 show that the 45 degree diagonal accelerator angle is the most appropriate for the MAPX accelerator—smaller angles reduce the exit velocity and total pressure, and larger angles are not physically viable.

As a final comparison of these alternate configurations, Figure 5.65 shows the electrical efficiencies of the 6 different configurations discussed in these sections—the baseline configuration, the "reflected" magnetic field configuration, the constant 2 T magnetic field, the constant 2.5 T magnetic field, the 15 degree accelerator diagonal angle configuration, and the 30 degree accelerator diagonal angle configuration.
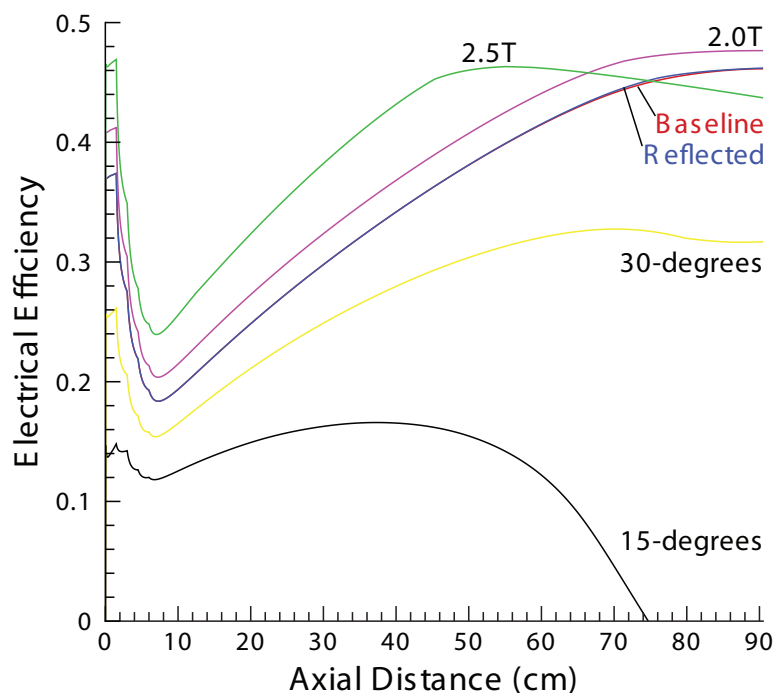
Figure 5.65: Comparison of the electrical efficiency as a function of the axial distance for the baseline, reflected magnetic field, constant 2 T magnetic field, constant 2.5 T magnetic field, 15 degree diagonal angle, and 30 degree diagonal angle cases.

Note that the details of constant 2 and 2.5 T magnetic field cases and the 15 and 30 degree diagonal angle cases are located in Appendix F. Most importantly, Figure 5.65 shows that there is no difference between the efficiencies of the baseline case and the reflected-magnetic field case. It also shows that, if it were possible, the constant 2 T case would offer the best overall electrical efficiency, even though the slope of the efficiency distribution for the 2 T case is lower than the baseline case for the final 15 cm of the accelerator. Figure 5.65 also shows that, while the 2.5 T case starts off very strong, the overpowering $\mathbf{u} \times \mathbf{B}$ field causes the efficiency to decline in the second half of the channel. The figure also shows that the 15 and 30 degree diagonal

accelerator angle cases have a much lower efficiency than the baseline (*i.e.*, 45 degree) case.

5.6.2   MAPX Test Recommendation

This dissertation recommends the following initial configuration for the NASA MSFC Magnetohydrodynamic Augmented Propulsion Experiment:

- Diagonal accelerator angle, $\theta = 45$ degrees (or $\theta_d = 135$ degrees, as defined in Section 3.3.2).

- Applied current, $I = 100$ A.

- The magnet pole flares, seen in Figure 5.10, should not be removed.

- The entrance should have a 5-electrode power takeoff, and the exit should have a 2-electrode power takeoff.

The 45 degree diagonal angle is explained in Sections 5.2.3 and 5.6.1.2, where the recommended angle is the largest that is physically-possible for this MAPX accelerator. Figures 5.65, F.5 and F.7 show that the 45 degree diagonal angle offers the best exit velocity and total pressure with the best efficiency. Based on the definition of the axial angle neutralized mode, from Section 4.3.4, it is no surprise that the 45 degree angle offers the best performance. The 100 A applied current, with its 5-electrode entrance power takeoff, is shown to be most efficient in Figure 5.32, and provides the best combination of exit velocity, total pressure, and low internal temperature. Figures 5.29, 5.30 and 5.31 show that the 100 A case makes the best use of the total power delivered to the flow.

The third recommendation—that the magnet pole flares seen in Figure 5.10 should not be removed—is different than the previous recommendations because there seems to be no overall performance difference when the pole flares are removed. As shown in Figures 5.60 and 5.63 and then in Figure 5.65, the exit parameters and efficiencies for the baseline case, with and without the magnet pole flares, are virtually identical. However, it is exactly because there is no reason to remove the flares that the flares should initially stay in place. That is, the real magnetic field distribution without the magnet pole flares is unknown—the distribution seen in Figure 5.62 is assumed. Since this assumption yields no advantages, the risk of running the MAPX accelerator under "unknown" circumstances far outweighs any expected benefit (which, in this case, is zero).

Furthermore, without the magnet pole flares, the magnetic field intensity would be much higher in the 9 cm un-powered region at the end of the MAPX accelerator. Recall from Figure 5.1 that the powered region of the MAPX accelerator ends 9 cm before the exit of the physical channel, and, since there is a magnetic field and un-powered electrodes in this region, it essentially functions as an open-circuit generator. Therefore, the higher the magnetic field in this region, the more intense the $\mathbf{u} \times \mathbf{B}$ Lorentz force. Appendix F shows what happens when a fast moving flow meets with an intense magnetic field—the flow is slowed. This 9 cm region represents approximately 10% of the length of the powered region; therefore, considerable deceleration of the flow could occur. Furthermore, with a 2-electrode power takeoff at the exit of the channel, the final 2 cm will not see the total 100 A of applied current, allowing the the $\mathbf{u} \times \mathbf{B}$ Lorentz force more distance to influence the flow. With the

magnetic pole flares in place, the magnetic field intensity near the end of the powered region and exit of the physical channel is lowered to a value that will not adversely influence the flow in the un-powered regions.

It is true that a large upstream-pointing gradient in the magnetic field can induce a negative $\hat{\mathbf{y}}$ flowing current in the channel (via the "Grad-B Drift" [94]), and that this drift velocity is not simulated in the MGMHD code [125]. Even though it effects both electrons and ions, this drift velocity is not strong in comparison to the externally applied field, or the $\mathbf{u} \times \mathbf{B}$ induced fields [94]. In the end, the electromagnet should remain in the known configuration. There seem to be no benefits from removing the poles, assumed or otherwise; and running an experiment under "unknown" conditions is never advisable. It is recommended, however, that the MAPX electromagnet magnetic field distribution should be measured without the pole flares in the downstream section. This will allow for a more accurate simulation and recommendation for the MAPX channel configuration.

CHAPTER 6

CONCLUSIONS

> *If I have seen further, it is by standing on
> the shoulders of giants.*
>
> —Isaac Newton

6.1 Overview

The objective of this research is to analyze the NASA Magnetohydrodynamic
Augmented Propulsion Experiment (MAPX) using a three-dimensional numerical
model. The results of this analysis are intended to offer a better understanding of
the critical physical processes within the MAPX accelerator, give details of a recom-
mended "baseline" configuration for initial testing, and provide pre-test performance
predictions of that baseline configuration. The NASA MAPX accelerator marks the
first experimental study of a diagonal MHD accelerator, and this dissertation is the
first detailed, three-dimensional numerical analysis of a diagonal MHD accelerator.

The three-dimensional nature of the electromagnetic effects inside the diagonal
MAPX accelerator requires the use of a proper three-dimensional numerical model.
Unfortunately, as explained in Section 1.1.3, no such model existed at the beginning
of the MAPX project. Therefore, in order to achieve the capabilities and accuracy
required by the MAPX channel, modifications and additions described in Chapter 4

302

were made to an existing three-dimensional model. The resulting code, with its integrated thermodynamic and electrical transport property models, was then used to simulate the flow inside the MAPX accelerator.

The results of the three-dimensional analysis of the MAPX accelerator are detailed in Chapter 5. The modeling indicates that the surface-to-volume ratio of the MAPX channel is too high, and that entropy-producing mechanisms dominate the flow. Furthermore, large local axial currents cause asymmetries in the flow, resulting in localized runaway heating. Using the baseline case of a 100 A applied current with a 45 degree diagonal accelerator angle (as described in Section 5.6) Figure 5.60 shows that the exit velocity of the MAPX accelerator is approximately 1.75 times the entrance velocity, the cross-sectional averaged temperature remains almost constant throughout the channel, and the cross-setional averaged total pressure falls to approximately 70% of its entrance value through the length of the channel. The electrical efficiency of the MAPX accelerator is 46% at the exit.

6.2   The UAH-MSFC MGMHD Numerical Model

At the start of the MAPX project, there were no suitable three-dimensional numerical models that met the requirements set forth in Section 2.3.1 to simulate the MAPX accelerator. Therefore, as Section 2.3.2 explains, it was decided that an existing numerical model would be modified to meet the requirements of the MAPX project—specifically, the Argonne National Laboratory Multigrid Magnetohydrodynamic (MGMHD) numerical model, detailed in Chapter 3, was determined to be the best candidate for modification. Chapter 4 explains the modifications and additions

to the MGMHD code. Section 2.3.3 outlines the approach taken to transform the MGMHD generator code into the UAH-MSFC MHD (UMM) numerical model, capable of fulfilling all the requirements set forth by the MAPX research group.

Chapter 3 details the original form of the MGMHD numerical model. In basic terms, the MGMHD code is a parabolic, three-dimensional MHD generator model, where the magnetohydrodynamic equation set comprises the mass continuity equation, three momentum equations, the energy equation, two turbulence models, and Maxwell's electrical equations. The parabolic assumption neglects diffusional losses in the axial direction and considers the pressure gradient in the axial momentum equation to be uniform over the channel cross-section. The MHD generator restriction dictates that diagonalization angles, θ_d, range from 0 to 90 degrees, and that the model could not be used for MHD accelerator simulations. Lastly, the original MGMHD numerical model assumes curve fits for the thermodynamic and electrical transport properties.

The additions to the original MGMHD numerical model are detailed in Chapter 4. The most important changes to the original MGMHD code include

- Addition of an MHD accelerator option which allows for diagonalization angles, θ_d, from 90 through 180 degrees.

- Integration with the NASA Chemical Equilibrium with Applications (CEA) numerical model for thermodynamic properties and species concentrations.

- Addition of a three-dimensional electrical conductivity model, which allows for partially ionized gas conductivity calculations because electrical transport properties are based on momentum-transfer cross-sections.

- Addition of a varying diagonal angle (through the channel) and axial current neutralized modes of operation.

- Addition of a proper inlet power takeoff (PTO) scheme.

Other than eliminating the curve fitting option for the calculation of thermoelectrical properties, all of the original capabilities of the MGMHD code remain in the modified version.

This new code is known as the UAH-MSFC MGMHD (UMM) numerical model, which consists of two primary sections—the MHD model and the thermoelectric model—as explained in Figure 4.1. The MHD portion of the UMM numerical model consists of the modified version of the MGMHD code, while the thermoelectric portion consists of the thermodynamic model (the modified CEA code) and the electrical conductivity model. The UMM code is the first three-dimensional MHD numerical model which can simulate all three MHD configurations—Faraday, Hall, and diagonal—in both modes of MHD operation—generator and accelerator—using three-dimensional thermodynamic and electrical transport property models. The UMM numerical model is also the only MHD code that can accurately model the MAPX diagonal accelerator.

The importance of a three-dimensional numerical model cannot be over emphasized. Recall that the MAPX accelerator was designed with a one-dimensional MHD code (described in Section 2.2); however—take J_x for example—simple inspec-

tion of Figures 5.26 and 5.51 shows the three-dimensional nature of an MHD flow that is overlooked when using cross-sectional averaged values. The objective of this dissertation is to model the MAPX flow; however, through the comparisons with the cross-sectional values in the MAPX channel and the one-dimensional output in Figure 2.9, this dissertation shows, as expected [20], that proper analysis of an MHD flow requires the use of a three-dimensional numerical model.

6.3 The NASA MAPX Accelerator

In Chapter 5, the three-dimensional UMM numerical model is used to simulate the flow inside the NASA Marshall Space Flight Center (MSFC) Magnetohydrodynamic Augmented Propulsion Experiment (MAPX) accelerator. Section 5.3 offers a parametric analysis of the different configurations of the MAPX accelerator, comparing various performance parameters—such as exit velocity, total pressure, and efficiency—to arrive at a "baseline" configuration. A more detailed, three-dimensional analysis of the baseline configuration is given in Section 5.4, along with explanations of the underlying physical phenomenon. The relative influence of certain input variables (their uncertainty magnification factors) on the most important exit parameters is given in Section 5.5, and the recommended initial MAPX test configuration can be found in Section 5.6.

The parametric analysis in Section 5.3 offers an interesting overview of the flow behavior in the MAPX accelerator. From the beginning, Figure 5.12 shows that blindly increasing the externally applied current is not the answer to achieving maximum exit velocity—there are limitations on the amount of applied current that

MAPX channel can accept. Figure 5.17 shows that, contrary to Figure 2.9, viscous effects dominate in the MAPX channel, and cross-sectional averaged total pressure falls through the entire length of the accelerator. The value of a three-dimensional numerical model is shown in Figure 5.26, where large differences between the center-line and cross-sectional averaged values for the J_x current density indicate that large, localized, opposing axial current densities exist in the MAPX accelerator. This could be due to localized eddy currents, but the UMM numerical model lacks the capability to model such behavior.

The more detailed three-dimensional analysis in Section 5.4 confirms that entropy production and the axial, J_x, current density prevent the MAPX accelerator from achieving the performance predicted in Figure 2.9. As the relatively slow-moving flow enters the accelerator, its main influence is the physical divergence of the channel. The externally applied current is low (still inside the PTO region); therefore, both J_y and J_x are not yet strong enough to influence the flow. Furthermore, as the channel walls are held constant at $1000\,\mathrm{K}$, the applied current can only heat a small region of the flow between the boundary layer and the core. In this entrance region, the duct divergence causes the secondary flow to start at the core and travel toward the walls. The shear at the walls retards the near-wall flow, thereby directing the flow back towards the center [126]. In this region, as the externally applied current ramps up to its prescribed value, the J_yB force begins to push the axial flow, while the $\hat{\mathbf{y}}$ directed velocities are influenced by the localized, but intense, J_xB forces, demonstrated in Figure 5.51.

Contrary to previous MHD generator studies [126, 129, 140], the MAPX accelerator has intense positive J_x core flows in the first half of the channel. The initial development of the local J_x current densities results from the end-to-end externally applied electric field. However, the changes in the axial current densities and the large gradients seen in Figure 5.51 result from the secondary flow inside the channel [126]—which, itself, is influenced and increased from the existence of the axial currents, and intensified by the small internal cross-sectional area of the channel. The gradients in the near-wall J_x current densities (*i.e.*, $\partial J_x / \partial y$) give rise to vorticity which induces flow rotation in opposing directions in the core and near-wall regions [126]. In short, the axial currents and the small cross-sectional area inside the channel contribute to the secondary flow, and the secondary flow increases the intensity and gradients in the axial currents.

As the flow travels downstream, the combination of the positive J_x core flow (which attempts to flow electrons in the opposite direction of the primary flow) and the positive J_y current density (in which, electrons flow from the top to the bottom electrode), the fast-moving electrons are lagging behind the primary flow, and collecting near the bottom of the channel. This is exacerbated by the fact that while the positive $J_y B$ Lorentz force pushes all charge particles in the downstream direction (which opposes the action of the positive J_x current), the positive $J_x B$ Lorentz force effectively tries to force all charged particles toward the bottom of the channel. As seen in Figures 5.24, 5.48 and 5.56, with increasing downstream distance, the effective J_y current and $J_y B$ Lorentz force decrease; therefore, the positive J_x current density and $J_x B$ Lorentz force eventually dominate, resulting in excess electrons near the

bottom of the channel. The excess fast-moving charge carriers increase the electrical conductivity in the bottom near-wall region; this increases current flow, which increases temperature; this, in turn, further increases electron number density. The eventual result of this snowballing effect is a large amount of J_x current flow near the bottom electrode, accompanied with the appropriate excessive heating in that region.

The overall effect of the axial currents causes the primary axial flow field to shift toward the bottom electrode. This is compounded by the fact that, as seen in Figure 5.42, the high surface-to-volume ratio inside the MAPX accelerator causes indentations in the top and side-wall flows and prevents the development of velocity overshoots in the near-wall regions. Strangely, the attenuation of the magnetic field in the second half of the accelerator seems to have no effect on the exit velocity of the flow. In previous studies, increasing the magnetic field resulted in increases in the primary exit parameters [20]; however, in the MAPX accelerator, viscous effects seem to retard the exit velocity and total pressure. Furthermore, as explained in Section 5.6.1.1, a high velocity and high magnetic field results in a high $\mathbf{u} \times \mathbf{B}$ opposing electric field, which effectively reduces the externally applied (*i.e.*, accelerating) current.

Therefore, the recommended initial testing configuration for the MAPX accelerator is a 45 degree accelerator diagonal angle with a 100 A externally applied current. Furthermore, a 5-electrode entrance, and 2-electrode exit power takeoff should be implemented to prevent electrode erosion and excessive heating (and subsequent flow reversal) at the channel entrance. Finally, as seen in Figures 5.60, 5.63 and 5.65, there are no compelling reasons to remove the electromagnet pole flares (seen in Fig-

ure 5.10), and since no experimental data of the "non-flared" magnetic field field exits, the electromagnetic pole flares should remain in place. In conclusion, the relatively poor (*i.e.*, less than 50%) efficiency of the MAPX accelerator is due, primarily, to the high surface-to-volume ratio inside the channel. The viscous and entropy-producing effects prevent the flow from developing properly and intensify the secondary flows (which furthers the development of detrimental axial currents). Even using the "axial current neutralized" angle, it is impossible to completely eliminate the local axial current flows inside the diagonal accelerator—the end-to-end loading of the diagonal accelerator will always have associated axial electric fields and currents. However, these detrimental effects can be mitigated with a properly designed diagonal accelerator, and, as this dissertation proves, this requires a three-dimensional numerical model.

6.4 MHD Accelerator Technology Advancements

This dissertation shows that the MAPX accelerator cannot achieve the level of performance described in Figure 2.9 because of entropy producing effects within the channel. However, this dissertation also shows that diagonal MHD accelerators are a worthwhile technology and their application to propulsion devices deserves further study. Figure 5.49 shows that, with the proper tools, a diagonal accelerator can be designed such that J_y remains relatively uniform and positive throughout the channel, which is paramount to MHD acceleration. Furthermore, this dissertation shows that, even with a high surface to volume ratio, a diagonal MHD accelerator is still capable of almost doubling the axial velocity of the flow, while increasing the overall center-

line total pressure. The low efficiency of the MAPX channel seems to be attributable to the physical design restrictions of this particular diagonal MHD accelerator, and is not indicative of inherent flaws in the diagonal MHD technology.

This dissertation also shows the importance of using a three-dimensional design tool (*i.e.,* numerical model) for the design of three-dimensional flows. The UMM numerical model described in this dissertation was developed out of necessity—in order to properly analyze and model the MAPX accelerator, a three-dimensional model was required. Since no suitable numerical model existed, the UMM code was developed. However, the UMM numerical model was not designed to be specific to the MAPX project—it was designed such that it could be used to model Faraday, Hall, and diagonal accelerators and generators, with proper thermodynamic and electrical transport properties. The UMM numerical model is the only code with this ability.

APPENDICES

APPENDIX A

ELECTRON MOMENTUM-TRANSFER COLLISION

CROSS-SECTIONS FOR SELECTED SPECIES

In this house, we obey the laws of thermodynamics.

—Homer Simpson

A.1 Overview

As Section 4.2.2 describes, the UMM numerical model has an electrical transport property model which calculates the electrical conductivity of an ionized gas based on a method from Devoto [153], which requires electron-neutral momentum-transfer cross-sectional data, as a function of incident electron energy. The advantage of this method is that, unlike the Spitzer equation which assumes full conductivity [88, 123], the Devoto method can accurately calculate electrical transport properties for partially ionized flow [153, 157, 158]. Since, as seen in Appendix D, the MAPX accelerator flow is approximately 1% ionized, an electrical conductivity calculation which allows for partially ionized flows is required.

A.2 Data

The electron-neutral momentum-transfer cross-sections, Q_{ij}^1 in $10^{-20}\,\mathrm{m}^2$ (or $\mathring{\mathrm{A}}^2$), for the 30 species are given as a function of incident electron energy, in eV, in Tables A.1, A.2 and A.3. The 30 species are Ar, CO, CO_2, Cs, CsOH, H, H_2, H_2O, He, K, K_2, KCl, KO, KOH, Mg, N, N_2, Na, Na_2, NaCl, NaO, NaOH, Ne, NO, O, O_2, OH, SF_6, SO_2, and Xe. The data presented in these tables comes from two sources: (1) a paper by Spencer and Phelps [151], and (2) the National Institute of Standards and Technology (NIST) Joint Institute for Laboratory Astrophysics (JILA) at the University of Colorado [152]. Using a Gauss-Laguerre quadrature to solve Equation 4.13, the Maxwellian velocity-averaged collision cross-sections for each species are calculated in the program `omega.f`, and output to a specific file.

In practice, `omega.f` creates a table of nine "omegas" for each of the 801 temperatures of interest (from $1000\,\mathrm{K}$ to $9000\,\mathrm{K}$ at $10\,\mathrm{K}$ intervals). The term "omegas" is derived from the "Omega integrals" mentioned in Section 4.2.2.2, and physically represent the different ℓ and s values of the average collision cross-section, from Equation 4.13. The program creates a separate file for each species, containing that species' Maxwellian velocity-averaged collision cross-section values, which are later used in the calculation of the q^{mn} elements, found in Appendix B. For each species' cross-sectional table, linear interpolation is used to obtain cross-sections for the parameters of the actual potentials (*i.e.*, the actual temperatures of interest).

Table A.1: Momentum-transfer cross-sections, in $10^{-20}\,\mathrm{m}^2$, for specific species.

Energy (eV)	Ar	CO	CO$_2$	Cs	CsOH	H	H$_2$	H$_2$O	K	KCl
0	0	0	0	0	0	0	0	0	0	0
0.010	4.6	7.8	170	10000	14900	41.5	7.3	3300	1776	18000
0.015	3.75	6.5	138	7100	9900	41.6	7.7	2170	7200	12000
0.020	3.25	5.9	120	5550	7500	41.8	8	1610	4300	9000
0.030	2.5	5.4	97	3530	5000	41.84	8.5	1060	1840	6000
0.040	2.05	5.2	85	2340	3700	41.8	8.96	830	1220	4500
0.050	1.73	5.4	76	1620	2980	41.7	9.28	650	960	3600
0.070	1.13	6.1	63	800	2130	41.3	9.85	456	720	2570
0.10	0.59	7.3	50	305	1490	40.6	10.5	318	550	1800
0.12	0.4	7.7	44	307	1240	39.7	10.85	265	500	1500
0.15	0.23	8.8	39	650	990	38.8	11.4	210	435	1200
0.17	0.16	9.3	34	1020	870	38.2	11.6	184	405	1060
0.20	0.103	10	29	1570	750	37.3	12	153	360	900
0.25	0.091	11.2	24	1793	600	36	12.5	124	313	720
0.30	0.153	12.1	18	1490	500	35	13	102	270	600
0.35	0.235	13	15	790	425	33.7	13.45	89	243	514
0.40	0.33	13.85	13	458	373	32.7	13.9	78	215	450
0.50	0.51	15.4	10	202	298	31	14.7	63.5	180	360
0.70	0.86	16.5	7.1	82	213	27.4	16.3	46.3	136	257
1.0	1.38	18.5	5.2	80	149	25.2	17.4	33.1	96	180
1.2	1.66	28	4.8	114	124	23.8	17.8	28	81	150
1.3	1.82	37	4.7	134	115	23	18	26	76	138
1.5	2.1	42	4.65	156	99.3	21.7	18.25	22.9	66	120
1.7	2.3	40	4.65	161	87.7	20.5	18.25	20	51	106
1.9	2.5	32	4.85	158	78.4	19.4	18.1	18.2	67	94.7
2.1	2.8	23.5	5.05	154	71	18.5	17.9	16.6	66	85.7
2.2	2.9	21.5	5.2	152	67.7	18.1	17.7	16	63	81.8
2.5	3.3	17.5	6.4	146	59.6	16.8	17	14.4	54	72
2.8	3.8	16	7.6	141	53.2	15.8	16.4	13.2	47	64.3
3.0	4.1	15.4	9	137	49.7	15.2	16	12.4	43	60
3.3	4.5	14.6	11.5	132	45.1	14.3	15.6	11.6	39.5	54.5
3.6	4.9	14.2	14	129	41.7	13.4	14.8	10.8	36.5	50
4.0	5.4	13.8	15.2	125	37.3	12.4	14	10	33.5	45
4.5	6.1	13.3	14.8	121	33.1	11.3	13.1	9.3	32	40
5.0	6.7	12.9	12.7	105	29.8	10.2	12.2	8.6	31	36
6.0	8.1	12.3	10	100	24.8	8.4	10.4	7.55	26	30
7.0	9.6	11.8	10	95	21.3	7.1	8.9	7.05	22	25.7
8.0	11.7	11.3	10.8	85	18.6	6.1	7.85	6.7	19.4	22.5
10.0	15	11.6	12.1	68	14.9	4.9	6	6.6	15.5	18
12.0	15.2	10.4	13.1	57	12.4	4.1	5.2	6.65	12.9	15
15.0	14.1	10.2	14.4	45	10.3	3.3	4.5	7.4	10.3	12.6
17.0	13.1	10.1	15	40	9.4	2.9	4.2	7.9	9.1	11.3
20.0	11	9.8	15.8	34	8.2	2.4	3.9	8.4	7.8	9.7
25.0	9.45	9.1	16	27	7	2	3.6	8.6	6.2	8.3
30.0	8.74	8.6	15.8	22.7	6.3	1.6	3.4	8.3	5.2	7.2
50.0	6.9	7.1	12.6	13.6	4.7	1	2.9	5	3.1	5.3

Table A.2: Momentum-transfer cross-sections, in $10^{-20}\,\mathrm{m}^2$, for specific species.

Energy (eV)	KO	KOH	K_2	N	NO	N_2	Na	NaCl	NaO	NaOH
0	0	0	0	0	0	0	0	0	0	0
0.010	1776	18000	3552	4.71	12	2.19	1243	18000	1243	18000
0.015	7200	12000	14400	4.715	8.1	2.55	5040	12000	5040	12000
0.020	4300	9000	8600	4.72	6.2	2.85	3010	9000	3010	9000
0.030	1840	6000	3680	4.73	4.65	3.4	1288	6000	1288	6000
0.040	1220	4500	2440	4.74	3.85	3.85	854	4500	854	4500
0.050	960	3600	1920	4.75	3.4	4.33	672	3600	672	3600
0.070	720	2570	1440	4.77	3	5.1	504	2570	504	2570
0.10	550	1800	1100	4.8	3.1	5.95	385	1800	385	1800
0.12	500	1500	1000	4.82	3.45	6.45	350	1500	350	1500
0.15	435	1200	870	4.85	4.05	7.1	304	1200	304	1200
0.17	405	1060	810	4.87	4.55	7.4	284	1060	284	1060
0.20	360	900	720	4.9	5.3	7.9	252	900	252	900
0.25	313	720	626	4.92	7	8.5	219	720	21.9	720
0.30	270	600	540	4.95	11.1	9	189	600	189	600
0.35	243	514	486	4.97	17.5	9.4	170	514	170	514
0.40	215	450	430	5	22.5	9.7	150	450	150	450
0.50	180	360	360	5.05	29	9.9	126	360	126	360
0.70	136	257	272	5.15	22.5	10	95	257	95	257
1.0	96	180	192	5.2	16.1	10	67	180	67	180
1.2	81	150	162	5.25	14.5	10.4	57	150	57	150
1.3	76	138	152	5.3	13.7	11	53	138	53	138
1.5	66	120	132	5.35	12.9	12	46	120	46	120
1.7	51	106	102	5.4	11.7	13.8	36	106	36	106
1.9	67	94.7	134	5.43	11.1	19.6	47	94.7	47	94.7
2.1	66	85.7	132	5.46	10.7	27	46	85.7	46	85.7
2.2	63	81.8	126	5.49	10.4	28.5	44	81.8	44	81.8
2.5	54	72	108	5.6	9.9	30	38	72	38	72
2.8	47	64.3	94	5.65	9.3	28	33	64.3	33	64.3
3.0	43	60	86	5.7	9.1	21.7	30	60	30	60
3.3	39.5	54.5	79	5.75	8.6	17.2	27.7	54.5	27.7	54.5
3.6	36.5	50	73	5.85	8.3	14.7	25.6	50	25.6	50
4.0	33.5	45	67	6	8.1	12.6	23.5	45	23.5	45
4.5	32	40	64	6.1	8.1	11.3	22.4	40	22.4	40
5.0	31	36	62	6.2	8.1	10.9	21.7	36	21.7	36
6.0	26	30	52	6.4	8.2	10.4	18.2	30	18.2	30
7.0	22	25.7	44	6.6	8.3	10.1	15.4	25.7	15.4	25.7
8.0	19.4	22.5	38.8	6.75	8.4	10	13.6	22.5	13.6	22.5
10.0	15.5	18	31	7.2	8.8	10.4	10.9	18	10.9	18
12.0	12.9	15	25.8	7.45	9.9	10.9	9	15	9	15
15.0	10.3	12.6	20.6	7.8	11.5	11	7.2	12.6	7.2	12.6
17.0	9.1	11.3	18.2	7.7	11.4	10.7	6.4	11.3	6.4	11.3
20.0	7.8	9.7	15.6	7.6	11	10.2	5.5	9.7	5.5	9.7
25.0	6.2	8.3	12.4	7.2	10.7	9.5	4.3	8.3	4.3	8.3
30.0	5.2	7.2	10.3	6.6	10.3	9	3.6	7.2	3.6	7.2
50.0	3.1	5.3	6.2	6.3	9.2	8.6	2.2	5.3	2.2	5.3

Table A.3: Momentum-transfer cross-sections, in $10^{-20}\,\mathrm{m}^2$, for specific species.

Energy (eV)	Na$_2$	O	OH	O$_2$	SO$_2$	He	SF$_6$	Ne	Xe	Mg
0	0	0	0	0	0	0	0	0	0	0
0.010	2486	4.71	2640	0.7	2570	5.28	800	0.37	116	8.7
0.015	10800	4.715	1700	0.87	1650	5.36	660	0.4	103	9.13
0.020	6020	4.72	1300	0.99	1250	5.42	560	0.423	80	9.4
0.030	2576	4.73	850	1.24	830	5.51	430	0.465	61	10.1
0.040	1708	4.74	660	1.44	650	5.59	430	0.505	48	10.8
0.050	1344	4.75	520	1.6	510	5.66	270	0.54	39.5	11.6
0.070	1008	4.77	360	2.1	360	5.77	175	0.6	29	13
0.10	770	4.8	257	2.5	250	5.91	90	0.7	20.2	15
0.12	700	4.82	214	2.8	206	5.98	62	0.76	17.2	19
0.15	609	4.85	170	3.1	164	6.08	35	0.825	13	23
0.17	567	4.87	151	3.3	146	6.13	27	0.87	11.6	20
0.20	504	4.9	122	3.6	120	6.21	19	0.93	8.4	23
0.25	438	4.92	100	4.1	97	6.32	12.5	1.02	5.35	26
0.30	378	4.95	82	4.5	80	6.4	9.7	1.09	3.15	30
0.35	340	4.97	71	4.7	69	6.47	8	1.14	2.1	33
0.40	301	5	62	5.2	61	6.54	7.3	1.21	1.75	37
0.50	252	5.05	51	5.7	50	6.64	7	1.31	1.38	44
0.70	190	5.15	37	6.1	36	6.77	7.1	1.48	1.36	58
1.0	134	5.2	26	7.2	26	6.88	7.7	1.62	1.28	80
1.2	113	5.25	22	7.9	22	6.93	8	1.69	3.35	78
1.3	106	5.3	21	7.9	20.2	6.95	8.2	1.7	3.9	76
1.5	92	5.35	18.3	7.6	17.8	6.98	8.8	1.75	5	75
1.7	71	5.4	16.1	7.3	15.6	6.99	9.2	1.77	6.3	74
1.9	94	5.43	14.5	6.9	14.1	7.01	9.7	1.79	7.5	73
2.1	92	5.46	13.2	6.6	12.9	7	10	1.8	9.1	70
2.2	88	5.49	12.8	6.5	12.4	6.99	10.1	1.81	9.9	68
2.5	76	5.6	11.5	6.1	11.2	6.95	10.8	1.85	12.5	65
2.8	66	5.65	10.6	5.8	10.3	6.9	11.5	1.88	15	61
3.0	60	5.7	9.9	5.7	9.7	6.86	11.6	1.9	17	58
3.3	55.3	5.75	9.3	5.5	9	6.79	12	1.93	18.9	55
3.6	51	5.85	8.7	5.45	8.4	6.71	12.1	1.96	21.3	53
4.0	47	6	8.1	5.5	7.8	6.62	12.5	1.98	24.8	50
4.5	45	6.1	7.5	5.55	7.2	6.47	13.1	2.03	27.6	45
5.0	43.4	6.2	6.9	5.6	6.7	6.32	13.5	2.08	30.8	40
6.0	36.4	6.4	6	6	5.9	5.99	14	2.13	30.5	38
7.0	30.8	6.6	5.6	6.6	5.5	5.67	14.5	2.23	28	37
8.0	27.2	6.75	5.4	7.1	5.2	5.35	15	2.35	23.5	35
10.0	21.7	7.2	5.3	8	5.1	4.76	16	2.45	16	32
12.0	18.1	7.45	5.3	8.5	5.2	4.21	16.2	2.6	13	30
15.0	14.4	7.8	5.9	8.8	5.8	3.8	16.5	2.83	10.2	20
17.0	12.7	7.7	6.3	8.7	6.2	3.1	16.5	2.95	8.3	13
20.0	10.9	7.6	6.7	8.6	6.6	2.58	16.5	3.15	7	10
25.0	8.7	7.2	6.9	8.2	6.7	1.95	16	3.2	5.9	6
30.0	7.2	6.6	6.7	8	6.6	1.74	15	3.2	5.1	5
50.0	4.3	6.3	6.1	7.7	6	1.1	14	2.8	4.3	4.2

APPENDIX B

EXPRESSIONS FOR THE q^{mn} ELEMENTS

The Earth is the cradle of humanity, but mankind cannot stay in the cradle forever.

—Konstantin Tsiolkovsky

B.1   Overview

The calculation of electrical conductivity from electron-neutral collisions is based on a method by Devoto [153], and is detailed in Section 4.2.2.2. The electron-neutral conductivity equation is as follows:

$$\sigma = \frac{e^2 n_1 n m_1}{\rho k T} D_{11},$$ (B.1)

where e is the electron charge, n is the total number density, n_1 is the electron number density (any subscript "1" denotes electrons), m_1 is the mass of an electron, ρ is the total mass density of all particles, k is the Boltzmann constant, T is the fluid temperature, and D_{ij} is the multicomponent diffusion coefficient (here, the subscript "1" is used for both the i and j components because only electron diffusion is considered in the calculation).

The solution of Equation 4.8 for $f_1(\mathbf{r}, \mathbf{v}, t)$ is accomplished through an expansion of the function in a finite series of Sonine polynomials [153], with the level of approximation of the transport coefficients being the number of terms in the expansion series. It has been shown that at least the second-order approximation is required for a reasonable level of accuracy [95, 161]. In the fourth-order approximation, the ordinary diffusion coefficient is given by [158]

$$[D_{11}]_4 = \frac{3n_1\rho}{2nm_1} \frac{\sqrt{2\pi kT/m_1}}{|q|} \begin{vmatrix} q^{11} & q^{12} & q^{13} \\ q^{21} & q^{22} & q^{23} \\ q^{31} & q^{32} & q^{33} \end{vmatrix}, \tag{B.2}$$

where $|q|$ is the determinant of the q^{mn} elements. The q^{mn} elements represent the coefficients to the simplified electron equilibrium Maxwellian distribution function and are dependent on $\bar{Q}_{ij}^{(\ell,s)}$, the Maxwellian velocity-averaged collision cross-section between species i and j.

B.2   Equations

The simplified expressions for the q^{mn} elements given below are based on the assumptions listed in Section 4.2.2.2 [158], and were first applied to the electrical conductivity of a partially ionized gas by DeVoto [153, 156–160], but were originally developed to describe transport properties of gases [154, 155]. In the expressions below, it is understood that the summation over j runs over all heavy species (*i.e.*, from 2 to ν). Furthermore, the q^{mn} are symmetric in m and n, as can be shown from

the general properties of the bracket integrals [155]. Therefore, since, for example, $q^{12} = q^{21}$, only the expression for q^{12} will be given.

$$q^{11} = 8\sqrt{2}\,n_1^2 \bar{Q}_{11}^{(2,2)} + 8\sum_i n_1 n_j \left[\frac{25}{4}\bar{Q}_{1j}^{(1,1)} - 15\bar{Q}_{1j}^{(1,2)} + 12\bar{Q}_{1j}^{(1,3)} \right] \tag{B.3}$$

$$q^{12} = 8\sqrt{2}\,n_1^2 \left[\frac{7}{4}\bar{Q}_{11}^{(2,2)} - 2\bar{Q}_{11}^{(2,3)} \right]$$
$$+ 8\sum_i n_1 n_j \left[\frac{175}{16}\bar{Q}_{1j}^{(1,1)} - \frac{315}{8}\bar{Q}_{1j}^{(1,2)} + 57\bar{Q}_{1j}^{(1,3)} - 30\bar{Q}_{1j}^{(1,4)} \right] \tag{B.4}$$

$$q^{13} = 8\sqrt{2}\,n_1^2 \left[\frac{63}{32}\bar{Q}_{11}^{(2,2)} - \frac{9}{2}\bar{Q}_{11}^{(2,3)} + \frac{5}{2}\bar{Q}_{11}^{(2,4)} \right]$$
$$- 8\sum_i n_1 n_j \left[\frac{252}{32}\bar{Q}_{1j}^{(1,1)} - \frac{315}{4}\bar{Q}_{1j}^{(1,2)} + 162\bar{Q}_{1j}^{(1,3)} - 160\bar{Q}_{1j}^{(1,4)} + 60\bar{Q}_{1j}^{(1,5)} \right] \tag{B.5}$$

$$q^{22} = 8\sqrt{2}\,n_1^2 \left[\frac{77}{16}\bar{Q}_{11}^{(2,2)} - 7\bar{Q}_{11}^{(2,3)} + 5\bar{Q}_{11}^{(2,4)} \right]$$
$$+ 8\sum_i n_1 n_j \left[\frac{1225}{64}\bar{Q}_{1j}^{(1,1)} - \frac{738}{8}\bar{Q}_{1j}^{(1,2)} + \frac{399}{2}\bar{Q}_{1j}^{(1,3)} - 210\bar{Q}_{1j}^{(1,4)} + 90\bar{Q}_{1j}^{(1,5)} \right] \tag{B.6}$$

$$q^{23} = 8\sqrt{2}\,n_1^2 \left[\frac{945}{128}\bar{Q}_{11}^{(2,2)} - \frac{261}{16}\bar{Q}_{11}^{(2,3)} + \frac{125}{8}\bar{Q}_{11}^{(2,4)} - \frac{15}{2}\bar{Q}_{11}^{(2,5)} \right]$$

$$+ 8\sum_i n_1 n_j \left[\frac{3675}{128}\bar{Q}_{1j}^{(1,1)} - \frac{11025}{64}\bar{Q}_{1j}^{(1,2)} + \frac{1953}{4}\bar{Q}_{1j}^{(1,3)} \right]$$

$$+ 8\sum_i n_1 n_j \left[-\frac{1505}{2}\bar{Q}_{1j}^{(1,4)} + 615\bar{Q}_{1j}^{(1,5)} - 210\bar{Q}_{1j}^{(1,6)} \right] \quad \text{(B.7)}$$

$$q^{33} = 8\sqrt{2}\,n_1^2 \left[\frac{14553}{1024}\bar{Q}_{11}^{(2,2)} - \frac{1215}{32}\bar{Q}_{11}^{(2,3)} + \frac{1565}{32}\bar{Q}_{11}^{(2,4)} \right]$$

$$+ 8\sqrt{2}\,n_1^2 \left[-\frac{135}{4}\bar{Q}_{11}^{(2,5)} + \frac{105}{8}\bar{Q}_{11}^{(2,6)} + \bar{Q}_{11}^{(4,4)} \right]$$

$$+ 8\sum_i n_1 n_j \left[\frac{11025}{256}\bar{Q}_{1j}^{(1,1)} - \frac{19845}{64}\bar{Q}_{1j}^{(1,2)} + \frac{17577}{16}\bar{Q}_{1j}^{(1,3)} \right]$$

$$+ 8\sum_i n_1 n_j \left[-\frac{4515}{2}\bar{Q}_{1j}^{(1,4)} + \frac{5535}{2}\bar{Q}_{1j}^{(1,5)} - 1890\bar{Q}_{1j}^{(1,6)} + 560\bar{Q}_{1j}^{(1,7)} \right] \quad \text{(B.8)}$$

APPENDIX C

DETAILED CALCULATIONS AND COMPARISONS OF THE DIAGONAL MHD GENERATOR AND ACCELERATOR MODES

Science is a way of thinking much more than it is a body of knowledge.

—Carl Sagan

C.1 Overview

Section 3.3.1 gives the formulation of the electrical model used in the original MGMHD numerical model, while Section 4.3.1.2 summarizes the changes made to allow for modeling of diagonal MHD accelerators in the UMM numerical model. This appendix derives a more detailed formulation of the electrical models given in those sections. Please note that the infinite segmentation assumption is implemented for both derivations given in this appendix. Finite segmentation effects on the global performance of MHD generators have been shown to become negligible for medium- or large-base-load generators that have a pitch-to-height ratio on the order of 1-5% [125, 137–139]. For smaller generators, finite segmentation effects become more important and should be considered—infinite segmentation analysis of small genera-

tors usually over predicts their global performance [138, 139]. It is assumed that the same finite/infinite segmentation limitations exist for MHD accelerators.

C.2 Diagonal Generator Mode

In the MGMHD code, the electrical governing equations consist of Maxwell's steady-state equations and Ohm's Law. The electrical field, $\mathbf{E}$, and the current density, $\mathbf{J}$, are obtained by solving the following equations:

$$\nabla \times \mathbf{E} = 0, \tag{C.1}$$

$$\nabla \cdot \mathbf{J} = 0, \tag{C.2}$$

and

$$\mathbf{J} = \sigma \left(\mathbf{E} + \mathbf{u} \times \mathbf{B} \right) - \frac{\beta}{B} \mathbf{J} \times \mathbf{B}, \tag{C.3}$$

where σ is the electrical conductivity, $\mathbf{u}$ is the velocity vector, $\mathbf{B}$ is the magnetic field vector (with B being the magnitude of the magnetic field), and β is the Hall parameter. As typical for MHD channel flows, these equations are valid for low magnetic Reynolds number flows, where the induced magnetic fields can be neglected [125, 128, 137]. Therefore, it is possible to define an electric potential, ψ, such that [91, 141]

$$\mathbf{E} = -\nabla \psi = -\frac{\partial \psi}{\partial x} - \frac{\partial \psi}{\partial y} - \frac{\partial \psi}{\partial z} = E_x + E_y + E_z, \tag{C.4}$$
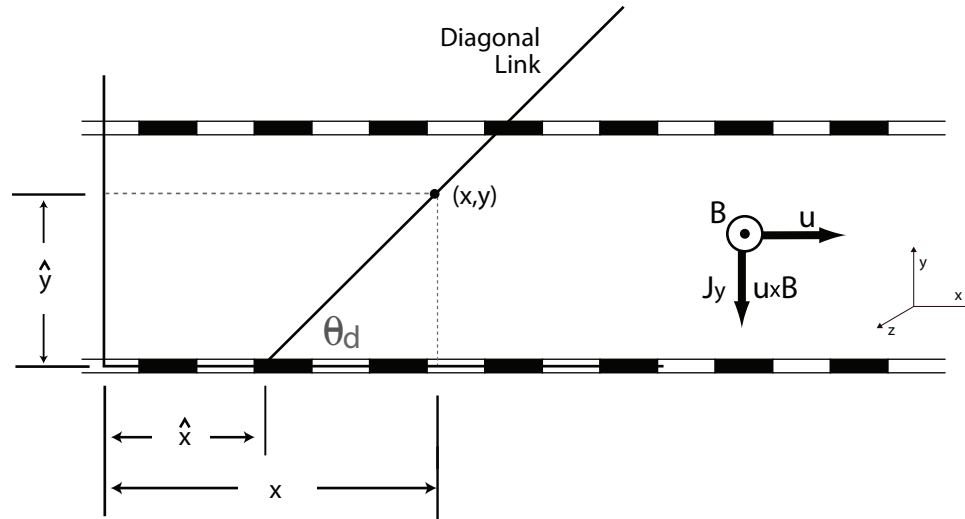
Figure C.1: Transformation relationship and coordinate system for a diagonal MHD generator.

which, because of the steady-state assumption ($\frac{\partial}{\partial t} = 0$), effectively reduces a vector problem to that of a scalar, where $\psi(x, y, z)$ is a three-dimensional potential. Also note that the MGMHD code assumes that the magnetic field, **B**, is sectionally uniform and oriented in the positive $\hat{\mathbf{z}}$ direction, as seen in Figures 3.1 and 3.2.

Figure C.1 shows the MHD generator oblique coordinate system used in this derivation, where Figures 3.1 and 3.2 show how this oblique coordinate system relates to a diagonal generator. The diagonal link lies along the oblique coordinate direction, and the following relations exits:

$$\tan \theta_d = \frac{\hat{y}}{x - \hat{x}} = \frac{y}{x - \hat{x}} \qquad (C.5)$$

and

$$\cot \theta_d = \frac{x - \hat{x}}{y}. \qquad (C.6)$$

Therefore, the transformation relationships are

$$\hat{x} = x - y \cot \theta_d, \qquad \text{(C.7)}$$

$$\hat{y} = y, \qquad \text{(C.8)}$$

and

$$\hat{z} = z. \qquad \text{(C.9)}$$

Therefore the electric potential becomes

$$\frac{\partial \psi}{\partial x} = \frac{\partial \psi}{\partial \hat{x}} = -E_x, \qquad \text{(C.10)}$$

$$\therefore \ \partial \psi = -E_x \partial \hat{x}, \qquad \text{(C.11)}$$

$$\therefore \ \psi_x = -\hat{x} E_x, \qquad \text{(C.12)}$$

where the above assumes the infinite segmentation model—neglecting axial varia-tions of the flow and electrical variables in comparison to their cross-plane variations. Furthermore, the $\hat{\mathbf{y}}$ and $\hat{\mathbf{z}}$ components are

$$\frac{\partial \psi}{\partial y} = \frac{\partial \psi}{\partial \hat{y}} = -E_y(y, z) \ \rightarrow \ \partial \psi_y = -E_y(y, z) \partial \hat{y} \qquad \text{(C.13)}$$

and

$$\frac{\partial \psi}{\partial z} = \frac{\partial \psi}{\partial \hat{z}} = -E_z(y, z) \ \rightarrow \ \partial \psi_z = -E_z(y, z) \partial \hat{z}. \qquad \text{(C.14)}$$

Therefore, combining the components of ψ from above yields

$$\psi = -\hat{x}E_x + \phi(y, z) = -\left(x - y \cot \theta_d\right) E_x + \phi(y, z), \tag{C.15}$$

where θ_d is the diagonalization angle (measured in a counter-clockwise direction from the positive x-axis), and $\phi(y, z)$ is a two-dimensional potential (in the cross-sectional plane). Please see Section 3.3.2 for a more detailed explanation of the diagonalization angle.

Going back to the diagonalization condition—where $\mathbf{B}$ is assumed to be uniform in the $\hat{\mathbf{z}}$ direction, $\mathbf{u}$ is a function of (x, y), and $\mathbf{E}$ and $\mathbf{J}$ are three-dimensional—from Section 1.2.2.3, the definition of the electric field angle is

$$\frac{E_y}{E_x} = \tan \theta \implies \frac{E_x}{E_y} = \cot \theta. \tag{C.16}$$

Therefore

$$\mathbf{u} = u\hat{i} + v\hat{j} + 0\hat{k}, \tag{C.17}$$

$$\mathbf{B} = 0\hat{i} + 0\hat{j} + B\hat{k}, \tag{C.18}$$

$$\mathbf{E} = E_x\hat{i} + E_y\hat{j} + E_z\hat{k}, \tag{C.19}$$

$$\mathbf{J} = J_x\hat{i} + J_y\hat{j} + J_z\hat{k}. \tag{C.20}$$

Taking the appropriate cross-products from above yields

$$\mathbf{u} \times \mathbf{B} = \begin{vmatrix} \hat{i} & \hat{j} & \hat{k} \\ u & v & 0 \\ 0 & 0 & B \end{vmatrix} = vB\hat{i} - uB\hat{j} + 0\hat{k}. \tag{C.21}$$

Which expands to the following:

$$(\mathbf{u} \times \mathbf{B})_x = vB, \tag{C.22}$$

$$(\mathbf{u} \times \mathbf{B})_y = -uB, \tag{C.23}$$

$$(\mathbf{u} \times \mathbf{B})_x = 0. \tag{C.24}$$

While the $\mathbf{J} \times \mathbf{B}$ Lorentz force is the following:

$$\mathbf{J} \times \mathbf{B} = \begin{vmatrix} \hat{i} & \hat{j} & \hat{k} \\ J_x & J_y & J_z \\ 0 & 0 & B \end{vmatrix} = J_y B\hat{i} - J_x B\hat{j} + 0\hat{k}. \tag{C.25}$$

Which expands to the following:

$$(\mathbf{J} \times \mathbf{B})_x = J_y B, \tag{C.26}$$

$$(\mathbf{J} \times \mathbf{B})_y = -J_x B, \tag{C.27}$$

$$(\mathbf{J} \times \mathbf{B})_x = 0. \tag{C.28}$$

Now, solve the Generalized Ohm's Law, Equation C.3, for the individual components of **J**:

$$J_x = \sigma E_x + \sigma v B - \beta J_y, \tag{C.29}$$

$$J_y = \sigma E_y - \sigma u B + \beta J_x, \tag{C.30}$$

and

$$J_z = \sigma E_z. \tag{C.31}$$

Equation C.31 requires no further reduction, but the J_y term needs to be eliminated from Equation C.29, and the J_x term should be eliminated from Equation C.30. So, substituting the right-hand-side of Equation C.30 into Equation C.29 to eliminate J_y in Equation C.29 yields

$$
\begin{aligned}
J_x &= \sigma E_x + \sigma v B - \beta \sigma E_y + \beta \sigma u B - \beta^2 J_x, & \text{(C.32)} \\
\left(1 + \beta^2\right) J_x &= \sigma \left[E_x - \beta E_y + (v + \beta u) B\right], & \text{(C.33)} \\
J_x &= \frac{\sigma}{1 + \beta^2} \left[E_x - \beta E_y + (v + \beta u) B\right], & \text{(C.34)} \\
J_x &= \sigma_n \left[E_x - \beta E_y + (v + \beta u) B\right], & \text{(C.35)}
\end{aligned}
$$

where $\sigma_n = \sigma/(1 + \beta^2)$. Similarly, substituting the right-hand-side of Equation C.29 into Equation C.30 to eliminate the J_x term yields

$$J_y = \sigma E_y - \sigma u B + \beta \sigma E_x + \beta \sigma v B - \beta^2 J_y, \tag{C.36}$$

$$\left(1 + \beta^2\right) J_y = \sigma \left[\beta E_x + E_y + (\beta v - u) B\right], \tag{C.37}$$

$$J_y = \frac{\sigma}{1 + \beta^2} \left[\beta E_x + E_y + (\beta v - u) B\right], \tag{C.38}$$

$$J_y = \sigma_n \left[\beta E_x + E_y + (\beta v - u) B\right]. \tag{C.39}$$

.

Expanding Equation C.1 yields the following:

$$\nabla \times \mathbf{E} = 0 = \begin{vmatrix} \hat{i} & \hat{j} & \hat{k} \\ \frac{\partial}{\partial x} & \frac{\partial}{\partial y} & \frac{\partial}{\partial z} \\ E_x & E_y & E_z \end{vmatrix} =$$

$$\left(\frac{\partial E_z}{\partial y} - \frac{\partial E_y}{\partial z}\right) \hat{i} - \left(\frac{\partial E_z}{\partial x} - \frac{\partial E_x}{\partial z}\right) \hat{j} + \left(\frac{\partial E_y}{\partial x} - \frac{\partial E_x}{\partial y}\right) \hat{k}. \tag{C.40}$$

Therefore, the following relationships must be true:

$$\frac{\partial E_z}{\partial y} - \frac{\partial E_y}{\partial z} = 0, \tag{C.41}$$

$$\frac{\partial E_z}{\partial x} - \frac{\partial E_x}{\partial z} = 0, \tag{C.42}$$

$$\frac{\partial E_y}{\partial x} - \frac{\partial E_x}{\partial y} = 0. \tag{C.43}$$

Furthermore, Equation C.2 becomes

$$\nabla \cdot \mathbf{J} = \frac{\partial J_x}{\partial x} + \frac{\partial J_y}{\partial y} + \frac{\partial J_z}{\partial z} = 0. \tag{C.44}$$

Recall Equation C.15 that reduces to

$$\psi = -\left(x - y \cot \theta_d\right) E_x + \phi(y, z). \tag{C.45}$$

Therefore, the following relationships must be true:

$$E_x = -\frac{\partial \psi}{\partial x} = E_x, \tag{C.46}$$

$$E_y = -\frac{\partial \psi}{\partial y} = -\cot \theta_d E_x - \frac{\partial \phi}{\partial y}, \tag{C.47}$$

$$E_z = -\frac{\partial \psi}{\partial z} = -\frac{\partial \phi}{\partial z}. \tag{C.48}$$

Now, substituting Equations C.35 and C.39 into Equation C.44 yields

$$\frac{\partial}{\partial x} \left(\sigma_n \left[E_x = \beta E_y + (v + \beta u)\, B\right]\right) + \frac{\partial}{\partial y} \left(\sigma_n \left[\beta E_x + E_y + (\beta v - u)\, B\right]\right)$$

$$+ \frac{\partial}{\partial z} \left(\sigma E_z\right) = 0, \tag{C.49}$$

where the infinite segmentation assumption dictates that the first term on the left-hand-side of Equation C.49—the partial derivative with respect to x—is negligible.

Therefore, this reduces to

$$\frac{\partial}{\partial y}\left[\sigma_n \beta E_x\right] + \frac{\partial}{\partial y}\left[\sigma_n E_y\right] + \frac{\partial}{\partial y}\left[\sigma_n B\left(\beta v - u\right)\right] + \frac{\partial}{\partial z}\left[\sigma E_z\right] = 0. \tag{C.50}$$

Now, eliminating the E_y and E_z terms from above yields the following:

$$\frac{\partial}{\partial y}\left[\sigma_n \beta E_x\right] - \frac{\partial}{\partial y}\left[\sigma_n\left(\cot\theta_d E_x + \frac{\partial\phi}{\partial y}\right)\right] + \frac{\partial}{\partial y}\left[\sigma_n B\left(\beta v - u\right)\right] - \frac{\partial}{\partial z}\left[\sigma\frac{\partial\phi}{\partial z}\right] = 0, \tag{C.51}$$

which reduces to

$$\frac{\partial}{\partial y}\left[\left(\beta - \cot\theta_d\right)\sigma_n E_x\right] - \frac{\partial}{\partial y}\left[\sigma_n\frac{\partial\phi}{\partial y}\right] + \frac{\partial}{\partial y}\left[\sigma_n B\left(\beta v - u\right)\right] - \frac{\partial}{\partial z}\left[\sigma\frac{\partial\phi}{\partial z}\right] = 0. \tag{C.52}$$

Equation C.52 can be rearranged, just as in Equation 3.35, to form the relationship:

$$\frac{\partial}{\partial y}\left(\sigma_n\frac{\partial\phi}{\partial y}\right) + \frac{\partial}{\partial z}\left(\sigma\frac{\partial\phi}{\partial z}\right) = E_x\frac{\partial}{\partial y}\left[\left(\beta - \cot\theta_d\right)\sigma_n\right] - \frac{\partial}{\partial y}\left[\sigma_n B\left(u - \beta v\right)\right]. \tag{C.53}$$

Since E_x is not known *a' priori*, and because Equation C.53 is linear in ϕ, a decomposition of the potential is permitted as follows [125]:

$$\phi(y, z) = E_x\phi_1 + \phi_2. \tag{C.54}$$

Substituting the decomposition yields the following:

$$\frac{\partial}{\partial y}\left[\sigma_n\left(\frac{\partial}{\partial y}E_x\phi_1 + \frac{\partial\phi_2}{\partial y}\right)\right] + \frac{\partial}{\partial z}\left[\sigma_n\left(\frac{\partial}{\partial z}E_x\phi_1 + \frac{\partial\phi_2}{\partial z}\right)\right]$$

$$= E_x\frac{\partial}{\partial y}\left[(\beta - \cot\theta_d)\,\sigma_n\right] - \frac{\partial}{\partial y}\left[\theta_n B\,(u - \beta v)\right]. \quad (C.55)$$

Therefore,

$$E_x\frac{\partial}{\partial y}\left[\sigma_n\frac{\partial\phi_1}{\partial y}\right] + E_x\frac{\partial}{\partial z}\left[\sigma\frac{\partial\phi_1}{\partial z}\right] + \frac{\partial}{\partial y}\left[\sigma_n\frac{\partial\phi_2}{\partial y}\right] + \frac{\partial}{\partial z}\left[\sigma\frac{\partial\phi_2}{\partial z}\right]$$

$$= E_x\frac{\partial}{\partial y}\left[(\beta - \cot\theta_d)\,\sigma_n\right] - \frac{\partial}{\partial y}\left[\sigma_n B\,(u - v\beta)\right], \quad (C.56)$$

where the E_x terms can be collected, giving

$$E_x\frac{\partial}{\partial y}\left[\sigma_n\frac{\partial\phi_1}{\partial y}\right] + E_x\frac{\partial}{\partial z}\left[\sigma\frac{\partial\phi_1}{\partial z}\right] = E_x\frac{\partial}{\partial y}\left[(\beta - \cot\theta_d)\,\sigma_n\right]. \quad (C.57)$$

All of the E_x terms from Equation C.57 can be canceled out, and the remaining terms from Equation C.56 can be collected as follows:

$$\frac{\partial}{\partial y}\left[\sigma_n\frac{\partial\phi_2}{\partial y}\right] + \frac{\partial}{\partial z}\left[\sigma\frac{\partial\phi_2}{\partial z}\right] = -\frac{\partial}{\partial y}\left[\sigma_n B\,(u - v\beta)\right]. \quad (C.58)$$

Now, the two functions, ϕ_1 and ϕ_2, can be described by the following equations [128]:

$$L(\phi_1) = \frac{\partial}{\partial y}\left[(\beta - \cot\theta_d)\,\sigma_n\right] \quad (C.59)$$

and

$$L(\phi_2) = -\frac{\partial}{\partial y}\left[\sigma_n B\left(u - \beta v\right)\right],\tag{C.60}$$

where the operator, L, is [128, 137]

$$L = \frac{\partial}{\partial y}\left(\sigma_n \frac{\partial}{\partial y}\right) + \frac{\partial}{\partial z}\left(\sigma \frac{\partial}{\partial z}\right).\tag{C.61}$$

Note that the function ϕ_1 in Equation C.59 is driven by the temperature nonuniformities, while ϕ_2 in Equation C.60 is driven by temperature and velocity nonuniformities. Both functions are independent of E_x, which is reduced to a parameter of the problem to be determined later from the specification of the external electrical connection and loading.

Now consider the x-component of Ohm's Law:

$$J_x = \sigma_n\left[E_x - \beta E_y + \left(\beta u + v\right)B\right] = \sigma_n E_x - \sigma_n \beta E_y + \left(\beta u + v\right)B\sigma_n,\tag{C.62}$$

where substituting Equation C.47 for E_y in the above equation yields

$$J_x = E_x\sigma_n\left(1 + \beta\cot\theta_d\right) + \sigma_n\left[\beta\frac{\partial\phi}{\partial y} + B\left(\beta u + v\right)\right].\tag{C.63}$$

The ϕ term can be eliminated using Equation C.54, resulting in Equation 3.40:

$$J_x = E_x\sigma_n\left(1 + \beta\cot\theta_d + \beta\frac{\partial\phi_1}{\partial y}\right) + \sigma_n\left[\left(\beta u + v\right)B + \beta\frac{\partial\phi_2}{\partial y}\right].\tag{C.64}$$

To find the cross-sectional average current, the cross-sectional spatial average, $\langle f \rangle$, must first be defined as

$$\langle f \rangle = \frac{1}{A} \int f(y, z) \, dA, \tag{C.65}$$

where A is the cross-sectional area normal to the channel. Therefore, Equation C.64 becomes [128, 137]

$$\langle J_x \rangle = E_x \left[\langle (1 + \beta \cot \theta_d) \, \sigma_n \rangle + \langle \sigma_n \beta \frac{\partial \phi_1}{\partial y} \rangle \right] + \langle \sigma_n \beta \frac{\partial \phi_2}{\partial y} \rangle + B \langle \sigma_n \left(\beta u + v \right) \rangle. \tag{C.66}$$

Now consider the y-component of Ohms Law:

$$J_y = \sigma_n \left[\beta E_x + E_y + B \left(\beta v - u \right) \right] = \sigma_n \beta E_x + \sigma_n E_y + \left(\beta v - u \right) B \sigma_n, \tag{C.67}$$

where substituting Equation C.47 for E_y in the above equation yields

$$J_y = E_x \sigma_n \left(\beta - \cot \theta_d \right) - \sigma_n \left[\frac{\partial \phi}{\partial y} + B \left(u - \beta v \right) \right]. \tag{C.68}$$

The ϕ term can be eliminated using Equation C.54, resulting in Equation 3.41:

$$J_y = E_x \sigma_n \left(\beta - \cot \theta_d - \frac{\partial \phi_1}{\partial y} \right) - \sigma_n \left[\left(u - \beta v \right) B + \frac{\partial \phi_2}{\partial y} \right]. \tag{C.69}$$

Applying Equation C.65 to Equation C.69 gives the following equation for the cross-sectional averaged J_y current density:

$$\langle J_y \rangle = E_x \left[\langle (\beta - \cot \theta_d) \, \sigma_n \rangle - \langle \sigma_n \frac{\partial \phi_1}{\partial y} \rangle \right] - \langle \sigma_n \frac{\partial \phi_2}{\partial y} \rangle - B \langle \sigma_n \left(u - \beta v \right) \rangle. \tag{C.70}$$

The z-component of Ohm's Law is much simpler in this case:

$$J_z = \sigma E_z, \tag{C.71}$$

where substituting Equation C.48 yields

$$J_z = -\sigma \frac{\partial \phi}{\partial z}, \tag{C.72}$$

Eliminating ϕ using Equation C.54 gives

$$J_z = -\sigma \frac{\partial}{\partial z} \left[E_x \phi_1 + \phi_2 \right]. \tag{C.73}$$

Therefore, the current density in the $\hat{\mathbf{z}}$ direction is

$$J_z = -\sigma E_x \frac{\partial \phi_1}{\partial z} - \sigma \frac{\partial \phi_2}{\partial z}. \tag{C.74}$$

C.3 Diagonal Accelerator Mode

As discussed in Section 4.3.1.2, there are many similarities between diagonal MHD generators and diagonal MHD accelerators. The governing equations for the
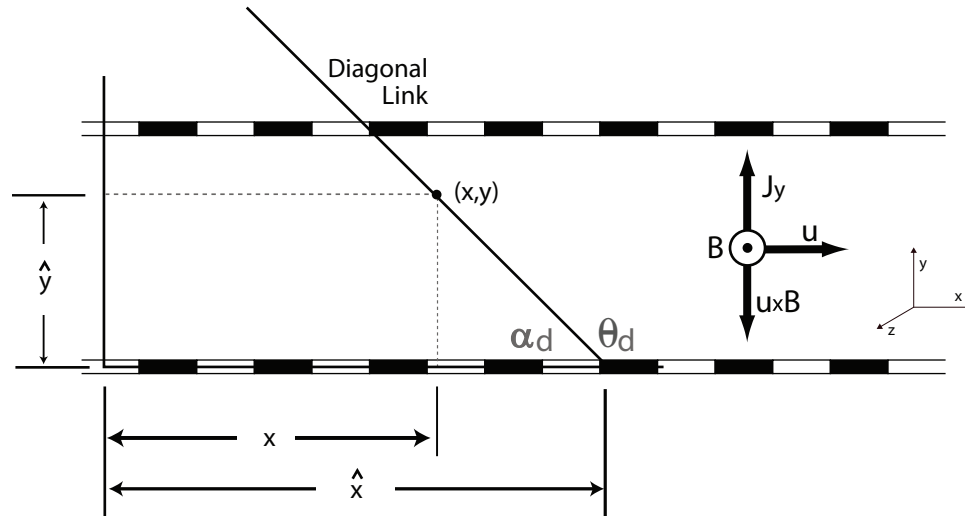
Figure C.2: Transformation relationship and coordinate system for a diagonal MHD accelerator.

diagonal accelerator mode are the same as the diagonal generator—therefore, Equation C.1 through Equation C.4 apply. As shown in Section 3.3.2, the primary physical difference between the diagonal accelerator and the diagonal generator is the diagonal link connecting the electrodes. Therefore, for an MHD accelerator, a new set of oblique coordinates must be defined, and for the purposes of this derivation, a new diagonal angle, α_d is used.

Figure C.2 shows the oblique coordinate system used in this diagonal accelerator derivation, where Figures 1.8, 3.3 and 3.4 show how this oblique coordinate system relates to a diagonal accelerator. The diagonal link lies along the oblique coordinate direction, and the following relations exits:

$$\tan \alpha_d = \frac{\hat{y}}{\hat{x} - x} \tag{C.75}$$

and

$$\cot \alpha_d = \frac{\hat{x} - x}{y}. \tag{C.76}$$

Therefore, the transformation relationships are

$$\hat{x} = x + y \cot \alpha_d, \tag{C.77}$$

$$\hat{y} = y, \tag{C.78}$$

and

$$\hat{z} = z. \tag{C.79}$$

The electric potential development is the same as for the diagonal generator. Therefore, Equation C.10 through Equation C.14 are the same. However, combining the components of ψ from Equation C.14 with the transformation in Equation C.77 yields

$$\psi = -\hat{x} E_x + \phi(y, z) = -(x + y \cot \alpha_d) E_x + \phi(y, z), \tag{C.80}$$

where α_d is the related to the diagonalization angle, $theta_d$ (measured in a counter-clockwise direction from the positive x-axis) through

$$\alpha_d = 180 - \theta_d, \tag{C.81}$$

and $\phi(y, z)$ is a two-dimensional potential (in the cross-sectional plane). Please see Section 3.3.2 for a more detailed explanation of the diagonalization angle and its relation to the electric field angle.

At this point, the derivation of the diagonal accelerator mimics that of the diagonal generator. The definition of the electric field angle—first given in Equation 1.46 and reiterated in Equation C.16—is true for both generators and accelerators. Furthermore, the development of the generalized Ohm's Law and Maxwell's Equations are identical in both modes. Therefore, please refer to Equation C.16 through Equation C.44 for their derivations.

Recall Equation C.80 that reduces to

$$\psi = - \left(x + y \cot \alpha_d \right) E_x + \phi(y, z). \tag{C.82}$$

Therefore, the following relationships must be true:

$$E_x = -\frac{\partial \psi}{\partial x} = E_x, \tag{C.83}$$

$$E_y = -\frac{\partial \psi}{\partial y} = \cot \alpha_d E_x - \frac{\partial \phi}{\partial y}, \tag{C.84}$$

$$E_z = -\frac{\partial \psi}{\partial z} = -\frac{\partial \phi}{\partial z}. \tag{C.85}$$

Using the above to eliminate the E_y and E_z terms from Equation C.50 yields the following:

$$\frac{\partial}{\partial y}\left[\sigma_n \beta E_x\right] + \frac{\partial}{\partial y}\left[\sigma_n\left(\cot\alpha_d E_x + \frac{\partial\phi}{\partial y}\right)\right] + \frac{\partial}{\partial y}\left[\sigma_n B\left(\beta v - u\right)\right] - \frac{\partial}{\partial z}\left[\sigma\frac{\partial\phi}{\partial z}\right] = 0,$$

(C.86)

which reduces to

$$\frac{\partial}{\partial y}\left[(\beta + \cot\alpha_d)\,\sigma_n E_x\right] - \frac{\partial}{\partial y}\left[\sigma_n\frac{\partial\phi}{\partial y}\right] + \frac{\partial}{\partial y}\left[\sigma_n B\left(\beta v - u\right)\right] - \frac{\partial}{\partial z}\left[\sigma\frac{\partial\phi}{\partial z}\right] = 0. \quad \text{(C.87)}$$

Equation C.87 can be rearranged, just as in Equation 4.31, to form the relationship:

$$\frac{\partial}{\partial y}\left(\sigma_n\frac{\partial\phi}{\partial y}\right) + \frac{\partial}{\partial z}\left(\sigma\frac{\partial\phi}{\partial z}\right) = E_x\frac{\partial}{\partial y}\left[(\beta + \cot\alpha_d)\,\sigma_n\right] - \frac{\partial}{\partial y}\left[\sigma_n B\left(u - \beta v\right)\right]. \quad \text{(C.88)}$$

The same decomposition that is used in Equation C.53 is permitted in Equation C.88:

$$\phi(y,z) = E_x\phi_1 + \phi_2. \tag{C.89}$$

Substituting the decomposition yields the following:

$$\frac{\partial}{\partial y}\left[\sigma_n\left(\frac{\partial}{\partial y}E_x\phi_1 + \frac{\partial\phi_2}{\partial y}\right)\right] + \frac{\partial}{\partial z}\left[\sigma_n\left(\frac{\partial}{\partial z}E_x\phi_1 + \frac{\partial\phi_2}{\partial z}\right)\right]$$
$$= E_x\frac{\partial}{\partial y}\left[(\beta + \cot\alpha_d)\,\sigma_n\right] - \frac{\partial}{\partial y}\left[\theta_n B\left(u - \beta v\right)\right]. \quad \text{(C.90)}$$

Therefore,

$$E_x \frac{\partial}{\partial y}\left[\sigma_n \frac{\partial \phi_1}{\partial y}\right] + E_x \frac{\partial}{\partial z}\left[\sigma \frac{\partial \phi_1}{\partial z}\right] + \frac{\partial}{\partial y}\left[\sigma_n \frac{\partial \phi_2}{\partial y}\right] + \frac{\partial}{\partial z}\left[\sigma \frac{\partial \phi_2}{\partial z}\right]$$
$$= E_x \frac{\partial}{\partial y}\left[(\beta + \cot \alpha_d)\,\sigma_n\right] - \frac{\partial}{\partial y}\left[\sigma_n B\,(u - v\beta)\right], \quad \text{(C.91)}$$

where the E_x terms can, again, be collected, giving

$$E_x \frac{\partial}{\partial y}\left[\sigma_n \frac{\partial \phi_1}{\partial y}\right] + E_x \frac{\partial}{\partial z}\left[\sigma \frac{\partial \phi_1}{\partial z}\right] = E_x \frac{\partial}{\partial y}\left[(\beta + \cot \alpha_d)\,\sigma_n\right]. \quad \text{(C.92)}$$

All of the E_x terms from Equation C.92 can be canceled out, and the remaining terms from Equation C.91 can be collected as follows:

$$\frac{\partial}{\partial y}\left[\sigma_n \frac{\partial \phi_2}{\partial y}\right] + \frac{\partial}{\partial z}\left[\sigma \frac{\partial \phi_2}{\partial z}\right] = -\frac{\partial}{\partial y}\left[\sigma_n B\,(u - v\beta)\right]. \quad \text{(C.93)}$$

Now, the two functions, ϕ_1 and ϕ_2, can be described by the following equations [128]:

$$L(\phi_1) = \frac{\partial}{\partial y}\left[(\beta + \cot \alpha_d)\,\sigma_n\right] \quad \text{(C.94)}$$

and

$$L(\phi_2) = -\frac{\partial}{\partial y}\left[\sigma_n B\,(u - \beta v)\right], \quad \text{(C.95)}$$

where the operator, L, is [128, 137]

$$L = \frac{\partial}{\partial y}\left(\sigma_n \frac{\partial}{\partial y}\right) + \frac{\partial}{\partial z}\left(\sigma \frac{\partial}{\partial z}\right). \quad \text{(C.96)}$$

Note that the function ϕ_1 in Equation C.94 is driven by the temperature nonuniformities, while ϕ_2 in Equation C.95 is driven by temperature and velocity nonuniformities. Both functions are independent of E_x, which is reduced to a parameter of the problem to be determined later from the specification of the external electrical connection and loading.

Now consider the x-component of Ohm's Law:

$$J_x = \sigma_n \left[E_x - \beta E_y + (\beta u + v) B \right] = \sigma_n E_x - \sigma_n \beta E_y + (\beta u + v) B \sigma_n, \qquad \text{(C.97)}$$

where substituting Equation C.84 for E_y in the above equation yields

$$J_x = E_x \sigma_n \left(1 - \beta \cot \alpha_d \right) + \sigma_n \left[\beta \frac{\partial \phi}{\partial y} + B \left(\beta u + v \right) \right]. \qquad \text{(C.98)}$$

The ϕ term can be eliminated using Equation C.89, resulting in Equation 4.32:

$$J_x = E_x \sigma_n \left(1 - \beta \cot \alpha_d + \beta \frac{\partial \phi_1}{\partial y} \right) + \sigma_n \left[(\beta u + v) B + \beta \frac{\partial \phi_2}{\partial y} \right]. \qquad \text{(C.99)}$$

The same cross-sectional spatial average, $\langle f \rangle$, from Equation C.65, can be applied here as well. Therefore, Equation C.99 becomes

$$\langle J_x \rangle = E_x \left[\langle (1 - \beta \cot \alpha_d) \sigma_n \rangle + \langle \sigma_n \beta \frac{\partial \phi_1}{\partial y} \rangle \right] + \langle \sigma_n \beta \frac{\partial \phi_2}{\partial y} \rangle + B \langle \sigma_n (\beta u + v) \rangle. \qquad \text{(C.100)}$$

Now consider the y-component of Ohms Law:

$$J_y = \sigma_n \left[\beta E_x + E_y + B\left(\beta v - u\right)\right] = \sigma_n \beta E_x + \sigma_n E_y + \left(\beta v - u\right) B \sigma_n, \qquad \text{(C.101)}$$

where substituting Equation C.84 for E_y in the above equation yields

$$J_y = E_x \sigma_n \left(\beta + \cot \alpha_d\right) - \sigma_n \left[\frac{\partial \phi}{\partial y} + B\left(u - \beta v\right)\right]. \qquad \text{(C.102)}$$

The ϕ term can be eliminated using Equation C.89, resulting in Equation 4.33:

$$J_y = E_x \sigma_n \left(\beta + \cot \alpha_d - \frac{\partial \phi_1}{\partial y}\right) - \sigma_n \left[\left(u - \beta v\right) B + \frac{\partial \phi_2}{\partial y}\right]. \qquad \text{(C.103)}$$

Applying Equation C.65 to Equation C.103 gives the following equation for the cross-sectional averaged J_y current density:

$$\langle J_y \rangle = E_x \left[\langle \left(\beta + \cot \alpha_d\right) \sigma_n \rangle - \langle \sigma_n \frac{\partial \phi_1}{\partial y}\rangle\right] - \langle \sigma_n \frac{\partial \phi_2}{\partial y}\rangle - B\langle \sigma_n \left(u - \beta v\right)\rangle. \qquad \text{(C.104)}$$

The z-component of Ohm's Law is the same for the diagonal accelerator as it is for the diagonal generator. Therefore, Equation C.74 also applies for the J_z current density for the diagonal accelerator mode.

This derivation shows that the only difference between the diagonal generator mode and diagonal accelerator mode is the treatment of the diagonal angle. The differences between the final current density equations for the generator and accelerator modes can be explained through Figures C.1 and C.2, and the equations

that result from them. Furthermore, substituting the definition of the angle α_d from Equation C.81 into the transformation equation, Equation C.82, results in the transformation equation for the diagonal generator, Equation C.45. Because of the periodic properties of the tangent and cotangent functions, if one uses an obtuse diagonalization angle, $180 > \theta_d > 90$, the result would be the same as if one used the angle α_d, described in this section. Therefore, in order to modify the MGMHD code to run in accelerator mode, one needs only to define the diagonalization angle in terms of the obtuse angle, θ_d (as illustrated in Figures 3.3 and 3.4). As the MHD part of the UMM numerical model (*i.e.*, `mhd.f`), the MGMHD code has been altered to accept obtuse diagonalization angles (which the user inputs in `mhd.in`). This was the only required modification to enable modeling of MHD accelerators.

C.4 Diagonal Accelerator Boundary Conditions

Just as Section 3.3.1.1 describes the calculation of E_x for the four configurations of the MHD generator mode in the MGMHD numerical model, this section details the calculation of E_x for the diagonal accelerator configuration. The Faraday accelerator configuration is detailed in Section 4.3.1.1. As the Hall accelerator configuration is a special case of the diagonal configuration (with $\theta_d = 90$), the same general procedure described for the diagonal accelerator can be applied to the Hall accelerator.

The $\langle J_x \rangle$ current density is described with Equation C.100 and the $\langle J_y \rangle$ current density is described using Equation C.104. The load current density for a diagonal generator is described in Equation 3.61, but the load current density, J_{ld} for a diagonal

accelerator is

$$J_{ld} = J_x + J_y \cot \alpha_d, \tag{C.105}$$

$$\therefore J_{ld} = \langle J_x \rangle + \langle J_y \rangle \cot \alpha_d, \tag{C.106}$$

where $J_{ld} = I/A$, and where, as defined in Section 1.2.2.3, I is the total applied current and A is the normal cross-sectional area of the channel. Substituting Equations C.100 and C.104 into Equation C.106 yields

$$J_{ld} = E_x \left[\langle (1 - \beta \cot \alpha_d) \, \sigma_n \rangle + \langle \sigma_n \beta \frac{\partial \phi_1}{\partial y} \rangle \right] + \langle \sigma_n \beta \frac{\partial \phi_2}{\partial y} \rangle + B \langle \sigma_n \left(\beta u + v \right) \rangle$$
$$+ \cot \alpha_d \left\{ E_x \left[\langle (\beta + \cot \alpha_d) \, \sigma_n \rangle - \langle \sigma_n \frac{\partial \phi_1}{\partial y} \rangle \right] - \langle \sigma_n \frac{\partial \phi_2}{\partial y} \rangle - B \langle \sigma_n \left(u - \beta v \right) \rangle \right\}. \tag{C.107}$$

Solving for E_x gives

$$E_x = \frac{J_{ld} - \langle \sigma_n \beta \frac{\partial \phi_2}{\partial y} \rangle - B \langle \sigma_n \left(\beta u + v \right) \rangle + \cot \alpha_d \langle \sigma_n \frac{\partial \phi_2}{\partial y} \rangle + \cot \alpha_d \langle \sigma_n \left(u - Bv \right) \rangle}{\langle (1 - \beta \cot \alpha_d) \, \sigma_n \rangle + \langle \sigma_n \beta \frac{\partial \phi_1}{\partial y} \rangle + \cot \alpha_d \langle (\beta + \cot \alpha_d) \, \sigma_n \rangle - \cot \alpha_d \langle \sigma_n \frac{\partial \phi_1}{\partial y} \rangle}, \tag{C.108}$$

which can be rewritten as

$$E_x = \frac{a}{b}, \tag{C.109}$$

where

$$a = J_{ld} - \langle \sigma_n \beta \frac{\partial \phi_2}{\partial y} \rangle - B\langle \sigma_n \beta u \rangle - B\langle \sigma_n v \rangle +$$

$$\cot \alpha_d \langle \sigma_n \frac{\partial \phi_2}{\partial y} \rangle + \cot \alpha_d B\langle \sigma_n u \rangle - \cot \alpha_n B\langle \sigma_n \beta v \rangle, \quad (C.110)$$

and

$$b = \langle \sigma_n \rangle - \langle \sigma_n \beta \rangle \cot \alpha_d + \langle \sigma_n \beta \frac{\partial \phi_1}{\partial y} \rangle$$

$$+ \langle \sigma_n \beta \rangle \cot \alpha_d + \langle \sigma_n \rangle \cot^2 \alpha_d - \cot \alpha_d \langle \sigma_n \frac{\partial \phi_1}{\partial y} \rangle. \quad (C.111)$$

Equation C.110 can be regrouped and the $\langle \sigma_n \beta \rangle \cot \alpha_d$ terms in Equation C.111 cancel, leaving

$$E_x = \frac{J_{ld} - \langle \sigma_n \left(\beta - \cot \alpha_d \right) \frac{\partial \phi_2}{\partial y} \rangle - \langle \sigma_n \left(\beta - \cot \alpha_d \right) uB \rangle - B\langle \sigma_n \left(1 + \beta \cot \alpha_d \right) v \rangle}{\left(1 + \cot^2 \alpha_d \right) \langle \sigma_n \rangle + \langle \sigma_n \left(\beta - \cot \alpha_d \right) \frac{\partial \phi_1}{\partial y} \rangle}.$$

$$(C.112)$$

Therefore, the axial electric field, E_x, for the diagonal accelerator case can be calculated using the following equation:

$$E_x = \frac{J_{ld} - \langle \sigma_n \left(\beta - \cot \alpha_d \right) \left(\frac{\partial \phi_2}{\partial y} + uB \right) \rangle - B\langle \sigma_n \left(1 + \beta \cot \alpha_d \right) v \rangle}{\left(1 + \cot^2 \alpha_d \right) \langle \sigma_n \rangle + \langle \sigma_n \left(\beta - \cot \alpha_d \right) \frac{\partial \phi_1}{\partial y} \rangle}. \quad (C.113)$$

As expected, Equation C.113 differs from Equation 3.62 only in the sign of $\cot \alpha_d$ (excluding the squared angle in the denominator, which is the same). This proves that the only difference between the diagonal generator and accelerator cases

is the sign of the angle, which (because of the properties of tangent and cotangent) can be properly controlled by using an obtuse θ_d accelerator mode, and an acute θ_d for generator mode. This is consistent with the previous derivations in this appendix.

APPENDIX D

THE UAH-MSFC-MGMHD NUMERICAL MODEL INPUT

PARAMETERS AND FILES

> *The greatest enemy of knowledge is not ignorance, it is the illusion of knowledge.*
>
> —Stephen Hawking

D.1 Overview

This appendix gives the input files to the UMM numerical model for the 100 A, 45 degree baseline case. Figure 4.1 shows the two main sections of the UMM numerical model—the thermoelectric and MHD models. The thermoelectric model consists of four program files—`thermhd.f`, `ceb.f`, `omega.f`, and `econ.h`—while the MHD model consists of a single program file, `mhd.f`. Section 4.2 gives the specific details of the UMM thermoelectric model, while Chapter 3 and Section 4.3 detail the MHD model.

There are thirteen files in the total UMM numerical model "kit." The only file not shown in Figure 4.1 is the `makefile`, which compiles, builds, and executes the programs; builds the necessary file structures; and handles all dependency and update issues. This file is written in GNU Make [182], is saved without extension, and is issued using the command "`make`."

D.2   Thermoelectric Model

As shown in Figure 4.1, the thermoelectric portion of the UMM numerical model consists of 8 files—4 input files and 4 program files. Two of the program files have no input files—`omega.f` is self-contained and runs independently, while `econ.h` is subordinate to `thermhd.f` (which has the input file `thermhd.in`). Also controlled by `thermhd.f`, `ceb.f` (the modified version of the CEA numerical model) has three input files—`thermo.inp`, `trans.inp`, and `mapx.in`. The thermoelectric input files are detailed below.

The input file to `thermhd.f` is `thermhd.in`, and is as follows:

```
mapx
500 60 60
.f.
.001 5.0
7.e5 3.5e7
1.
```

The first line, "`mapx`," gives the name of the input file for the `ceb.f` code. The second line denotes the number of steps in the enthalpy loop, the number of steps in the pressure loop, and the pressure step at which an output file should be created, respectively. In the third line, the "`.f.`" tells the program to create the pressure table in a linear format (where "`.t.`" would denote a logarithmic pressrue table). The fourth line defines the minimum and maximum pressures, respectively, in the pressure loop. Similarly, the numbers in the sixth line define the minimum and

maximum points in the enthalpy loop. Finally, the last line tells the `ceb.f` code the

percent of fuel in the mixture (in this case, 1% by mass).

Called by `thermhd.f`, the program `ceb.f` has multiple input files. First, the

files `thermo.inp` and `trans.inp` consist of thermodynamic and transport property

tabular data, respectively, which `ceb.f` automatically uses to create the library files

that it needs to operate. (The `makefile` runs these two input files before `thermhd.f` is

allowed to run.) The third input filename is defined by the first line of `thermhd.in`—

in this case, it is called `mapx.in`, and its contents are as follows:

```
reac
   ox N2         wt%= 100.00    t(k)=2700
   fuel Na       wt%= 22.00     t(k)=300
   fuel K        wt%= 78.00     t(k)=300
prob             hp ions
outp siunits trace=1.e-04 transport
  plot t p %fuel rho h e- vis gam m Ar CO CO2 Cs CsOH H H2 H2O
  K KCL KO KOH K2 N NO N2 Na NaCL NaO NaOH Na2 O OH O2 SO2 He
  SF6 Ne Xe Mg
end
```

The first line simply indicates that the thermodynamic process is a reaction. Lines 2–4

indicate the "oxidizer" and "fuel" of the flow, with their respective weight percentages

and temperatures—in the case of the MAPX accelerator, these are the working fluid

(nitrogen gas) and the seed (NaK), respectively. Line 5 indicates that the input is in

terms of enthalpy and pressure, and that the CEA code should consider ions during the

calculations. The sixth line formats the output. Lines 7–9 tell the code the output

that it should "plot" (or print to a file)—in this case, the output is temperature,

pressure, fuel percentage, density, enthalpy, electron number density, viscosity, ratio

of specific heats, molecular weight, and the concentrations of the 30 species detailed in Appendix A.

During execution, the `thermhd.f` code actually uses the above `mapx.in` file to create an input file for the CEA code at every enthalpy and pressure step. This file is called `mapx.inp`, and it is actually the one that is read and used by `ceb.f`. This file is basically the same as the above `mapx.in`, but with three extra lines. The file `mapx.inp` is as follows:

```
reac
   ox N2        wt%= 100.00    t(k)=2700
   fuel Na      wt%= 22.00     t(k)=300
   fuel K       wt%= 78.00     t(k)=300
prob            hp ions
  %fuel=  1.000,
  h/r=   0.42096E+04,
  p(bar)=  0.50000E+01,
outp siunits trace=1.e-04 transport
  plot t p %fuel rho h e- vis gam m Ar CO CO2 Cs CsOH H H2 H2O
  K KCL KO KOH K2 N NO N2 Na NaCL NaO NaOH Na2 O OH O2 SO2 He
  SF6 Ne Xe Mg
end
```

Lines 6–8 are new, and do not appear in `mapx.in`. They represent the percent fuel, the current enthalpy of the mixture divided by the gas constant, and current pressure of the gas. This is the file that is actually read by `ceb.f`.

D.3   MHD Model

As shown in Figure 4.1, the magnetohydrodynamic portion of the UMM numerical model consists of the `mhd.f` fortran code. This model is a modified version

(as described in Chapter 4) of the MGMHD code, described in Chapter 3. The main input file for the `mhd.f` code is the file `mhd.in`. For the baseline case (100 A applied current at a 45 degree diagonal accelerator angle), the input file, `mhd.in`, is as follows:

```
mhd
mapx
mapxaccelerator
falstruetruefalsfals/klam,kener,compr,iread,iwrite
2,3,20,20,6,120,78316/kcoor,ngrid,ncelx,ncely,nscalr,npstep,nsize
20*0.00078/dxf
20*0.00078/dyf
0.0005,0.905/zstep,zlen
0.0,0.0,0.0,0.0/dwthdz,dhgtdz,dxwdz,dysdz
2,2/nzwdth,nzhght
0.0,0.905/zwdth(n)
0.0156,0.03455/wdth(n)
0.0,0.905/zhght(n)
0.0156,0.03455/hght(n)
40,40,40,40/nswp
3*0.005,2.0e-2/err,erpot
1.0/relpot
21*0/iprint:u,v,w,p,rh,visc,h,t,tk,td,sig,bta,3pot,2e,3j,mach
1,1,1,1,5/kbxm,kbxp,kbym,kbyp,isumry
1,30,0/iplot,nplot,ibug
0.000,0.002,0.010,0.025,0.050,0.075,0.100,0.125,0.150,0.175,0.200,
    0.225,0.250,0.300,0.375,0.450,0.525,0.600,0.650,0.675,0.700,
    0.725,0.750,0.775,0.800,0.825,0.850,0.875,0.900,0.905/zplot
3,1.228,0.0/iprop,gamma,emit
28.8966,1290,0.0,0.0,1.84109e-05,2.388471e-08,-6.389553e-13
    /wmol,acp,bcp,ccp,amu,b
3*1.0,0.7/prl
0.0,0.0,0.4091,0.130/u,v,rh,flow
3.24240e05,2700.0,0.0,0.0/pin,tin,rhgt,dpdz
2/nztwal
0.0,0.905/ztwal(n)
1000.0,1000.0/twal(n)
3,135.0,100.0,40.0,0.0,1000.0/iopt,angle,ajlin,sigin,btain,tarc
28,2,2,2/nzbfld,nzload,nzress,nzptch
0.00,0.02,0.05,0.08,0.12,0.20,0.26,0.34,0.40,0.44,0.50,0.56,0.60,
    0.64,0.66,0.68,0.70,0.74,0.78,0.80,0.81,0.82,0.84,0.85,0.86,
    0.88,0.90,0.905/zbfld(n)
```

```
1.70,1.73,1.76,1.78,1.80,1.83,1.84,1.85,1.86,1.86,1.85,1.84,1.83,
   1.81,1.80,1.78,1.75,1.68,1.57,1.50,1.46,1.41,1.30,1.22,1.08,
   0.86,0.68,0.65/bfld(n)
0.0,0.905/zload(n)
0.0,0.0/aload(n)
0.0,0.905/zress(n)
0.0,0.0/ress(n)
0.0,0.905/zptch(n)
0.015,.015/ptch(n)
0,0,160000,0.0,0.0/iopt3,iopt4,zjcnt,zjcrt1,zjcrt2
0.083, 5, 0.0, 0/dajlin,najlin,dajlex,najlex
```

Note that, in the above, the indented lines indicate continuations of the previous line. Most of the `mhd.in` input parameters are explained in the MGMHD manual [125]. Additions and modifications to the original MGMHD code are explained in Section 4.3, with the appropriate input parameters given.

When the user chooses the option to vary the diagonal angle through the MHD channel (as described in Section 4.3.3), `mhd.f` looks for a second input file, `angle.in`. Within this input file, the user defines the desired axial locations and the diagonal angles. The baseline case uses a constant diagonal angle, and therefore `angle.in` is not used; however, an example of `angle.in` is

```
# Diagonal Angle Data Table
# Axial Distance [m]    Angle[deg]
0.00                    105.0
0.005                   105.0
0.00505                 110.0
0.01                    110.0
0.015                   115.0
0.02                    125.0
0.04                    130.0
0.06                    135.0
0.78545                 135.0
0.80545                 130.0
```

```
0.82545              125.0
0.84545              115.0
0.8505               110.0
0.86                 105.0
0.905                100.0
```

As evident by the file, the user enters the axial location in meters and the desired diagonalization angle (θ_d) in degrees on the same line. There are no limitations to the number of locations/angles entered, and `mhd.f` assumes a linear distribution between entries.

The last input file required by `mhd.f` is a common file, `mhncom.h`, which simply serves to share data between the different subroutines in `mhd.f`. This file also sets various global parameters, common blocks, and grid sizes/parameters. This file also ensures that the same variable names are not used in multiple cases. The file `mhncom.h` is not a proper user-input file, and therefore does not require display in this appendix.

APPENDIX E

UNCERTAINTY MAGNIFICATION FACTORS

As we know, there are known knowns. There are things we know we know. We also know there are known unknowns. That is to say, we know there are some things we do not know. But there are also unknown unknowns, the ones we don't know we don't know.

—Donald Rumsfeld

E.1   Overview

Section 5.5 determines the relative influence of certain input (*i.e.*, user-defined) variables on important exit parameters. To accomplish this analysis, uncertainty magnification factors (UMF), as described by Coleman and Steele [180], are calculated for the relationship of ten input variables to each of three exit parameters. Section 5.5 gives an overview of the results of the analysis; however, this appendix offers the details of the baseline, perturbation, and difference values used in the UMF calculations.

E.2   UMF Calculations

As explained in Section 5.5, in order to determine the uncertainty magnification factor of a certain input variable for a certain exit parameter, the particular input variable is perturbed by a very small amount (1% in this case) while all other input variables are held at their baseline values. The "perturbed" value for each of the exit parameters of interest (3 in this case) is recorded and later compared to their baseline values. The three exit parameters used in this analysis are given in Table 5.4, while the input variables (that are perturbed) are listed in Table 5.5.

Coleman and Steele [180] define the uncertainty magnification factor as

$$\text{UMF}_i = \frac{X_i}{r}\frac{\partial r}{\partial X_i}, \tag{E.1}$$

where r is the result of the experiment/analysis and X_i is the variable of interest. The UMF for a given variable X_i indicates the level of influence in the uncertainty of the overall result (r) that comes from the uncertainty in the variable X_i [180]. In this case, the $\partial r/\partial X_i$ factor is approximated using the difference between a baseline value and a 1% perturbation of that baseline value; while X_i and r in the X_i/r fraction are their baseline values. The following sections detail the UMF calculations for each of the 10 input variables and 3 exit parameters; a more detailed discussion of UMF values is found in Coleman and Steele [180]. In this appendix, subscript e denotes exit conditions/values, subscript b indicates a baseline condition/value, and subscript a denotes "accelerator" values (relating to earlier equations).

Table E.1: Temperature Sensitivity Data.

Parameter	Baseline Value	1% Perturbation	Δ
T (K)	2700	2727	27
P_{0e} (atm)	5.6843	5.7001	0.0158
u_e (m/s)	2345.7	2346.3	0.6
η_a	0.46137	0.46475	0.00338

E.2.1 Temperature

Table E.1 gives the baseline, 1% perturbation, and difference values for the temperature UMF analysis. The baseline inlet temperature is 2700 K; therefore, the 1% perturbation value (baseline value $\times$ 1.01) is 2727 K, with the ΔT being 27 K. Equations E.2, E.3 and E.4 detail the UMF calculations for total pressure (P_{0e}), exit velocity (u_e), and electrical efficiency (η_a), respectively. Recall, as described in Section 5.5, that all the values used in all the UMF calculations are cross-sectional averaged.

$$\text{UMF}(P_{0e})_T = \frac{T_b}{P_{0e_b}} \frac{\Delta P_{0e}}{\Delta T} = \frac{2727}{5.6843} \frac{0.0158}{27} = 0.2780 \tag{E.2}$$

$$\text{UMF}(u_e)_T = \frac{T_b}{u_{e_b}} \frac{\Delta u_e}{\Delta T} = \frac{2727}{2345.7} \frac{0.6}{27} = 0.0256 \tag{E.3}$$

$$\text{UMF}(\eta_a)_T = \frac{T_b}{\eta_{a_b}} \frac{\Delta \eta_a}{\Delta T} = \frac{2727}{0.46137} \frac{0.00338}{27} = 0.7326 \tag{E.4}$$

Table E.2: Static Pressure Sensitivity Data.

Parameter	Baseline Value	1% Perturbation	Δ
P (Pa)	324240	327482.4	3242.4
P_{0e} (atm)	5.6843	5.64	-0.0443
u_e (m/s)	2345.7	2341.3	-4.4
η_a	0.46137	0.45699	-0.00438

E.2.2 Static Pressure

Table E.2 gives the baseline, 1% perturbation, and difference values for the static pressure (P) UMF analysis. The baseline inlet static pressure is 324.240 kPa; therefore, the 1% perturbation value (baseline value $\times$ 1.01) is 327.4824 kPa, with the ΔP being 3242.4 Pa. Equations E.5, E.6 and E.7 detail the UMF calculations for total pressure (P_{0e}), exit velocity (u_e), and electrical efficiency (η_a), respectively. Note that while they are included in the final UMF values, the UMF signs (*i.e.*, positive or negative), are of no importance [180], and in Section 5.5 all UMF values are treated as positive.

$$\text{UMF}(P_{0e})_P = \frac{P_b}{P_{0e_b}} \frac{\Delta P_{0e}}{\Delta P} = \frac{234240}{5.6843} \frac{-0.0443}{3242.4} = -0.7793 \tag{E.5}$$

$$\text{UMF}(u_e)_P = \frac{P_b}{u_{e_b}} \frac{\Delta u_e}{\Delta P} = \frac{324240}{2345.7} \frac{-4.4}{3242.4} = -0.1876 \tag{E.6}$$

$$\text{UMF}(\eta_a)_P = \frac{P_b}{\eta_{a_b}} \frac{\Delta \eta_a}{\Delta P} = \frac{324240}{0.46137} \frac{-0.00438}{3242.4} = 0.9494 \tag{E.7}$$

Table E.3: Mass Flow Rate Sensitivity Data.

Parameter	Baseline Value	1% Perturbation	Δ
$\dot{m}$ (kg/s)	0.130	0.1313	0.0013
P_{0e} (atm)	5.6843	5.779	0.0947
u_e (m/s)	2345.7	2349.9	4.2
η_a	0.46137	0.46218	0.00143

E.2.3   Mass Flow Rate

Table E.3 gives the baseline, 1% perturbation, and difference values for the mass flow ($\dot{m}$) UMF analysis. The baseline inlet mass flow rate is 0.130 kg/s; therefore, the 1% perturbation value (baseline value $\times$ 1.01) is 0.1313 kg/s, with the $\Delta\dot{m}$ being 0.0013 kg/s. Note that the MGMHD and UMM codes calculate inlet velocity, u, from mass flow rate, density, and area at the entrance of the channel; therefore, the inlet mass flow rate UMF is values are calculated instead of inlet velocity. Equations E.8, E.9 and E.10 detail the UMF calculations for total pressure (P_{0e}), exit velocity (u_e), and electrical efficiency (η_a), respectively.

$$\text{UMF}(P_{0e})_{\dot{m}} = \frac{\dot{m}_b}{P_{0e_b}}\frac{\Delta P_{0e}}{\Delta\dot{m}} = \frac{0.130}{5.6843}\frac{0.0947}{0.0013} = 1.6660 \tag{E.8}$$

$$\text{UMF}(u_e)_{\dot{m}} = \frac{\dot{m}_b}{u_{e_b}}\frac{\Delta u_e}{\Delta\dot{m}} = \frac{0.130}{2345.7}\frac{4.2}{0.0013} = 0.1791 \tag{E.9}$$

$$\text{UMF}(\eta_a)_{\dot{m}} = \frac{\dot{m}_b}{\eta_{a_b}}\frac{\Delta\eta_a}{\Delta\dot{m}} = \frac{0.130}{0.46137}\frac{0.00143}{0.0013} = 0.3099 \tag{E.10}$$

Table E.4: Diagonal Angle Sensitivity Data.

Parameter	Baseline Value	1% Perturbation	Δ
θ_d (degrees)	135	136.35	1.35
P_{0e} (atm)	5.6843	5.7483	0.064
u_e (m/s)	2345.7	2350.0	4.3
η_a	0.46137	0.46473	0.00336

E.2.4   Diagonal Angle

Table E.4 gives the baseline, 1% perturbation, and difference values for the diagonalization angle (θ_d) UMF analysis. The baseline diagonal angle is 135 degrees; therefore, the 1% perturbation value (baseline value $\times$ 1.01) is 136.35 degrees, with the $\Delta\theta_d$ being 1.35 degrees. Please see Section 3.3.2 for the definitions and relationships of the different diagonal angles. Equations E.11, E.12 and E.13 detail the UMF calculations for total pressure (P_{0e}), exit velocity (u_e), and electrical efficiency (η_a), respectively.

$$\text{UMF}(P_{0e})_{\theta_d} = \frac{\theta_{d_b}}{P_{0e_b}}\frac{\Delta P_{0e}}{\Delta \theta_d} = \frac{135}{5.6843}\frac{0.064}{1.35} = 1.1259 \tag{E.11}$$

$$\text{UMF}(u_e)_{\theta_d} = \frac{\theta_{d_b}}{u_{e_b}}\frac{\Delta u_e}{\Delta \theta_d} = \frac{135}{2345.7}\frac{4.3}{1.35} = 0.1833 \tag{E.12}$$

$$\text{UMF}(\eta_a)_{\theta_d} = \frac{\theta_{d_b}}{\eta_{a_b}}\frac{\Delta \eta_a}{\Delta \theta_d} = \frac{135}{0.46137}\frac{0.00336}{1.35} = 0.7283 \tag{E.13}$$

Table E.5: Applied Current Sensitivity Data.

Parameter	Baseline Value	1% Perturbation	Δ
AJLIN (A)	100	101	1
P_{0e} (atm)	5.6843	5.6937	0.0094
u_e (m/s)	2345.7	2348.7	3.0
η_a	0.46137	0.46145	0.00008

E.2.5 Applied Current

Table E.5 gives the baseline, 1% perturbation, and difference values for the applied current (AJLIN) UMF analysis. The baseline applied current is 100 A; therefore, the 1% perturbation value (baseline value $\times$ 1.01) is 101 A, with the ΔAJLIN being 1.0 A. Note that, due to the power take off region, applied current at the entrance of the channel is 20 A; however, the current input by the user (AJLIN) and applied over most of the channel is the full 100 A value. Furthermore, the PTO region is held constant for all UMF tests. Equations E.14, E.15 and E.16 detail the UMF calculations for total pressure (P_{0e}), exit velocity (u_e), and electrical efficiency (η_a), respectively.

$$\text{UMF}(P_{0e})_{\texttt{AJLIN}} = \frac{\texttt{AJLIN}_b}{P_{0e_b}} \frac{\Delta P_{0e}}{\Delta \texttt{AJLIN}} = \frac{100}{5.6843} \frac{0.0094}{1.0} = 0.1654 \qquad (E.14)$$

$$\text{UMF}(u_e)_{\texttt{AJLIN}} = \frac{\texttt{AJLIN}_b}{u_{e_b}} \frac{\Delta u_e}{\Delta \texttt{AJLIN}} = \frac{100}{2345.7} \frac{3.0}{1.0} = 0.1279 \qquad (E.15)$$

$$\text{UMF}(\eta_a)_{\texttt{AJLIN}} = \frac{\texttt{AJLIN}_b}{\eta_{a_b}} \frac{\Delta \eta_a}{\Delta \texttt{AJLIN}} = \frac{100}{0.46137} \frac{0.00008}{1.0} = 0.0173 \qquad (E.16)$$

Table E.6: Channel Divergence Sensitivity Data.

Parameter	Baseline Value	1% Perturbation	Δ
H,W (m)	0.03455	0.0348955	0.0003455
P_{0e} (atm)	5.6843	5.6966	0.0123
u_e (m/s)	2345.7	2358.2	12.5
η_a	0.46137	0.46275	0.00138

E.2.6 Channel Divergence

Table E.6 gives the baseline, 1% perturbation, and difference values for the channel divergence (H,W) UMF analysis. The baseline divergence is 0.03455 m; therefore, the 1% perturbation value (baseline value $\times$ 1.01) is 0.0348955 m, with the ΔH or ΔW being 0.0003455 m. As explained in Section 5.2.1, the channel divergence (which is actually 0.6 degrees) is calculated using the channel height and width at the entrance and exit, and the overall length. Because this analysis perturbs only entrance variables, the entrance height and width (each being 0.03455 m, because the cross-section is a square) were perturbed by the 1% values already given. For the purposes of this example, entrance height, H, will be used. Equations E.17, E.18 and E.19 detail the UMF calculations.

$$\text{UMF}(P_{0e})_H = \frac{H_b}{P_{0e_b}} \frac{\Delta P_{0e}}{\Delta H} = \frac{0.03455}{5.6843} \frac{0.0123}{0.0003455} = 0.2164 \qquad \text{(E.17)}$$

$$\text{UMF}(u_e)_H = \frac{H_b}{u_{e_b}} \frac{\Delta u_e}{\Delta H} = \frac{0.03455}{2345.7} \frac{12.5}{0.0003455} = 0.5329 \qquad \text{(E.18)}$$

$$\text{UMF}(\eta_a)_H = \frac{H_b}{\eta_{a_b}} \frac{\Delta \eta_a}{\Delta H} = \frac{0.03455}{0.46137} \frac{0.00138}{0.0003455} = 0.2991 \qquad \text{(E.19)}$$

Table E.7: Wall Temperature Sensitivity Data.

Parameter	Baseline Value	1% Perturbation	Δ
T_{wall} (K)	1000	1010	10
P_{0e} (atm)	5.6843	5.6982	0.0139
u_e (m/s)	2345.7	2346.9	1.2
η_a	0.46137	0.46167	0.0003

E.2.7 Wall Temperature

Table E.7 gives the baseline, 1% perturbation, and difference values for the wall temperature (T_{wall}) UMF analysis. The baseline wall temperature is 1000 K; therefore, the 1% perturbation value (baseline value $\times$ 1.01) is 1010 K, with the ΔT_{wall} being 10 K. Even though T_{wall} deals with three-dimensional characteristics of the flow, as discussed in Section 3.4.3, the MGMHD and UMM codes' treatment of T_{wall} and T_{arc} are not three-dimensional in the calculation of the characteristics at a particular cross-sectional location [125]. Furthermore, the UMF from the wall temperatures is important due to the difficult nature of accurately measuring the wall temperatures in the experimental MAPX facility. Equations E.20, E.21 and E.22 detail the UMF calculations.

$$\text{UMF}(P_{0e})_{T_{wall}} = \frac{T_{wall_b}}{P_{0e_b}} \frac{\Delta P_{0e}}{\Delta T_{wall}} = \frac{1000}{5.6843} \frac{0.0139}{10} = 0.2445 \tag{E.20}$$

$$\text{UMF}(u_e)_{T_{wall}} = \frac{T_{wall_b}}{u_{e_b}} \frac{\Delta u_e}{\Delta T_{wall}} = \frac{1000}{2345.7} \frac{1.2}{10} = 0.0512 \tag{E.21}$$

$$\text{UMF}(\eta_a)_{T_{wall}} = \frac{T_{wall_b}}{\eta_{a_b}} \frac{\Delta \eta_a}{\Delta T_{wall}} = \frac{1000}{0.46137} \frac{0.0003}{10} = 0.0650 \tag{E.22}$$

Table E.8: Arcing Temperature Sensitivity Data.

Parameter	Baseline Value	1% Perturbation	Δ
T_{arc} (K)	1000	1010	10
P_{0e} (atm)	5.6843	5.6843	0.0
u_e (m/s)	2345.7	2345.7	0.0
η_a	0.46137	0.46137	0.0

E.2.8 Arcing Temperature

Table E.8 gives the baseline, 1% perturbation, and difference values for the wall temperature (T_{arc}) UMF analysis. The baseline arcing temperature is 1000 K; therefore, the 1% perturbation value (baseline value $\times$ 1.01) is 1010 K, with the ΔT_{arc} being 10 K. As discussed with the wall temperature in Section E.2.7, T_{arc} deals with three-dimensional characteristics of the flow, but is not calculated as such in the MGMHD code [125] (see Section 3.4.3). Furthermore, the UMF from the arcing temperatures is important because it is virtually impossible to physically "measure" in a flowing plasma—some values can be calculated, but in most cases they are simply estimated. Fortunately, this analysis shows that the uncertainty in T_{arc} is not very important. Equations E.23, E.24 and E.25 detail the UMF calculations.

$$\text{UMF}(P_{0e})_{T_{arc}} = \frac{T_{arc_b}}{P_{0e_b}} \frac{\Delta P_{0e}}{\Delta T_{arc}} = \frac{1000}{5.6843} \frac{0.0}{10} = 0.0 \tag{E.23}$$

$$\text{UMF}(u_e)_{T_{arc}} = \frac{T_{arc_b}}{u_{e_b}} \frac{\Delta u_e}{\Delta T_{arc}} = \frac{1000}{2345.7} \frac{0.0}{10} = 0.0 \tag{E.24}$$

$$\text{UMF}(\eta_a)_{T_{arc}} = \frac{T_{arc_b}}{\eta_{a_b}} \frac{\Delta \eta_a}{\Delta T_{arc}} = \frac{1000}{0.46137} \frac{0.0}{10} = 0.0 \tag{E.25}$$

Table E.9: Magnetic Field Sensitivity Data.

Parameter	Baseline Value	1% Perturbation	Δ
$\mathbf{B}$ (T)	(data)	(data)$\times$1.01	$0.01x$
P_{0e} (atm)	5.6843	5.7197	0.0354
u_e (m/s)	2345.7	2350	4.3
η_a	0.46137	0.46314	0.00177

E.2.9 Magnetic Field

As discussed in Section 5.2.3 and shown in Figure 5.9, the magnetic field used in the UMM numerical model is not a constant over the length of the channel—it actually has heavy attenuation in the second half of the channel. The input file `mhd.in` in Appendix D shows the 28 "data points" that the UMM codes uses to approximate the magnetic field distribution described in Section 5.2.3. Therefore, instead of perturbing a single value by 1%, each of the 28 points used to describe the magnetic field are multiplied by 1.01—effectively "bumping-up" the entire magnetic field distribution seen in Figure 5.9 by a multiple of 1.01. Table E.9 shows the details (baseline values, perturbation values, and differences) of the magnetic field UMF analysis.

Since the magnetic field is not constant and no single entrance value is perturbed by 1%, the UMF equations already presented in this appendix require rearranging. However, note that all equations are of the form:

$$\mathrm{UMF}(r)_{X_i} = \frac{X_i}{r_b} \frac{\Delta r}{\Delta X_i}, \tag{E.26}$$

which can be rearranged as such

$$\text{UMF}(r)_{X_i} = \frac{\Delta r}{r_b} \frac{X_i}{\Delta X_i}.$$ (E.27)

In this case, where the magnetic field is increased by a factor of 1%, the value of the fraction $X_i/\Delta X_i$ is 100. Therefore,

$$\frac{X_i}{\Delta X_i} = \frac{\text{B-Field}}{\Delta \text{B-Field}} = 100,$$ (E.28)

and the UMF equations can be written

$$\text{UMF}(P_{0e})_{\text{B-Field}} = \frac{\Delta P_{0e}}{P_{0e_b}} \times 100 = \frac{0.345}{5.6843} \times 100 = 0.6228,$$ (E.29)

$$\text{UMF}(u_e)_{\text{B-Field}} = \frac{\Delta u_e}{u_{e_b}} \times 100 = \frac{4.3}{2345.7} \times 100 = 0.1833,$$ (E.30)

and

$$\text{UMF}(\eta_a)_{\text{B-Field}} = \frac{\Delta \eta_a}{\eta_{a_b}} \times 100 = \frac{0.00177}{0.46137} \times 100 = 0.3836.$$ (E.31)

E.2.10   Seeding

Table E.10 gives the baseline, 1% perturbation, and difference values for the NaK seeding (%NaK) UMF analysis. The baseline NaK seeding is 1% by weight; therefore, the 1% perturbation value (baseline value $\times$ 1.01) is 1.01, with the Δ%NaK being 0.01. The NaK seeder is described in Section 2.1.1, and one should note that, of

Table E.10: Seeding Sensitivity Data.

Parameter	Baseline Value	1% Perturbation	Δ
NaK Seed (%)	1.0	1.01	0.01
P_{0e} (atm)	5.6843	5.6817	-0.0026
u_e (m/s)	2345.7	2345.0	-0.7
η_a	0.46137	0.4614	0.00003

all the entrance variables, the NaK seeding percentage is the most difficult to control and experimentally measure [165]. Therefore, knowing how the uncertainty in the NaK measurement effects the exit parameters of the MAPX accelerator is of upmost importance. Fortunately, however, the UMF values indicate that the NaK seeding uncertainty plays a small roll in the overall uncertainty of exit values of total pressure, velocity, and efficiency. Equations E.32, E.33 and E.34 detail the UMF calculations for total pressure (P_{0e}), exit velocity (u_e), and electrical efficiency (η_a), respectively.

$$\text{UMF}(P_{0e})_{\%\text{NaK}} = \frac{\%\text{NaK}_b}{P_{0e_b}} \frac{\Delta P_{0e}}{\Delta \%\text{NaK}} = \frac{1.0}{5.6843} \frac{0.0026}{0.01} = 0.0457 \qquad (\text{E.32})$$

$$\text{UMF}(u_e)_{\%\text{NaK}} = \frac{\%\text{NaK}_b}{u_{e_b}} \frac{\Delta u_e}{\Delta \%\text{NaK}} = \frac{1.0}{2345.7} \frac{0.7}{0.01} = 0.0298 \qquad (\text{E.33})$$

$$\text{UMF}(\eta_a)_{\%\text{NaK}} = \frac{\%\text{NaK}_b}{\eta_{a_b}} \frac{\Delta \eta_a}{\Delta \%\text{NaK}} = \frac{1.0}{0.46137} \frac{0.00003}{0.01} = 0.0065 \qquad (\text{E.34})$$

APPENDIX F

ALTERNATE MAPX CONFIGURATION TESTING

It is difficult to say what is impossible, for the dream of yesterday is the hope of today and the reality of tomorrow.

—Robert H. Goddard

F.1   Overview

As Section 5.6.2 explains, the recommended baseline MAPX test configuration uses a $100\,\mathrm{A}$ applied current with a $45\,$degree diagonal accelerator angle, and the magnet pole flares, shown in Figure 5.10, should remain. However, Section 5.6.1 explores alternate configurations for the MAPX accelerator—relatively simple variations on the baseline configuration that do not require redesign or remanufacture of the MAPX channel or any part of the MAPX facility. These alternate configurations consist of variations in the magnetic field profile (*i.e.*, removal of the magnet pole flares) and alterations in the diagonal accelerator angle. Furthermore, as discussed in Section 5.6.1.1, two non-realistic cases with constant magnetic field distributions are included in this appendix to offer more evidence of the interplay of the magnetic field intensity with the axial velocity and transverse, J_y, current density.

F.2 Constant, High-Intensity Magnetic Field

Section 5.6.1.1 discusses the result of removing the magnet pole flares, shown in Figure 5.10, from the MAPX electromagnet. The magnetic field intensity in the downstream half of the MAPX accelerator no longer attenuates, as seen in Figures 5.9 and 5.62; however, the resulting exit parameters remain virtually unchanged. As theorized in Section 5.6.1.1, the increase in the magnetic field has no affect on the exit parameters because of the interplay between the magnetic field intensity, the axial velocity, and the transverse current density.

A detailed analysis is outside the scope of this dissertation; however, simply put, Section 5.6.1.1 theorizes that the increase in the pushing $\mathbf{J} \times \mathbf{B}$ Lorentz force is essentially canceled out by the retarding $\mathbf{u} \times \mathbf{B}$ Lorentz force (which sets un an electric field that opposes the externally applied, accelerating, electric field). This implies that simply increasing the intensity of the magnetic field in an MHD accelerator would not always be beneficial—the way the magnetic field influences the flow depends on the intensity of the field and the axial velocity and transverse current at that particular plane in the flow.

To emphasize this phenomenon, two theoretical accelerator cases—with constant 2.0 T and 2.5 T magnetic field distributions, respectively—are shown in this appendix. Aside from the increased magnitude and constant magnetic field distribution, all other input variables are the same as the baseline case. For each case, the normalized flow and electrical parameters are shown, allowing one to see the how an
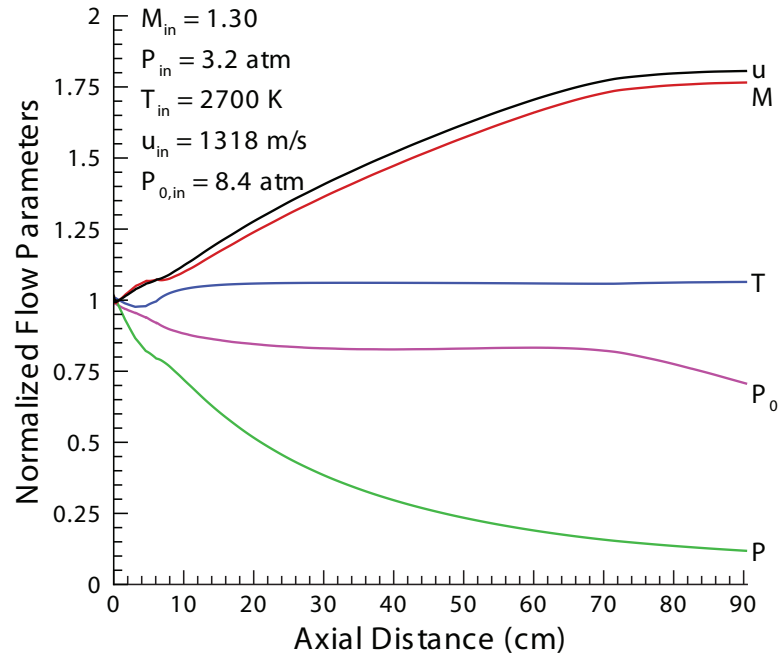
Figure F.1: Normalized flow parameters for the constant $2\,\mathrm{T}$ magnetic field case.

increase in magnetic field effects an MHD accelerator. Further analysis is outside the scope of this dissertation.

Figure F.1 shows the normalized flow parameters for the constant $2\,\mathrm{T}$. This graph is very similar to Figure 5.60 for the baseline case, with one notable exception— for the $2.0\,\mathrm{T}$ case, the slopes for axial velocity, u, and Mach number, M, are higher (steeper) in the first half of the MAPX channel, and lower (flatter) in the last $20\,\mathrm{cm}$ of the channel. This indicates that the constant $2.0\,\mathrm{T}$ case has higher acceleration in the first half of the channel, and lower acceleration near the end of the channel. This is consistent with the theory proposed in Section 5.6.1.1—in the first half of the MAPX channel, where the axial velocity is relatively slow and the positive transverse, J_y, current density is relatively high, the more intense magnetic field offers better acceleration of the flow; however, as the axial velocity increases and the positive J_y
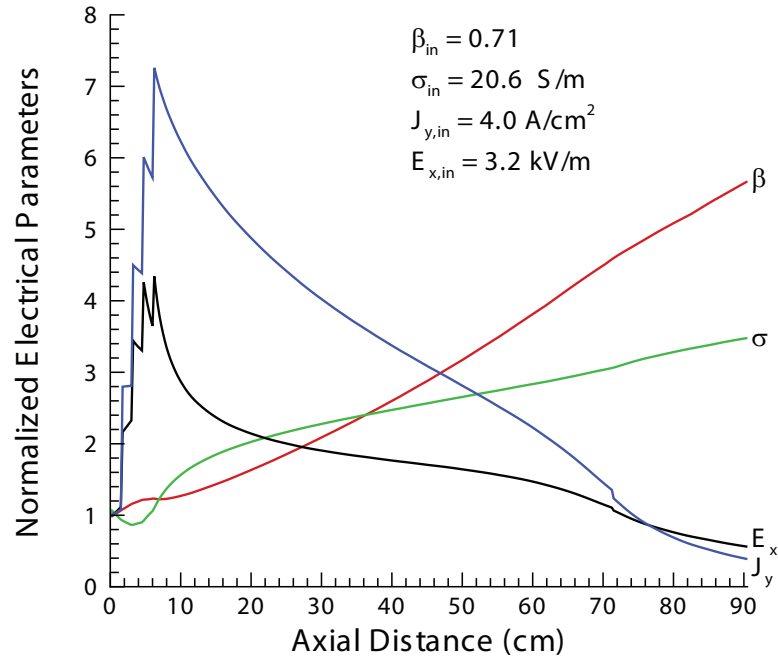
Figure F.2: Normalized electrical parameters for the constant $2\,\mathrm{T}$ magnetic field case.

current density decreases, the more intense magnetic field has a detrimental effect on the MAPX flow-field.

The reasons for the deceleration of the flow is explained in Figure F.2, where the J_y current density experiences a sharp decline at approximately $70\,\mathrm{cm}$ downstream. The decreasing J_y current density indicates an increase in the opposing electric field powered by the $\mathbf{u} \times \mathbf{B}$ Lorenz force (which is logical, as the axial velocity is high at this point). This graph shows that, with a high magnetic field intensity, as the axial velocity increases, the accelerating J_y current density decreases, eventually resulting in decreased acceleration in the flow.

As expected, all of the affects seen in Figure F.1 are intensified in Figure F.3, as the magnetic field intensity is increased to a constant $2.5\,\mathrm{T}$ throughout the MAPX
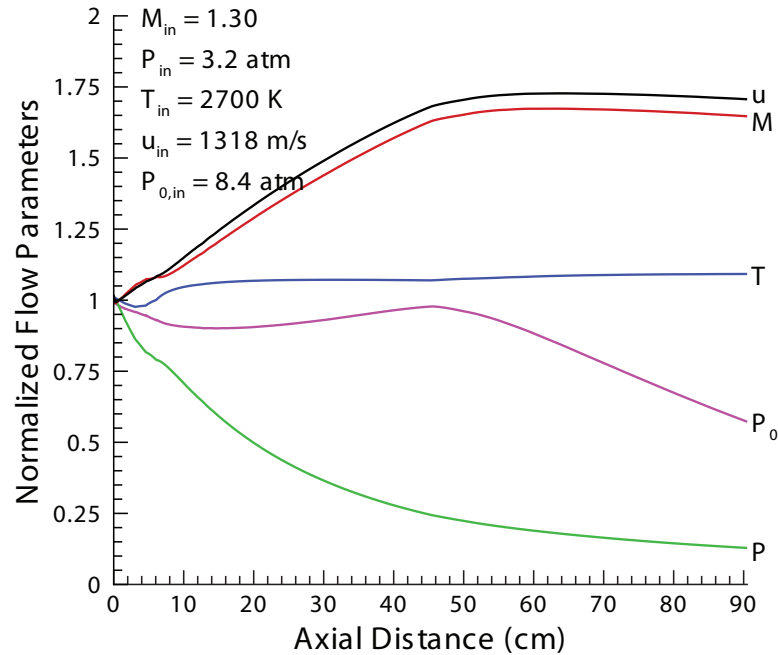
Figure F.3: Normalized flow parameters for the constant 2.5 T magnetic field case.

channel. For the 2.5 T case, the acceleration seen in the first half of the MAPX channel is very high; however the flow is quickly overcome, as acceleration halts at approximately 45 cm. The flow actually begins to slow as it approaches the exit of the MAPX channel. Therefore, even though acceleration is very high in the first half of the channel, the point at which this acceleration stops is pushed farther forward in the channel, and the flow even experiences deceleration before it exits the accelerator. This phenomenon is reflected in the plot of total pressure, P_0, in Figure F.3.

Figure F.4 shows why the flow behaves this way. At approximately 45 cm, the positive J_y current density experiences a sharp decline, and asymptotically approaches zero through the rest of the channel. The axial electric field, E_x, experiences a similar drop half-way through the MAPX channel, and falls throughout the rest of the accelerator, which indicates increases in the axial current density, J_x. The accelerator
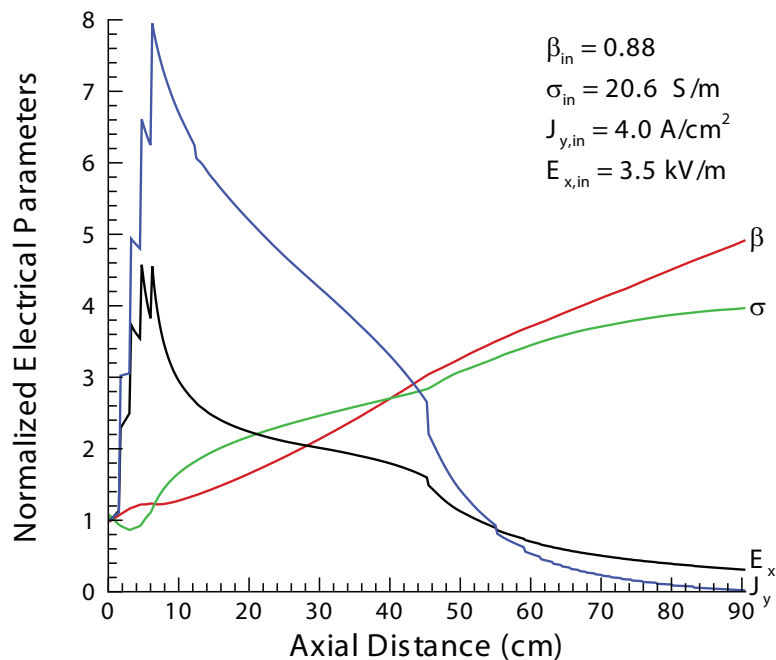
Figure F.4: Normalized electrical parameters for the constant $2.5\,\text{T}$ magnetic field case.

never experiences current flow reversal (a negative J_y current density); therefore, the deceleration seen in Figure F.3 is most likely a combination of low "pushing" $\mathbf{J} \times \mathbf{B}$ Lorentz force (from the low J_y current density), viscous effects, and other flow losses resulting from an increase in the axial current flow. However, Figures F.3 and F.4 show that increasing the magnetic field intensity can have adverse effects on the exit flow parameters.

F.3 Diagonal Angles

As described in Section 5.6.1.2, another relatively simple variation in the MAPX baseline configuration is the diagonal accelerator angle. The axial current neutralized case, explained in Section 4.3.4 and plotted in Figure 5.11, calculates

that the MAPX accelerator should use a diagonal accelerator angle of $\theta \approx 55$ degrees throughout the channel. An angle this steep is, however, physically impossible in an MHD accelerator [166], so the largest physically-possible angle, $\theta = 45$ degrees, is used for the baseline analysis. For completeness, however, the effects of lesser angles should be explored.

Because the MAPX channel is a diagonal, insulating-sidewall configuration, Figure 2.6 shows that the diagonal accelerator angle can be changed with relative ease. The lesser angles explored in this section are 15 degrees and 30 degrees (which are diagonal accelerator angles, or electric field angles, θ, as defined in Section 3.3.2— the equivalent diagonalization angles would be $\theta_d = 105$ degrees and 120 degrees, respectively). The results of the diagonal angle alterations are expressed in normalized plots, as in the previous section. A more detailed analysis of the underlying physical phenomenon resulting from a change in the diagonal accelerator angle is outside the scope of this dissertation.

Figure F.5 shows the normalized flow parameters for the 15 degree diagonal angle case. In comparison to the baseline case, these parameters are extremely poor. Axial velocity and Mach number are low, and fall to entrance levels before the exit of the channel. Furthermore, some sort of flow reversal occurs, because calculations stop before the exit of the channel. (The UMM code stops calculations at approximately 80 cm downstream, 10 cm before the exit of the MAPX channel. Stopping of calculations occurs when the code senses some sort of flow reversal, because the parabolic assumption cannot deal with negative flow.) Figure F.5 shows that the 15 degree case, obviously, is inferior to the baseline case.
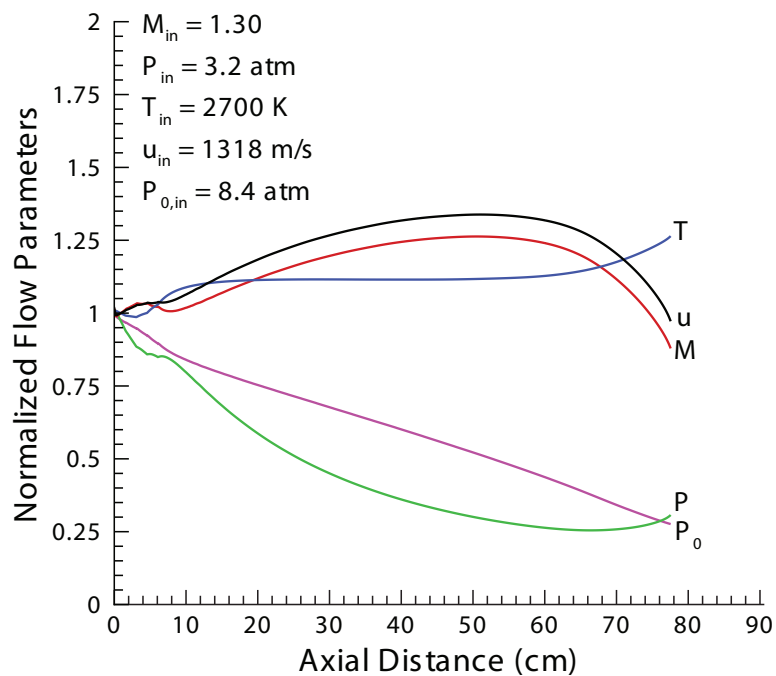
Figure F.5: Normalized flow parameters for the 15 degree diagonal angle case.
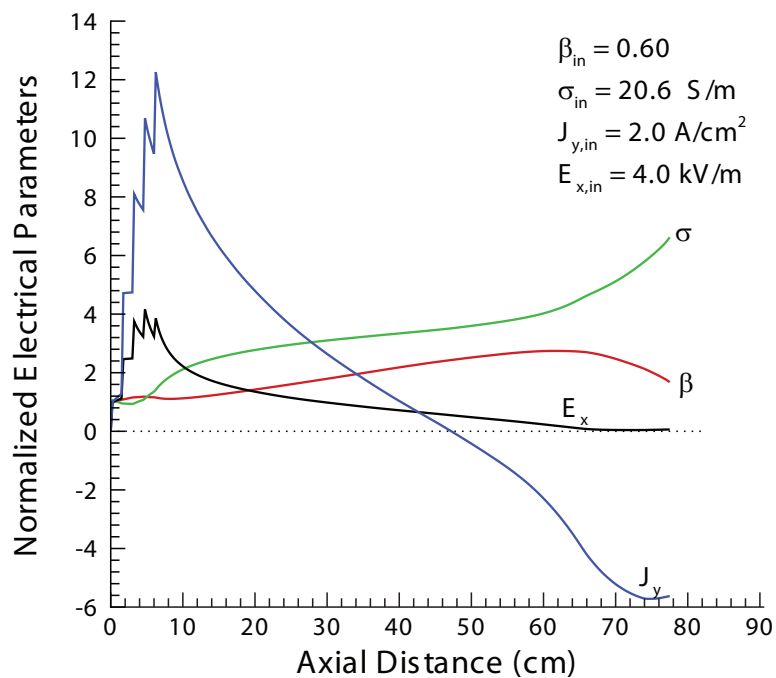
Figure F.6: Normalized electrical parameters for the 15 degree diagonal angle case.

The poor performance seen in Figure F.5 can be explained in Figure F.6. The transverse, J_y, current density experiences a reversal (*i.e.*, it becomes negative) at approximately 45 cm. At this point, the MAPX channel essentially operates in generator mode, where the J_y current density serves to slow the flow. Furthermore, the low axial, E_x, electric field indicates higher levels of axial current density, J_x. As discussed in Section 5.4.2.9, the axial current serves to increase the entropy in the channel (through heat production and facilitating wall losses), and effectively "steals" applied current from the accelerating J_y current density (*i.e.*, there is only so much applied current in the MAPX channel; if more of the applied current goes into axial current, that leaves less for the transverse current). It was obvious from Figure F.5 that the 15 degree case is inferior to the baseline configuration; however, Figure F.6 helps explain why.

The 30 degree diagonal accelerator angle case shows slightly better performance than the 15 degree case. Figure F.7 shows the normalized flow parameters for the 30 degree diagonal angle case. The axial velocity and Mach number do not decrease, as in the 15 degree case; however, the exit values of velocity and Mach number are lower than the baseline case, indicating poorer overall performance.

Figure F.8 shows why the 30 degree diagonal angle case has such poor performance. The transverse J_y current density is very low—it crosses into negative territory at approximately 80 cm, recovering back to positive territory because of the attenuation in the magnetic field. Similar to the 15 degree case, the axial electric field is low, indicating excessive, detrimental, axial current in the flow. The combination
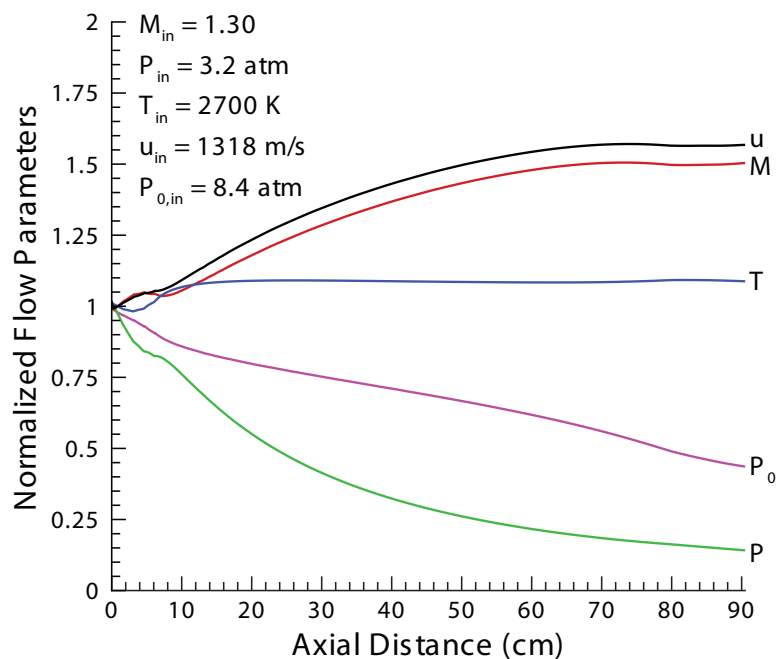
Figure F.7: Normalized flow parameters for the 30 degree diagonal angle case.
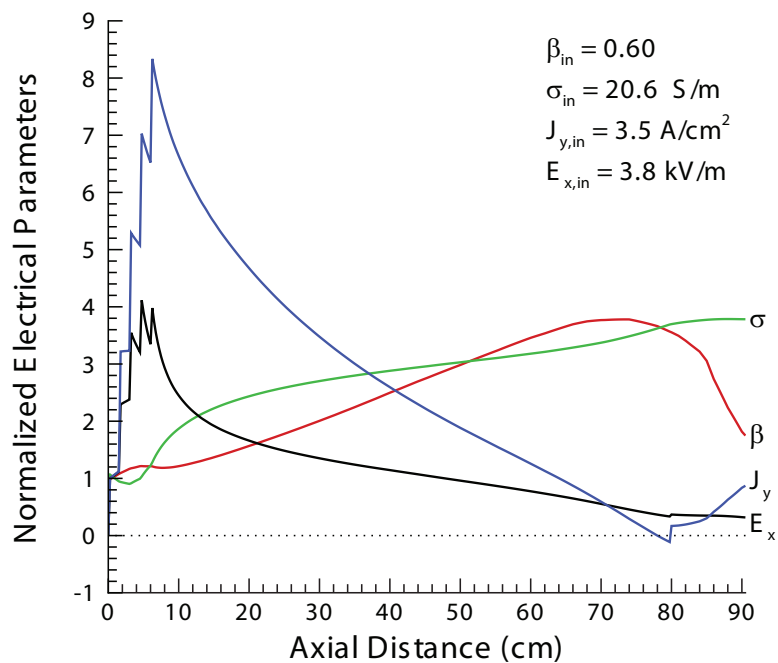
Figure F.8: Normalized electrical parameters for the 30 degree diagonal angle case.

of low transverse current and increased axial current result in the poor performance seen in Figure F.7.

As discussed in Section 4.3.4, for an diagonal MHD accelerator, it is typically advantageous to reduce the axial current density in the flow. Sections 5.3.3.5 and 5.4.2.9 show the detrimental impacts that J_x can have on an MHD channel flow-field, and, as discussed in Section 5.3.1, the 45 degree angle of the baseline configuration is the best possible angle for the MAPX accelerator.

REFERENCES

The secret of creativity is knowing how to hide your sources.

—Albert Einstein

[1] LyTec. An mhd accelerator simulator for application to advanced propulsion: Monthly report 2. Technical Report LyTec-R-00-008, NASA, Marshall Space Flight Center, Sep 30, 2000.

[2] LyTec. An mhd accelerator simulator for application to advanced propulsion: Monthly report September 2001. Technical Report LyTec-R-01-024, NASA, Marshall Space Flight Center, Sep 30, 2001.

[3] Wernher Von Braun. *The Mars Project.* The University of Illinois Press, Urbana, IL, 1953.

[4] Wernher Von Braun and Frederick I. Ordway, III. Space vehicles: Space carriers, spacecraft, space stations, and spaceships. Technical Report MSFC-HT-1, National Aeronautics and Space Administration, Marshall Space Flight Center, 1961.

[5] Douglas Fiehler and Steve Oleson. A comparison of electric propulsion systems for mars exploration. Technical Report NASA TM-2003-212593, National Aeronautics and Space Administration, Glenn Research Center, Sep 2003. also AIAA 2003-4573.

[6] Terry Kammash, Myoung-Jae Lee, and David I. Poston. High-thrust-high-specific impulse gasdynamic fusion propulsion system. *Journal of Propulsion and Power*, 13(3):412–427, May-Jun 1997.

[7] George P. Sutton. *Rocket Propulsion Elements.* John Wiley and Sons, Inc., New York, 6th edition, 1992.

[8] Lee S. Mason and Steven R. Oleson. Spacecraft impacts with advanced power and electric propulsion. Technical Report NASA TM-2000-209912, National Aeronautics and Space Administration, Glenn Research Center, Mar 2000.

[9] W.E. Moeckel. Comparison of advanced propulsion concepts for deep space exporation. Technical Report NASA TN D-6968, National Aeronautics and Space Administration, Lewis Research Center, Sep 1972.

[10] John S. Clark, Jeffrey A. George, Leon P. Gefert, Michael P. Doherty, and Robert J. Sefcik. Nuclear electric propulsion: A "better, safer, cheaper" transportation system for human exploration to mars. Technical Report NASA TM-106406, National Aeronautics and Space Administration, Lewis Research Center, Mar 1994.

[11] Les Johnson and Stephanie D. Leifer. Propulsion options for interstellar exploration. In *36th AIAA/ASME/SAE/ASEE Joint Propulsion Conference and Exhibit*, number AIAA 2000-3334, Huntsville, AL, 2000. American Institute of Aeronautics and Astronautics.

[12] Francis M. Curran and Lisa Wood Callahan. The NASA electric propulsion program. Technical Report NASA TM-107102, National Aeronautics and Space Administration, Lewis Research Center, May 1996. also IEPC 1995-0133.

[13] William J. Emrich Jr. and Archie C. Young. Nuclear propulsion system options for mars missions. In *AIAA Space Programs and Technologies Conference*, number AIAA 1992-1496, Huntsville, AL, 1992. American Institute of Aeronautics and Astronautics.

[14] Ron J. Litchford, John W. Cole, John T. Lineberry, James N. Chapman, Harold J. Schmidt, and Charles W. Lineberry. Magnetohydrodynamic augmented propulsion experiment: I. Performance analysis and design. In *33rd AIAA Plasmadynamics and Lasers Conference*, number AIAA 2002-2184, Maui, HI, 2002. American Institute of Aeronautics and Astronautics.

[15] George W. Sutton and Arthur Sherman. *Engineering Magnetyhydrodynamics*, volume 25 of *Mechanical Engineering*. McGraw-Hill, Inc., New York, 1st edition, 1965.

[16] Robert G. Jahn. *Physics of Electric Propulsion*, volume 6 of *Missile and Space Technology*. McGraw-Hill, Inc., New York, 1968.

[17] Igor V. Adamovich, J. William Rich, and Gordon L. Nelson. Feasibility study of magnetohydrodynamic acceleration of unseeded and seeded airflows. *AIAA Journal*, 36(4):590–597, Apr 1998.

[18] L.S. Frost. Conductivity of seeded atmospheric pressure plasmas. *Journal of Applied Physics*, 32(10):2029–2036, Oct 1961.

[19] Leon E. Ring. General considerations of mhd accelerator for aerodynamic testing. Technical Report AEDC-TDR-64-256, U.S. Air Force, Arnold Engineering Development Center, Dec 1964.

[20] Roger A. Crawford, James N. Chapman, and Robert P. Rhodes. Potential application of magnetohydrodynamic acceleration to hypersonic environmental testing. Technical Report AEDC-TR-90-6, U.S. Air Force, Arnold Engineering Development Center, Aug 1990.

[21] George P. Wood and Arlen F. Carter. Considerations in the design of a steady DC plasma accelerator. In A.B. Cambel and J.B. Fenn, editors, *Dynamics of Conducting Gases, Proceedings of the Third Biennial Gas Dynamics Symposium*, pages 201–212. Northwestern University Press, Evanston, IL, 1960.

[22] Sterge T. Demetriades and Richard W. Ziemer. Energy transfer to plasmas by continuous lorentz forces. In T.P. Anderson and M.M Slawsky, editors, *Magnetohydrodynamics, Proceedings of the Fourth Biennial Gas Dynamics Symposium*, pages 185–205. Northwestern University Press, Evanston, IL, 1962.

[23] Sterge T. Demetriades, G.L. Hamilton, Richard W. Ziemer, and P.D. Lenn. Three-fluid nonequilibrium plasma accelerators (Part I). In E. Stuhlinger, editor, *AIAA Progress in Astronautics and Aeronautics: Electric Propulsion Development*, volume 9, pages 461–511. Academic Press, Inc., New York, 1963.

[24] Sterge T. Demetriades. Experiments with high specific impulse cross-field accelerators. In Gordon and Breach, editors, *Proceedings of the 3rd Symposium on Engineering Aspects of Magnetohydrodynamics (SEAM)*, pages 507–525. Science Publishers, Inc., New York, 1963.

[25] P.D. Lenn, J.R. Bodoia, D.L. Ward, G.L. Hamilton, and Sterge T. Demetriades. Three-fluid nonequilibrium plasma accelerators (Part II). In *AIAA Electric Propulsion Conference*, number AIAA 1963-047, Colorado Springs, CO, 1963. American Institute of Aeronautics and Astronautics.

[26] V.H. Blackman and R.J. Sunderland. Experimental performance of a cross-field plasma accelerator. *AIAA Journal*, 1(9):2047–2052, Sep 1963.

[27] R.J. Sunderland and A.R. Asam. Magnetogasdynamic rocket for space propulsion. Technical Report NASA CR-54040, National Aeronautics and Space Administration, MHD Research, Inc., May 1964.

[28] George P. Wood, Arlen F. Carter, Alexander P. Sabol, Donald R. McFarland, and William R. Weaver. Research on linear cross-field steady-flow DC plasma accelerators at Langley Research Center, NASA. In *Arc Heaters and MHD Accelerators for Aerodynamic Purposes: Supplement to AGARDograph 84*, Proceedings of the AGARD Specialists Meeting, pages 1–27. North Atlantic Treaty Organization, Advisory Group for Aeronautical Research and Development, Rhode-Saint-Genese, Belgium, 1964.

[29] George P. Wood, Arlen F. Carter, Alexander P. Sabol, and Richard H. Weinstein. Experiments in steady-state cross-field acceleration of plasma. *Physics of Fluids*, 4(5):652, May 1961.

[30] Arlen F. Carter, George P. Wood, Alexander P. Sabol, and Richard H. Weinstein. Experiments in steady-state high density plasma acceleration. In C. Mannal and N.W. Mather, editors, *Proceedings of the 3rd Symposium on the Engineering Aspects of Magnetohydrodynamics (SEAM)*, pages 45–55. Columbia Univeristy Press, New York, 1962.

[31] Arlen F. Carter, George P. Wood, Donald R. McFarland, and William R. Weaver. Research on a linear direct-current plasma accelerator. *AIAA Journal*, 3(6):1040–1045, Jun 1965. also AIAA 1964-699.

[32] Arlen F. Carter, Donald R. McFarland, William R. Weaver, Stephen K. Park, and George P. Wood. Operating characteristics, velocity and pitot distribution, and material evaluation tests in the langley one-inch-square plasma accelerator. In *AIAA Plasmadynamics Conference*, number AIAA 1966-180, Monterey, CA, 1966. American Institute of Aeronautics and Astronautics.

[33] William R. Weaver, Donald R. McFarland, Arlen F. Carter, and George P. Wood. Design and operational characteristics of the langley 20-megawatt plasma accelerator facility. In *Proceedings of the 11th Symposium on the Engineering Aspects of Magnetohydrodynamics (SEAM)*, volume Mar, pages 77–81. California Institute of Technology, Pasadena, CA, 1970.

[34] Arlen F. Carter, William R. Weaver, Donald R. McFarland, Stephen K. Park, and George P. Wood. Design of the 20-megawatt linear plasma accelerator facility. Technical Report NASA TN-D-6115, National Aeronautics and Space Administration, Langley Research Center, Jan 1971.

[35] G.L. Whitehead, W.N. MacDermott, L.G. Siler, and R.G. Roepke. Assessment of mhd applications to hypersonic propulsion testing facilities. Technical Report AEDC-TRM-87-V54, U.S. Air Force, Arnold Engineering Development Center, Dec 1984.

[36] L.E. Rittenhouse, J.C. Pigott, J.M. Whoric, and D.R. Wilson. Theoretical and experimental results with a linear magnetohydrodynamic accelerator operated in the hall current neutralized mode. Technical Report AEDC-TR-67-150, U.S. Air Force, Arnold Engineering Development Center, Nov 1967.

[37] L.E. Rittenhouse, J.M. Whoric, and J.C. Pigott. Experimental results with a linear magnetohydrodynamic accelerator operated with water-cooled beryllia magnetic field walls. Technical Report AEDC-TR-70-40, U.S. Air Force, Arnold Engineering Development Center, Apr 1970.

[38] J. Teno, Thomas R. Brogan, and S.W. Petty. Research studies and the development of mhd generators and accelerators. Technical Report AEDC-TR-70-14, U.S. Air Force, Arnold Engineering Development Center, Jan 1970.

[39] Thomas R. Brogan. The 20mw lorho mhd accelerator for wind tunnel drive-design, construction and critique. In *30th Plasmadynamics and Lasers Conference*, number AIAA 1999-3720, Norfolk, VA, 1999. American Institute of Aeronautics and Astronautics.

[40] S.R. Pate, L.G. Siler, D.W. Stallings, and D.A. Wagner. Development of an mhd-augmented, high enthalpy, shock tunnel facility. *AIAA Journal*, 12(3):289–297, Mar 1974. also AIAA 1972-993.

[41] Peter J. Vernace and R.R. Walker. Plasma generator and magnetohydrodynamic accelerator research and development facility. Technical Report ALLIS CHALMERS-MISC-1, U.S. Army, Redstone Arsenal, Sep 23, 1971.

[42] D.L. Denzel, L.J. Davis, Y.C. Lin Wu, J. Muehlhauser, R.E. Taylor, R.H. Oliver, and John B. Dicks. Experimental study of diagonal conducting wall generators using solid propellants. *AIAA Journal*, 6(9):1647–1651, Sep 1968.

[43] Richard V. Shanklin III. Diagonal conducting wall mhd generator channel flows. *AIAA Journal*, 7(5):975–976, May 1969.

[44] Leon E. Ring, George W. Garrison, Thomas R. Brogan, and Harold J. Schmidt. Design of an mhd performance demonstration experiment. In *Proceedings of the 13th Symposium on the Engineering Aspects of Magnetohydrodynamics (SEAM)*, pages v.8.1–v.8.7. Stanford University Press, Stanford, CA, 1973.

[45] G.S. Argyropoulos, Sterge T. Demetriades, Ezzat Danial Doss, and D.A. Oliver. Electron nonequilibrium in open-cycle mhd generators. *AIAA Journal*, 12(5):669–671, May 1974.

[46] R.F. Starr, L.S. Christensen, George W. Garrison, and G.L. Whitehead. Preliminary faraday performance of a large megnetohydrodynamic generator at high magnetic field. *Journal of Energy*, 6(3):163–170, May-Jun 1982.

[47] Ezzat Danial Doss and Y.C. Lin Wu. State-of-the-art of mhd generator development. *Journal of Energy*, 6(3):161–162, May-Jun 1982.

[48] James Lee Smith. Magnetohydrodynamic power generation. Technical Report NASA TP-2331, NASA, Marshall Space Flight Center, 1984.

[49] J.R. Maus, B.J. Griffith, K.Y. Szema, and J.T. Best. Hypersonic mach number and real gas effects on space shuttle orbiter aerodynamics. *Journal of Spacecraft and Rockets*, 21(2):136–141, Mar-Apr 1984.

[50] B.J. Griffith, J.R. Maus, B.M. Majors, and J.T. Best. Addressing the hypersonic simulation problem. *Journal of Spacecraft and Rockets*, 24(4):334–341, Jul-Aug 1987.

[51] G.L. Whitehead. Analytical studies of high-pressure mhd accelerators. Technical Report AEDC-TR-81-18, U.S. Air Force, Aronold Engineering Development Center, Sep 1981.

[52] Subrata Roy and B.P. Pandey. Plasma-wall interaction inside a hall thruster. *Journal of Plasma Physics*, 68(4):305–319, 2002.

[53] Balachandrudu Narapusetty and Subrata Roy. Comparison of sgm and ldg algorithms for magneto fluid problems. In *41st Aerospace Sciences Meeting and Exhibit*, number AIAA 2003-0323, Reno, NV, 2003. American Institute of Aeronautics and Astronautics.

[54] Subrata Roy and B.P. Pandey. Modeling the effect of plasma-wall interaction in a hall thruster. In *41st AIAA Aerospace Sciences Meeting and Exhibit*, number AIAA 2003-0493, Reno, NV, 2003. American Institute of Aeronautics and Astronautics.

[55] Subrata Roy and B.P. Pandey. Hydrodynamic model of a hall thruster with ionization and recombination. In *39th AIAA/ASME/SAE/ASEE Joint Propulsion Conference*, number AIAA 2003-4858, Huntsville, AL, 2003. American Institute of Aeronautics and Astronautics.

[56] Shigeki Harada, Klaus A. Hoffmann, and Justin Augustinus. Numerical solution of the ideal magnetohydrodynamic equations for supersonic channel flow. *Journal of Thermophysics and Heat Transfer*, 12(4):507–513, Oct-Dec 1998.

[57] Ramesh K. Agarwal and H.S. Raharjaya Reksoprodjo. Implicit kinetic schemes for the euler and ideal magnetohydrodynamic equations. In *41st AIAA Aerospace Sciences Meeting and Exhibit*, number AIAA 2003-0249, Reno, NV, 2003. American Institute of Aeronautics and Astronautics.

[58] Jean-Francois Dietiker and Klaus A. Hoffmann. Numerical simulations of mhd flows with the generalized ohm's law. In *41st AIAA Aerospace Sciences Meeting and Exhibit*, number AIAA 2003-0327, Reno, NV, 2003. American Institute of Aeronautics and Astronautics.

[59] Jean-Francois Dietiker and Klaus A. Hoffmann. Numerical simulation of magnetohydrodynamic flows. *Journal of Spacecraft and Rockets*, 41(4):592–602, Jul-Aug 2004.

[60] J. Poggie. Numerical simulation of electrode sheaths in a magnetized plasma. In *41st AIAA Aerospace Sciences Meeting and Exhibit*, number AIAA 2003-0359, Reno, NV, 2003. American Institute of Aeronautics and Astronautics.

[61] Ying-Ming Lee, Gloyd A. Simmons, Leon E. Ring, Sergey O. Macheret, and Mikhail N. Shneider. Mhd accelerator performance predictions and plans for experimental verification. In *22nd AIAA Aerodynamic Measurement Technology and Ground Testing Conference*, number AIAA 2002-3132, St. Louis, MO, 2002. American Institute of Aeronautics and Astronautics.

[62] Sergey O. Macheret, Mikhail N. Shneider, and Richard B. Miles. Magneto-hydrodynamic and electrohydrodynamic control of hypersonic flows of weakly ionized plasmas. *AIAA Journal*, 42(7):1378–1387, Jul 2004.

[63] Motoo Ishikawa and Juro Umoto. A new approach to calculation of three-dimensional flow in mhd genertors. *Journal of Propulsion and Power*, 2(1):11–17, Jan-Feb 1986.

[64] Motoo Ishikawa, K. Tamai, K. Tateishi, Juro Umoto, and Valentine A. Bityurin. Three-dimensional behavior of mhd plasma near electrode of mhd generator. In *28th AIAA Plasmadynamics and Lasers Conference*, number AIAA 1997-2373, Atlanta, GA, 1997. American Institute of Aeronautics and Astronautics.

[65] Ding Li, Dennis Keefer, Robert P. Rhodes, Charles L. Merkle, and Konstantin Kolokolnikov. Analysis of mhd generator power generation. In *39th AIAA/ASME/SAE/ASEE Joint Propulsion Conference and Exhibit*, number AIAA 2003-5050, Huntsville, AL, 2003. American Institute of Aeronautics and Astronautics.

[66] Ding Li, S. Venkateswaran, J. Lindau, and Charles L. Merkle. A unified computational formulation for multi-component and multi-phase flows. In *43rd AIAA Aerospace Sciences Meeting and Exhibit*, number AIAA 2005-24906, Reno, NV, 2005. American Institute of Aeronautics and Astronautics.

[67] Ding Li, Dennis Keefer, Robert P. Rhodes, Charles L. Merkle, and R Thibodeaux. Analysis of mhd generator power generation. *Journal of Propulsion and Power*, 21(3):424–432, Jun-Jul 2005.

[68] Ding Li, Xiaoqiang Zeng, Charles L. Merkle, E.J. Felderman, and J.M. Sheeley. Coupled fluid-dynamic electromagnetic modeling of arc heaters. In *37th AIAA Plasmadynamics and Lasers Conference*, number AIAA 2006-3768, San Francisco, CA, 2006. American Institute of Aeronautics and Astronautics.

[69] Nobuhiro Harada, J. Ikewada, and Y. Terasaki. Basic studies on an mhd accelerator. In *33rd AIAA Plasmadynamics and Lasers Conference*, number AIAA 2002-2175, Maui, HI, 2002. American Institute of Aeronautics and Astronautics.

[70] Makbul Anwari, Satoru Takahashi, and Nobuhiro Harada. Numerical simulation for performance of an mhd accelerator. In *35th AIAA Plasmadynamics and Lasers Conference*, number AIAA 2004-2363, Portland, OR, 2004. American Institute of Aeronautics and Astronautics.

[71] Makbul Anwari, Noboumi Sakamoto, Triwahju Hardianto, and Nobuhiro Harada. Performance study of a diagonal type mhd accelerator. In *43rd AIAA Aerospace Sciences Meeting and Exhibit*, number AIAA 2005-0366, Reno, NV, 2005. American Institute of Aeronautics and Astronautics.

[72] Nobuomi Sakamoto, Makbul Anwari, Junichi Kondo, and Nobuhiro Harada. Three-dimensional analyses of an mhd accelerator. In *36th AIAA Plasmadynamics and Lasers Conference*, number AIAA 2005-4922, Toronto, Canada, 2005. American Institute of Aeronautics and Astronautics.

[73] Nobuomi Sakamoto, Junichi Kondo, and Nobuhiro Harada. Computational study of mhd accelerator. In *37th AIAA Plasmadynamics and Lasers Conference*, number AIAA 2006-2893, San Francisco, CA, 2006. American Institute of Aeronautics and Astronautics.

[74] Ramon L. Chase, Unmeel B. Mehta, David W. Bogdanoff, Chul Park, Scott L. Lawrence, Michael J. Aftosmis, Sergey O. Macheret, and Mikhail N. Shneider. Comments on an mhd energy bypass engine powered spaceliner. In *AIAA 9th International Space Planes and Hypersonic Systems and Technologies Conference and 3rd Weakly Ionized Gases Workshop*, number AIAA 1999-4975, Norfolk, VA, 1999. American Institute of Aeronautics and Astronautics.

[75] Chul Park, David W. Bogdanoff, and Unmeel B. Mehta. Theoretical performance of frictionless magnetohydrodynamic-bypass scramjets. *Journal of Propulsion and Power*, 17(3):591–598, May-Jun 2001.

[76] Chul Park, Unmeel B. Mehta, and David W. Bogdanoff. Magnetohydrodynamics energy bypass scramjet performance with real gas effects. *Journal of Propulsion and Power*, 17(5):1049–1057, Sep-Oct 2001.

[77] Hiromasa Kato, John C. Tannehill, and Unmeel B. Mehta. Numerical simulation of turbulent mhd flows using an iterative pns algorithm. In *41st AIAA Aerospace Sciences Meeting and Exhibit*, number AIAA 2003-0326, Reno, NV, 2003. American Institute of Aeronautics and Astronautics.

[78] David W. Bogdanoff and Unmeel B. Mehta. Experimental demonstration of magneto-hydro-dynamic (mhd) acceleration. In *34th AIAA Plasmadynamics and Lasers Conference*, number AIAA 2003-4285, Orlando, FL, 2003. American Institute of Aeronautics and Astronautics.

[79] Chul Park, David W. Bogdanoff, and Unmeel B. Mehta. Theoretical performance of a magnetohydrodynamic-bypass scramjet engine with nonequilibrium ionization. *Journal of Propulsion and Power*, 19(4):529–537, Jul-Aug 2003.

[80] Hiromasa Kato, John C. Tannehill, Sumeet Gupta, and Unmeel B. Mehta. Numerical simulation of a 3-D supersonic viscous flow in an experimental mhd channel. In *42nd AIAA Aerospace Sciences Meeting and Exhibit*, number AIAA 2004-0317, Reno, NV, 2004. American Institute of Aeronautics and Astronautics.

[81] Sumeet Gupta, John C. Tannehill, and Unmeel B. Mehta. Simulation of 3-D nonequilibrium seeded air flow in the NASA-Ames mhd channel. In *43rd AIAA Aerospace Sciences Meeting and Exhibit*, number AIAA 2005-0165, Reno, NV, 2005. American Institute of Aeronautics and Astronautics.

[82] Datta V. Gaitonde. Three-dimensional flow-through scramjet simulation with mgd energy-bypass. In *41st AIAA Aerospace Sciences Meeting and Exhibit*, number AIAA 2003-0172, Reno, NV, 2003. American Institute of Aeronautics and Astronautics.

[83] Ron J. Litchford, John W. Cole, Valentine A. Bityurin, and John T. Lineberry. Thermodynamic cycle analysis of magnetohydrodynamic-bypass hypersonic air-breathing engines. *Journal of Propulsion and Power*, 17(2):477–480, Mar-Apr 2001.

[84] David W. Riggins. Analysis of the magnetohydrodynamic energy bypass engine of high-speed airbreathing propulsion. *Journal of Propulsion and Power*, 20(5):779–792, Sep-Oct 2004.

[85] W.H. Heiser and D.T. Pratt. Comment on "anaylsis of the magnetohydrodynamic energy bypass engine for high-speed airbreathing propulsion". *Journal of Propulsion and Power*, 21(6):1140, Nov-Dec 2005.

[86] David W. Riggins. Reply by the author to W.H. Heiser and D.T. Pratt. *Journal of Propulsion and Power*, 21(6):1140, Nov-Dec 2005.

[87] Richard J. Rosa. *Magnetohydrodynamic Energy Conversion*. McGraw-Hill, Inc., New York, 1st edition, 1968.

[88] Boris M. Smirnov. *Physics of Ionized Gases*. John Wiley and Sons, New York, 2001.

[89] T.G. Cowling. *Magnetohydrodynamics*. Interscience Publishers, Inc., New York, 1957.

[90] Ron J. Litchford. Performance theory of diagonal conducting wall magneto-hydrodynamic accelerators. *Journal of Propulsion and Power*, 20(4):742–750, Jul-Aug 2004.

[91] David J. Griffiths. *Introduction to Electrodynamics*. Prentice-Hall, Inc., Upper Saddle River, NJ, 2nd edition, 1989.

[92] Peter Alan Davidson. *An Introduction to Magnetohydrodynamics*. Cambridge University Press, Cambridge, United Kingdom, 2001.

[93] Steven Lawrence Girshick. *Secondary Flow in a Magnetyhydrodynamic Channel*. Ph.D. Dissertation, Stanford University, 1985.

[94] Francis F. Chen. *Plasma Physics and Controlled Fusion, Volume 1: Plasma Physics*. Plenum, New York, 2nd edition, 1985.

[95] Morton Mitchner and Charles H. Kruger. *Partially Ionized Gases*. John Wiley and Sons, New York, 1973.

[96] Zhongmin Li. *Experimental Study of a Hall Current Plasma Accelerator*. Ph.D. Dissertation, The University of Alabama in Huntsville, 2003.

[97] James Klepeis and Richard J Rosa. Experimental studies of strong hall effects and $\mathbf{U} \times \mathbf{B}$ induced ionization. *AIAA Journal*, 3(9):1659–1666, Sep 1965.

[98] Jonathan E. Jones. *As Assessment of Microwave Generated Plasmas for Use in Magnetohydrodynamic Accelerators*. Ph.D. Dissertation, The University of Alabama in Huntsville, 2000.

[99] A. de Montardy. An m.p.d. generator with series connected electrodes. In *Proceedings of the International Symposium on Magnetoplasmadynamic Electrical Power Generation*, pages 66–68. The Institution of Electrical Engineers, Savoy Place, England, 1962.

[100] John B. Dicks. Improvements in design of mhd accelerator channels for aerodynamic purposes. In *Arc Heaters and MHD Accelerators for Aerodynamic Purposes: Supplement to AGARDograph 84*, Proceedings of the AGARD Specialists Meeting, pages 127–174. North Atlantic Treaty Organization, Advisory Group for Aeronautical Research and Development, Rhode-Saint-Genese, Belgium, 1964.

[101] Aerotherm. Operating and maintenance information for hyperthermal convective heating system. Manual Contract NAS8-98041, NASA, Marshall Space Flight Center, Oct 30, 1998.

[102] Richard Bukac. *Experimental Performance Characterization of 1MW Continuous Duty Arc Heater*. Masters Thesis, The University of Alabama in Huntsville, 2007.

[103] LyTec. An mhd accelerator simulator for application to advanced propulsion: Monthly report 3. Technical Report LyTec-R-00-012, NASA, Marshall Space Flight Center, Oct 31, 2000.

[104] V.I. Alferov. Current status and potentialities of wind tunnels with mhd accelerators. *High Temperature*, 38(2):300–313, Mar 2000.

[105] Kenneth E. Tempelmeyer, Alfred K. Windmueller, and L.E. Rittenhouse. Development of a steady-flow $\mathbf{J} \times \mathbf{B}$ accelerator for wind tunnel application. Technical Report AEDC-TDR-64-261, U.S. Air Force, Arnold Engineering Development Center, Dec 1964.

[106] Stanford Gordon and Bonnie J. McBride. Computer program for calculation of complex chemical equilibrium compositions and applications: I. Analysis. Technical Report NASA RP-1311, National Aeronautics and Space Administration, Lewis Research Center, Oct 1994.

[107] Bonnie J. McBride and Stanford Gordon. Computer program for calculation of complex chemical equilibrium compositions and applications: II. Users manual and program description. Technical Report NASA RP-1311, National Aeronautics and Space Administration, Lewis Research Center, Jun 1996.

[108] Y.C. Lin Wu. Performance theory of diagonal conducting wall mhd generators. *AIAA Journal*, 14(10):1362–1368, Oct 1976.

[109] G.S. Argyropoulos, Sterge T. Demetriades, and A.P. Kendig. Current distribution in nonequilibrium $\mathbf{J} \times \mathbf{B}$ devices. *Journal of Applied Physics*, 38(13):5233–5239, Dec 1967.

[110] Gustave J. Hokenson. On wall friction in mhd channel flows. *AIAA Journal*, 15(9):1350–1353, Sep 1977.

[111] LyTec. An mhd accelerator simulator for application to advanced propulsion: Monthly report December 2001. Technical Report LyTec-R-01-030, National Aeronautics and Space Administration, Marshall Space Flight Center, Dec 31, 2001.

[112] Roy J. Schulz, James N. Chapman, and Robert P. Rhodes. Mhd augmented chemical rocket propulsion for space applications. In *AIAA 23rd Plasmadynamics and Lasers Conference*, number AIAA 1992-3001, Nashville, TN, 1992. American Institute of Aeronautics and Astronautics.

[113] LyTec. User's manual, LyTec mhd accelerator code: A computer code for analysis and design of mhd accelerator assisted propulsion devices. Technical Report LyTec-R-01-016, NASA, Marshall Space Flight Center, 2001.

[114] Stanford Gordon and Bonnie J. McBride. Computer progam for calculation of complex chemical equilibrium compositions, rocket performance, incident and reflected shocks, and chapman-jouget detonations. Technical Report NASA SP-273, National Aeronautics and Space Administration, Lewis Research Center, 1971.

[115] Richard J Rosa. Hall and ion slip effects in a nonuniform gas. *Physics of Fluids*, 5(9):1081–1090, Sep 1962.

[116] D.E. Chriss. An experimental investigation of ducted, reactive turbulent jet mixing with recirculation. Technical Report AEDC TR-77-56, U.S. Air Force, Arnold Engineering Development Center, Sep 1976. also AFOSR TR-77-0749 and ADA-044110.

[117] D. Pfirsch and R.N. Sudan. Nonlinear ideal magnetohydrodynamics instabilities. *Physics of Fluids B*, 5(7):2052–2061, 1993.

[118] Hermann Schlichting, Klaus Gersten, Egon Krause, and Herbert Oertel Jr. *Boundary Layer Theory*. Springler, Berlin, 8th edition, 2004.

[119] Richard J Rosa, Larry Farrar, and Dan Trudnowski. Electric arc behavior in a boundary layer. *Journal of Propulsion and Power*, 5(5):466–471, Sep-Oct 1988.

[120] Ezzat Danial Doss, G.S. Argyropoulos, and Sterge T. Demetriades. Influence of hall currents on flow seperation and asymmetry in mhd channels. In *AIAA 7th Fluid and Plasma Dynamics Conference*, number AIAA 1974-0509, Palo Alto, CA, 1974. American Institute of Aeronautics and Astronautics.

[121] Yen-Cheng Pan and Ezzat Danial Doss. Power takeoff analysis for diagonally connected mhd channels. *Journal of Energy*, 4(6):252–259, Nov-Dec 1980. also AIAA 1980-0253.

[122] Michael H. Frese. Mach2: A two-dimensional magnetohydrodynamic simulation code for complex experimental configurations. Technical Report AMRC-R-874, U.S. Air Force, Air Force Weapons Laboratory, Sep 1987.

[123] Robert E. Peterkin, Jr and Michael H. Frese. Mach: A reference manual - first edition. Technical report, U.S. Air Force, Air Force Research Laboratory: Phillips Research Site, Sep 14, 1998.

[124] Jason T. Cassibry. *Numerical Modeling Studies of a Coaxial Plasma Accelerator as a Standoff Driver for Magnetized Target Fusion.* Ph.D. Dissertation, The University of Alabama in Hunstville, 2004.

[125] Jacques X. Bouillard, John L. Krazinski, Surya Pratap Vanka, and Greg F. Berry. User's manual for mgmhd: A multigrid three-dimensional computer code for the analysis of magnetohydrodynamic generators and diffusers. U.S. Department of Energy ANL/MHD-89/1, U.S. Department of Energy, Argonne National Laboratory, Sep 1989.

[126] Surya Pratap Vanka and Rajesh K. Ahluwalia. Three-dimensional flow and thermal development in magnetohydrodynamic channels. *Journal of Energy*, 6(3):218–224, May-Jun 1982. also AIAA 1981-0247.

[127] Surya Pratap Vanka and G.K. Leaf. An efficient finite-difference calculation procedure for multi-dimensional fluid flows. In *AIAA/SAE/ASME 20th Joint Propulsion Conference*, number AIAA 1984-1244, Cincinnati, OH, 1984. American Institute of Aeronautics and Astronautics.

[128] Surya Pratap Vanka, Rajesh K. Ahluwalia, and Ezzat Danial Doss. Three-dimensional analysis of mhd generators and diffusers. Technical Report ANL/MHD-82-4, Department of Energy, Argonne National Laboratory, Mar 1982.

[129] Surya Pratap Vanka and Rajesh K. Ahluwalia. Coupled three-dimensional flow and electrical calculations for faraday mhd generators. *Journal of Energy*, 7(1):65–72, Jan-Feb 1983. also AIAA 1981-1230.

[130] Surya Pratap Vanka. Block-implicit computation of viscous internal flows - recent results. In *AIAA 25th Aerospace Sciences Meeting*, number AIAA 1987-0058, Reno, NV, 1987. American Institute of Aeronautics and Astronautics.

[131] S.V. Patankar and D.B. Spalding. A calculation procedure for heat, mass, and momentum transfer for three-dimensional parabolic flows. *International Journal of Heat and Mass Transfer*, 16:1787–1806, 1972.

[132] S.V. Patankar and D.B. Spalding. *Heat and Mass Transfer in Boundary Layers*. Intertext Books, London, 1975.

[133] Frank M. White. *Viscous Fluid Flow*. McGraw-Hill, Boston, MA, 2nd edition, 1991.

[134] W.P. Jones and B.E. Launder. The prediction of laminarization with a two-equation model of turbulence. *International Journal of Heat and Mass Transfer*, 15:301–314, 1972.

[135] B.E. Launder and D.B. Spalding. The numerical comutation of turbulent flows. *Computer Methods in Applied Mechanics and Engineering*, 3:269–289, 1972.

[136] C.V. Jayatillaka. *Resistance of Laminar Sublayer to Heat and Mass Transfer in Boundary Layers*. Ph.D. Dissertation, University of London, 1965.

[137] Rajesh K. Ahluwalia, Surya Pratap Vanka, Kwan H. Im, and Stanley A. Zwick. Formulation and assesment of a cross-plane electrical model for magnetyhydrodynamic channels. *Journal of Energy*, 6(5):314–322, Sep-Oct 1982.

[138] Stanley A. Zwick, Ezzat Danial Doss, Yuan C. Pan, and Shawky E. Shamma. Mhd channel electric boundary-layer theory and applications. *Journal of Energy*, 7(2):118–127, Mar-Apr 1983.

[139] Takehisa Hara and Juro Umoto. Three-dimensional effects of electrode configuration on diagonal mhd generator performance. *Journal of Energy*, 3(1):16–22, 1979.

[140] Rajesh K. Ahluwalia and Surya Pratap Vanka. Secondary flow effects in diagonal mhd channels. *Journal of Energy*, 7(5):387–388, Sep-Oct 1983.

[141] John David Jackson. *Clasical Electrodynamics*. John Wiley and Sons, Inc., New York, 3rd edition, 1999.

[142] Ezzat Danial Doss, H.A. Dwyer, and M.A. Hoffman. Influence of segmentation and ambipolar diffusion on mhd nonequilibrium boundary layers. *AIAA Journal*, 12(2):155–162, Feb 1974.

[143] Carlson C.P. Pian. Data analysis of diagonally connected magnetohydrodynamic power generator experiments. *Journal of Propulsion and Power*, 3(2):128–135, Mar-Apr 1987.

[144] Ezzat Danial Doss and Rajesh K. Ahluwalia. Three-dimensional flow development in mhd generators at part load. *Journal of Energy*, 7(4):289–290, Jul-Aug 1983. also AIAA 1982-0324.

[145] Surya Pratap Vanka. Block-implicit multigrid solution of navier stokes equations in primitive variables. *Journal of Computational Physics*, 65(1):138–158, 1986.

[146] Surya Pratap Vanka. Block-implicit calculation of steady turbulent recirculating flows. *International Journal of Heat and Mass Transfer*, 28(11):2033–2103, 1985.

[147] Surya Pratap Vanka. A calculation procedure for three-dimensional steady recirculating flow using multigrid methods. *Computer Methods in Applied Mechanics and Engineering*, 55:321–338, 1986.

[148] Surya Pratap Vanka. Block-implicit multigrid calculation of two-dimensional recirculating flows. *Computer Methods in Applied Mechanics and Engineering*, 59:29–48, 1986.

[149] A. Brandt. Multi-level adaptive solutions to boundary-value problems. *Mathematics of Computation*, 31(138):333–350, Apr 1977.

[150] A. Brandt. *Multigrid Techniques - 1984 Guide with Applications to Fluid Dynamics*. Lecture Series 1984-04. Von Karman Institute, Rhode Saint Genese, Belgium, 1984.

[151] F.E. Spencer and Arthur V. Phelps. Momentum transfer cross-sections and conductivity integrals for gases of mhd interest. In *15th Symposium of the Engineering Aspects of Magnetohydrodynamics (SEAM)*, University of Pennsylvania, Philadelphia, PA, 1976.

[152] Arthur V. Phelps. Jila collision data compilation, Accessed Jun 10, 2004. `ftp://jila.colorado.edu/collision_data/`.

[153] Ralph Stephen Devoto. *The Transport Properties of a Partially Ionized Monatomic Gas*. Ph.D. Dissertation, Stanford University, 1965.

[154] Joseph O. Hirschfelder, Charles F. Curtis, and R. Byron Bird. *Molecular Theory of Gases and Liquids*. John Wiley and Sons, New York, 2nd edition, 1964.

[155] Sydney Chapman and T.G. Cowling. *The Mathematical Theory of Non-Uniform Gases*. Cambridge University Press, Cambridge, 1970.

[156] Ralph Stephen Devoto. Transport coefficients of high pressure argon in a magnetic field. Unclassified ARL-71-0075, U.S. Air Force, Wright-Patterson Air Force Base, Apr 1971.

[157] Ralph Stephen Devoto. Transport properties of ionized monatomic gases. *The Physics of Fluids*, 9(6):1230–1240, Nov 1, 1966.

[158] Ralph Stephen Devoto. Simplified expressions for the transport properties of ionized monatomic gases. *The Physics of Fluids*, 10(10):2105–2112, Aug 8, 1967.

[159] Ralph Stephen Devoto. Transport coefficients of partially ionized argon. *The Physics of Fluids*, 10(2):354–364, Oct 17, 1967.

[160] Ralph Stephen Devoto. Transport coefficients of ionized argon. *The Physics of Fluids*, 16(5):616–623, Jun 30, 1973.

[161] S. Schweitzer and Morton Mitchner. Electrical conductivity of partially ionized gases. *AIAA Journal*, 4(6):1012–1019, Jun 1966.

[162] James S. Ball. Half-range generalized hermite polynomials and the related gaussian quadratures. *SIAM Journal on Numerical Analysis*, 40(6):2311–2317, 2003.

[163] Stephen Biagi. Professor, Department of Physics, University of Liverpool, Aug 25, 2005. Personal Communication via email.

[164] R.J. Zollweg and R.W. Liebermann. Electrical conductivity of nonideal plasmas. *Journal of Applied Physics*, 62(9):3621–3627, Nov 1, 1987.

[165] Ron J. Litchford. Senior research scientist, NASA Marshall Space Flight Center, 2006. Personal Communication.

[166] John T. Lineberry. President and CEO, LyTec LLC, 2006. Personal Communication.

[167] F.L. Galanga, John T. Lineberry, Y.C. Lin Wu, M.H. Scott, W.E. Baucum, and R.W. Clemons. Experimental results of the UTSI coal-fired mhd generator and investigations of various power takeoff schemes. In *AIAA 19th Aerospace Sciences Meeting*, number AIAA-1981-0030, St. Louis, MO, 1981. American Institute of Aeronautics and Astronautics.

[168] S. Kou and E. Levi. Analysis of power takeoff in diagonal conducting wall channels. *Journal of Energy*, 6(2):96–103, Mar-Apr 1982.

[169] John D. Anderson. *Modern Compressible Flow with Historical Perspective*. McGraw-Hill, Inc., New York, 1990.

[170] Jonathan E. Jones. Senior research scientist, NASA Marshall Space Flight Center, 2006. Personal Communication.

[171] Bryan Thompson. Magnetic field measurements of the MAPX electromagnet, 2006. Thompson Mechanical and Electrical Technologies, Box 83 Winchester, TN 37398.

[172] R.L. Fredrickson and J.C. Wu. Effects of hall currents on the performance of crossed field mhd accelerators. In Gordon and Breach, editors, *Proceedings of the 3rd Symposium on Engineering Aspects of Magnetohydrodynamics (SEAM)*, pages 527–537. Science Publishers, Inc., New York, 1963.

[173] Ezzat Danial Doss, G.S. Argyropoulos, and Sterge T. Demetriades. Two-dimensional flow inside mhd ducts with transverse asymmetries. *AIAA Journal*, 13(5):545–546, May 1975.

[174] Rajesh K. Ahluwalia and Ezzat Danial Doss. Convective heat transfer in mhd channels and its influence on channel performance. In *AIAA 18th Aerospace Sciences Meeting*, number AIAA 1980-0178, Pasadena, CA, 1980. American Institute of Aeronautics and Astronautics.

[175] Sterge T. Demetriades, C.D. Maxwell, Ezzat Danial Doss, and D.A. Oliver. Nonlinear loss mechanisms in advanced mhd generators. AFOSR Final Report AFOSR-TR-75-1432, Air Force Office of Scientific Research, 1975.

[176] Ezzat Danial Doss and B.P. Curry. Studies of the 3-D coupled flow between the electrode and side wall of mhd channels. In *AIAA 9th Fluid and Plasma Dynamics Conference*, number AIAA 1976-0311, San Diego, CA, 1976. American Institute of Aeronautics and Astronautics.

[177] A. Maciulaitis and A.L. Loeffler Jr. A theoretical investigation of mhd channel entrance flows. *AIAA Journal*, 2(12):2100–2103, Dec 1964.

[178] Merritt L. Hougen and James E. McCune. Magnetohydrodynamic instabilities in a weakly ionized, rotating plasma. *AIAA Journal*, 9(10):1947–1956, Oct 1971.

[179] Fujihiko Sakao. Some physical interpretations of magnetohydrodynamic duct flows. *AIAA Journal*, 1(4):915–916, Apr 1963.

[180] Hugh W. Coleman and W. Glenn Steel, Jr. *Experimentation And Uncertainty Analysis for Engineers*. John Wiley and Sons, Inc., New York, 2nd edition, 1999.

[181] Leon E. Ring. Optimization of mhd cross-field accelerators and generators. Technical Report AEDC-TDR-64-278, U.S. Air Force, Arnold Engineering Development Center, Jan 1965.

[182] Robert Mecklenberg. *Managing Projects with GNU Make*. O'Reilly, Sebastopol, CA, 3rd edition, 2005.

OK, so you're a Ph.D. Just don't touch anything.

—from the Internet